EXPERIMENTAL AND NUMERICAL MODELING-BASED CHARACTERIZATION OF FRACTURE PROCESS ZONE IN QUASI-BRITTLE MATERIALS

by
Prasoon Garg

A thesis submitted to the Faculty and the Board of Trustees of the Colorado School of Mines in partial fulfillment of the requirements of the degree of Doctor of Philosophy (Civil and Environmental Engineering).

Golden, Colorado

Date _____

Signed: _____
Prasoon Garg

Signed: _____
Dr. Ahmadreza Hedayat
Thesis Co-Advisor

Signed: _____
Dr. D.V. Griffiths
Thesis Co-Advisor

Golden, Colorado

Date: _____

Signed: _____
Dr. Junko Munakata Marr
Professor and Department Head
Civil and Environmental Engineering

ABSTRACT

Fracturing in quasi-brittle materials such as rocks involves the development of a significant size of the inelastic zone around the pre-crack tip, also known as the fracture process zone (FPZ). A comprehensive characterization of the FPZ is crucial for predicting the associated macroscopic cracking process, as it plays a vital role in the estimation of various crack properties, such as fracture toughness and tensile strength of the material. This thesis focused on investigating FPZ development in quasi-brittle material under different loading conditions using a combination of experimental testing and numerical modeling.

The work conducted in this thesis begins with developing a novel methodology for characterizing the FPZ evolution in pre-cracked Barre granite specimens under mode I loading. This novel methodology was based on the Digital image correlation (DIC) approach and facilitated the identification of a suitable constitutive model for material softening inside the FPZ. This is followed by an investigation of FPZ development under mode II loading using DIC in two different testing geometries. The analysis of these two geometries showed that novel methodology is reliable for characterizing the FPZ evolution in various loading conditions, and most mode II geometries don't result in a pure mode II fracture until a high level of confinement is applied to the specimen. This thesis identifies the short beam in compression (SBC) as a better alternative for estimating mode II fracture toughness than existing punch through shear testing configuration. The main advantage of the SBC geometry lies in the fact that it can be monitored using optical techniques such as DIC, which provide explicit evidence of fracture mode along with detailed information of about deformation characteristics of crack geometry.

The XFEM-based numerical models were used in this work to simulate the FPZ evolution in quasi-brittle materials due to their ability to model the multiple crack propagation without the need for remeshing. In this research, a novel XFEM-based user element was developed with the capability to model FPZ development in various crack types, especially in compression-induced shear cracks. This was done by implementing a new cohesive zone model that accounts for both cohesion degradation and frictional sliding in propagating shear cracks. The XFEM-based user element, through the implementation of advanced branching algorithms, is able to simulate multiple crack types from the body of pre-existing cracks, thereby removing the limitation of traditional XFEM models. As a result, the XFEM-based user element can reliably predict paths of secondary cracks along with crack coalescence mechanisms in pre-cracked rock specimens under compression loading.

TABLE OF CONTENTS

LIST OF FIGURES

LIST OF TABLES

LIST OF SYMBOLS

AE	Acoustic emission
ASED	Average strain energy density criterion
ASFPB	Anti-symmetric four-point bending
COV	Coefficient of Variation
CSTBD	Cracked straight-through Brazilian disc
CZM	Cohesive Zone model
DIC	Digital image correlation
DOF	Degree of freedom
EMTSN	Extended Maximum Tangential Strain
FPZ	Fracture process zone
FPZ-I	Fracture process zone initiation
GMTS	Generalized maximum tangential stress criterion
GSED	Generalized strain energy density criterion
GSA	Global sensitivity analysis
LCZM	Linear Cohesive Zone model
LEFM	Linear elastic fracture mechanics
MC	Mohr-Coulomb criterion
MCS	Monte Carlo simulation
MPS	Maximum Principal Stress criterion
MSS	Maximum shear stress criterion
MTS	Maximum tangential stress criterion
MTSN	Maximum Tangential Strain criterion
NDB	Notched deep beam
NEFM	Non-elastic fracture mechanics
NSE	Nash–Sutcliffe efficiency
PDF	Probability distribution function
PTS	Punch through shear
RBF	Radial basis function
RMS	Root mean square
SBC	Short beam in compression

SCC	Short core compression
SS	Subset size
SIF	Stress intensity factor
TFZ	Traction free zone
XFEM	Extended Finite Element Method
a	half flaw length
a_o	Notch length
A_1, B_1, A_2, B_2	Material constants
$a_J, b_{I\alpha}$	Degrees of freedom of the enriched nodes
$\hat{a}_{J,k}$	Enriched degrees of freedom for kth fracture
$\hat{b}_{m,l}$	Enriched degrees of freedom for lth crack junction
B	Specimen thickness
B^{std}, B^{enr}	Derivatives of standard and enriched shape functions
c	Ligament length of SBC specimen
C	Elastic stiffness tensor
COD	Crack opening displacement
CSD	Crack sliding displacement
COD_e, COD_s	Elastic and critical crack opening displacement
CSD_e, CSD_s	Elastic and critical crack sliding displacement
$CTOD$	Crack tip opening displacement
$CTSD$	Crack tip sliding displacement
$CMOD$	Crack mouth opening displacement
d	Half span of NDB beams
d_1, d_2	Distances for wing crack initiation from two flaw tips
D^{tan}	Tangent stiffness matrix of a crack
E	Young's modulus
E_{ae}, E_{Gae}	Local and accumulated value of AE energy
$E_{e,}E_o$	AE event energy and its minimum value
F	Normalized crack driving force
$f(\bar{\boldsymbol{\sigma}})$	Crack driving force

F_n, F_s	Normal and shear force on the double-edge notched specimen
f_t	Yield envelop for tensile-dominated crack
f_s^{com}, f_s^{ten}	Yield envelop for shear crack under compressive and tensile loading regime
$\boldsymbol{f}_u^{ext}, \boldsymbol{f}_a^{ext}$	External force vector corresponding to standard and enriched degrees of freedom
$\boldsymbol{f}_u^{int}, \boldsymbol{f}_a^{int}$	Internal force vector corresponding to standard and enriched degrees of freedom
G_F	Fracture energy
G_{IC}, G_{IIC}	Critical values of mode I and mode II fracture energy
G_f	Dissipated energy in a unit area of FPZ
H	Specimen height
H_o	Thickness of the knife-edge
h_c	Length of secondary crack
$H(x), J(x)$	Heaviside and Junction enrichment functions
$J_I(x), J_{II}(x)$	Junction enrichment functions for first and second secondary fractures
$\boldsymbol{K}_{uu}, \boldsymbol{K}_{ua}, \boldsymbol{K}_{aa}$	Components of the element stiffness matrix
k	Equivalent crack stiffness
k_s	Shear crack stiffness
k_P	Penalty stiffness of crack
L	Specimen's height
l_g	Ligament length between two flaws
l, L_{FPZ}	Developing and fully developed fracture process zone
l_{TFZ}	Length of traction free zone
L	Strain differential operator
N^{std}, N^{enr}	Standard and enriched shape functions
$N_I(x)$	Standard nodal shape functions
K_{Ic}, K_{IIc}	Mode I and Mode II fracture toughness
K_I, K_{II}	Mode I and II stress intensity factor
K_{II}^{num}	Numerical mode II stress intensity factor

W	Specimen's Width
ν	Poisson's ratio
P_{peak}	Peak load
P_{norm}	Normalized applied load
p_C	Confining pressure applied on clay specimens
Q4	Plane strain user element in Abaqus
s	Spacing
Y_I, Y_{II}	Mode I and Mode II geometric factor
x, y	Coordinates
x_1, y_1	Local coordinates along the crack plane
$\hat{x}, \hat{y}$	Local coordinates along the notch plane
$\boldsymbol{n}, \boldsymbol{s}$	Normal and tangent vectors of an imaginary axis
U, V	Displacement in x and y direction
U_1, V_1	Displacement in $\hat{x}$ and $\hat{y}$ direction
$\partial U \,/\, \partial x$	Gradient of horizontal displacement with respect to x direction
$\partial V \,/\, \partial x$	Gradient of vertical displacement with respect to x direction
x_i, y_i, z_i	AE sensor location
t_0, t_1	Start and end time of the AE signal
r_i	Distance of the event from the i^{th} channel
V	Voltage of the AE signal
δ	Load-point displacement
δ_{peak}	Load-point displacement at peak load
δ_{norm}	Normalized load-point displacement
$\partial CTOD/\partial(\delta_{norm})$	CTOD derivative
σ_t	Tensile strength of rock
σ_y	Applied vertical stress on gypsum specimens
ϵ_{xx}	Horizontal strain
w	Crack opening displacement
w_e, w_c	Elastic and critical crack opening displacement

w^{ct}, w_{ne}^{ct}	Total and Inelastic components of CTOD
w_{ne}	Inelastic component of COD
w_{ne}^{c}	Critical value of the inelastic component of COD
σ	Cohesive stress
σ_e	External tensile stress
σ^{ct}	Cohesive stress at the notch tip
α	Proportionality coefficient between fracture energy and AE energy
Δa	Crack extension length
C	Continuity
w	Crack opening displacement
w_e	Elastic opening displacement
w_{ne}	Inelastic crack opening displacement
w_c	Critical crack opening displacement
w_{ne}^{c}	Critical inelastic crack opening displacement
δ	Load-point displacement
δ_{peak}	Load-point displacement at peak load
δ_{norm}	Normalized load-point displacement
σ_n	Cohesive stress
σ_e	External tensile stress
σ_t	Tensile strength of rock
$\sigma_{n,max}$	Cohesive strength
S_i	First order Sobol's index for i^{th} input parameter
S_{T_i}	Total effects Sobol' index for i^{th} input parameter
$u(x)$	Total displacement
$u_{cont}(x), \mathrm{u}_{disc}(x)$	Continuous and discontinuous parts of displacement
$F_\alpha(x)$	Crack tip enrichment functions
u_I	Nodal displacement for standard nodes
K_Γ, K_Λ	Nodal subsets containing crack
τ_f	Shear strength of SBC specimens
σ_t	Tensile strength of rock

σ_c	Confining pressure on the SBC specimen
σ_{11}	Maximum principal stress
τ_{xy}	Shear stress
ϵ_{22}	Minimum principal strain
γ_{max}	Maximum shear strain
$\partial COD/\partial(\delta_{norm})$	COD derivative
$[\![N^{enr}]\!]$	Jump of enriched shape function
$N_I^{std}(x)$	Standard shape function of node I
t_n, t_s	Normal and shear components of crack traction
$\Delta t_s, \Delta t_n$	Increment value of normal and shear crack traction
t_c^{max}, t_c	Maximum value and the current value of crack cohesion
u_n	Normal displacement applied on the double-edge notched specimen
u_y	Vertical displacement applied on clay specimen
$\overline{u}, \overline{t}$	Prescribed value of displacement and traction vector on the domain boundary
u^h	Total displacement field
u_{std}^h, u_{enr}^h	Continuous and discontinuous parts of the displacement field
u^+, u^-	Displacement on positive and negative surfaces of the crack
$[\![u]\!]$	Displacement jump vector between two crack surfaces
$[\![u]\!]_n, [\![u]\!]_s$	Normal and shear components of crack displacement
$\Delta[\![u]\!]_s, \Delta[\![u]\!]_n$	Increment value of normal and shear components of crack displacement
$[\![u]\!]_{eq}^o, [\![u]\!]_{eq}^{max}$	Initial and current maximum value of equivalent crack displacement
$[\![u]\!]_s^o, [\![u]\!]_s^{max}$	Initial value and current maximum value of shear crack displacement
δu	Virtual displacement field
$\delta[\![u]\!]$	Virtual displacement jump vector
$\delta\hat{\boldsymbol{u}}, \delta\hat{\boldsymbol{c}}$	Test function of virtual displacement and strain field

$\hat{u}_I, \hat{a}_J$	Standard and enriched degrees of freedom
σ	Cauchy stress tensor
Ω	Domain
Γ_d	Total crack boundary
Γ_u, Γ_t	Dirichlet and Neumann boundary
Γ_{fpz} , Γ_{tf}	Fracture process zone and traction-free part of the crack boundary
$n^+_{\Gamma_d}, n^-_{\Gamma_d}$	Positive and negative direction of the normal vector to crack surface
n_Γ	Outward unit normal vector to external boundary of the body
ε	Strain tensor
∇, ∇^s	Divergence operator and its symmetry part
$\delta\varepsilon$	Virtual strain field
$t_{eq}, [\![u]\!]_{eq}$	Equivalent value of traction and crack displacement on crack surface
β	Weighting parameter
$\mathcal{N}$	Set of all nodes in the mesh
$\mathcal{N}^{dis}$	Set of nodes containing Heaviside enrichment
$\Phi_J(x)$	Special enrichment function for node J
$\varphi(x)$	Signed distance function
$\mathcal{M}_b$	Number of fractures in the domain
$\varphi_I(x), \varphi_{II}(x)$	Signed distance function of crack 1 (main fracture) and crack 2 (secondary fracture)
$\mathcal{N}^{junc}$	Set of nodes supported by crack junction
$\mathcal{M}_c$	Number of crack intersections
μ	Coefficient of friction
ϕ	Friction angle of the material
θ_f	Angle of failure in compression test of clay specimens
θ_w	Wing crack initiation angle
β_w	Flaw inclination angle
ϕ	Friction angle

η	Imaginary axis
$\bar{\boldsymbol{\sigma}}$	Average crack stress tensor
σ_0	Material strength
θ	Angle of Imaginary axis with respect to the x_1-axis.
θ_0	Crack propagation angle with respect to the x_1-axis

ACKNOWLEDGEMENTS

It has been a great journey through my Ph.D. at the Colorado School of Mines. The support and love I have received is unmatchable. I consider myself fortunate to be one of the graduates of this great university. In this journey, I have received help, support, and motivation from the number of people whom I owe at least a “thank you.”

I take this opportunity to acknowledge every person who helped me in this journey, and without their support, this scientific contribution was impossible. I would like to express sincere gratitude towards my Ph.D. advisors, Dr. Ahmadreza Hedayat, and Prof. D.V. Griffiths, for their guidance and encouragement throughout my research. I am immensely grateful to them for giving me this opportunity and trusting my ability to explore the technical aspects. I have always appreciated their mentorship style, critical thoughts, and questions during our weekly meetings. Their approach to a problem and views on the applicability of research has been a great lesson for me and would certainly help to improve myself in my professional career continuously. I feel fortunate and honored to have worked with them. I am also thankful to Dr. Omid Moradian for his suggestions on this work. I would also like to express my most profound appreciation to my thesis committee members, Dr. Mohsen Asle Zaeem, Dr. Lori Tunstall, and Dr. Jamal Rostami, for guiding me through my research.

I would also acknowledge the help and support from my great colleagues at the Colorado School of Mines: Dr. Ketan Arora, Dr. Sankhneel Sinha, Dr. Deepanshu Shirole, Dr. Vivek Kashyap, Akash Chaurasia, and Rohit Bardapurkar. The research was supported by the National Science Foundation under Award number 1644326.

To the most intelligent people, I have ever known,

To the most industrious person, who motivated me to pursue higher studies,

To my Mom and Dad, whose values will remain with me Forever.

CHAPTER 1

THESIS INTRODUCTION

1.1 Introduction

Rock behavior is often governed by various fracturing processes, such as crack initiation, propagation, and interaction between new and existing fractures. These fracturing processes also have an essential role in the stability of rock structures (e.g., slopes, foundations, and tunnels) and other activities such as geologic sequestration of nuclear waste, geothermal energy production, and hydraulic fracturing (Hoek et al., 1995; Zoback et al., 1997). Therefore, a thorough understanding of rock materials' deformation and cracking behavior can be a useful tool for the design analysis of rock structures. Fracturing in geomaterials such as rocks is preceded by the damage initiation at the micro-scale (~ μm), which physically represents inter and intra-granular cracks (Nasseri et al. 2010; Tianyang, 2020). The micro-scale cracking in geomaterials results in the formation of an inelastic region around the tip of preexisting flaws, also known as the fracture process zone (FPZ) (Labuz et al., 1987). In geomaterials, the size of the FPZ can be large enough to introduce significant nonlinearity in the stress-strain curve, typically in the form of strain-softening behavior in the post-peak regime (Dutler et al., 2018; Brook et al., 2013). Thus, geomaterials such as rocks are considered "quasi-brittle" as they derive their fracture resistance based on subcritical micro-cracking instead of ideal-brittle behavior (Shah et al., 1995). The fracturing in ideal-brittle material results in linearly elastic stress-strain behavior up to peak strength followed by a complete failure of the specimen due to sudden propagation of fracture from the tip of preexisting flaw (Shah et al., 1995). The FPZ typically

represents a highly damaged region ahead of the crack tip, which can have a significant impact on macroscopic fracture behavior and overall failure of rock, especially in cases where its size is comparable to preexisting cracks (Backers et al., 2005; Ghamgosar and Erarslan, 2016; Tarokh et al., 2017). Various studies (Wang et al., 2016; Wei et al., 2016; Lin et al., 2018; Wong and Guo et al., 2019) have shown that the FPZ plays a vital role in the accurate characterization of crack properties such as fracture energy, toughness and tensile strength of most-quasi-brittle materials. Therefore, conducting a comprehensive investigation of FPZ development in quasi-brittle materials is essential.

Crack initiation and propagation in quasi-brittle materials have been extensively investigated using analytical, experimental, and numerical methods (Park and Bobet, 2009; Yao et al., 2011; Aliha et al., 2013; Wu and Wong, 2012, 2013; Ayatollahi et al., 2015). Numerical modeling provides valuable insight into the mechanism of cracking processes, especially in cases of complex geometry or loading conditions, which are difficult to test in the laboratory. Over the years, various numerical methods were developed to simulate the cracking process of quasi-brittle materials, such as the gradient-enhanced damage model (Perling et al., 1996,1998), Displacement discontinuity method (Bobet and Einstein, 1998; Goncalves and Einstein, 2013), numerical manifold method (Wu and Cai., 2014; Yang and Tang, 2016), and the extended finite element method (XFEM) (Well and Sullys, 2001; Zi and Belytschko, 2003; Karihaloo and Xiao, 2003). Most of the aforementioned numerical models rely on one or more crack initiation criteria for proper predictions of fracture characteristics, such as its direction, crack type, and length. Several crack initiation and propagation criteria have been proposed for quasi-brittle materials such as rocks and rock-like materials. These criteria are typically divided into three categories:

(a) stress-based criteria (Bobet, 1997; Khan and Khraisheh, 2000), (b) energy-based criteria (Hussain et al., 1974; Sih, 1974), and (c) strain-based criteria (Chang, 1981; Reyes, 1991; Gonçalves and Einstein, 2013). Most of these crack initiation criteria are, however, based on linear elastic fracture mechanics (LEFM) theory that assumes small-scale yielding, i.e., the small size of the inelastic region (FPZ) around the crack tip, and thus elastic deformation of rock is approximated for crack propagation (Gonçalves, 2009). This assumption contrasts with the observation of experimental studies (Labuz et al., 1987; Lin et al., 2019a-b; Zhao et al., 2016; Zhao et al., 2018) that have found the significant size of the FPZ around the crack tip in various laboratory-scale rocks. Therefore, it is essential to implement crack growth criteria that account for FPZ development in rocks.

This thesis characterized the formation of FPZ in a quasi-brittle material such as Barre granite using laboratory experiments and numerical modeling. Barre granite and other granodiorite rocks are common felsic intrusive rocks in the upper Earth's crust, making them a promising host in many geosciences engineering practices, such as high-level nuclear waste disposal and enhanced geothermal systems (Li et al., 2019; Tianyang, 2020). The Barre granite is a crystalline rock forming a part of the Devonian New Hampshire pluton series located in the southwest region of Burlington, Vermont (USA) (Shirole et al., 2020). It has been extensively studied under various loading conditions (Goldsmith et al., 1976; Dai and Xia, 2010; Morgan et al., 2013; Moradian et al., 2016; Saadat and Taheri, 2019; Iqbal and Mohanty, 2007; Li and Einstein, 2017; Li et al., 2019) which provide good data set for its fracture properties. The data from the above studies is also valuable for quantifying variability in Barre granite's material properties.

1.1.1 Fracture Process Zone (FPZ) and its Characterization

The fracture process zone (FPZ) in quasi-brittle materials refers to the cluster of microcracks formed at the tip of a macroscopic crack under elevated loading. The FPZ formation results in considerable energy dissipation and thus increases the fracture resistance of the material. The fracture growth in rocks can be characterized by the initiation and propagation of micro-cracks inside the FPZ, which then undergo large-scale coalescence to form macro-scale discontinuities and macroscopic fracture surfaces (Dutler et al., 2018).

Direct observation of FPZ is difficult because of the small scale at which micro-structural events interact with a failure process. The FPZ in some rocks, such as Carrara marble and Barre granite, can be observed as white patches (Wong and Einstein, 2009a; Morgan et al., 2013). However, it is difficult to detect the FPZ through visual inspection due to cracking at the microscopic scale. It is conventionally identified using high-resolution microscopic imaging techniques such as SEM and optical microscopes (Lu et al., 2019; Li and Einstein, 2017). These techniques provide a qualitative assessment of micro-deformation inside the FPZ in the form of changes in micro-crack density and surface morphology (Nasseri et al., 2005; Wong and Einstein, 2009b; Cheng et al., 2018). However, they don't provide any quantitative information about the material behavior inside FPZ, such as the stress or strain field around the crack tip that can be used in a crack initiation criterion to incorporate the inelastic deformation due to the formation of the FPZ. Consequently, it is imperative to develop techniques that can quantitatively estimate the material behavior inside the FPZ and assess the conditions required for macroscopic crack initiation. Alternatively, non-destructive techniques (NDT) such as ultrasonic methods, speckle interferometry, and digital image correlation (DIC) offer distinct

advantages over traditional approaches due to their capability to characterize the micro-cracking processes in both intact rock (Martin et al., 2018a-b; Dautriat et al., 2011; Shirole et al., 2019) and pre-cracked specimens (Le et al., 2014; Modiriasari et al., 2017, 2018; Aliabadian et al., 2019) during the entire loading stage while allowing easy and noninvasive implementation. Among these methods, AE and DIC have attracted much attention. The ability of AE to trace the inelastic deformation inside the cracked specimens has made it a very powerful technique for characterizing the FPZ (Zhang et al., 2018). At the same time, the DIC provides detailed information about surface displacements and can be used to estimate the various fracture characteristics, such as critical crack displacements and crack geometry (Zhao et al., 2022).

The nonlinear fracture mechanics-based criterion, such as the cohesive zone model (CZM), has been extensively used in characterizing the cracking in quasi-brittle materials due to its simple and robust representation of the complex micro-cracking process inside the FPZ. The model was developed by Hillerborg et al. (1976) from the work of Barenblatt (1959) and (Dugdale, 1960), which assumes crack length being composed of a traction-free part and a process zone (FPZ). The CZM represents the finite-width FPZ using a thin interface that undergoes progressive softening based on the traction-displacement law (Rinehart et al., 2015). Various types of CZMs, such as linear, bilinear, and exponential softening law inside FPZ, have been used to predict the fracture behavior in different quasi-brittle materials such as concrete, asphalt mixtures, and rock (Bazant and Planas, 1997; Elices et al., 2002; Roesler et al., 2007; Song et al. 2006; Rinehart et al., 2015). Identifying a suitable softening law plays an essential role in predicting fracture behavior (Shet and Chandra, 2004; De Borst, 2003) which can be done

using various NDT techniques such as DIC and AE. These techniques provide essential information about different material characteristics inside the FPZ.

1.1.2 Numerical Simulation of FPZ

Numerical simulations can provide valuable insights into the kinematic of the FPZ during fracture propagation in quasi-brittle materials, as shown by various studies in concrete (Roesler et al., 2007; Song et al., 2006; Parisio et al., 2019) and rocks (Xie et al., 2017; Jia and Zhou, 2022). Over the years, various numerical methods were developed to simulate the complex micro-cracking process in the FPZ, including the phase field method (Zhang et al., 2017; Bryant and Sun, 2018), the gradient-enhanced damage model (Perling et al., 1996,1998), cracking particles (Rabczuk et al., 2004), and the extended finite element method (XFEM) (Well and Sullys, 2001; Karihaloo and Xiao, 2003). In particular, the XFEM has attracted considerable attention due to its effectiveness in modeling discontinuities without needing the remeshing process, along with the capability of simulating multiple fracture interactions in the same domain (Daux et al., 2000; Moës and Belytschko, 2002; Zi and Belytschko, 2003). The XFEM-based models have been increasingly used in various crack problems in quasi-brittle materials, such as multiple crack interaction during hydraulic fracturing (Youn, 2016; Cruz et al., 2019; Yang et al., 2019), crack propagation from open or closed preexisting flaws in rocks (Sharafisafa and Nazem, 2014; Zhuang et al., 2014), and softening in rock faults (Liu and Borja, 2008, 2009).

1.2 Research Questions and Needs

The NDT technique, such as DIC, has been extensively used to study the development of the FPZ in various quasi-brittle materials such as rocks and concrete (Li and Einstein, 2017; Dong et

al., 2017; Zhou et al., 2018; Chen et al., 2019). However, most of these studies lack a consistent methodology for characterizing the FPZ evolution and its transition to macro-crack, which often results in inconsistencies in estimating the FPZ initiation and macro-crack initiation stage. For instance, some studies (Miao et al., 2018; Zhang et al., 2018; Lu et al., 2019) assumed that macro-crack initiates at the peak load, which leads to a decrease in the global load. However, other studies such as Aggelis et al. (2013), Yu et al. (2018), and Lin et al. (2019a), based on the combination of AE and DIC techniques, have found the FPZ being partially developed at the peak load which results in macro-crack initiation occurring in the post-peak regime. The identification of these stages is further complicated by highly localized material behavior around the crack tip which is significantly influenced by various structural inhomogeneity such as micro-defects and grain size (Lin et al., 2019a). As a result, a considerable variation in fracture properties is found for rocks, as seen, for example, in Berea sandstone (Lin and Labuz, 2013; Lin et al., 2019b), with significant scatter in the critical opening displacement (30–100 μm) and fracture energy (75–140 J/m2). These uncertainties make it difficult to characterize the softening behavior inside FPZ properly. Thus, developing a methodology that can characterize the FPZ evolution consistently is essential for minimizing the uncertainty in the fracture properties and parameters of CZM.

The large variability in fracture properties is also the primary reason for the limited application of CZM in most quasi-brittle material, especially in rocks (Fakhimi and Tarokh, 2013; Khoramishad et al., 2013; Rinehart et al., 2015; Yang et al., 2019). For instance, Rinehart et al. (2015), based on the implementation of the LCZM in Limestone specimens, found that accurate estimation of material properties is vital for the proper prediction of fracture processes

and the global response of the rock specimens. Besides material heterogeneity, uncertainties can also occur due to other sources, such as the natural variation of properties, imperfections, and unpredictability caused by insufficient information on parameters or models (Baecher and Christian, 2003). The recent studies by Aliha et al. (2012), Aliha and Ayatolllahi (2014), and Aliha et al. (2018) attempted to quantify the extent of variability in fracture properties using statistical analyses on a more significant number of test data (~15 samples) of various rocks such as Harsin marble and Guiting Limestone. However, these studies were based on LEFM (assuming the elastic stress distribution around the crack tip) and thus didn't account for the FPZ and its influence on overall fracture behavior. To characterize uncertainty in the CZM, variability in its input parameters can be identified by testing a large number of specimens (Bažant and Yu, 2011; Khoramishad et al., 2013; Rinehart et al., 2015) which can be time costly and thus may not be cost-effective. This would be complicated by multiple fracture properties required as different tests would be needed for each property. A better solution would be to conduct a large number of tests for properties that significantly influence the fracture behavior of the rocks. Therefore, it is essential to implement an integrated approach that quantifies uncertainty in the input parameters of the CZM, which can then be used to find the most significant material parameters of rock that results in considerable variability in its fracture characteristics.

While the evolution of FPZ in mode I fracture has been extensively investigated, there are limited studies on FPZ development for pure mode II fractures in quasi-brittle materials such as concrete and rocks (Ji et al., 2016; Lin et al., 2019c; Lin et al., 2020b; Zhao et al., 2022). Various geometries such as anti-symmetric four-point bending (ASFPB) (Wang et al., 2016), semicircular bend (SCB) with an inclined notch (Aliha et al., 2006), short core in compression

(SCC) (Xu et al., 2020) and punch-through shear (PTS) (Backers et al., 2002) have been proposed for mode II fracture testing. The application of most of these geometries is based on linear elastic fracture mechanics (LEFM), which assumes that the pure mode II loading results in a pure mode II fracture. However, this is not always as case, as shown by recent studies (Ji et al., 2016; Liu et al., 2018; Zhao et al., 2022) that have found the formation of mode I fracture despite the application of mode II loading at the notch tip in various quasi-brittle materials. Additionally, some studies (Merlin et al., 1986; Rao et al., 2003; Lin et al., 2019) have suggested that pure mode II fracture in most quasi-brittle materials can be very difficult to create unless the tensile stresses at the crack tip are eliminated by applying a high level of confining stresses. The proper investigation of fracture mode and other characteristics requires a detailed analysis of FPZ evolution under mode II loading, which is lacking in existing studies (Ji et al., 2016; Lin et al., 2020b; Fan et al., 2022; Zhao et al., 2022). Thus it is essential to answer the question, "how does mode II loading fundamentally affects the development of the FPZ and governs different crack characteristics such as crack type?". A proper understanding of FZP development under mode II loading would require a suitable testing configuration that generates mode II fracture in quasi-brittle materials.

Even though XFEM has been increasingly used for simulating FPZ development in quasi-brittle materials such as concrete and rocks (Moës and Belytschko, 2002; Meschke and Dumstorff, 2007; Wang et al., 2015; Xie et al., 2017; Jia and Zhou, 2022), most of these studies have been mainly focused on simulating fracture growth under tensile or tensile-shear loading. The fracturing under compression or compression-shear loading using the XFEM-based numerical model has rarely been investigated except for a few studies (Liu and Borja, 2008;

Sanborn and Prévost, 2011; Mikaeili and Liu, 2018). The compression-induced shear fractures in most geomaterials have a few distinct characteristics compared to tensile loading-induced fractures. First, friction contact exists between two surfaces of the compression-induced shear fracture, which plays a vital role in crack propagation mechanics and creates a residual shear strength of the crack (Borja and Foster, 2007). Second, the softening inside the FPZ of shear fractures strongly depends on existing confining pressure as it affects both the peak and residual strength of the crack (Gill, 2021) and thus requires an adequate strength degradation law to account for confinement-dependent material softening. The few existing XFEM studies on shear cracks have mainly used the standard plasticity model in conjunction with the Mohr-Coulomb (MC) criterion to simulate the propagation of frictional cracks (Liu and Borja, 2008; Sanborn and Prévost, 2011; Khoei, 2014). As a result, these models can only capture pressure dependency of peak shear strength and don't account for material softening inside the FPZ of the shear cracks. Therefore, it is essential to implement a reliable softening model which accounts for both cohesion degradation and frictional sliding in shear cracks to ensure proper incorporation of confinement-dependent softening inside the FPZ.

Modeling complex cracking patterns in quasi-brittle materials is another major challenge for most XFEM-based numerical models. The cracking in quasi-brittle materials such as rocks and rock-like materials under compressive loading typically results in various secondary cracks, which are often responsible for their failure (Park and Bobet, 2009). These secondary cracks typically comprise different shear crack patterns, such as coplanar, oblique, and out-of-plane (Bobet, 1997; Cheng et al., 2016). In most rocks, these secondary cracks often involve complex combinations of tensile (mode I) and shear (mode II) fractures, such as horsetail cracks and anti-

wings, mixed tensile–shear cracks (Wong and Einstein, 2009a; Morgan et al., 2013; Wong and Li, 2011; Lee and Jeon, 2011). The central observation of these experimental studies is the formation of multiple fractures emanating from a preexisting crack, which can be called crack branching based on the theory of fracture mechanics (Fatehi Marji, 2014; Chen and Zhou, 2020). The mechanism of crack branching is a complicated process and typically requires a reliable branching criterion to estimate the bifurcation point, defined as a point where the single crack tip results in the formation of two cracks (Rabczuk, 2013; Sun et al., 2021). These complex crack branching mechanisms have not been investigated using XFEM-based numerical methods. Most of the current XFEM studies are limited to modeling crack coalescence/intersection involving two or more cracks interacting with each other. As a result, these studies can only predict tensile cracks in rocks, which are more likely to initiate first and are known as primary cracks for specimens under compression loading. Therefore, it is essential to develop proper techniques to simulate crack branching in XFEM that can be used to predict the formation of secondary cracks in quasi-brittle materials.

1.3 Research Objectives

The primary goals of this thesis were to achieve an improved understanding of FPZ development in a quasi-brittle material using laboratory experiments and to develop a robust numerical modeling program for its simulation in various loading conditions. To achieve the research goal, the following objectives have been pursued:

1. Characterization of FPZ development for mode I fracture and identification of suitable fracture criteria that predict material softening inside the FPZ of Barre granite.

2. Evaluation of LCZM's performance in predicting the FPZ evolution in pre-cracked Barre granite specimens using an integrated approach.
3. Determination of a suitable geometry for mode II fracture testing along with investigating the influence of pure mode II loading on the FPZ evolution in pre-cracked Barre granite specimens.
4. Development of a new XFEM-based user element capable of simulating FPZ development and crack branching in quasi-brittle materials.
5. Application of XFEM-based user element in modeling the secondary cracks in rock-like material under compressive loading.

The aforementioned objectives provided a consistent rationale for analyzing FPZ development in pre-cracked quasi-brittle material under both tensile and compressive loading.

1.4 Research Tasks

The objectives of the thesis were achieved through a combination of experimental testing and numerical simulation programs involving a detailed analysis of experimental data and the implementation of various constitutive models for fracture growth. The tasks that were performed to accomplish the research objectives are described in the following sub-sections.

1.4.1 Tasks Related to "Objective 1"

- Developed a DIC-based novel methodology to characterize FPZ evolution in a consistent manner for Barre granite specimens.
- Performed three-point bending tests on pre-cracked Barre granite specimens subjected to mode I loading along with simultaneous monitoring of its surface using 2D-DIC and AE.

- Identified a suitable softening model for defining the inelastic deformation inside the FPZ.
- Corroborated DIC-based FPZ characteristics, such as its length and width, with AE-based measurements at various loading stages.

1.4.2 Tasks Related to "Objective 2"

- Implemented an integrated approach to test the performance of the linear cohesive zone model, which involves an XFEM-based numerical model, uncertainty quantification of overall fracture behavior, and global sensitivity analysis.
- Investigated the accuracy of the XFEM-based numerical model in predicting the FPZ characteristics, such as its length and initiation stage for pre-cracked Barre granite specimens, based on average values of its material properties.
- Implemented a regression model (Radial basis function) that acted as a surrogate to the XFEM fracture model under mode I loading
- Investigated the effect of uncertainty in material parameters of Barre granite on the variability of its overall fracture behavior using Monte Carlo simulation
- Determined relative importance ranking of fracture properties of Barre granite towards its global behavior.

1.4.3 Tasks Related to "Objective 3"

- Characterized the FPZ evolution in Barre granite under pure mode II loading using 2D-DIC.

- Explore the existing geometries for mode II fracture testing in rocks to identify the suitable configuration resulting in a pure mode II fracture
- Identify the suitable mode II geometry based on fracture mode and overall failure patterns observed in Barre granite specimens.

1.4.4 Tasks Related to "Objective 4"

- Develop an XFEM-based user element in Abaqus capable of simulating multiple crack interactions, including crack branching, which allows the formation of different crack types from the body of a preexisting fracture.
- Develop a novel branching methodology that can predict crack branching purely based on the stress state around preexisting fractures.
- Implement cohesive zone models that simulate material softening inside the FPZ formed in various fracture types, such as mode I crack, mixed-mode I/II crack, and compression-induced mode II crack.
- Validate the XFEM-based user element in predicting the FPZ characteristics of quasi-brittle materials under various loading conditions.
- Assess the branching capability of XFEM-based user element in predicting various crack types formed in rock-like material with an inclined flaw subjected to uniaxial compression loading.

1.4.5 Tasks Related to "Objective 5"

- Assessed the applicability of XFEM-based user element in simulating secondary cracks in gypsum specimens under compression loading

- Implemented a mixed-mode I/II criteria capable of predicting secondary cracks
- Compared the influence of crack initiation criteria on various characteristics of secondary cracks, such as its overall path and crack type in the cases of gypsum specimens with one and two flaws
- Predicted the overall crack pattern in specimens rock-like material containing two flaws at different configurations.

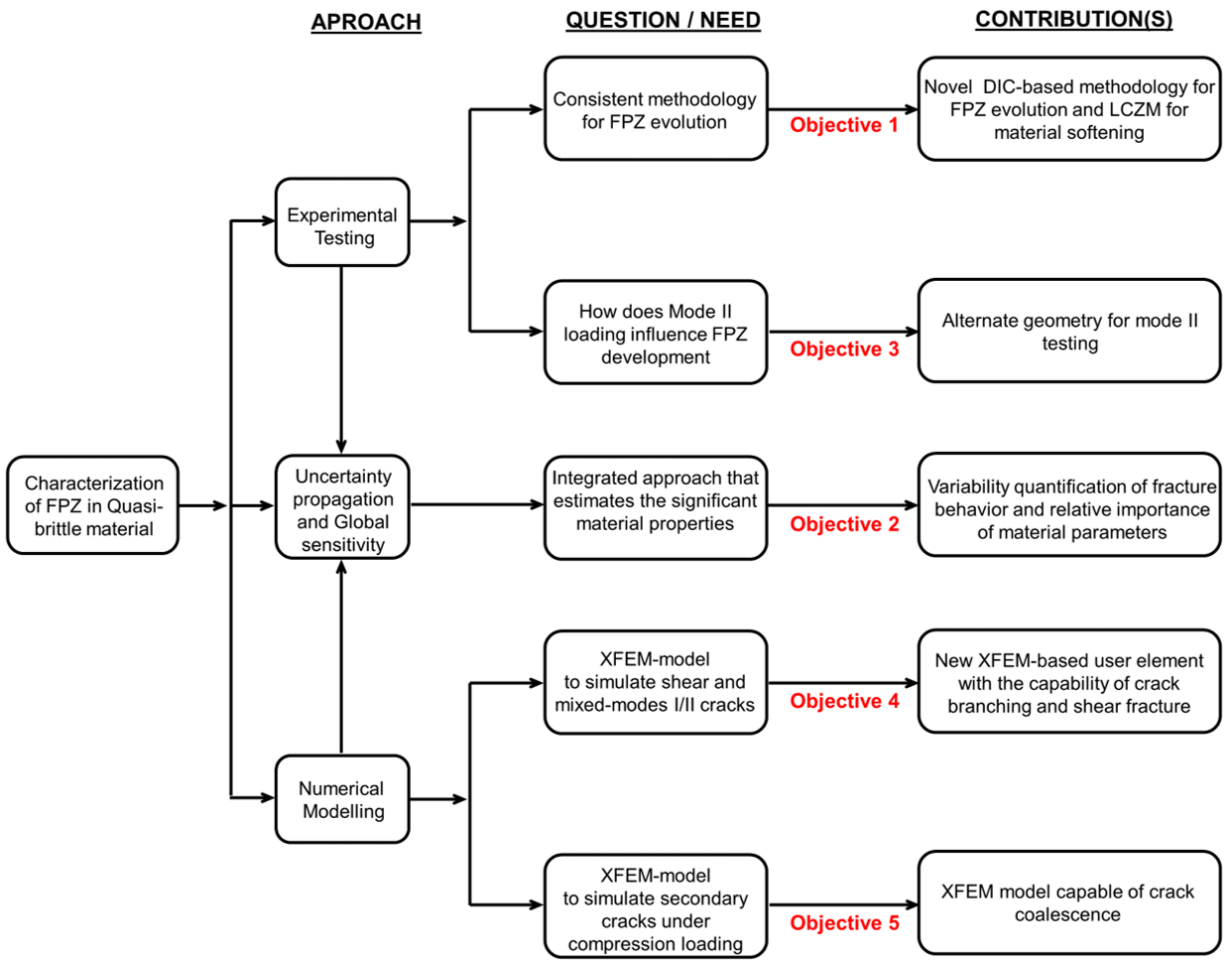

Figure 1-1 Infographic showing the main contribution of each research objectives achieved in this research.

1.5 Research Contribution

Figure 1-1 presents a flow chart of approaches used along with the main contributions of this thesis. The main goal here is to characterize FPZ in quasi-brittle material, for which two main approaches are being used: experimental testing and numerical modeling. The aim of experimental testing is to address the gaps in existing studies on FPZ development under mode I and mode II loading. For this purpose, a novel DIC-based methodology was developed that characterized the FPZ evolution in quasi-brittle material under both loading conditions, irrespective of obtained fracture mode. This study also identified a suitable mode II geometry which was rarely used for quasi-brittle material and had several advantages over traditional geometries. The review of existing studies on numerical modeling indicated a lack of reliable methods that can simulate FPZ development for different crack types. To address this, a novel XFEM-based user element was developed with the capability to simulate the FPZ development for mode II and mixed-mode I/II cracks. This XFEM-based user element can address another limitation of most numerical models: the ability to simulate complex crack patterns, including crack-branching and crack coalescence mechanisms obtained in quasi-brittle material under compressive loading. Additionally, an integrated approach involving experimental testing, numerical modeling, uncertainty quantification, and global sensitivity analysis was used (Figure 1.1) to evaluate the performance of CZM in predicting variability in FPZ characteristics. The main aim of this integrated approach was to assess how the variability of material properties of a quasi-brittle material affects its overall fracture behavior.

1.6 Scope Limitation

To understand the fracture characteristic of intact rocks, it is crucial, to begin with small-scale representative specimens, where the behavior of rock can be studied in a controlled way. Accordingly, the scope of the present research is limited to the fracture evolution in laboratory-scale rock specimens with one or multiple preexisting cracks, also commonly known as a 'flaw' or 'notch'.

1.7 Thesis Outline

This is a manuscript-based thesis, where the majority of the main chapters have either been published, accepted, or are undergoing review in international journals and conferences. The main chapters of this thesis are similar to the originally published or submitted individual manuscripts. Each main chapter has its specific abstract, introduction, main body text, results, discussions, conclusions, and acknowledgments. The references are presented at the end of the thesis. This thesis is organized into six chapters with four main chapters (Chapters 2 to 5) added in order of the thesis objectives as described in Section 1.3.

In Chapter 1 of the thesis, a brief background of FPZ and its characterization using laboratory experiments and numerical modeling has been presented, followed by identifying associated gaps in the existing literature. Specific research objectives and associated tasks were defined in this chapter.

Chapter 2 is based on the characterization of FPZ for mode I fracture using a combination of DIC and AE. In this chapter, a novel DIC-based methodology was developed to identify the various stages of FPZ evolution and quantify material softening behavior.

Chapter 3 presents an integrated approach used for assessing the performance of the linear cohesive zone model in predicting FPZ development and global behavior of Barre granite specimens under mode I loading.

Chapter 4 presents an investigation of FPZ development under mode II loading using two testing configurations. In addition, the influence of confining pressure on mode II fracture toughness was analyzed.

In Chapter 5, a novel XFEM-based user element was developed and implemented in Abaqus, capable of simulating cracking in quasi-brittle materials. The cohesive zone model was also implemented with the user element to model material softening to account for the FPZ development in different crack types.

Chapter 6 evaluated the performance of various crack initiation criteria in predicting the path of secondary cracks. This chapter simulated gypsum specimens containing one or two flaws under compression loading to assess the capability of the XFEM-based user element in predicting types of secondary cracks and crack coalescence mechanism

Chapter 7 summarizes the main findings and contributions of this research. It also gives an outline of suggested areas for future research.

CHAPTER 2

A NOVEL METHODOLOGY FOR CHARACTERIZING FRACTURE PROCESS ZONE IN BARRE GRANITE SPECIMENS UNDER THREE-POINT BENDING

This article has been published in the journal Theoretical and Applied Fracture Mechanics, 123 (Garg et al., 2023), Copyright Elsevier (2023)*

Prasoon Garg[1], Sana Zafar[1], Ahmadreza Hedayat[1], Omid Moradian[1], D.V. Griffiths[1]

2.1 Abstract

Fracturing in quasi-brittle such as rock involves the development of an inelastic zone around the pre-crack tip, also known as the fracture process zone (FPZ). The evolution of FPZ, while influencing the fracture behavior of rocks, is difficult to characterize due to the localized nature of material behavior and microstructural heterogeneities. This study presents a digital image correlation technique (DIC)-based method that consistently describes the FPZ evolution in Mode I fracture of Barre granite specimens. The FPZ characteristics were also evaluated using acoustic emission (AE) monitoring. The evolution of the crack tip opening displacement (CTOD) was analyzed to estimate the various fracture parameters, such as threshold values of the elastic and critical opening displacements and the size of the fully developed FPZ. The comparison of DIC-based measurements with the AE-based micro-cracking activities demonstrated that the displacement approach of the former could be used independently to identify the transition among the three stages of FPZ evolution, namely, (1) elastic stage, (2) formation of FPZ, and (3)

[1] Colorado School of Mines, Civil and Environmental Engineering
* See Appendix A for permission and citation

macro-crack initiation. Experimental results also indicate a linear relationship between the FPZ length and the inelastic component of the CTOD, along with the quadratic relationship between the local dissipated energy and the FPZ length, which is consistent with the linear softening law for material inside the FPZ.

2.2 Introduction

Rock behavior is typically governed by various presence of various discontinuities and their interactions rather than the constitutive behavior of intact material. Fracturing in quasi-brittle materials is often influenced by an inelastic region near the pre-crack tip, also known as the fracture process zone (FPZ) (Labuz and Biolzi, 1991). The FPZ physically represents a highly damaged region ahead of the crack tip formed due to large-scale nucleation and coalescence of micro-cracks (Labuz et al., 1987). The evolution of the FPZ has a significant impact on macroscopic fracture behavior and overall failure of rock, especially when its size is proportional to pre-existing cracks (Backers et al., 2005). In recent years, the cohesive zone model has been used by various studies (Yu et al., 2018; Xing et al., 2019; Rinehart et al., 2015) to classify the cracking process of rocks into three stages, namely, (1) elastic stage signified by linear deformation, (2) formation of FPZ signified by nucleation and propagation of micro-cracks, resulting in the non-linear deformation around the pre-crack tip and (3) onset of macro-cracks, resulting in the onset of unstable crack propagation due to large scale coalescence of micro-cracks. The cohesive zone model (Hillerborg et al., 1976) defines the FPZ as a cohesive crack that transmits stresses across its face as a function of the crack opening displacement (w) in the case of Mode I fracture. A critical opening displacement (w_c) defines the end of the FPZ and the start of the macro-crack, thus, representing the boundary between the two stages. The macro-crack is also referred to as traction-free zone (TFZ) or cohesionless crack, with the former term

being more widely used and therefore adopted in this study. It is difficult to pinpoint the boundary between these stages in laboratory-scale rock specimens as material behavior around the pre-crack tip is highly localized and significantly influenced by grain-scale heterogeneities (Lin et al., 2019a). This study proposes a method based on the displacement approach of 2D-DIC to characterize three stages of FPZ evolution for Barre granite specimens under Mode I loading.

The FPZ has been studied using various optics-based and acoustic-based non-destructive techniques such as holographic interferometry (Maji and Wang, 1992), computer tomography (Ghamgosar and Erarslan 2016), digital image correlation (DIC) (Miao et al., 2020), and acoustic emission (AE) (Li and Einstein, 2017). Both AE and DIC have become the most popular techniques to characterize FPZ development due to their simple setup and preparation process. In AE, the FPZ initiation is typically characterized by the cluster of micro-cracks resulting in an energy release in elastic waves. Using the source and energy of AE events, FPZ size and energy dissipation can be estimated (Lu et al., 2019). The AE's ability to trace the location of micro-cracking events inside the material makes it a powerful tool for determining the FPZ characteristics. At the same time, DIC provides accurate information about surface deformation and thus can be used to estimate various fracture parameters, such as the fracture path and critical opening displacement (Wu et al., 2011; Sharafisafa et al., 2018).

Despite widespread applications of the above techniques, the accurate characterization of FPZ remains a challenging task, especially in identifying the transitions among the three stages of its evolution. The tip of FPZ, representing the boundary between the FPZ and the elastic deformation, is determined by the merged position of the opening displacement contour obtained using the 2D-DIC (Le et al., 2014; Zhang et al., 2018). However, other studies (Bhowmik and Ray, 2019; Miao et al., 2020) have shown that the merged position of displacement contour is

not an accurate characterization of the FPZ tip for materials with coarse grains such as concrete and Beishan granite due to significant fluctuations in displacements values. Alternatively, the displacement gradient method (Wu et al., 2011; Bhowmik and Ray, 2019) has been suggested where the FPZ tip is represented by the cross-section with a negligible horizontal displacement gradient. The studies above assume that the FPZ tip in quasi-brittle materials such as concrete and rocks is characterized by negligible or very small opening displacement (1-3μm). In contrast, a recent study by Lin et al. (2019a) on Mode I testing of Berea sandstone showed that rocks could have significant opening displacements (8-10μm) under elastic deformation before the initiation of the FPZ. A similar challenge exists in identifying the FPZ's transition to macro-crack, with some studies assuming it to occur at the peak load based on the change in the slope of incremental horizontal displacement profile along the fracture plane (Miao et al., 2020; Lu et al., 2019). However, other studies (Aggelis et al., 2013; Yu et al., 2018) that used both DIC and AE techniques have found the FPZ being only partially formed at the peak load, which results in macro-crack initiation at a post-peak stage. These conflicting observations have led to a significant variation in fracture properties found for some rocks, such as Berea sandstone, by different studies (Lin et al. 2014; Lin et al. 2019b), e.g., the critical opening displacement ranging from 30-100 μm.

The main shortcoming of DIC-based studies is the lack of a consistent methodology that can be used to estimate the transition points between the three stages of FPZ evolution, especially the tip of the macro-crack. The location of the macro-crack tip is often identified based on fracture properties such as material softening law inside the FPZ and critical opening displacement (w_c), typically estimated from the cohesive zone model (Zang et al., 2018). The softening behavior inside the FPZ of quasi-brittle materials is often calculated using inverse analysis, which can

give non-unique softening law (Richefeu et al., 2012). To overcome these limitations, this study proposes a consistent method based on the displacement approach of 2D-DIC that characterizes the three stages of FPZ evolution in center-notch Barre granite specimens under Mode I loading. Additionally, the AE technique used in this study complemented the DIC analysis by describing the micro-cracking activity, such as event locations and local energy dissipation inside FPZ. Three-point bending tests were conducted on Barre granite specimens containing center notch, along with simultaneous monitoring of fracture processes using AE and DIC techniques. The proposed methodology involved analyzing the evolution of the crack tip opening displacement ($CTOD$) to determine the transition points between the three stages of FPZ evolution, which were also confirmed using AE-based measurements such as the event rate and energy release rate. The FPZ size at various loading stages was determined using locations of high-energy AE event clusters and the crack opening profiles from the 2D-DIC analysis. Finally, parameters of the cohesive zone model, such as elastic (w_e), the critical crack opening displacement (w_c), the size of fully developed FPZ (L) were determined to characterize inelastic deformation inside the FPZ of Barre granite specimens.

2.3 Experimental Design

2.3.1 Sample Preparation and Testing Procedure

Barre granite (BG) tested in this study is a fine to medium-grained crystalline rock primarily comprised of 65% feldspar, 25% quartz, and 6% biotite (Iqbal and Mohanty, 2007). Various minerals in BG result in grain size that varies from 0.25 mm to 3mm, with an average value of 0.87 mm (Nasseri et al. 2010). It has a small porosity (< 0.6%) due to its crystalline nature and following average values of material properties, namely: bulk density= 2590 kg/m^3, Young modulus under tension (E_t) = 28 GPa, Tensile strength =14 MPa, and Uniaxial compressive

strength= 168 MPa (Shirole et al., 2020; Goldsmith et al., 1976). A large block of Barre granite was cut to produce prismatic specimens having nominal dimensions of 150 mm x 75mm x 25mm. The Colorado WaterJet Company created the through-going center notch with a length of 25 mm and an aperture of 1.02 mm in each specimen (Figure 2-1).

This study tested four center-notched Barre granite specimens (BG-1, BG-2, BG-3, BG-4) along with the implementation of AE and 2D-DIC techniques to characterize the evolution of FPZ under Mode I loading (Figure 2-2). The specimens were loaded at a constant vertical displacement (load-point displacement at the mid-span) rate of 0.2 µm/sec using a servo-controlled MTS loading machine. Additionally, the crack mouth opening displacement ($CMOD$) was measured using a clip-on extensometer which was attached to the beam's bottom surface (Figure 2-2) and had a gauge length of 12mm

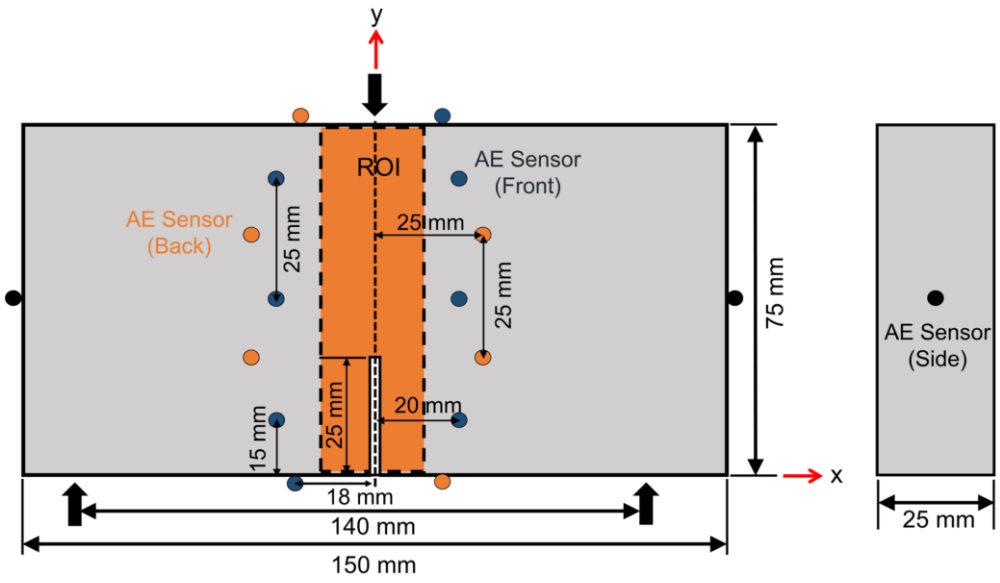

Figure 2-1 Schematic view of specimen geometry under three-point bending test

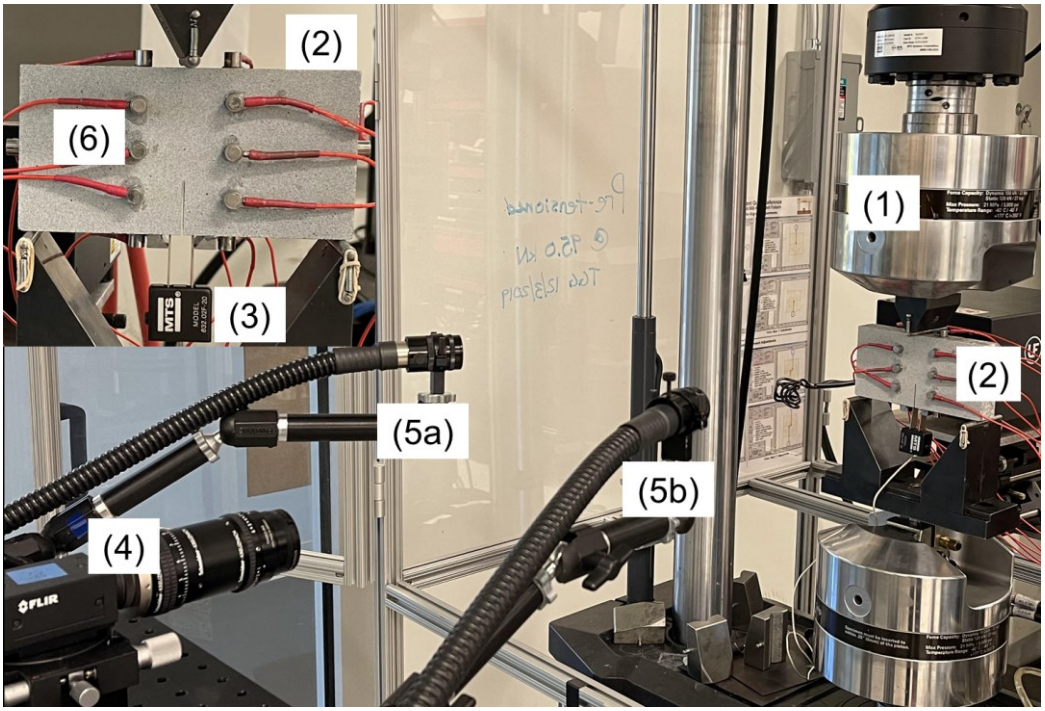

Figure 2-2 The experimental setup of the three-point bending test, along with the characterization of the cracking process using AE and 2D-DIC. (1) MTS testing frame; (2) Barre granite specimen with a center notch; (3) Clip-on gauge extensometer (4) CCD camera; (5a-b) two light sources; (6) AE sensors.

2.3.2 Acoustic Emission (AE) Technique

Acoustic emission (AE) has been extensively used to characterize the cracking process in intact (Eberhardt et al., 1998) as well as pre-cracked rock specimens (Kao et al., 2011; Moradian et al., 2016). The AE estimates material damage by characterizing micro-cracking activity that often releases high-frequency stress waves. These stress waves create small vibrations registered by the AE sensors in the form of hits after passing through various signal conditioning equipment such as amplifiers and frequency filters. In AE, the micro-cracks are located using AE events when multiple sensors register the same hit. The event localization is typically done based on the first arrival of P-waves which in the current study involves using the Akaike information criterion (AIC) (Kurz et al., 2005). Locations were determined using a constant velocity model for a minimum distance error of 4 mm and optimized using MATLAB's "fmincon" function (Li

et al., 2019). In three dimensions, the source localization would require the value of four unknowns (x, y, z, and t) and thus need at least four channels where the AE signal is registered. Additionally, a parametric analysis of AE signals was performed to characterize the extent of micro-cracking inside the FPZ, which involved analyzing the rate and cumulative value of AE events and energy release. The AE event rate refers to the total number of AE events per second. The AE energy associated with each event is typically the consequence of energy released from micro-cracking activity. Even though AE energy is not based on an absolute scale that requires sensor calibration (Shah and Labuz, 1995), it still, to some extent, reflects the part of the energy released from the source. Therefore, it has been used as a relative measure of the local energy dissipation inside FPZ for each experiment, as the sensor's coupling conditions do not change during an experiment. In this study, AE energy was estimated using the root mean square (RMS) value of the signal from each channel (Wang et al., 2021):

$$RMS = \sqrt{\int_{t_o}^{t_1} [V(t)]^2 dt} \tag{3-1}$$

where V denotes the voltage of the signal, t_0 and t_1 refers to the start and end time of the AE signal. The AE event energy (E_e) is defined by considering geometric attenuation between each sensor and source (Muralidhara et al., 2010) as given by:

$$E_e = \frac{1}{N}\sum_{i=1}^{N} r_i^2 \cdot RMS_i^2$$

$$r_i = \sqrt{(x_i - x)^2 + (y_i - y)^2 + (z_i - z)^2} \tag{3-2}$$

where RMS_i and r_i are energy and distance of i[th] channel respectively. Therefore, AE event energy (E_e) represents relative energy with unit [mV^2 x μs x mm^2]. Based on the AE energy released during the microcracking, the events can be classified into three levels of magnitude, as illustrated in Table 2-1:

Table 2-1 Categories of AE event energy

Level	**Event Energy range (mV^2 x μs x mm^2)**
Level 1	$E_{e1} > 10^2 \times E_0$
Level 2	$10 \times E_0 \leq E_{e2} \leq 10^2 \times E_0$
Level 3	$E_{e3} < 10 \times E_0$

Where E_0 denotes the minimum energy of all AE events within each Barre granite test. E_{e1} , E_{e2} and E_{e3} are energy values in level 1, level 2, and level 3, respectively.

For continuous AE monitoring, the specimens were instrumented with sixteen piezoelectric AE sensors (Nano 30), sixteen preamplifiers (2/4/6 PAC), and a data acquisition system (Express-8 based AE system from MISTRAS) which was controlled by real-time software AEwin. The sensors were strategically placed on all sides of the Barre granite specimen to ensure the 3D coverage required for accurate source location (Figure 2-1a). In these experiments, a sampling rate of 5 million samples per second (MSPS) was taken with a sample length of 15K and a pre-trigger of 256μs. The threshold was set to 55 dB for all channels to ensure no background noise influences during the test, and thus a signal above the threshold limit will be registered as an AE hit. The Nano-30 AE sensors used for detection have a resonant frequency of 300 kHz and can detect signals within a frequency range of 125-750 kHz. The recorded signals were conditioned using preamplifiers with a gain of 20 dB that amplified its voltage.

2.3.3 2D-Digital Image Correlation (2D-DIC)

Since its introduction to experimental solid mechanics in the 1980s (Chu et al., 1985), DIC has become the most popular non-destructive optical tool for non-contact estimation of full-field surface deformation on geomaterials (Aggelis et al., 2013; Skarżyński et al., 2013; Shirole et al., 2020a). This technique provides full-field planar deformation by tracking the motion of groups of pixels (also known as subsets) between two images of a specimen's surface (Pan et al., 2009). The implementation of the 2D-DIC technique primarily involves three main steps: specimen preparation, experimental setup and acquisition of digital images, and finally, the image correlation process. The specimen preparation process is vital for ensuring accurate 2D-DIC measurement. It involves creating a unique and random pattern of grey-scale intensity (speckle pattern) on its surface (Sutton et al., 2007; Aliabadian et al., 2019). The experimental setup of 2D-DIC requires two steady light sources and a digital camera placed perpendicular to the specimen's surface so that its optical axis coincides with the specimen center (Figure 1b). In the image correlation process of 2D-DIC, first, a region of interest (ROI) is defined where surface deformation and strain field will be calculated. This is followed by creating an evenly spaced square grid inside the ROI. The grid points formed as a result have a regular spacing equal to "step size." The displacement at a grid point is calculated by tracking the surrounding region defined as a subset, as it can be uniquely identified in every digital image of the specimen. The correlation process is performed using a statistical correlation criterion which tracks subsets between the current and the reference images to provide the displacement field at their center (Hedayat et al., 2014). The reference image is generally selected at the start of the test representing the undeformed state of the specimen. Similarly, the displacement is estimated for all grid points present in the ROI to get full-field surface deformation of the specimen. The strain

tensor on the surface of a material is computed from the full-field displacements by implementing a numerical differentiation procedure. The procedure involves smoothing the displacement field (assuming a linear distribution) within a local calculation window (size represented by the "filter size") before subsequently differentiating (numerically) to calculate the strain fields.

The randomness of grayscale intensity values over the specimen surface in DIC application is of fundamental importance. The specimen surface was first cleaned to remove any visible contaminants (oil, grit, etc.), followed by a light coating of white paint. Once the white paint was dried, the coated surface was painted with black spray paint, which provided high contrast intensity values of generated speckles compared to the white background. Before testing, the quality of the speckle pattern on each specimen was assessed based on two features, namely: (a) the distribution of grayscale intensity values of the generated speckle pattern and (b) the average size of the speckles (Lin and Labuz, 2013). The optimal speckle pattern required for accruement measurement of displacement fields should have a well-distributed histogram of the grayscale intensity to ensure no measurement bias and low background noise (Sharpe, 2008). Figure 2-3 shows the produced speckle pattern along with grayscale distribution inside a small region above the notch tip (indicated by a red rectangle) on the surface of specimen BG-2. The average speckle size also plays a vital role in proper image sampling; thus, each speckle is recommended to contain 3-7 pixels (Sutton et al., 2007). The combination of white and black paint used in this study has a speckle size of 200-300 μm. Figure 2-3a shows the average pixel size of 50μm, with the speckle size ranging from 5 to 7 pixels. The pixel size was determined using the magnification factor of 50 μm/pixel, commonly applied for transforming the pixel measurements to the physical dimensions.

During the testing of Barre granite specimens, their surface was monitored using the 2D-DIC system, which captured digital images at the rate of 12 frames/sec. The high image acquisition rate facilitated near-continuous monitoring of crack tip behavior and ensured accurate characterization of the FPZ evolution. The images were recorded using a charge-coupled device (CCD) camera, which in conjunction with a Fujinon lens of 35 mm focal length (Model CF35HA-1), provided a capacity of 2448 by 2048 square pixels. These DIC images in the post-processing were analyzed using image correlation software VIC-2D, which involves the estimation of the full-field deformation of a small region of interest (ROI) at the specimen surface. For the three-point bending tests, the ROI of 15×75 mm^2 around the notch was used (Figure 2-3a).

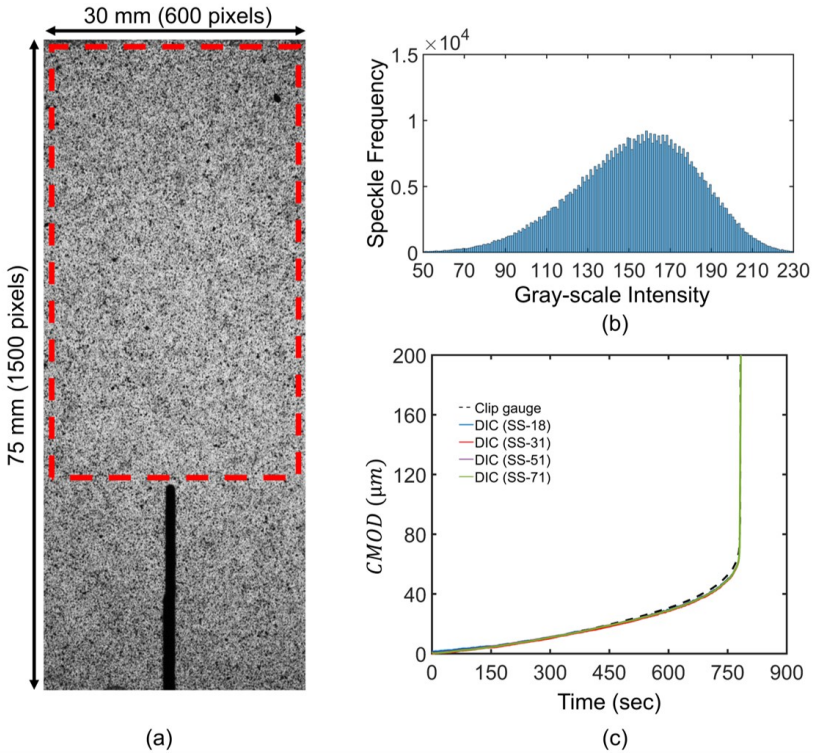

Figure 2-3 Specimen BG-2 with (a) image of the speckle pattern; (b) distribution of grayscale intensity values inside the small region above the notch tip (highlighted by a red rectangle); (c) the CMOD value obtained from clip-gage extensometer (dashed line) and 2D-DIC (solid line). SS denotes the subset size.

2.4 Results

2.4.1 Calibration of DIC Parameters

The resolution and accuracy of full-field displacement and strain fields from DIC analysis depend on input parameters of VIC-2D software, including step size, subset size, and filter size. To determine the optimum value of these DIC parameters, a calibration procedure and verification of the calibrated parameters are described in this section.

The initial calibration includes comparing crack mouth opening displacement ($CMOD$) values obtained from DIC analysis with the one recorded through the clip-on gauge extensometer. The $CMOD$ value using DIC analysis can be obtained using the following equation (Wu et al., 2011; Bhowmik and Ray, 2019):

$$CMOD = \frac{\Delta a + a_o + H_o}{\Delta a} CTOD \tag{2-3}$$

where a_o and H_o are notch length and the thickness of the knife edge used for holding the clip gauge. $CTOD$ is the crack opening displacement at the notch tip, and Δa is the crack extension length (both FPZ and macro-crack) length obtained from DIC imaging. The crack extension length is calculated based on the displacement approach (see section 2.4.4).

Various subset sizes ranging from 18 to 71 pixels with a step size of 5 were used for analysis to calibrate DIC parameters. According to Sutton et al. (2007), a subset should contain a minimum of three speckles for good image correlation. Assuming the speckle size of 6 pixels for the pattern used in the current study, the minimum subset size needs to be at least 18 pixels. However, a small subset size has the drawback of relatively high background noise in the DIC results (Xing et al., 2020). Additionally, a very large subset size can lead to considerable errors

in strain and displacement calculations (Hedayat et al., 2014); thus, the optimum subset size needs to be identified. Step size signifies the measurement resolution in the displacement field and is typically chosen as smaller than half the subset size (Hedayat et al., 2014). However, a smaller step size requires significantly longer computational time. Therefore, the step size of 5 pixels was used to ensure optimal computational efficiency and large subset overlapping for high displacement resolution. Figure 2-3c clearly showed a reasonable consistency of DIC data (solid line) with the clip-gauge measurements (dashed line) based on the variation of $CMOD$ values with time for the Barre granite specimen BG-2. It also indicates that the subset size has no significant influence on crack mouth opening displacement ($CMOD$) values.

The DIC parameters also need to be calibrated to ensure that DIC can adequately characterize localized strain inside the FPZ. Various studies have shown that the accuracy of the strain field inside the FPZ is sensitive to DIC parameters such as length resolution, subset size, and filter size (Skarżyński et al., 2013; Dutler et al., 2018; Aliabadian et al., 2019). Figure 2-4a compares contour plots of horizontal strain (ϵ_{xx}) around the notch calculated using different subset sizes (SS-18 to SS-71 pixels) at 60% of peak load in the post-peak regime for specimen BG-2. Figure 2-4a show a strong influence of the subset size (SS-18 to SS-71 pixels) on the strain localized zone that defines the FPZ. The width of the strain localized zone increases with an increase in the subset size, which can be attributed to a larger area of influence of the crack discontinuity with the larger subset size. Therefore, a large subset size (e.g., SS-71 pixels) results in a wider strain localized zone along with lower values (Figure 2-4a), which implies that the high strain concentration inside FPZ could not be accurately captured using a large subset size. On the other hand, a very small subset size (e.g., SS-18 pixels) provides a smaller width of the localized zone, but the observed strain at some points is missing and, therefore, not acceptable

(Figure 2-4a). To find the optimum subset value, the horizontal strain (ϵ_{xx}) profile along a horizontal cross-section at the notch tip (y = 26 mm) was compared (Figure 3b) for different subset sizes (SS-31 to SS-71 pixels). It can be inferred from Figure 2-4a-b that DIC with adequate subset size (SS-31 pixels in the current case) can identify the high strains values inside the FPZ along with an accurate estimation of the small width of the localized zone (3.5 mm) as it minimizes the influence of crack discontinuity on the nearby area of the strain localized zone. However, increasing the subset value (SS-51 and 71 pixels) smears the strain concentration and results in a wider localized zone (Figure 2-4b) and therefore fails to accurately determine the localized zone's size. The accuracy of strain measurements also depends on the step size and the filter size that influence the smoothing of the strain field. Among these parameters, only the filter size is shown to have a major influence on both strain inside the localized zone (Dautriat et al., 2011) and its size (Dutler et al., 2018; Shirole et al., 2020b). Dutler et al. (2018) observed that a large filter size overestimated the width of the strain localized zone inside the FPZ due to the large smoothing window and recommended that the smoothing region should be less than half the width of the localized zone. In the current study, a filter size of 5 points was selected, which results in a square smoothing window with a length of 25 pixels based on the step size of 5 pixels. This value is equivalent to about 1.25 mm (1 pixel =50 μm), which is below the half-width of the localized zone, being 1.5 mm (Figure 2-4b).

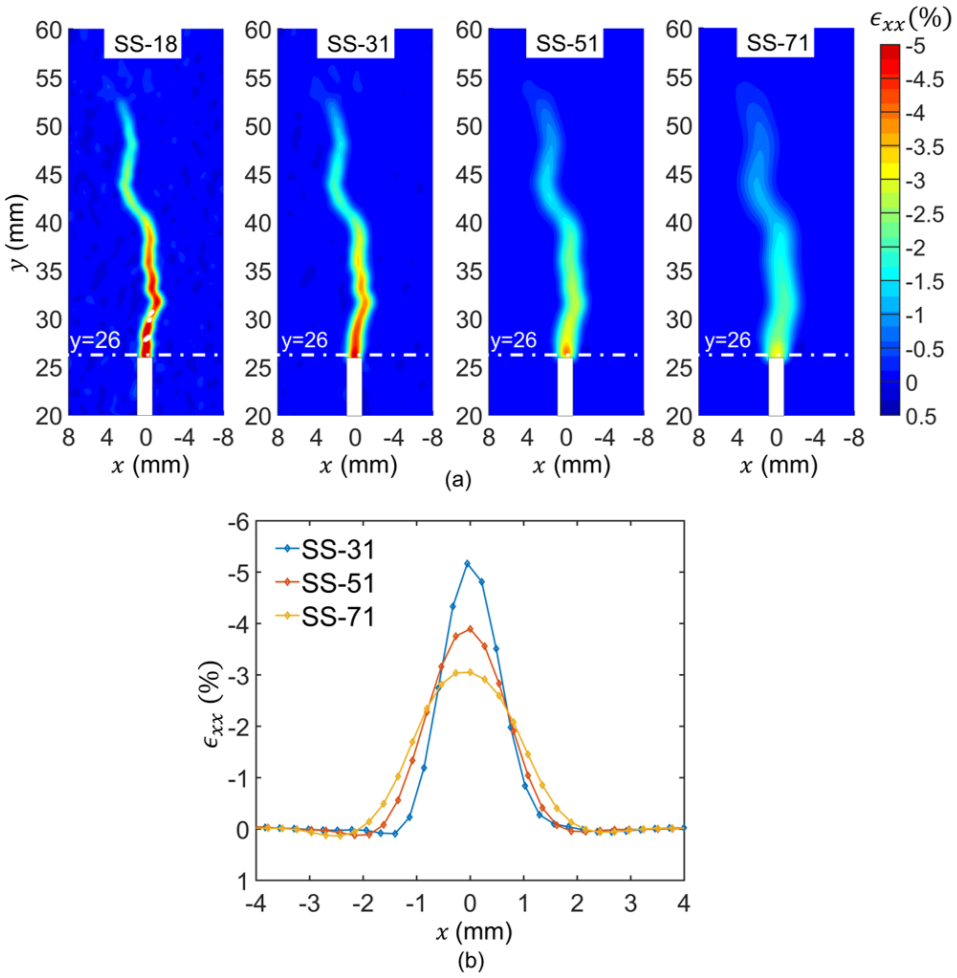

Figure 2-4 (a) Influence of subset size on the strain values inside the FPZ (colors represent the contour of horizontal strain, ϵ_{xx}) (b) ϵ_{xx} distribution along the along horizontal cross-section at the notch tip (y =26mm) at various subset sizes. SS denotes the subset size.

2.4.2 FPZ Characterization using Displacement Approach of 2D-DIC

The displacement approach of the 2D-DIC characterizes the FPZ as a zone of displacement discontinuity that results in the merging of horizontal displacement contour, as seen at 80% of the peak load in the post-peak regime for specimen BG-1 (Figure 2-5a). The displacement discontinuity also results in a high positive displacement gradient ($\partial U/\partial x$) in the horizontal displacement profile across the fracture plane as observed for various cross-sections such as y = 25 mm, 35 mm, and 48 mm at 80% of the peak load in the post-peak regime (Figure 2-5b). The shaded region in Figure 2-5b represents the maximum range over which the positive displacement gradient ($\partial U/\partial x > 0$) was observed in the horizontal displacement profile along various cross-sections. The evolution of the horizontal displacement profile with applied loading can be used to identify the three stages of FPZ evolution. However, it is difficult to pinpoint the boundary between these three stages based on the displacement profile alone, as seen in identifying the FPZ tip. The tip of the FPZ is typically estimated using the merged position of the horizontal displacement contours (shown by the red circle in Figure 2-5a), lying at y = 48 mm for the BG-1 specimen at 80% of the peak load in the post-peak regime. The horizontal displacement profile at this location showed a significant displacement jump of 8.2 μm (Figure 2-5b), which is in contradiction with other studies (Lin et al., 2014; Miao et al., 2020) that have found negligible or small displacement jumps (1-3 μm) before initiation of the FPZ. Therefore, in this study, the transitions between the three stages of the FPZ were identified based on the elastic (w_e) and the critical crack opening displacement (w_c). The elastic crack opening displacement (w_e) is defined as the threshold value of the displacement jump below which material undergoes elastic deformation while the critical crack opening displacement (w_c) represents the stage where the FPZ transitions to macro-crack. Both parameters are used in the

cohesive zone model as material properties in order to characterize the material behavior inside the FPZ.

To estimate these parameters in a consistent manner, the crack opening displacement at the notch tip ($CTOD$) was evaluated. The $CTOD$ at various loading stages was determined as a relative difference in horizontal displacements between two vertical lines located at $x \pm 3$ mm from the notch plane ($x = 0$) (Figure 2-5a). These lines were selected to represent the virtual surfaces of the crack plane. Additionally, the significant distance between virtual crack planes also overcomes other limitations, such as the tortuous crack path and smooth horizontal profile, which minimize the errors in the calculation of opening displacements (Figure 2-5a-b).

2.4.3 Methodology for FPZ Evolution

In this study, the three stages of FPZ evolution were characterized based on the combination of DIC and AE techniques. Using the displacement approach of the 2D-DIC, the crack opening displacement at the notch tip ($CTOD$) was analyzed (see section 2.4.3), which was also compared with various AE parameters such as AE event and AE energy release. Figure 2-6a-b show the variation of the applied load, the $CTOD$, and its first derivative ($\partial CTOD/\partial(\delta_{norm})$), where $CTOD$ is in mm and δ_{norm} (δ/δ_{peak}) represents the normalized value of the load-point displacement (δ) with respect to its value at the peak load stage. Figure 2-6c-d present the rate and cumulative plots of the AE event and AE event energy as a function of normalized load-point displacement (δ_{norm}) for Barre granite specimen BG-1. During the initial loading stage (0-87% peak load, up to point A in Figure 2-6a), the $CTOD$ varied linearly, resulting in a near-constant value of its derivative ($\partial CTOD/\partial(\delta_{norm})$ ~ 0.1 mm) (Figure 2-6b). This constant rate of increase in the $CTOD$ can be associated with elastic deformation of the material near the notch

tip as it only resulted in a few isolated AE events as evident by a negligible AE activity (see inset in Figure 2-6c). Furthermore, these events are associated with small energy, as indicated by the very low AE energy release rate ($E_e/E_o \leq 10$) (see inset in Figure 2-6d) and thus signifies the quiet phase of the test.

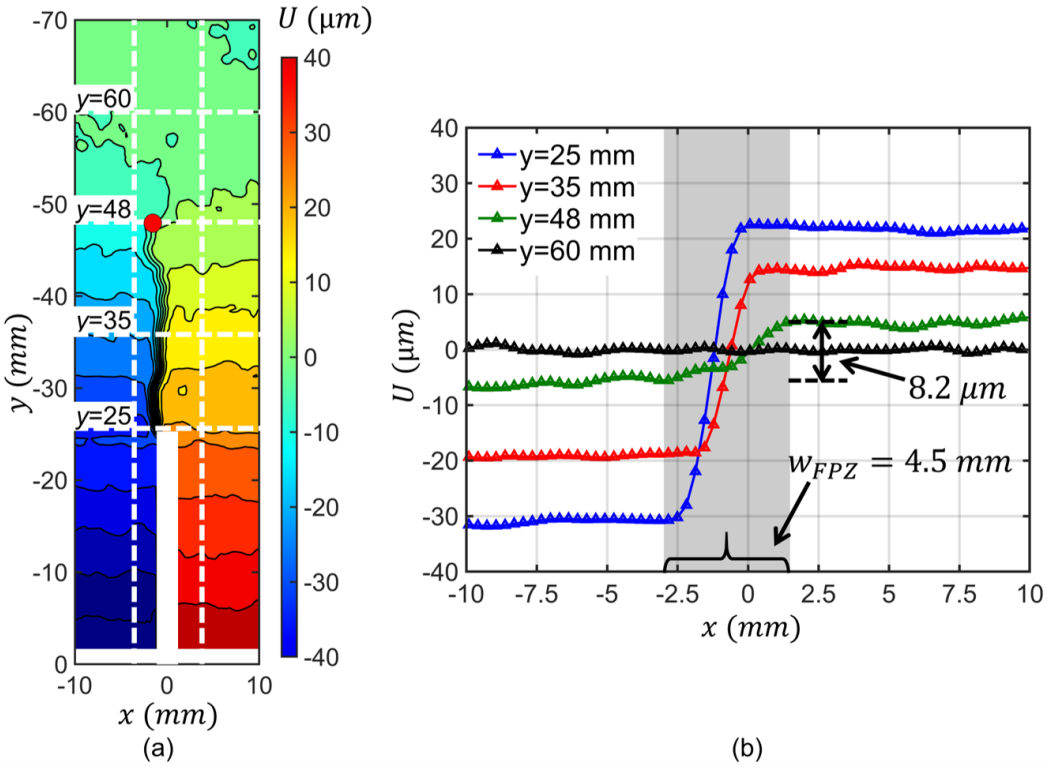

Figure 2-5 Horizontal displacements (U) at 80% of the peak value in the post-peak regime for specimen BG-1 with (a) distribution around notch tip and (b) plot of displacement profiles along various horizontal cross sections. The w_{FPZ} denotes DIC- based FPZ width.

With further loading, the $CTOD$ increased at an accelerated rate (Figure 2-6b), resulting in its non-linear variation starting from (point A in Figure 2-6a) at 87% of the peak load in the pre-peak regime for specimen BG-1. The onset of non-linearity in the $CTOD$ - normalized load-point displacement (δ_{norm}) curve is identified as the point of the first significant change in $CTOD$ derivative (Figure 2-6b). This point can be associated with micro-cracking around the notch tip, as confirmed by the occurrence of consistent AE activity at a rate of 1-2 events/sec (see inset in

Figure 2-6c), which consequently leads to a significant increase in cumulative AE events from point A (Figure 2-6c). Additionally, some of these events (see inset in Figure 2-6d) were associated with a large AE energy release ($E_e/E_o \geq 100$), thereby indicating the formation of an inelastic zone (known as the FPZ) around the notch tip. This observation is consistent with the study by Wong et al. (2019, 2020) that characterized the FPZ development based on consistent micro-cracking activity for various granite rocks. Therefore, the $CTOD$ at the onset of non-linearity in $CTOD$ - normalized load-point displacement curve (point A in Figure 2-6a) can be regarded as the threshold value of the elastic opening displacement (w_e) above, which FPZ initiated from the notch tip.

After the FPZ initiation, as the material around the notch-tip entered the damaged state, large-scale propagation and coalescence of micro-cracks started to occur, resulting in high AE activity (3-12 events/sec) along with a significant amount of AE energy release around peak load stage (see insets in Figure 2-6c-d). The large-scale micro-cracking was reflected by a non-linear $CTOD$ increase with the normalized load-point displacement (Figure 2-6a), which resulted in a linear increase in its derivative ($\partial CTOD/\partial(\delta_{norm})$) as shown by the inclined dashed line in Figure 2-6b. At 90% of peak load in the post-peak regime, the $CTOD$ underwent a rapid jump from 40 μm to 90 μm (shown by point 'B' in Figure 2-6a) in specimen BG-1. This rapid jump in the $CTOD$ value can be associated with the unstable crack propagation from the notch tip resulting from the initiation of macro-crack (traction-free zone) at this location. It also leads to a rapid jump in both AE events and energy release (point 'B' in Figure 2-6c-d). Sharafisafa et al. (2018) and Aliabadian et al. (2019) adopted a similar DIC-based criterion to identify the macro-crack initiation stage. Therefore, the crack tip opening displacement ($CTOD$) at the onset of unstable crack propagation is considered the critical crack opening displacement (w_c), which can

be used to identify the macro-crack initiation stage. Figure 2-7a-b presents a consistent trend of the $CTOD$ evolutions for the remaining three Barre granite specimens (BG-2, BG-3, and BG-4, respectively). Table 2-2 shows the elastic (w_e) and the critical crack opening displacement (w_c) along with other FPZ characteristics for all four tested Barre granite specimens. Both the elastic (w_e) and the critical crack opening displacement (w_c) values are consistent material properties along with the macro-crack initiation in the post-peak stage in all Barre granite specimens (Table 2-2). This observation of macro-crack formation at the post-peak stage is consistent with other experimental studies (Kao et al., 2011; Aggelis et al., 2013; Lin et al., 2019a) on various quasi-brittle materials such as concrete and rocks.

Table 2-2 Summary of experimental results.

Test #	**BG-1**	**BG-2**	**BG-3**	**BG-4**	**Average ± Standard Deviation**
Peak load (kN)	3.96	3.60	3.50	4.59	3.91 ± 0.49
Elastic opening displacement w_e (μm)	7.90	8.60	4.90	4.30	6.40± 2.10
FPZ initiation load (kN)	3.45	2.91	2.96	3.94	3.32 ± 0.48
Critical opening displacement w_c (μm)	40.00	34.00	36.00	33.00	35.80 ± 3.10
Crack initiation load (kN)	3.56	3.42	3.05	4.27	3.58 ± 0.51
Fully developed FPZ (L) (mm)	18.00	12.20	17.60	13.20	15.30 ± 3.00

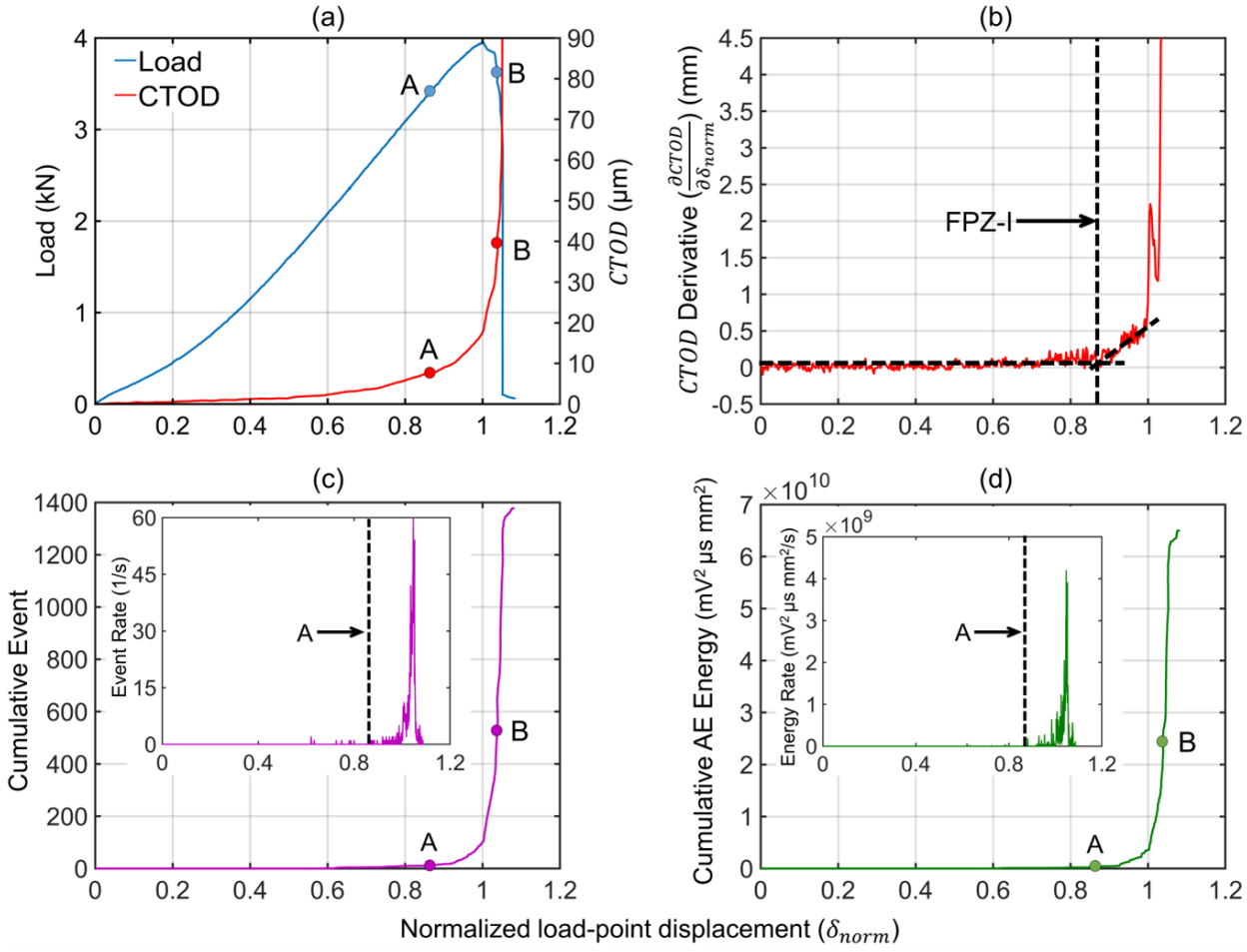

Figure 2-6 Barre granite specimen (BG-1) with the evolution of (a) Crack tip opening displacement (CTOD) and applied load, (b) CTOD derivative, and (c-d) rate and the cumulative value of AE event and AE event energy as a function of normalized load-point displacement (δ_{norm}). The insets present the rate of both AE-based parameters. FPZ-I denotes the FPZ initiation stage.

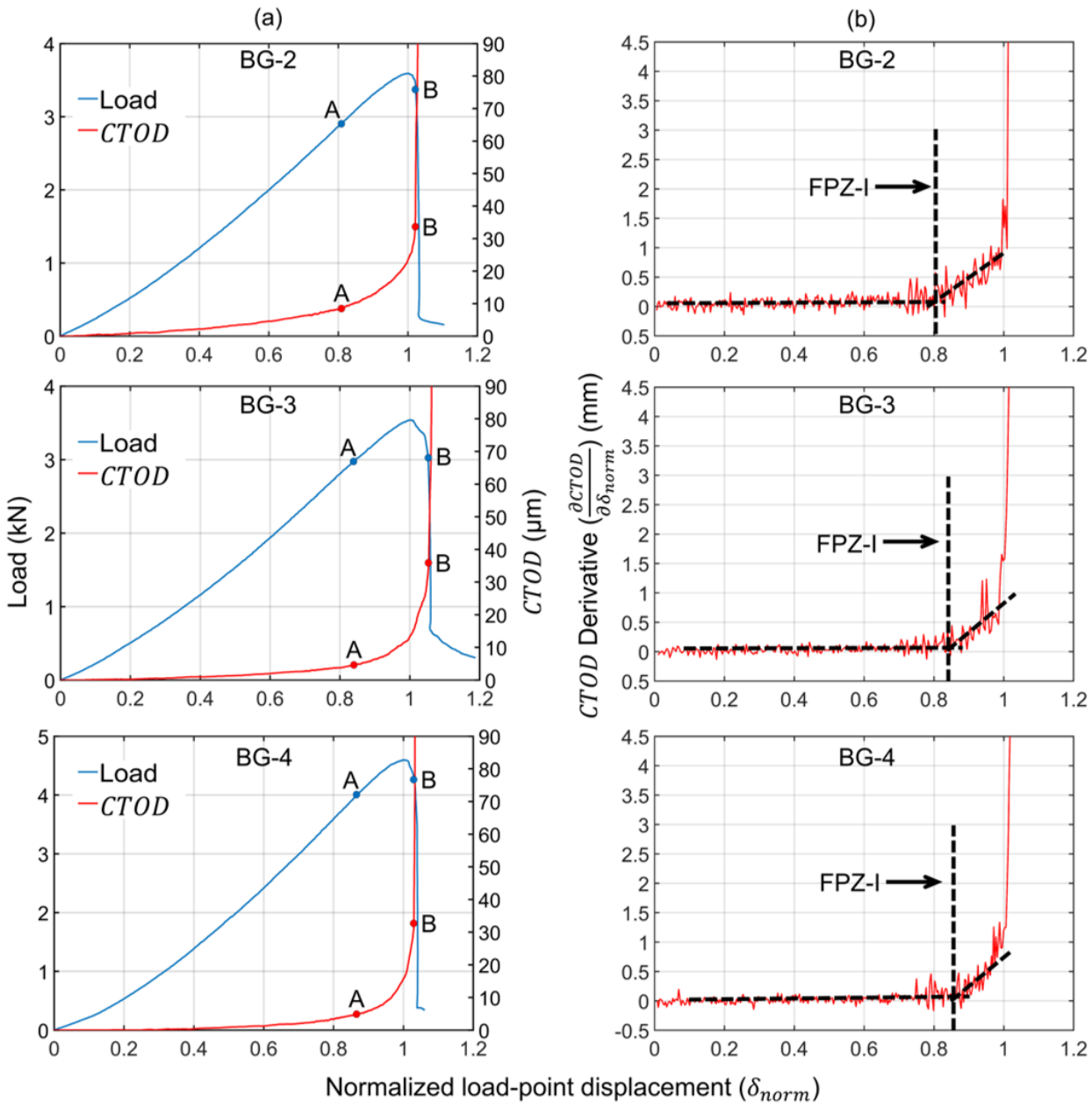

Figure 2-7 Variation of (a) Applied load and the crack tip opening displacement (CTOD) and (b) CTOD derivative as a function of normalized load-point displacement (δ_{norm}) in all three Barre granite specimens (BG-2, BG-3, BG-4). FPZ-I denotes the FPZ initiation stage.

2.4.4 Estimation of the FPZ's Size

This section presents the estimation of FPZ size based on the displacement approach of 2D-DIC, which was also corroborated by AE-based measurements such as AE event energy. In the

current study, the FPZ length based on the displacement approach is defined as the distance between the tip of the FPZ and that of the macro-crack. The FPZ tip is determined as the position where crack opening displacement (w) is equal to elastic opening displacement (w_e). Similarly, the macro-crack tip (the transition point between the macro-crack and the FPZ) is identified using critical opening displacements (w_c) (i.e., $w = w_c$).

The FPZ's size was also characterized based on the AE energy released during the fracturing process. Although AE energy is not a direct measure of fracture energy (representing only a portion of the total energy released in the fracturing process), it can still be treated as a valuable index to evaluate energy localization along the FPZ (Xing et al., 2019). Therefore, it can provide a reasonable estimate of the FPZ development, which involves large-scale nucleation and coalescence of the microcrack above the notch tip. In this study, the AE-based estimation of the FPZ's size is primarily based on identifying the high-energy event cluster and calculating the AE energy distribution along the crack path. Each AE event was classified into three energy levels, as shown in Table 2-1. The micro-cracking associated with the FPZ formation was identified using AE events of Energy Level 1 ($E_e/E_o \geq 100$). Various studies (Lin et al., 2019b; Wong and Guo, 2019) have shown that these high-energy events account for the majority of energy dissipated during the fracturing of various rocks, such as Barea sandstone and Kowloon granite. The remaining events of lower energy release, i.e., within Level 2 and Level 3 ($E_e/E_o < 100$) are typically known to have a small impact on overall energy dissipation (Zhang et al. 2018). Additionally, low energy events are generally associated with isolated micro-cracking (outer zone surrounding the FPZ) with energy levels smaller by orders of magnitude than those in Energy Level 1 (Otsuka and Date, 2000; Xing et al., 2019). The histogram of AE energy distribution was obtained by summing the values of AE event energy horizontally with respect to

its position along the fracture path (y-axis) from the notch tip. The FPZ length at a given loading stage was identified as the region containing the cluster of high AE energy (Level 1) events, resulting in the dissipation of almost 80% of AE energy being released along the ligament length. The AE-based FPZ tip was identified as the farthest boundary between the cluster of high-energy (Level 1) events and low-energy events (Level 2 and Level 3) from the notch tip. The region of 80% AE energy dissipation as a measure of the FPZ length was selected based on the study Wang et al. (2021) on sandstone specimens under Mode I loading.

Figure 2-8 FPZ development based on DIC and AE parameters at different loading stages: (a) peak load stage, (b) 90% post-peak, (c) 80% post-peak, (d) 70% post-peak. presents FPZ's size estimation using crack opening displacements (COD) profile, AE event locations, and energy histogram at various loading stages for specimen BG-1. Here, the COD profiles at a given loading stage represent total opening displacements from the start of the test. In contrast, the AE-based measurements are plotted based on increment time at each loading stage. The AE events with Energy Level 1 are shown with red squares, while the remaining events with lower energy (Level 2 and 3) are presented using black circles (

Figure 2-8a-d). At the peak load stage, the tip of the FPZ lies approximately at y = 31 mm (

Figure 2-8a) based on the COD profile ($w \sim w_e$), which is also confirmed by the presence of the high-energy AE events cluster (red squares in

Figure 2-8a) at this location. Despite the significant amount of scattering in high-energy AE events, the energy histogram (

Figure 2-8a) indicates that the region of 80% AE energy dissipation (shown by the shaded region) from the AE-based FPZ tip coincides with the FPZ length (l~ 6mm) predicted by the

displacement approach of DIC. The DIC-based FPZ is shown by length (l~ 6mm) between two red circles in the COD profile at the peak load (

Figure 2-8a) and is identified using the COD profile, i.e., w_e < COD < w_c. At 90% of the peak load in the post-peak regime, a fully developed FPZ has formed above the notch tip, with its tip approximately at y = 43 mm based on the COD profile (

Figure 2-8b). A similar length of the fully developed FPZ (L~ 18mm) above the notch tip was predicted by the region of the high-energy AE event cluster, which also resulted in 80% AE energy dissipation from the AE-based FPZ tip, as shown by the shaded portion in energy histogram at this loading stage (

Figure 2-8b). Additionally, these high-energy AE events form an inner zone of 18 x 10 mm^2 surrounded by low-energy events (black circles), creating a large outer zone (

Figure 2-8b). Therefore, the AE-based fully developed FPZ can be represented by the inner zone with its width approximately equal to 10 mm (

Figure 2-8b), which is two times larger (~ 4.5 mm) as compared to the value obtained from DIC as shown by the shaded region in Figure 2-5b. The width of the FPZ using the displacement approach is defined as the distance between the two ends of the region containing a positive displacement gradient ($\partial U/\partial x > 0$) in the horizontal displacement profile (shown by the shaded area in Figure 2-5b).

In subsequent loading stages, a similar length of both FPZ (l) and macro-crack/traction free zone (TFZ) (l_{TFZ}) were obtained from DIC and AE-based measurements (

Figure 2-8c-d). The DIC-based TFZ (l_{TFZ}) is identified with COD > w_c, represented by the length between dark purple and red circles in the COD profile (

Figure 2-8c-b). The AE-based TFZ at a given loading stage is identified as a low AE activity region above the notch tip associated with a small amount of AE energy release, i.e., within Level 2 and Level 3 ($E_e/E_o < 100$). Figure 7b-d clearly showed fewer AE events with low AE energy dissipation inside the TFZ in both cases of 80 % and 70% of the peak load in the post-peak regime. It provides explicit evidence of completely opened crack surfaces with few microcracks inside DIC-based TFZ.

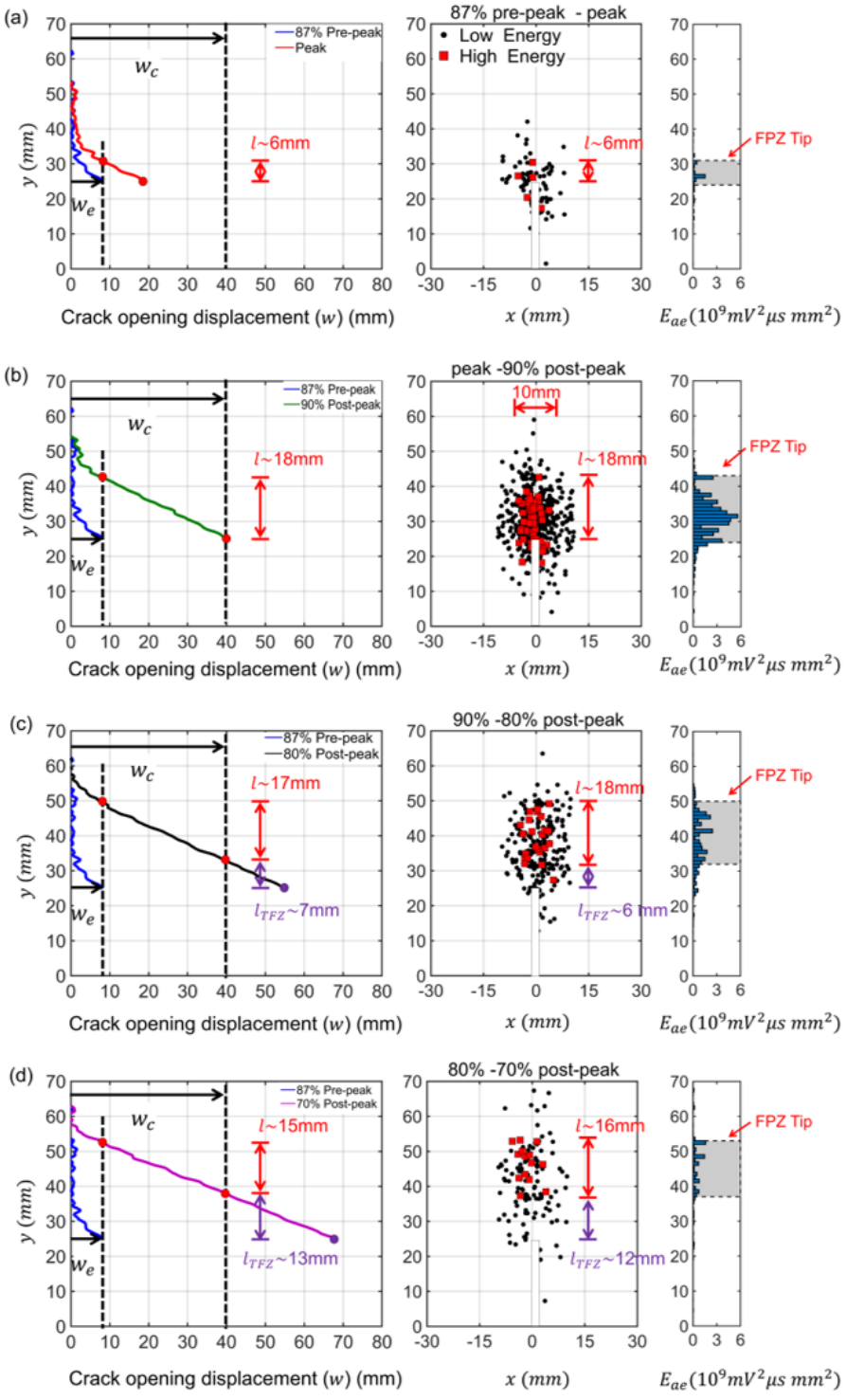

Figure 2-8 FPZ development based on DIC and AE parameters at different loading stages: (a) peak load stage, (b) 90% post-peak, (c) 80% post-peak, (d) 70% post-peak.

2.4.5 Failure Mode Evaluation using DIC and AE

To determine the mode of deformation through AE in Barre granite specimens, moment tensor analysis was performed on the located AE events based on the study by Li et al. (2019). The method is based on the 2D SiGMA (Grosse and Ohtsu, 2008) algorithm, which characterizes crack type using values of double couple (DC) components. The shear mode is identified for the events with a DC value greater than 50%; the tensile mode for the events with a DC value less than 50% and positive ISO and CLVD; the events with non-DC less than 50% and negative ISO and CLVD are classified as compressive mode events. Here our focus is on shear and tensile events.

In the pre-peak region, a similar amount of tensile and shear microcracking occurred (

Figure 2-9a). While in the post-peak region, the contribution of tensile microcracking increased compared to shear events with the increase in the loading stage (

Figure 2-9a). The spatial distribution of AE events at various loading stages (

Figure 2-9b-c) presents a large scattering of shear microcracks compared to tensile ones, especially in the ligament region above the notch tip. The region around the notch tip (20 mm < y < 27 mm), especially at its left side, showed a formation of a large cluster of shear microcracks (

Figure 2-9c) which can be attributed to the tortuous path of macro-crack obtained at the front surface of specimen BG-1 (represented by the solid black line). The waviness of the macro-crack around the notch tip along with the relatively coarse grain structure of Barre granite resulted in a large number of shear microcracks being formed across multiple grain boundaries compared to tensile ones around this location (

Figure 2-9b-c). Additionally, the significant number of shearing events in the region around the notch tip (20 mm < y < 27 mm in Figure 8b-c) is responsible for its considerable contribution to the temporal evolution of events inside the fully developed FPZ (represented by point 'B' in

Figure 2-9a) for specimen BG-1. In the remaining ligament region above the notch tip (y > 27 mm), shear microcracks show significant scattering (

Figure 2-9c). In comparison to this, tensile microcracks are more concentrated towards formed macro-cracks (represented by the solid and dashed lines) and have a dominant orientation in the vertical direction (

Figure 2-9b). It is to be noted that a significant number of tensile microcracks are also oriented in random directions, which can be again attributed to the tortuous macro-crack path (

Figure 2-9b). Additionally, the FPZ width identified by high-energy event clusters (-5 mm < x < 5 mm) in

Figure 2-9a-c seems to contain a more significant concentration of tensile microcracks compared to shear events (

Figure 2-9b-c).

The DIC-based strain field characterizes the FPZ formed due to the accumulation of the microcracks as the strain localized zones and thus can be used to identify its failure mode. In this study, the DIC-based failure mode was estimated by analyzing the minimum principal strains (ϵ_{22}; negative ($-$) strains represent tension) and maximum shear strain (γ_{max}) inside the FPZ. Various studies (Jian-po et al., 2015; Shirole et al., 2020a; Zafar et al., 2021) have used these strain fields to provide a quantitative estimate of the damage due to tensile and shear

microcracks. Figure 2-10a-b present the contours of the minimum principal strain (ϵ_{22}) and the maximum shear strain (γ_{max}) for specimen BG-1 at 80 % of the peak load in the post-peak stage. This loading stage contains both FPZ (l ~ 17 mm) and macro-crack (l_{tfz} ~ 7 mm) as shown in

Figure 2-8c. It is clear from Figure 2-10a-b that both FPZ and macro-crack have a significantly higher concentration of the tensile strain with large negative values minimum principal strain (ϵ_{22}) as compared to the maximum shear strain (γ_{max}) (Figure 2-10a-b). For instance, the high strain zone (highlighted by the shaded region in Figure 2-10c-d) in the horizontal strain profile along the cross-section at the notch tip (y = 25 mm) has the peak tensile strain (ϵ_{22}) of -5.5%, which is approximately eight times the value obtained from maximum shear strain (γ_{max} ~0.7%). Similarly, the remaining two cross-sections (y = 35 mm, 48 mm) that lie inside FPZ also showed the concentration of minimum principal strain (ϵ_{22}) being higher by order of magnitude compared to values of the maximum shear strain (γ_{max}) (Figure 2-10c-d). This suggests that the strain localized zone representing both FPZ and macro-crack is predominantly comprised of the mode I component according to 2D-DIC analysis. A non-negligible amount of maximum shear strain (γ_{max}) indicates the presence of shear microcracking, which is corroborated by the formation of randomly distribution AE-based shear events (Figure 2-10b). However, due to the significant scattering of these shear events, the concentration of maximum shear strain is considerably small ($\gamma_{max} < 0.5\%$) for most points inside the strain-localized zone except at the notch tip. It can be concluded that both AE and DIC analysis showed the FPZ and macro-crack are dominantly mode I with some amount of shear micro-cracking.

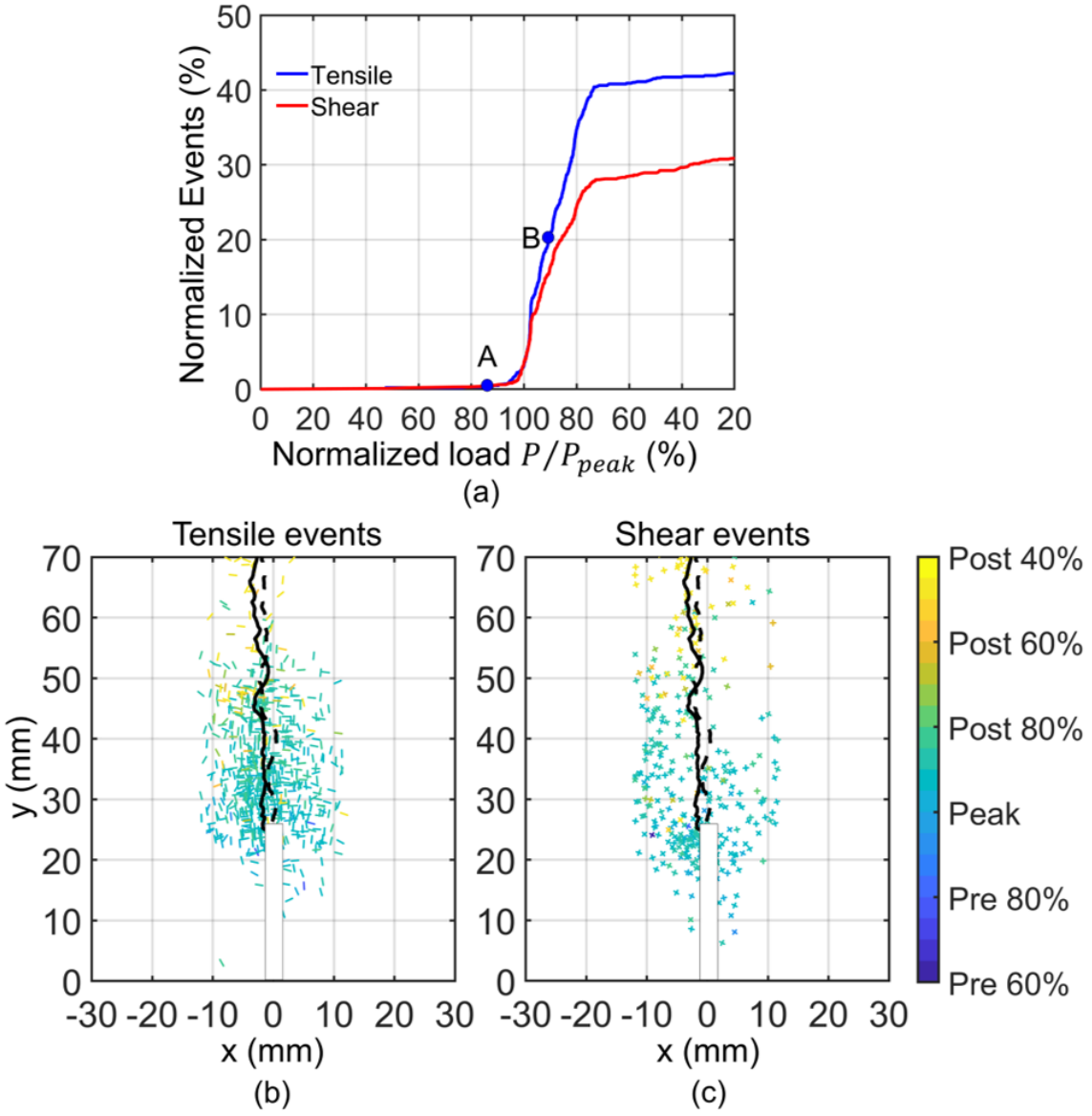

Figure 2-9 Specimen BG-1 with (a) Temporal evolution of two types of AE events; Spatial distribution of the AE events: (b) Tensile microcracks, (c) Shear microcracks. Points 'A' and 'B' represent FPZ and Macro-crack initiation stages, respectively. Color indicates the loading stages of AE events in (b-c). The black solid and dashed lines represent paths of macrocrack on the front and back surfaces of the specimens, respectively.

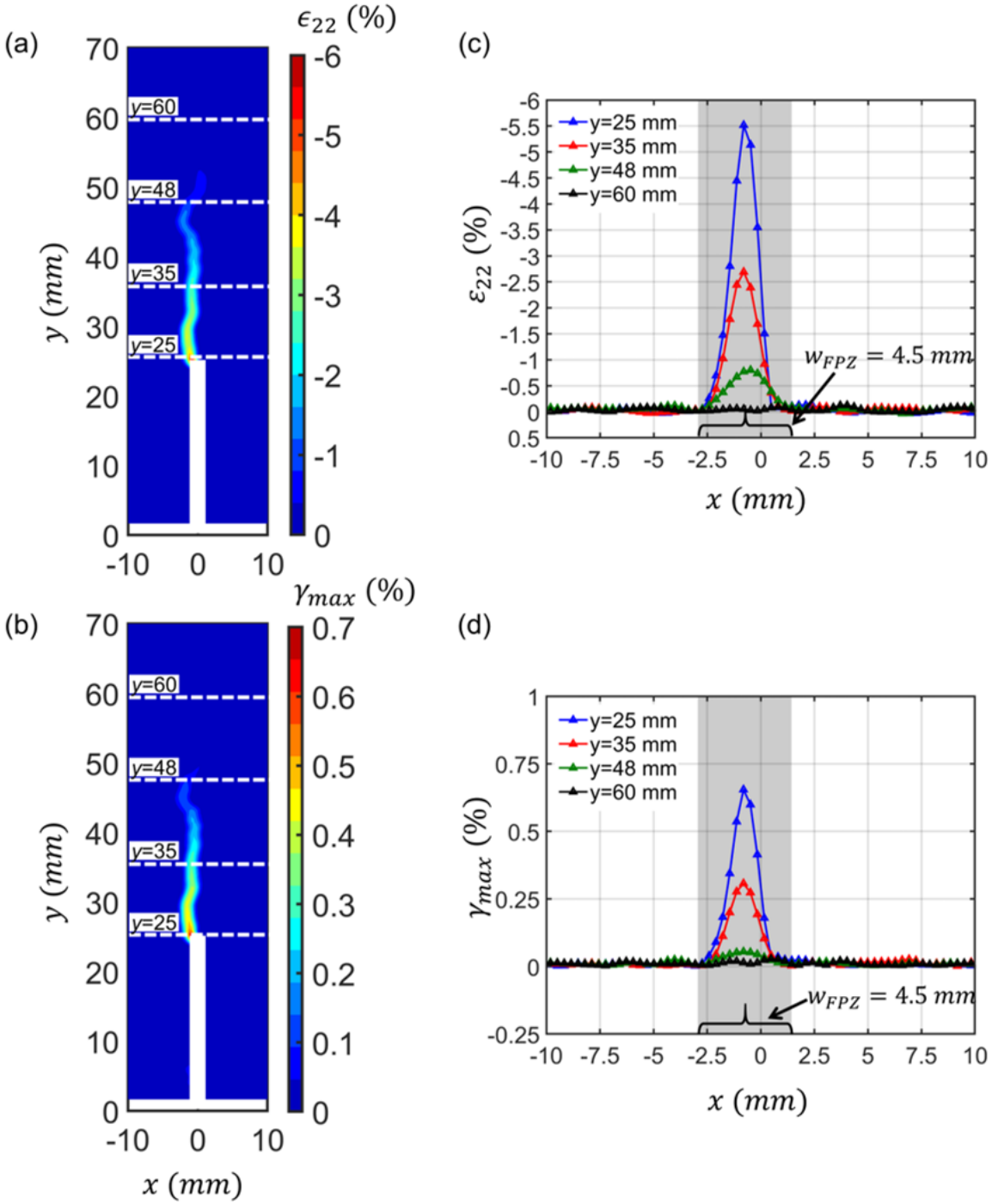

Figure 2-10 Specimen BG-1 at 80% of the peak load in the post-peak regime: Contours of (a) minimum principal strain (ϵ_{22}), (b) maximum shear strain (γ_{max}); four horizontal cross-sections, i.e., y = 25 mm, 35 mm, 48 mm, and 60 mm, showing (c) plot of minimum principal strain (ϵ_{22}) profiles (d) plot of maximum shear strain (γ_{max}) profiles. The W_{FPZ} denotes DIC- based FPZ width. Positive (+) and negative (−) strains represent contraction and extension, respectively.

2.5 Characterization of the Cohesive Zone Model

The constitutive behavior of material inside the FPZ can be described using the cohesive zone model (Bažant, 2002; Bažant and Yu, 2011). The cohesive zone model characterizes the fracturing process in quasi-brittle materials by utilizing the concept of an effective crack length, which considers the total crack composed of FPZ and a traction-free zone (real crack) (Figure 2-11a). In this model, the FPZ is represented by a thin interface that can sustain the cohesive stresses (σ) across its virtual faces (Figure 2-11a-b). The cohesive stress (σ) varies as a function of crack opening displacement (w) in the case of Mode I fracture, which shows a linear increase at the initial loading stages till it reaches the material's tensile strength (σ_t) (Figure 2-11c). This stage of linear increase in cohesive stress (σ) represents the elastic response of the material with an associated value of elastic crack opening displacement (w_e) (Figure 2-11c). The stage of maximum cohesive stresses ($\sigma = \sigma_t$) marked the initiation of the FPZ at the notch tip. With additional loading, the material softening starts to occur inside the FPZ, resulting in a decrease in cohesive stress (σ) as a function of crack opening displacement (w) (Figure 2-11c). Eventually, the cohesive stress (σ) is reduced to zero as critical opening displacement (w_c) is reached, signifying the formation of a macro-crack (traction-free zone). The area under the softening part of the cohesive stress (σ)- crack opening displacement (w) curve is typically defined as fracture energy (G_f) (Figure 2-11c) and represents the critical energy dissipation for a unit area of crack growth. The fracture energy (G_f) and fully developed FPZ length (L) are considered material properties usually determined from various fracture parameters such as material tensile strength (σ_t), elastic crack opening (w_e) and critical crack opening displacements (w_c) for Mode I fracture. However, an accurate characterization of non-linear deformation inside FPZ is challenging due to various limitations, such as large variations in critical opening displacement

(w_c) and uncertainty in softening law of the cohesive zone model. The softening curve can be assumed either based on polynomial law (Karihaloo and Xiao, 2003), bilinear law (Petersson, 1981), or linear law (Bažant, 2002).

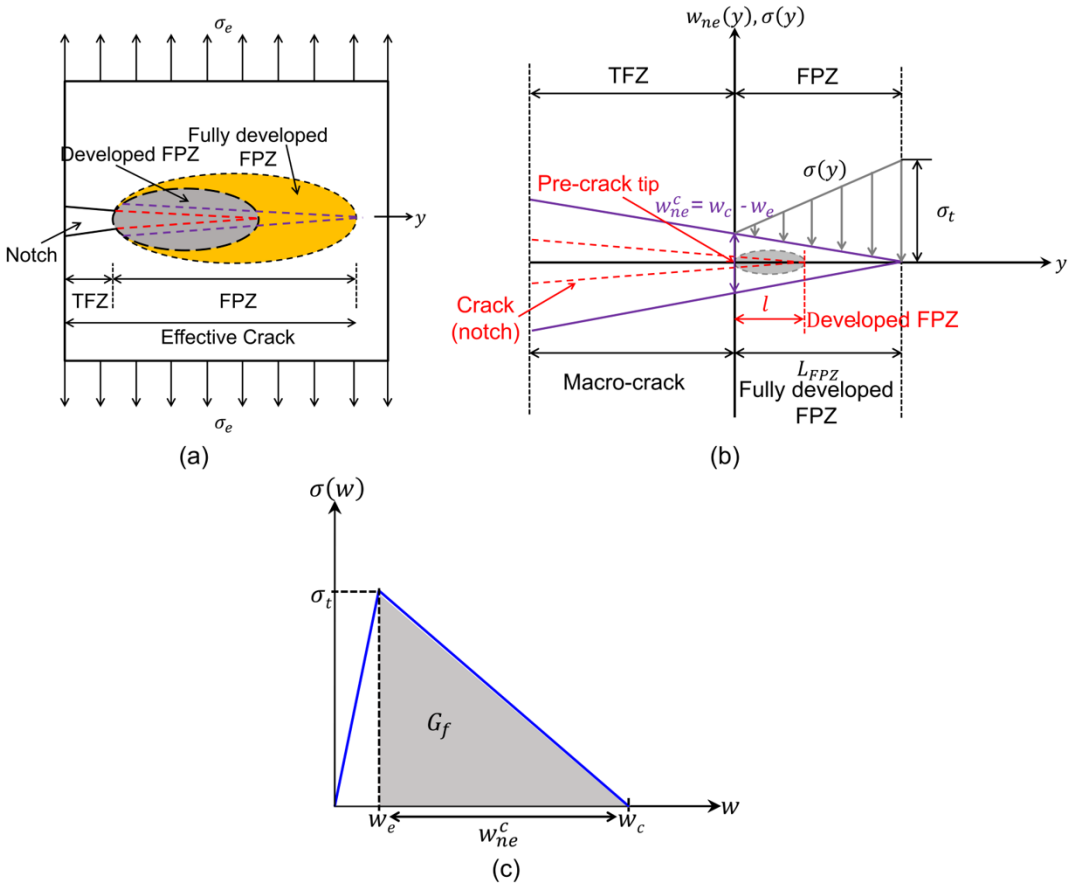

Figure 2-11 (a) FPZ formation in Barre granite; (b) linear traction-based cohesive zone model inside the FPZ; (c) linear softening law used for quasi-brittle materials (Zhang et al., 2018), TFZ-traction free zone.

The characteristics of the cohesive zone model in Barre granite specimens were determined using a combination of AE parameters and the displacement approach of 2D-DIC. For Barre granite specimens, the values of elastic crack opening (w_e) and critical crack opening displacements (w_c), were estimated based on the variation of the $CTOD$ with the normalized load-point displacement (δ_{norm}) (Table 3-2). Based on relatively lower critical opening

displacements (w_c~35μm) of Barre Granite specimens compared to concrete (w_c~100μm), moderate softening of the Barre granite specimens was assumed, which indicates a linear softening law and is given by the following expression:

$$\begin{cases} \sigma(w) = \sigma_t\left(\dfrac{w}{w_e}\right) & (0 \le w \le w_e) \\ \sigma(w) = \sigma_t\left(1 - \dfrac{(w - w_e)}{(w_c - w_e)}\right) = \sigma_t\left(1 - \dfrac{(w_{ne})}{(w_{ne}^c)}\right) & (w_e \le w \le w_c) \end{cases} \tag{2-4a}$$

$$w_{ne} = w - w_e;\ w_{ne}^c = w_c - w_e \tag{2-4b}$$

where σ_t denotes material tensile strength, w represents crack opening displacement, w_e is elastic opening displacement, w_c denotes critical crack opening displacement. w_{ne} and w_{ne}^c represent the inelastic component of COD and its critical value, respectively. The softening law, also called LCZM, assumes the linear distribution of cohesive stress (σ) over the FPZ (Labuz and Biolzi, 1991), with its maximum value equal to the material's tensile strength (σ_t) at the FPZ tip, as shown in Figure 2-11b. As a result, a linear relationship between the length of FPZ (l) and notch tip cohesive stress (σ^{ct}) at a given load can be written as:

$$\sigma^{ct}(l) = \sigma_t\,(1 - l/L) \tag{2-5a}$$

$$\sigma^{ct}(w_{ne}^{ct}) = \sigma_t\left(1 - \frac{w_{ne}^{ct}}{w_{ne}^c}\right);\ w_{ne}^{ct} = w^{ct} - w_e \tag{2-5b}$$

where L is the fully developed length of FPZ, w^{ct} is total $CTOD$, w_{ne}^{ct} denotes an inelastic component of the $CTOD$. Equating the value of cohesive stress at the notch tip from Eqs. 2-5a and 2-5b, a linear relationship is found between FPZ length (l) and inelastic $CTOD$ as given by:

$$w_{ne}^{ct}(l) = l(w_{ne}^c/L) \tag{2-6}$$

Figure 2-12a-d shows the values of FPZ length (l) and the inelastic component of $CTOD$ (w_{ne}^{ct}) obtained from DIC as well, as best fitted curve for all four specimens. It is clear that linear relationships exist between two parameters with R^2 0.98-0.99 for all four specimens.

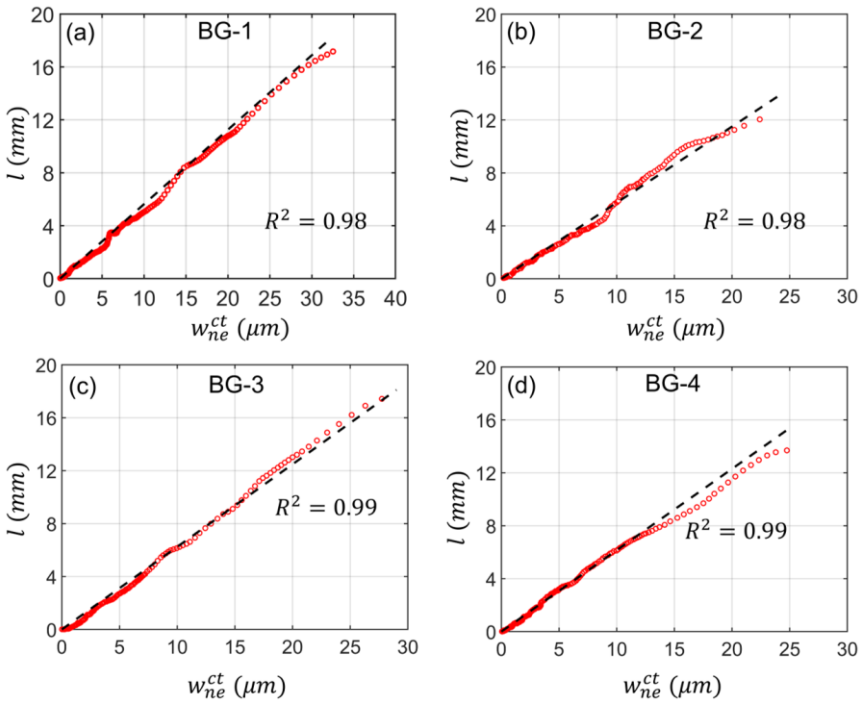

Figure 2-12 The relation between the FPZ length (l) and the inelastic component of *CTOD* (w_{ne}^{ct}) (both identified by DIC) along with best-fit linear curve for four Barre granite specimen (BG-1, BG-2, BG-3, BG-4).

2.6 Conclusion

While the influence of FPZ on Mode I fracture in rocks has been previously investigated, it is still challenging to identify the transition points between the different stages of FPZ evolution, especially the macro-crack initiation stage, which is often influenced by material heterogeneity near the pre-crack tip. In this study, a novel methodology using the displacement approach of 2D-DIC was implemented to characterize the FPZ evolution in a consistent manner for Barre granite specimens under Mode I loading. AE complemented the DIC-based analysis, which

provided various characteristics of the micro-cracking events inside the FPZ. The main findings of the investigation are:

1. Both $CTOD$ and AE-based measurements, such as AE event rate and associated energy release, can be independently used to characterize three stages of the FPZ evolution. The elastic stage was described by the linear variation of $CTOD$, which also resulted in negligible AE activity. The FPZ initiation from the notch tip was characterized by an accelerated rate of increase in $CTOD$, which was found to be a consequence of consistent AE activity with the initiation of high-energy events ($E_e/E_o \geq 100$). The macro-crack initiation, which results in unstable crack propagation, was marked by the rapid jump in all three parameters $CTOD$, cumulative AE events, and cumulative AE event energy. Additionally, the macro-crack initiation occurred in the post-peak regime in all Barre granite specimens.
2. The material behavior inside FPZ is typically defined using the cohesive zone model, whose parameters, such as elastic opening (w_e) and critical opening (w_c) displacements were identified based on the evolution of the $CTOD$. A significant value of the elastic opening displacement (w_e) within the range of 4–9μm was obtained in the Barre granite specimens. This observation agrees with the work of Lin et al. (2019b), which for Berea sandstone, shows that the material can have a significant elastic opening displacement before the FPZ initiation. Additionally, a small variation in critical opening displacements (w_c) was observed in Barre granite specimens, which makes the $CTOD$ a reliable parameter in characterizing the cohesive zone model for Mode I fracture in Barre granite.
3. The FPZ length at a given load stage was identified using the DIC-based COD profile (i.e., $w_e < \text{COD} < w_c$) along the fracture plane, which was compared using AE-based measurement. The FPZ identification using AE analysis included localized AE energy

release inside the FPZ. Both approaches showed a similar variation of FPZ length with applied load except for the small difference (~ 1 mm) after the macro-crack initiation from the notch tip.

4. The linear cohesive zone model (LCZM) was found most suitable for characterizing material behavior inside the FPZ for Barre granite, based on the linear relationship between FPZ length (l) and inelastic $CTOD$ (w_{ne}^{ct}) (both identified using DIC) for all four Barre granite specimens.

2.7 Acknowledgement

Funding for this research was provided by the National Science Foundation under award number 1644326. The authors are grateful for this support.

2.8 Coauthor Contributions

Sana Zafar and Dr. Omid Moradian aided in collecting and analyzing Acoustic emission data (Section 2.3.2 and 2.4.5).

CHAPTER 3

AN INTEGRATED APPROACH FOR EVALUATION OF LINEAR COHESIVE ZONE MODEL'S PERFORMANCE IN FRACTURING OF ROCKS

This paper has been published in the journal Rock Mechanics and Rock Engineering (Garg et al., 2021)*

Prasoon Garg[2], Bhardwaj Pandit[1], Ahmadreza Hedayat[2], D.V. Griffiths[2], G. L. Sivakumar Babu[1]

3.1 Abstract

Fracturing in rocks results in the formation of an inelastic region surrounding the crack tip called the fracture process zone (FPZ), which is often characterized using the Linear Cohesive Zone Model (LCZM). Various numerical studies have shown that the prediction of the FPZ characteristics is significantly influenced by variability in the input parameters of LCZM, such as crack tip opening displacement and tensile strength. In this study, an integrated approach was used for evaluating the LCZM performance in predicting fracture processes of Barre granite specimens, as a representative rock, under mode I loading. The approach involved experimental testing, numerical simulation, uncertainty quantification of overall fracture behavior, and global sensitivity analysis. First, parameters of the LCZM were estimated from three-point bending tests on center notch Barre granite specimen using the two-dimensional digital image correlation (2D-DIC) technique. This was followed by the implementation of the LCZM in the XFEM-based numerical model to simulate the evolution of the FPZ in tested geometry. The results from the

[1]Indian Institute of Science, Bangalore, Civil Engineering
[2]Colorado School of Mines, Civil and Environmental Engineering
* See Appendix A for permission and citation

deterministic numerical simulation showed that while LCZM can predict all stages of FPZ evolution, the variability in the experimental results, such as the FPZ size, cannot be accounted. The variability of the material response was quantified using a random variable analysis, which involved treating the LCZM's parameters as random variables. This was followed by the global sensitivity analysis that revealed the most sensitive input parameter is the tensile strength for accurate prediction of the global response of rock specimens under mode I loading.

3.2 Introduction

The rock behavior is typically governed by the various fracturing processes, such as the initiation of new cracks and their interaction, and not by the intact matrix, as these processes often act as precursors of ultimate failure. The fracturing in rocks and other quasi-brittle such as concrete, is often characterized by a significant size of an inelastic region surrounding the crack tips (Hoagland et al. 1973; Labuz et al. 1987). The inelastic deformation occurs due to the formation of a micro-cracking zone, also known as the fracture process zone (FPZ), which has a significant impact on the overall failure of laboratory-scale rock specimens, as its size is often comparable to pre-existing cracks (Backers et al. 2005; Ghamgosar and Erarslan, 2016; Parisio et al., 2019). In recent years, various studies (Wang and Hu, 2017; Zhang et al., 2018; Yu et al., 2018; Lin et al., 2019a-b, 2020; Yang et al., 2019) have used the cohesive zone model (CZM) to characterize the formation of the FPZ in rocks. The CZM lumps the FPZ into a thin interface with a softening response in the form of traction (cohesive stresses inside FPZ) -separation (crack opening displacement (w)) law (Hillerborg et al., 1976; Planas et al., 2003). Despite its extensive application in characterizing the FPZ based on laboratory experiments, its implementation in simulating rock fracture has been limited to a few geometries of Mode I loading, such as three-point bending test, disk-shaped compact tension test, short-rod fracture

test, etc (Fakhimi and Tarokh, 2013; Khoramishad et al., 2013; Rinehart et al., 2015; Yang et al., 2019).

In this study, the Linear Cohesive Zone Model (LCZM) was used to simulate the FPZ evolution. This study's main objective was to assess the LCZM's capability in predicting various fracturing characteristics, such as the evolution of the FPZ and its size, along with the global response of the material. To achieve the main objective, fracturing in notched Barre granite specimens under Mode I loading was explored through an integrated approach involving experimental testing, numerical simulation, uncertainty quantification, and global sensitivity analysis.

Over the years, the CZM, based on different softening law such as linear, bilinear, and exponential law has been used to predict the fracture behavior in different materials such as concrete, polymers based composites, and asphalt mixtures (Bazant and Planas 1997; Elices et al. 2002; Soares et al. 2003; Roesler et al. 2007; Song et al. 2006). The identification of suitable softening law plays an important role in the prediction of fracture behavior (Shet and Chandra, 2004; De Borst, 2003), which is typically done using various indirect methods that require inverse analysis (Elices et al., 2002; Oh and Kim, 2013; Chen et al., 2014; Xu et al., 2014; Lin et al., 2020). These inverse analysis-based methods mainly rely on matching the global response of the specimens and thus can provide non-unique softening law (Bažant and Yu, 2011). Alternatively, non-destructive optical techniques such as Acoustic emission (Zhang et al., 2018), speckle interferometry (Lin et al., 2009), and digital image correlation (DIC) (Le et al., 2014) have been increasingly used to characterize the CZM for rocks due to their ability to provide the fundamental information about different fracture characteristics inside the FPZ. Various studies (Ji et al., 2016; Zhang et al., 2018) using DIC have characterized the evolution of the FPZ in

three stages, namely; (1) elastic phase, (2) formation and propagation of the FPZ, and (3) macro-crack initiation. However, there is no consistent method to pinpoint the transition between these three stages. For instance, most studies (Le et al., 2014; Ji et al., 2016; Lu et al., 2019; Maio et al., 2020) characterized the tip of the FPZ, i.e., the boundary between the elastic zone and the FPZ, as a merged position of displacement contour without any support from existing fracture model (Lin et al. 2020). As a result, a considerable variation in parameters of CZM is found for rocks as seen in Berea sandstone (Lin and Labuz 2013; Lin et al. 2019b), with significant scatter in the critical opening displacement (30-100 μm) and fracture energy (75-140 J/m^2). Additionally, due to their localized nature, these fracture properties are strongly influenced by material inhomogeneity and grain size and, thus, are difficult to estimate (Lin et al. 2019a).

Numerical simulations can provide valuable insights into the kinematic of the FPZ during fracture propagation compared to laboratory experiments. However, due to the uncertainty in the parameters of the CZM, few applications can be found in rocks (Yao et al., 2012; Fakhimi and Tarokh, 2013; Khoramishad et al., 2013; Rinehart et al., 2015; Xie at al., 2017; Yang et al., 2019). For instance, Rinehart et al. (2015), based on the implementation of the LCZM in Limestone specimens, found that accurate estimation of material properties is vital for the proper prediction of fracture processes and the global response of the rock specimens. The accuracy of prediction from the CZM is further complicated by material heterogeneity in rocks, which is responsible for a large variation in its fracture properties, such as tensile strength (σ_t) and fracture toughness (Aliha and Ayatolllahi, 2014; Aliha et al., 2018). Besides material heterogeneity, uncertainties can also occur due to other sources, such as the natural variation of properties, imperfections, and unpredictability caused by the lack of sufficient information on parameters or models (Baecher and Christian, 2003). Therefore, it is vital to quantify the extent

of variability in fracture properties for proper characterization of the fracture behavior. The recent studies by Aliha et al. (2012) Aliha and Ayatolllahi (2014), and Aliha et al. (2018) tried to achieve this by implementing statistical analyses that involved estimation of the probability of fracture using a larger number of test data (~15 samples) of various rocks such as Harsin marble and Guiting Limestone. However, these studies were based on LEFM (assuming the elastic stress distribution around the crack tip) and thus didn't account for the FPZ and its influence on overall fracture behavior. To characterize uncertainty in the CZM, variability in its input parameters is identified by testing a large number of specimens (Bažant and Yu 2011; Khoramishad et al. 2013; Rinehart et al. 2015). Alternatively, based on a range of limited data (4-5 tests), uncertainty in input parameters of the CZM is quantified and subsequently treated as random variables, which then can be used in a numerical model to provide a quantification of uncertainty in fracture characteristics such as the FPZ initiation and its size. Additionally, it is also essential to study the contribution of the variability of input parameters toward the variability in overall fracture behavior. This can be accomplished by conducting global sensitivity analysis (GSA) and ranking the input parameters according to their relative contribution. Two global sensitivity measures are widely used in the literature, namely: (a) variance based (Sobol 1993) and (b) moment independent sensitivity measures (Borgonovo 2007). Variance based sensitivity measure is most often adopted due to its ability to provide a good understanding of the model structure (Oakley and O'Hagan, 2004). Sobol indices quantify the relative percentage contribution of each input parameter in the total variance of the output. This is achieved by estimating the first-order effects (i.e., the percentage contribution of the individual variable alone) and total effects (i.e., first-order in addition to the contribution caused by its interaction with other parameters). Literature involving the application of these methods to study the sensitivity of input parameters

on rock engineering problems is sparse. Pandit et al. (2019) estimated global sensitivity measure-Sobol indices for rockmass parameters defined by the Hoek-Brown constitutive model for the jointed rock slope.

The objective of this study was to assess the ability of CZM to predict the overall fracture behavior of Barre granite rock using an integrated approach involving the four major steps, namely: (a) experimental analysis, (b) numerical simulation, (c) uncertainty quantification of fracture behavior, and (d) identification of most influence input parameters of th*e* CZM. The previous study by authors (for details, see Garg et al. 2020) found that the LCZM (based on linear softening law) is suitable for characterizing the non-linear deformation inside FPZ of Barre granite specimen under Mode I loading. Additionally, various experimental studies have also found the LCZM to be a reasonable approximation of material behavior inside FPZ for various rocks (Yang et al., 2016; Xie et al., 2017; Zhang et al., 2018; Xing et al., 2019; Lin et al., 2019a-b). A series of three-point bending tests were performed on center-notch Barre granite specimens to estimate parameters of LCZM, which was then implemented in XFEM based numerical model. The uncertainty in the fracture behavior in terms of the peak load and the FPZ characteristics were then quantified by treating the fracture properties as random variables and conducting Monte Carlo simulation (MCS) on the surrogate augmented radial basis function (RBF) based response surface of the numerical model. This is followed by a variance-based global sensitivity analysis for the identification of the most influential input parameters.

3.3 Experimental Design

This study used data from three-point bending tests on four Barre granite specimens (BG-1, BG-2, BG-3, BG-4) (Figure 3-1a-c) performed in section 2.3.

3.4 XFEM based Numerical Modeling

Since its inception, XFEM has been widely used in various fracture mechanics problems due to its effectiveness in modeling discontinuities in various static and dynamic crack problems (Elguedj et al., 2009; Khoei and Mohammadnejad 2011; Fan and Jing, 2013; Sharafisafa and Nazem, 2014; Zhuang et al., 2014; Eftekhari et al. 2015; Zhou et al., 2020). In the conventional FEM, modeling discontinuities such as cracks requires conformity of the mesh to the geometric discontinuities (Khoei, 2014). Additionally, cracks in conventional FEM can only propagate along element edges and thus require remeshing with the formation of new cracks (Sharafisafa and Nazem, 2014). The XFEM alleviates these problems by using the partition of unity method, which allows elements that are intersected by discontinuities to be locally enriched while retaining properties of the stiffness matrix of the standard FEM. (Moës and Belytschko, 2002). In XFEM, cracks or voids are represented independently of the FE mesh by adding enrichment functions and additional degrees of freedom to the elements intersected by the crack (Karihaloo and Xiao 2003). The important concepts of XFEM, along with the details of the implementation in the commercial software Abaqus, are presented in this section.

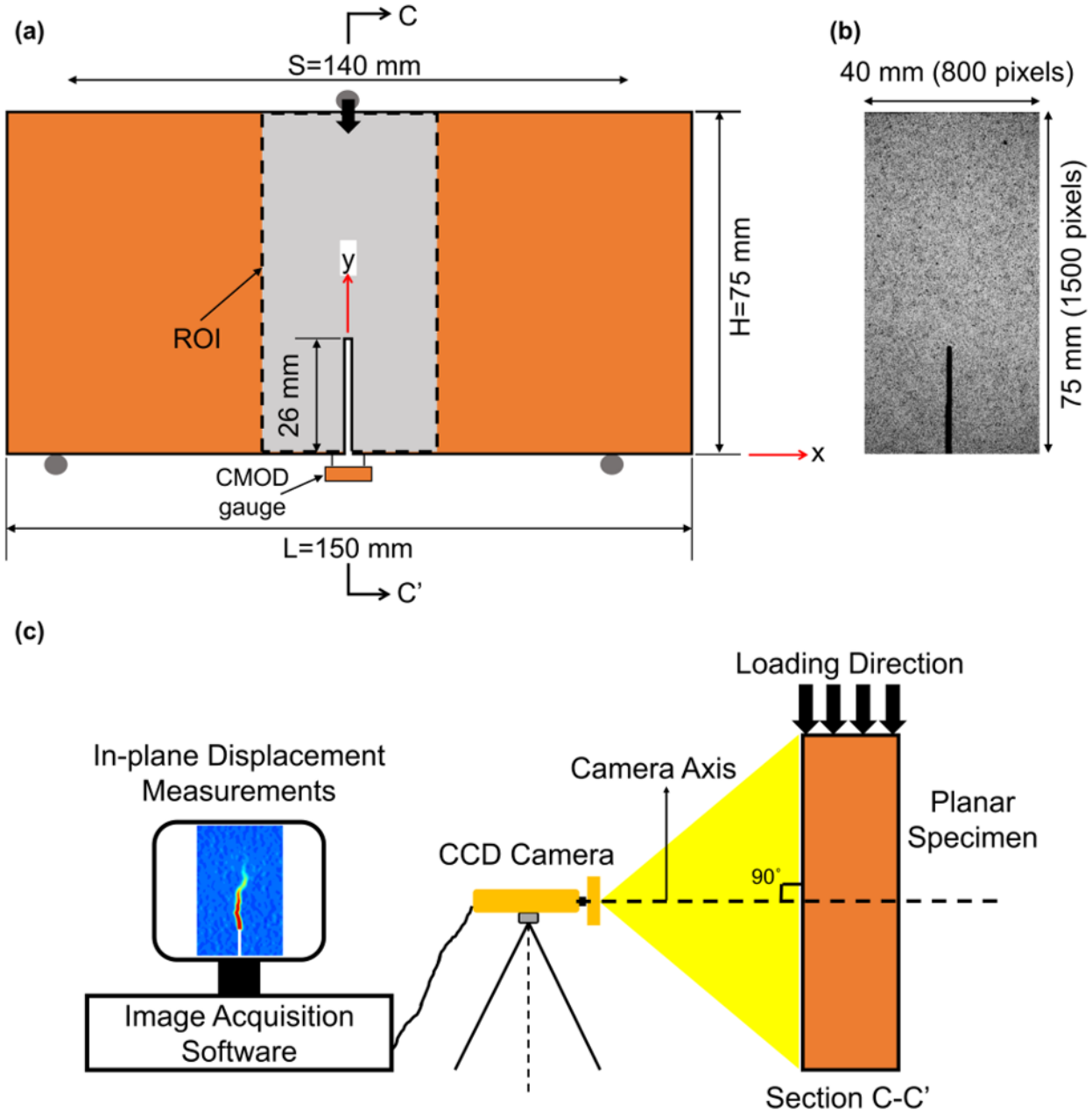

Figure 3-1 (a) Loading geometry of the three-point bending test along with the field of view for DIC analysis, (b) Image of the speckle pattern obtained on specimen BG-1, and (c) The schematic of the experimental setup used for a three-point test for synchronously capturing the crack propagation using the 2D-DIC. Figure not in scale.

3.4.1 XFEM Representation of Cracks

In XFEM formulation, displacement field (u) is approximated as a combination of continuous part and discontinuous part as given by (Belytschko and Black, 1999; Zi and Belytschko, 2003):

$$u(x) = u_{cont}(x) + \mathrm{u}_{disc}(x) \tag{3-1}$$

where x represents the position vector, $u_{cont}(x)$ is continuous displacement field and $\mathrm{u}_{disc}(x)$ represents the discontinuous displacement field, which incorporates local enrichment functions to account for the presence of a crack. The displacement field in Eq. 1 can be rewritten as:

$$u(x) = \sum_{I} N_I(x)\, u_I + \sum_{I \in K_\Gamma} N_I(x)\, H(x) a_J + \sum_{I \in K_\Lambda} \left[N_I(x) \sum_{\alpha=1}^{4} F_\alpha(x) b_{I\alpha} \right] \tag{3-2}$$

where $N_I(x)$ represents standard shape functions and u_I represents the nodal displacement contribution due to the continuous part of the standard finite element solution. The $H(x)$ is the Heaviside enrichment function that accounts for displacement jump across crack interior faces and $F_\alpha(x)$ represent the crack tip enrichment functions that account for the elastic asymptotic fields near the crack tip (Giner et al. 2009). a_J and $b_{I\alpha}$ are the degrees of freedoms (DOFs) vectors of the enriched nodes. The displacement contribution of the continuous part, i.e., the first term at the right-hand side of Eq. 3-2, is estimated for all the nodes in the model domain. K_Γ and K_Λ belongs to the nodal subsets containing the crack interior (shown by red circles in Figure 3-2) and the crack tip (shown by yellow rectangles in Figure 3-2). In XFEM, each node is only enriched with a single type of enrichment function and additional DOFs. For the 2D-problems,

nodes enriched with the Heaviside function have two additional DOFs, while nodes with crack tip enrichment functions have eight additional DOFs.

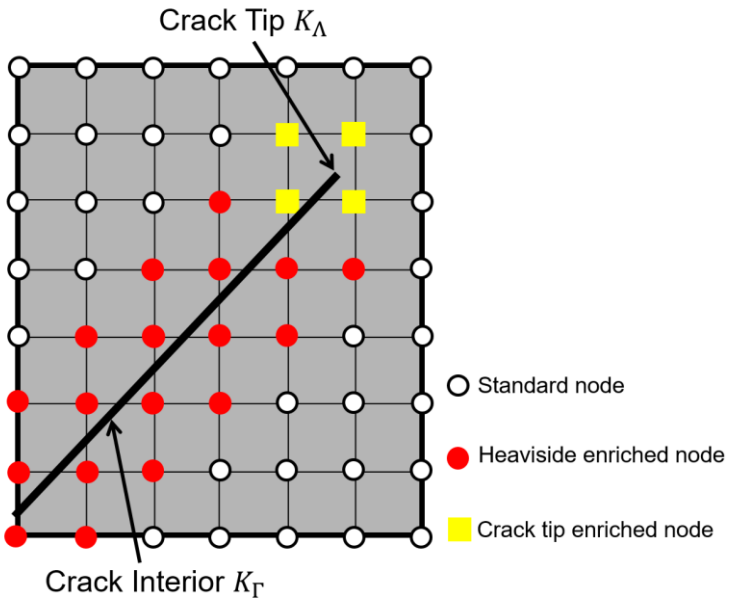

Figure 3-2 Enriched elements in XFEM (after Xie et al., 2017).

3.4.2 Crack Initiation and Propagation Criteria

The CZM is typically used to simulate the inelastic behavior of the material inside the FPZ of quasi-brittle materials such as rock and concrete (Roesler et al., 2007; Song et al., 2006; Reinhart et al., 2015; Xie et al., 2017; Zhang et al., 2018). The CZM (Hillerborg et al., 1976) lumps the FPZ ahead of the crack tip into a thin interface (also known as a cohesive zone) that can transmit stresses across its faces (Figure 3-3a). In the current study, LCZM was used as it was experimentally verified for Barre granite, as shown in section 2.5. The LCZM assumes the material behavior to be linearly elastic from $\sigma_n = 0$ to $\sigma_n = \sigma_{n,max}$ (cohesive strength) with the associated limit of elastic opening displacement (w_e) (Figure 3-3c). At this stage, the FPZ initiates at the crack tip, which subsequently undergoes softening with the further increase in the crack opening displacement (w) and thus results in the degradation of the material's elastic

stiffness (highlighted by light gray in Figure 3-3c). The softening of the cohesive zone is characterized by a linear decrease in cohesive stress from $\sigma_n = \sigma_{n,max}$ with opening displacement at the elastic limit (w_e) to a critical opening displacement (w_c) where the cohesive stress reaches zero ($\sigma_n = 0$). This implies that the material has undergone complete failure, resulting in the formation of a macro-crack (traction-free crack).

The softening curve provides information about the energy dissipated inside the FPZ. The area under the softening curve is typically defined as the critical value of energy dissipation, also known as fracture energy (G_F) (Bazant and Plaňas, 1997; Zhang et al., 2018; Lin et al., 2019b). The fracture energy (G_F) obtained from LCZM is equivalent to the critical energy release rate *(G_{Ic})* when the assumption of LEFM is valid (Lin et al., 2019b). For Mode I fracture, the constitutive relationship between cohesive stresses ($\sigma_n(w)$) and crack opening displacement *(w)* is given in Eqs 2-4a-b. The fracture energy *(G_F)* (area under the softening curve) can be written as:

$$G_F = \frac{1}{2}(\sigma_{n,max}) w_{ne}^c \tag{3-3}$$

Therefore, LCZM characterize FPZ as a cohesive zone having a linear distribution of the normal stresses along its length with its maximum value ($\sigma_n = \sigma_{n,max}$) at the tip of FPZ as shown in Figure 3-3b.

In Abaqus, the elastic response of the traction-separation law of the LCZM (Figure 3-3c) is implemented based on the tensile elastic modulus *(E_t)* of the material instead of using the elastic opening displacement (w_e) (Abaqus, 2016). The FPZ initiation stage is then predicted using the Maximum Principal Stress (MPS) criterion as given by:

$$F = \left\{ \frac{\langle -\sigma_{max} \rangle}{\sigma_{n,max}} \right\} = 1 \tag{3-4}$$

The tensile stress is negative in the current study, and thus, the minimum principal stress is used to represent σ_{max} in Eq 3-4, $\langle . \rangle$ represent the tensile component of stress, i.e., $\langle -\sigma_{max} \rangle$ is equal to 0 when stresses are under pure compression ($\sigma_{max} \geq 0$). Therefore, at the FPZ initiation stage, the minimum principal stress in an element exceeds the cohesive strength of the material ($\sigma_{n,max}$). The cohesive strength $\sigma_{n,max}$ is typically assumed equal to the indirect tensile strength (σ_t) of the material, estimated from Brazilian tests (Bazant and Planas, 1997; Song et al., 2006). After the FPZ initiation, the softening is implemented by decreasing the cohesive stresses as a function of the inelastic crack opening displacement (w_{ne}). In the present study, various parameters of the LCZM, such as critical inelastic crack opening (w_{ne}^{c}) and the size of the fully developed fracture process zone (L_{FPZ}) were estimated using the displacement approach of 2D-DIC.

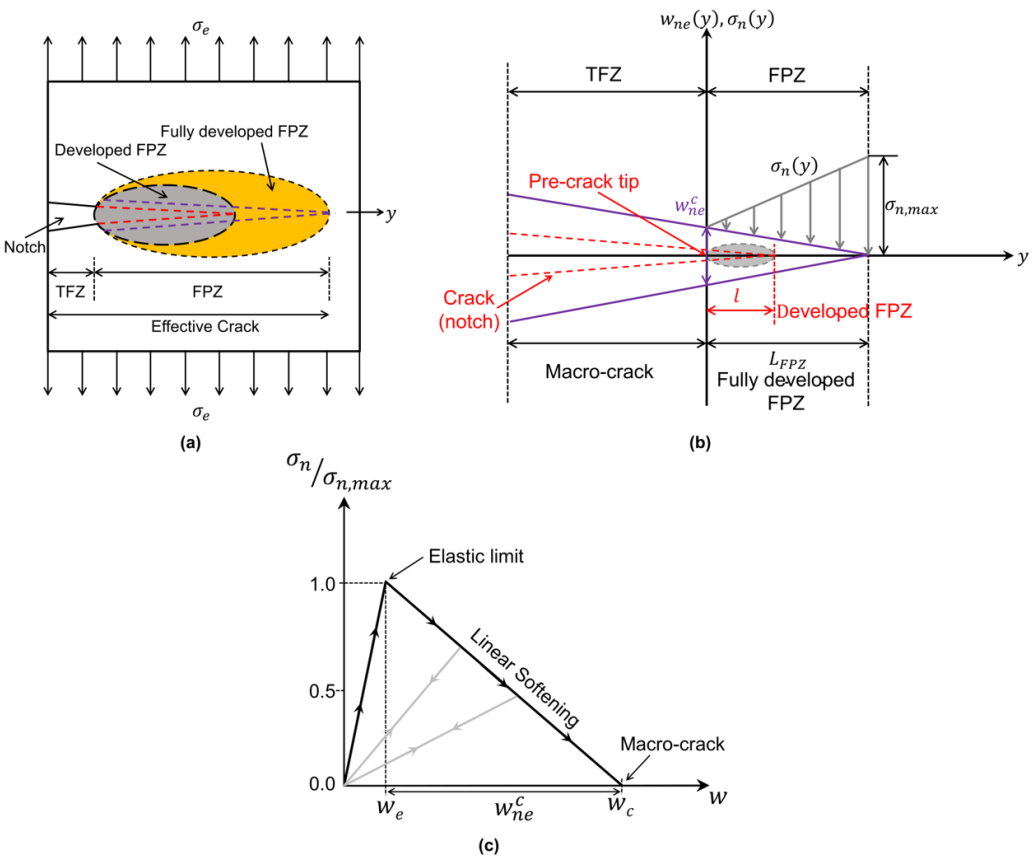

Figure 3-3 (a) FPZ development in rocks, Linear cohesive zone model (LCZM) (b) with linear distribution of traction along the FPZ, and (c) linear softening law, traction free zone (TFZ) (after Zhang et al., 2018).

3.4.3 Model Setup

The commercial general-purpose finite element package Abaqus was used to simulate the crack propagation using the XFEM approach in the center notched Barre granite specimen. Figure 3-4 shows the 2D model of the three-point bend test on barre granite specimen under plane stress conditions. Due to the small specimen thickness (B = 25 mm) compared to other dimensions, the 2-D model represents planar crack propagation through its entire thickness. The assumption agrees with other studies such as Rinehart et al. (2015) and Obara et al. (2020) that, based on a 3D model of three-point bending test, found crack propagation through entire specimen thickness with a straight crack front. The modeled specimen in the current study had

the same nominal dimensions as the experiments with a 1 mm wide blunt notch (Figure 3-1a and 3-4), which resulted in a finite concentration of stresses at the notch tip, comparable to values excepted in test specimens. To simulate actual laboratory testing conditions, bottom rollers fixed in both x and y directions, and top roller fixed in x-direction were used (Figure 3-4). To model three-point bending, a displacement rate of 0.1 mm/step (1step =1sec) was applied at the top roller. The crack (notch) mouth opening displacement (CMOD) was recorded at the gage length of 12 mm in the numerical simulation. The entire specimen was divided into three partitions to achieve a finer mesh in the area around the notch tip with a lower computational time (Figure 3-4). The model was discretized using 4-node bilinear plane stress quadrilateral elements with a mean size of 0.2 mm in the central partition, while the remaining area had a coarser mesh with a mean size of 2 mm (Figure 3-4). The element size of 0.2 mm (around 20% of notch width) ensures a smooth and accurate stress distribution around the notch tip, as recommended by Rehinhart et al. (2015) and Luzio et al. (2018).

The material parameters of Barre granite are listed in Table 3-1. In the deterministic numerical model, the mean value of each parameter was used. The elastic parameters (E_t ,ϑ) were taken from the work of Goldsmith et al. (1976) to represent the elastic stiffness of Barre granite under tension. Goldsmith et al. (1976), based on uniaxial compression and uniaxial tensile strength tests on Barre granite, found its tensile elastic modulus (E_t) to be less than the compressive modulus (E_c) by a factor of 0.5. In the case of the tensile strength (σ_t), its most reported value based on the work of Goldsmith et al. (1976) and Ching et al. (2018) was used in the deterministic numerical model (Table 3-1). The average value of the critical inelastic crack opening (w_{ne}^c) from four Barre granite specimens (BG-1, BG-2, BG-3, BG-4) was used in the deterministic numerical model (see mean in Table 3-1).

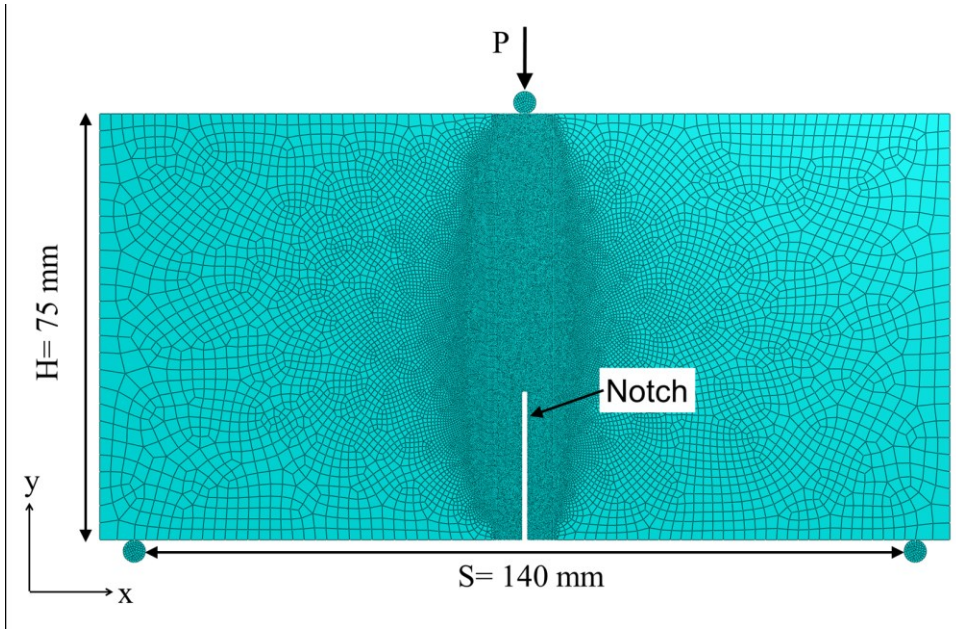

Figure 3-4 Model geometry used for three-point bending test in Abaqus.

3.5 Random Variable Analysis

The presence of natural discontinuities (such as micro-defect) typically lead to a scatter in fracture properties of Barre granite, such as tensile strength (σ_t) and critical inelastic crack opening (w_{ne}^{c}) as shown in Table 3-1. The uncertainties in the estimation of these parameters (used as input parameters in the numerical model) can lead to uncertainty in the determination of some fracture characteristics, such as the peak load and the FPZ size. To statistically characterize the overall fracture behavior, the input rock properties can be considered as random variables. Two widely used methods for this purpose are the Monte Carlo simulation (MCS) and point estimate methods (Harr 1989; Hong 1998). In this study, the MCS is adopted as it is simple and easy to implement. It involves repeated evaluation of the numerical model with randomly generated input parameters values from their respective probability distribution function (PDF). Since it is computationally expensive to directly conduct MCS on the numerical model, an alternative method such as explicit function (also known as the metamodel or the response

surface) can be used as it acts as a surrogate to the numerical model. A linear polynomial augmented radial basis function (RBF) is adopted in this study since it can provide higher accuracy for both linear and nonlinear responses (Krishnamurthy, 2003). This response surface methodology was employed in several other rock engineering problems (Wang et al., 2016; Pandit et al., 2019).

Table 3-1 Input properties used in the deterministic model and random variable analysis

Parameter	Mean	Range	Coefficient of Variation (COV)	Distribution	Truncation limit
Young's modulus (E_t) (GPa)	28	19-80	20%	Lognormal	10-80
Tensile stress (σ_t) (MPa)	14	5-20	20%	Lognormal	5-22
Critical inelastic crack opening (w_{ne}^c) (μm)	32.5	21-58	27%	Lognormal	10-100
Poisson's ratio (ν)	0.16	-	-	-	-

3.5.1 Input Property Distribution

In this study, only three input parameters, namely: (a) tensile elastic modulus (E_t), (b) tensile strength (σ_t) and (c) inelastic crack opening (w_{ne}^c) are treated as uncorrelated random variables. The variation in tensile strength (σ_t) of barre granite (see the range in Table 3-1) in the literature is typically smaller as compared to other igneous rocks (see rock database by Ching et al. 2018). Therefore, the lognormal distribution type with the Coefficient of Variation (COV) of 20% was used for tensile strength (σ_t) in the current study, which is the lowest COV for typical granite rocks (Aladejare and Wang 2017). Additionally, tensile strength (σ_t) is truncated (see the limits in Table 1) to the range of values based on lab experiments available in the literature (Goldsmith et al. 1976; Miller, 2008; Morgan et al., 2013; Ching et al., 2018; ASTM, D3967).

For a similar reason, the distribution of tensile elastic modulus (E_t), is assumed to be lognormal with a COV of 20%. It is also truncated to ensure values from its distribution lie within the range of experimental data of Barre granite available in the literature (see the limits in Table 3-1). The inelastic crack opening displacement (w_{ne}) varies from 21-58 μm based on DIC analysis of four lab experiments in the current study (Table 3-1). The COV of 27 % was assumed for inelastic crack opening displacement (w_{ne}) (Table 3-1), which lies in the range of observed variation (COV=10-35%) of various quasi-brittle materials such as concrete and rocks (Bazant and Giraudon 2002; Yang et al. 2019). Additionally, the truncated limit of inelastic crack opening displacement (w_{ne}) (see the limits in Table 3-1) was selected based on typically observed values for rocks (Zhang et al., 2018; Lin et al. 2019b). All the input random variables are assumed to be independent lognormal distribution as it is widely adopted for most rock properties in the literature (Jiang et al., 2016; Pandit et al., 2019).

3.5.2 Response Surface

The numerical model is approximated using the RBF-based response surface augmented with a linear polynomial. Response surface construction involves solving numerical models on LH samples extracted from input space that serves as training data. The type of RBF adopted in this article is compact support function type II RBF developed by Wu (1995). For detailed methodology pertaining to the construction and performance assessment of the augmented RBF, Pandit et al. (2019) can be referred.

3.6 Global Sensitivity Analysis

Since uncertainty in the input parameters leads to uncertainty in the output, it is necessary to study the contribution of each input parameter variability toward the output's variability. By

identifying the sensitive input parameters, resources can be directed toward reducing the uncertainty in those parameters. Ranking of input parameters according to their magnitude of contribution towards the variability of output can be achieved by the global sensitivity analysis (GSA). GSA based on Sobol indices (Saltelli et al. 2008), quantifies the relative contribution of input parameters on the output variability. The individual contribution of each input parameter in output variability is denoted by first-order Sobol's indices (S_i). The total effect (S_{T_i}) include the individual contribution in addition to the individual contribution. The estimate of S_i and S_{T_i}can be obtained by MC based approach, details of which are mentioned in the literature (Saltelli et al., 2008; Pandit and Babu, 2020).

3.7 Results

3.7.1 FPZ Characterization

This section presents the characterization of the FPZ in Barre granite specimens done in section 2.4.3. This methodology in that section used the concept of the LCZM to identify the transition between the three stages of FPZ evolution, namely: (a) the elastic deformation, (b) the FPZ initiation and its propagation, and (c) the macro-crack initiation that leads to unstable crack propagation. According to the LCZM, elastic opening displacement (w_e) represents the tip of the FPZ (i.e., the boundary between the elastic zone and the FPZ), while critical opening displacement (w_c) can be used to represent the tip of the macro-crack (the boundary between the FPZ and macro-crack). In the adopted methodology, both elastic (w_e) and critical opening displacement (w_c), were estimated based on the evolution of crack opening displacement at the notch tip ($CTOD$) for Barre granite specimens (section 2.4.3). Figure 3-5a presents the contour of horizontal displacement at 75% of the peak during the post-peak stage of the test (i.e., 25% load drop from the peak was reached. Figure 3-5b shows the crack opening displacements (w)

profiles at various loading stages. In order to quantify the $CTOD$ in a consistent manner, two vertical lines at location $x \pm 3$ mm from the notch plane ($x = 0$) were selected to represent the virtual surfaces of the crack plane (Figure 3-5a). The horizontal (normal) displacements were calculated between these two lines (Figure 3-5a), also known as crack opening displacement (w).

Figure 3-6a show the evolution of the $CTOD$ with the normalized load-point displacement (δ_{norm}) for four Barre granite specimens (BG-1, BG-2, BG-3, BG-4). The load-point displacement (δ) was normalized with respect to its value at the peak load stage ($\delta_{norm} = \delta/\delta_{peak}$) for each specimen. The FPZ initiation from the notch tip is denoted by FPZ-I, and the macro-crack initiation is shown by colored circles in all four specimens (Figure 3-6a). These two stages along with other parameters of LCZM, were estimated for all four specimens in section 2.4.4 and are summarized in Table 2-2 and 3-2. It can be concluded that the evolution of $CTOD$ provides a reliable method for the estimation of LCZM's parameters as it has shown consistent behavior for characterizing the three-stages of the FPZ evolution in all Barre granite specimens (BG-1, BG-2, BG-3, BG-4) in accordance with the finding of the study in section 2.4.

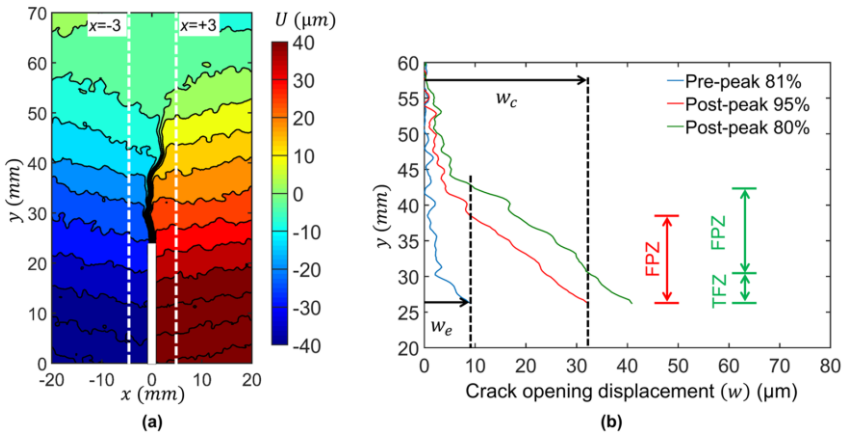

Figure 3-5 (a) Contour of horizontal displacement (U) obtained using the DIC at 75% of the peak load in post-peak stage, and (b) Crack opening displacements (w) at various loading stages along with the method to identify the size of FPZ and TFZ using displacement approach.

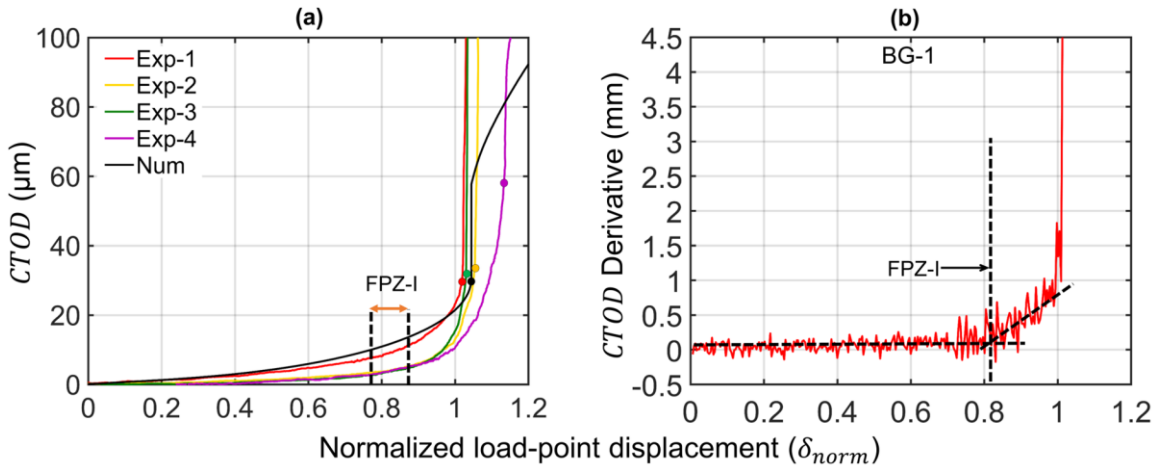

Figure 3-6 Variation of (a) Crack tip opening displacement ($CTOD$) in numerical model and four Barre granite specimens (BG-1, BG-2, BG-3, BG-4), and (b) $CTOD$ derivative for specimen BG-1 FPZ-I denotes FPZ initiation stage.

Table 3-2 Comparison among output parameters obtained from different analyses

Output Parameter	**Mean**	**Standard deviation (COV)**	**95% Confidence interval**	**Best fit distribution (Parameters)**	**Deterministic Numerical Model**	**Experimental results**
Peak load (kN)	4.8	0.74 (15%)	3.5-6.3	Normal (4.8, 0.74)	4.83	3.5-4.6
FPZ initiation load (%)	38	5.07 (14%)	28.8-49.2	Lognormal (37.6, 5.07)	38	80-92
FPZ length (L_{FPZ}) (mm)	16.3	3.7 (23%)	10-24.5	Normal (16.3, 3.7)	15.4	12-23
Macro-crack initiation load (%) (Post-peak regime)	91.6	3.3 (3.6%)	84- 96.8	Weibull (92.9, 34.17)	92	75-95

3.7.2 Deterministic Model

Figure 3-7a provides a comparison between the experimental and numerical results in terms of the applied vertical load as a function of the CMOD. It is clear from Figure 3-7a that pre-peak responses of the numerical model lie within the range of four experiments, indicating that the

tensile elastic modulus (E_t) of 28 GPa is an appropriate value to capture the elastic behavior of the Barre granite beam. However, the peak load stage was overestimated by the numerical model as both the simulated peak load (4.83 kN) and peak CMOD (68 μm) lie outside the range of values obtained from experiments (Figure 3-7a). Similarly, the numerical model's post-peak response differed significantly with a steeper post-peak slope of the load-CMOD curve compared to experimental results. The difference in peak and post-peak response between numerical simulation and four experiments can be attributed to the material heterogeneity of granodiorite rocks such as Barre granite. Various studies (Nasseri et al., 2010; Wang and Hu, 2017; Yu et al., 2018) have shown that the variability in different fracture characteristics, such as the FPZ size and the tensile strength (σ_t) of granite rocks typically depend on various factors such as microstructural anisotropy, grain size, initial notch length (a_o), etc. For instance, Wang and Hu (2017), based on a three-point bending test on yellow granite, found that variability in peak load depends on initial notch length (relative to beam height) with a large fluctuation in peak load in the beam with smaller notches. Additionally, parameters of the LCZM were estimated based on average values of four Barre granite experimental data (Table 3-1), which were then directly used in the numerical model without any calibration. The fracture properties, such as the critical crack opening displacement (w_c) (estimated from experiments in the current study) are highly dependent on the material behavior at a localized level and thus were strongly influenced by structural inhomogeneities such as micro-defects and grain size. As a result, various CZM-based numerical studies (Song et al., 2006; Roesler et al., 2007; Im et al., 2014; Rinehart et al., 2015) typically used a calibration process where parameters of CZM such as critical crack opening displacement (w_c), tensile strength (σ_t) and tensile elastic modulus (E_t) are iteratively changed

until the entire global response (both pre-peak and post-peak regime) from the numerical model provides a good fit with experimental data.

Figure 3-7b shows the evolution of the FPZ length (l) with normalized load ($P_{norm} = P/P_{peak}$) between four experiments results and the numerical simulation. The FPZ length (l) in four experiments were calculated using DIC analysis (section 2.4.5). In the numerical model, the FPZ is represented by elements undergoing progressive damage, denoted by the STATUSXFEM parameter (Figure 3-8a-c). The parameter indicates the status of the element with values between 0 and 1. A value of 1 (red color in Figure 3-8a-c) denotes a "completely fractured or traction-free crack," while a value 0 indicates an elastic state. The elements with the value between 0 and 1 indicate the elements under softening and thus represent the FPZ. Figure 3-8a-c clearly shows the progression of the FPZ at three different loading stages, namely (a) when 80% of the peak load, (b) when the peak load was applied, and (c) when 80% of the peak load was applied during the post-peak stage of the test (i.e., 20% load drop from the peak was reached).

Figure 3-7b clearly presents a consistent trend in the evolution of the FPZ length (l) between the numerical model and experiment results, except for the FPZ initiation stage. The numerical model showed the FPZ initiation at an early stage (38% of peak load) compared to four experiments (80-92 % of peak load). After initiation (Figure 3-7b), both the numerical model and four experimental tests showed a steady increase in the FPZ length (l) until the peak load (approximately 97-99% of peak load) followed by the rapid increase in post-peak regime to its maximum value around the macro-crack initiation stage (95-75% of peak load in the post-peak regime). The observation of the macro-crack initiation stage in the post-peak regime is consistent with various acoustic emission (AE) based studies (Kao et al., 2011; Aggelis et al., 2013; Lin et al., 2019b) on rocks and other quasi-brittle materials. The FPZ at the macro-crack initiation stage

is known as fully developed FPZ, and its length (L_{FPZ}) (Figure 3-3) is considered as a material property based on the LCZM. It can be inferred from figure 7b that, after reaching its maximum value in the post-peak regime, the FPZ length (l) remains nearly constant in the numerical model and four experiments (BG-1, BG-2, BG-3, BG-4) with the exception of a slight decrease (1-3 mm). The observation agrees with the other studies (Lin and Labuz, 2013; Lin et al., 2014; Zhang et al., 2018) on various rocks, such as Berea sandstone and Sichuan sandstone. Additionally, the length of fully developed FPZ (L_{FPZ}) obtained from the numerical model lie within the experimental range (Figure 3-7b and Table 3-2), which is expected as its input parameters were based on average values of critical inelastic opening displacements (w_{ne}^{c}) from four experiments (Table 3-1).

The early prediction of the FPZ initiation stage in the numerical model can be mainly attributed to the assumption of finite width FPZ as a thin interface by the LCZM. As a result, in the numerical model, the damage initiation is confined within the local element just above the notch tip and directly depends on the stress concentration within the element. In comparison, the FPZ initiation in the experiments is estimated based on the damage accumulation in the finite width micro-cracking zone, which leads to the overall inelastic behavior of material around the notch tip. In the current study, the evolution of $CTOD$ was used to evaluate the material behavior over the notch tip, which is similar to the numerical model and four experiments (Figure 3-6a). Additionally, various AE-based studies (Zhang et al., 2018; Lin et al. (2019b, 2020)) have shown a small amount of material damage outside FPZ, suggesting that the assumption of linearly elastic behavior of material before FPZ initiation by the LCZM might not be entirely valid and thus can lead to errors in the prediction of FPZ initiation stage. The prediction of early FPZ initiation is consistent with the observation of various studies such as Moës and Belytschko

(2002) and Ha et al. (2015), which have also found that the LCZM can predict the global response of quasi-brittle material such as concrete despite showing an early FPZ initiation stage. It can be concluded that LCZM estimated from standard tests can predict the FPZ evolution in mode I fracture of Barre Granite with reasonable accuracy.

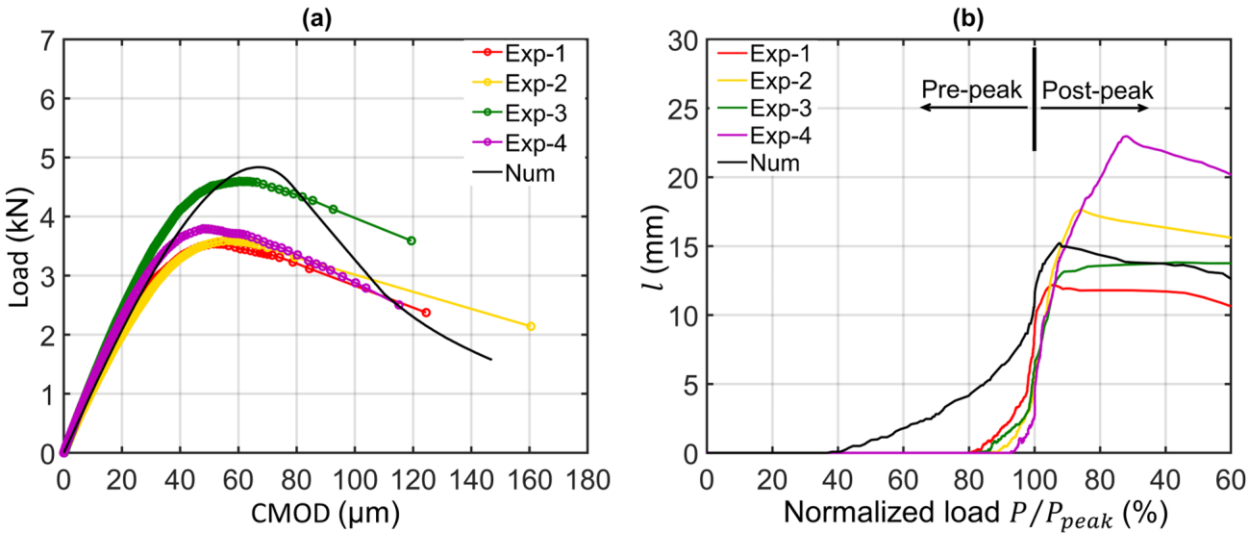

Figure 3-7 Comparison between experimental and numerical results in terms of (a) applied load vs. crack mouth opening displacements (CMOD), and (b) FPZ length (l) vs. normalized applied load.

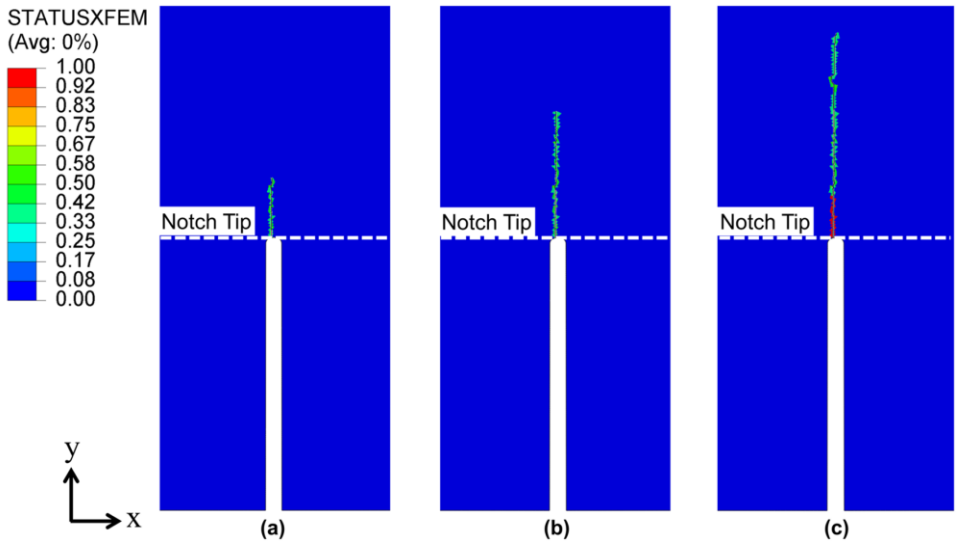

Figure 3-8 FPZ evolution in the numerical model at (a) 80% of the peak load (pre-peak stage), (b) peak load, and (c) post-peak stage when the load reached 80% of the peak load.

3.7.3 Random Variable Model

In this study, 30 Latin Hypercube (LH) samples based on the study by Montgomery (2019) were extracted from input parameter distributions (Table 3-1), which were then used in the numerical simulation of notched Barre granite specimens. The generated data from the numerical model was then used to construct an augmented RBF metamodel in MATLAB for each output parameter. The accuracy of the generated response surfaces was evaluated based on the error between the numerical models and augmented RBF obtained for additional 15 data sets (used as test samples). Moriasi et al. (2007) recommended Nash-Sutcliffe efficiency (NSE) as a quantitative index for performance assessment of the response surfaces. The NSE values of the response surface for each output (Table 3-3) suggest that the performance is *Very Good* (Moriasi et al. 2007), i.e., the numerical model approximation by augmented RBF response surface is *Very Good.* Figure 3-9 presents the Load-CMOD curves of 45 LH realizations (obtained from numerical simulation) against the experimental results. It is observed that the experimental

curves lie within the range of the LH realized samples, i.e., the experimental data can be viewed as one of the realizations from the input probability distribution.

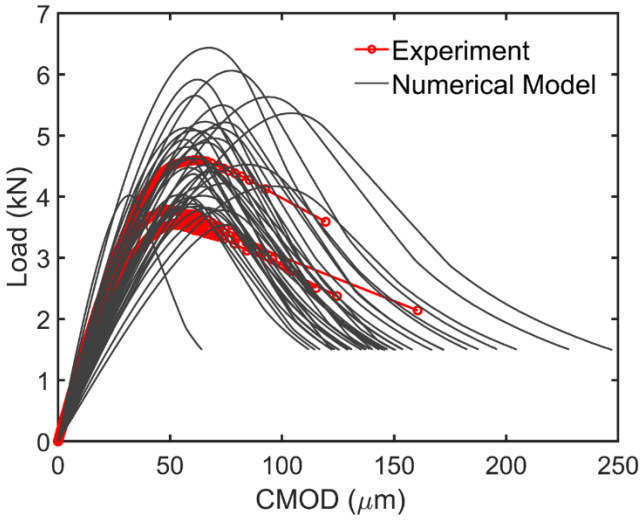

Figure 3-9 Load versus CMOD curves predicted from Monte Carlo simulation along with experiments results of four Barre granite specimens.

Uncertainty quantification of output variables is conducted by performing MCS on the response surface. Figure 3-10 presents the convergence of statistical moments of peak load for a different sequence of random numbers with increasing MCS. It can be seen that the variation in mean and standard deviation decreases with an increase in the number of realizations and become constant for 10^5 realizations. Thus, 10^5 realizations are utilized for uncertainty quantification of outputs, and the results obtained are mentioned in Table 3-2. Table 3-4 presents the correlation coefficients between each output parameter obtained from MCS. It can be inferred from Table 3-2 that the mean of all four output parameters matches closely with values obtained from the deterministic numerical model, which again confirms the robustness of the response surface in the accurate approximation of the numerical model. Among all output parameters, the length of fully developed FPZ (L_{FPZ}) has the maximum COV of 23%, which also lies within the range of the input parameters COVs (Table 3-1and 3-2). While the COV of other

output parameters is smaller than the input COVs, with the macro-crack initiation load having the smallest COV of 3.6%. Additionally, the 95% confidence interval (CI) of all output parameters (except the FPZ initiation load) is similar to the range of experimental results (Table 3-2). The 95% CI of FPZ initiation load is significantly lower than the experimental range, which can be attributed to the numerical model's limitation as it underestimates the FPZ initiation stage (section 3.7.2). Best-fit PDFs were estimated for each output parameter (Figure 3-11 and Table 3-2).

A large variation of fully developed FPZ length (L_{FPZ}) in both MCS and experimental results can be attributed to it being a local property and thus strongly influenced by the material heterogeneity. Additionally, the 95% CI of fully developed FPZ (L_{FPZ}) from MCS is comparable to the notch length ($0.38 < L_{FPZ}/a_o < 0.94$), indicating large scale yielding around notch tip and thus the assumption of LEFM (assume elastic stress distribution around crack tip) is not valid for the three-point bend specimens of Barre granite used in this study. Due to the significant size of the FPZ around the notch tip, macro-crack initiation is most likely to occur during the post-peak stage of the test as shown in Figure 3-11 with 95% CI of macro-crack initiation load around 84-97% of peak load in post-peak regime (Table 3-2). This can be further explained by a strong positive correlation between two parameters (Table 3-4), which indicates a higher energy dissipation inside the FPZ due to an increase in the FPZ length and thus delays macro-crack initiation. A similar correlation between the FPZ size and macro-crack initiation stage has been found by various studies (Hoagland et al. 1973; Parisio et al. 2019) in various rocks such as Salem limestone, Berea sandstone, and Adelaide black granite. Table 4 also shows a strong negative correlation between FPZ initiation load with FPZ length (L_{FPZ}) and macro-crack initiation load. It can be attributed to an increase in the tendency of material towards brittle

fracture with an increase in the FPZ initiation load, which, based on the LCZM, directly depends on the tensile strength of the material (σ_t). A higher FPZ initiation load (due to high tensile strength (σ_t)) can lead to smaller FPZ length (L_{FPZ}) and thus lower the energy dissipation across the fracture surface. As a result, higher energy can be available for macro-crack formation, which is more likely to occur at an early stage near the peak load stage. This observation is consistent with other studies, such as Wang (2012) and Ha et al. (2015), that have found the FPZ length (L_{FPZ}) inversely proportional to tensile of the material (σ_t) that provides a measure of brittle fracture.

Table 3-3 Accuracy of RBF-based response function for four output variables

Statistics	**NSE Value**	**Performance**
Peak load	0.998	Very good
FPZ initiation load	0.8069	Very good
FPZ length	0.9944	Very good
Macro-crack initiation load	0.9969	Very good

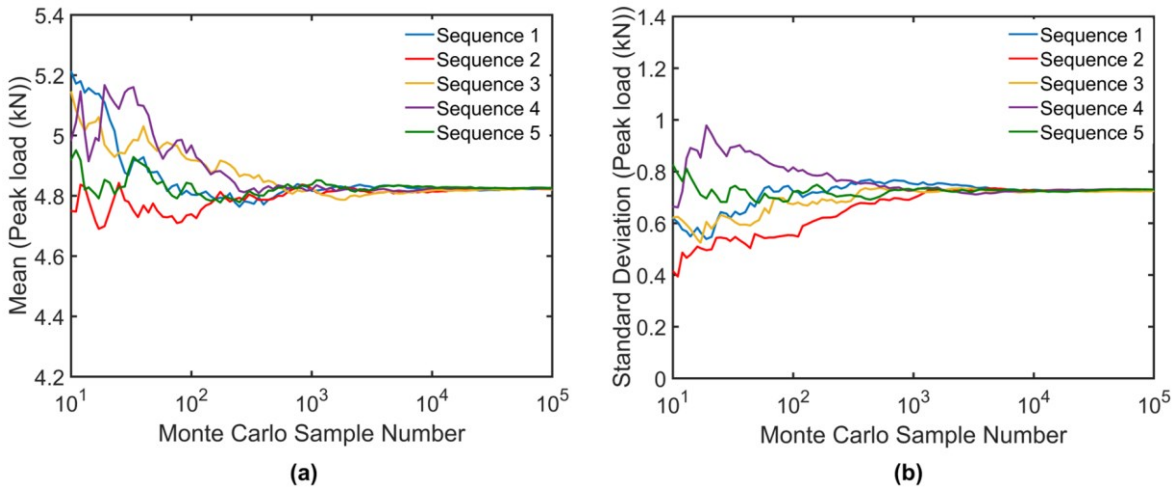

Figure 3-10 Effect of the number of MCS on the mean and standard deviation of the peak load.

Table 3-4 Correlation coefficient between each output parameters obtained from MCS

	Peak load	**FPZ initiation load**	**FPZ length (L_{FPZ})**	**Macro-crack initiation load**
Peak load	1	-0.1385	0.071	0.097
FPZ initiation load	-0.1385	1	-0.8883	-0.9206
FPZ length (L_{FPZ})	0.071	-0.8883	1	0.9472
Macro-crack initiation load	0.097	-0.9206	0.9472	1

3.7.4 Global Sensitivity Analysis

The first order and total effect Sobol indices for output peak load are shown in Figure 12a. It can be seen that the highest contribution (60%) towards the variability observed in peak load is caused by the variability in tensile strength (σ_t) (Figure 3-12a). The variabilities in the other two input parameters,.i.e., critical inelastic crack opening (w_{ne}^c) and tensile elastic modulus (E_t) have a similar contribution of around 20% toward the total variability of peak load (Figure 3-12a). A high contribution of the tensile strength (σ_t) is expected as it is a critical parameter of the MPS criterion used for fracture initiation in the current study. A high tensile strength (σ_t) can result in a beam with a large load-carrying capacity, thereby increasing its peak/failure load. The recent studies by Wang and Hu (2017) and Zhang et al. (2018) using this assumption developed an empirical formula for estimating tensile strength (σ_t), fracture toughness (K_{Ic}) based on Peak load measurements from three-point bending tests of various granite rocks. The critical inelastic crack opening (w_{ne}^c) is proportional to energy dissipation along the unit length of the FPZ before macro-crack initiation. A higher critical inelastic crack opening (w_{ne}^c) leads to higher resistance of material towards failure/fracture, thus consequently increasing the peak load of the specimen. The high contribution of the tensile strength (σ_t) towards the variability of peak load is consistent with the observation by various studies (Song et al. 2006; Roesler et al. 2007) that have found a larger influence of tensile strength (σ_t) than fracture energy (G_f) (proportional to

critical inelastic crack opening (w_{ne}^{c})) in different quasi-brittle materials such as concrete, asphalt mixture, etc. Similar to critical inelastic crack opening (w_{ne}^{c}), tensile elastic modulus (E_t) also have a minor contribution towards variability of peak load. This can be attributed to the change in the specimen's elastic stiffness, which also leads to the change in FPZ characteristics, such as its size (discussed below), thereby changing the material resistance to failure. Additionally, the sum of first-order indices is 0.984 (less than 1, but close to 1), suggesting a negligible contribution from the higher-order interaction of input parameters (Figure 3-12a).

The source of variability in the FPZ initiation load is predominantly due to the variability in tensile strength (σ_t) which accounts for over 90% of the total contribution (Figure 3-12b), which can be attributed to the MPS criterion that predicts the FPZ initiation only based on material tensile strength (σ_t). The small contribution of elastic modulus (E_t) (9%) can be attributed to minor changes in local stresses at the notch tip at a given load-point displacement (δ) due to the change in elastic stiffness of the specimen (Figure 3-11Figure 3-12b). The LCZM uses critical inelastic crack opening (w_{ne}^{c}) only for material softening and thus theoretically should have zero contribution toward variability of the FPZ initiation load. The small contribution (~ 3%) from inelastic crack opening (w_{ne}^{c}) can be considered as an error of the GSA.

The FPZ length (L_{FPZ}) is most sensitive to critical inelastic crack opening (w_{ne}^{c}), which accounts for 39% contribution towards its variability (Figure 3-12c). This is expected as an increase in the critical inelastic crack opening (w_{ne}^{c}) also increases the energy dissipation per unit length of the FPZ and thus facilitates a large FPZ size by increasing the material resistance towards fracture. This observation is consistent with the study by Ha et al. (2015) that found fracture energy (G_f) (proportional to critical inelastic crack opening (w_{ne}^{c})) directly proportional

to the FPZ size. Similar to critical inelastic crack opening (w_{ne}^{c}), tensile elastic modulus (E_t) also has a significant contribution towards FPZ length (L_{FPZ}) (Figure 3-12c), which typically results in a large FPZ size. This can be explained using the concept of characteristic length, which provides a theoretical estimate of the FPZ size (Bazant and Planas 1997) and is proportional to the tensile elastic modulus (E_t). The tensile strength (σ_t) as mentioned earlier, increase the tendency of material towards brittle fracture; as a result, a material with high tensile strength (σ_t) is more likely to have a small FPZ length (L_{FPZ}). Therefore, tensile strength (σ_t) will likely to have a significant contribution (~28%) towards variability in the FPZ length (L_{FPZ}) due to its negative correlation with the FPZ size (Figure 3-12c). This observation is consistent with the various studies, such as Wang (2012) and Ha et al. (2015), that found the FPZ size inversely proportional to the square of the tensile strength (σ_t) in the LCZM. For FPZ length, the higher-order interaction effects are to be negligible (Figure 3-12c).

Similar to the FPZ length (L_{FPZ}), variabilities in all three input parameters had a significant contribution towards the variability in the macro-crack initiation load, with the highest contribution (45%) of critical inelastic crack opening (w_{ne}^{c}) followed by the contribution of tensile elastic modulus (E_t) (~37%) and tensile strength(σ_t) (~27%) (Figure 3-12d). This is expected as a high positive correlation exists in the FPZ length (L_{FPZ}) and macro-crack initiation load (Table 3-4 Correlation coefficient between each output parameters obtained from MCS).

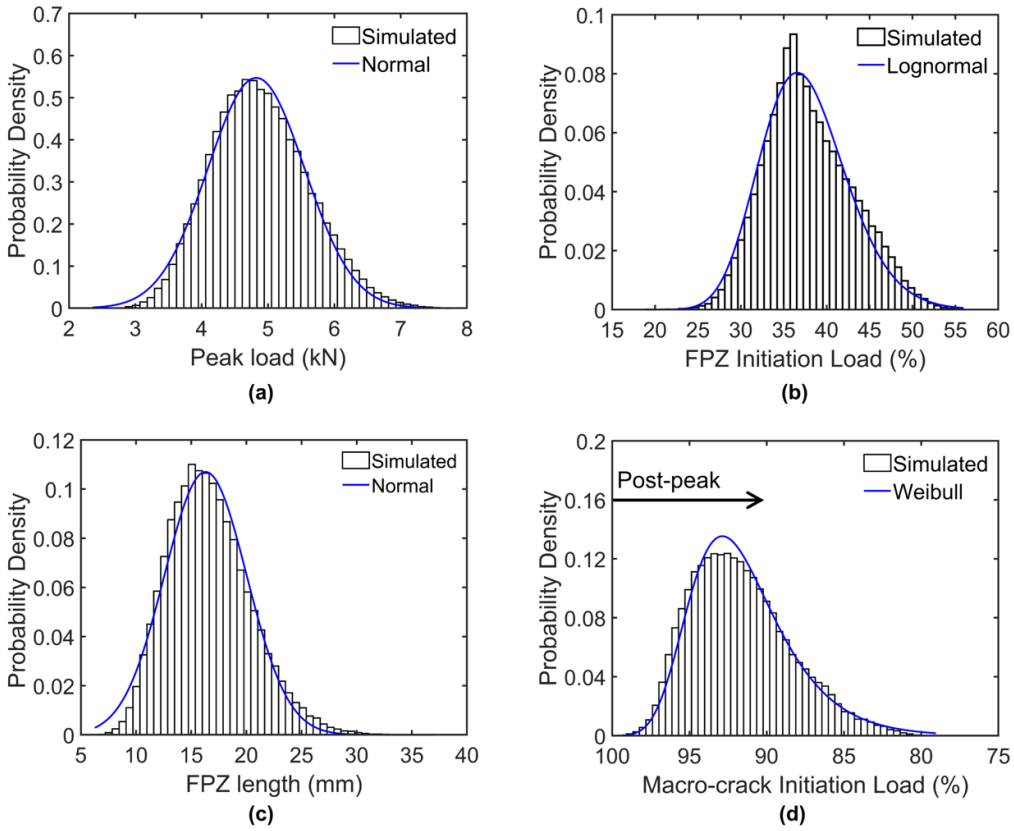

Figure 3-11 Histograms of each output parameter along best-fit PDFs.

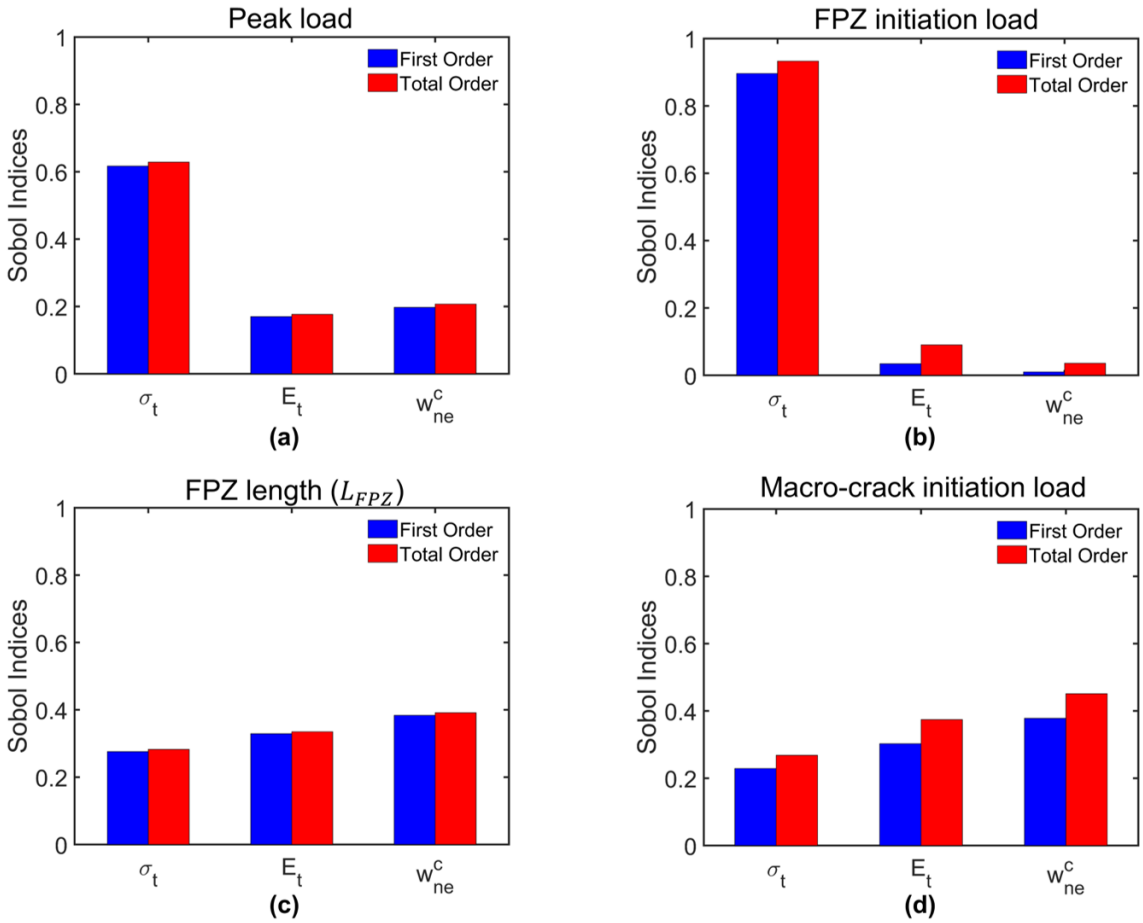

Figure 3-12 Sobol indices of the input parameters for each output parameter. Parameters include tensile strength (σ_t), critical inelastic crack opening (w_{ne}^c) and elastic modulus (E_t).

3.8 Conclusion

While CZM is widely used to predict the overall fracture behavior of various quasi-brittle materials such as concrete and asphalt mixtures, its applicability in rocks has been limited due to large uncertainty in its parameters, which can be attributed to various factors. For instance, the inherent variability in tensile strength (σ_t) and critical opening displacement (w_c) can lead to variation in the global response of the rock specimens. In this study, an integrated approach was used to evaluate the LCZM's capability in predicting the fracture processes in notched Barre granite specimens by addressing three issues: (a) consistent methodology for estimation of LCZM parameters, (b) variability in the input parameters of LCZM, and (c) most influential

parameters of LCZM to minimize the uncertainty in overall rock fracture behavior. This approach was based on four steps: (a) experimental testing, (b) numerical simulation, (c) uncertainty quantification of material response, and (d) global sensitivity analysis. The main findings are summarized as follows:

1. The evolution of $CTOD$ obtained from DIC analysis can be used to characterize three stages of FPZ evolution in a consistent manner and thus provide a reliable method for estimating the parameters of the LCZM.
2. The LCZM implementation using the deterministic numerical model (XFEM-based simulation) was inadequate in representing the variability in fracture behavior defined in terms of the peak load and the FPZ size observed in laboratory-scale Barre granite specimens. This variability can be attributed to variability in its input parameters, such as tensile strength (σ_t), critical inelastic crack opening (w_{ne}^c) and elastic modulus (E_t).
3. The variability of peak load (COV=15%) obtained from MCS was consistent with variation typically found in three-point bend specimens of various rocks such as yellow granite and Harsin marble (Wang and Hu 2017; Aliha et al. 2018; Zhang et al. 2018).
4. Despite variability in input parameters of the LCZM, a significant size of the FPZ around the notch tip was observed, indicating the large scale yielding in the laboratory scale Barre granite specimens under mode I loading. As a result, macro-crack initiation is most likely to occur in the post-peak regime.
5. The results from GSA indicate that tensile strength (σ_t) is the predominantly sensitive parameter towards variability in the global response of the Barre granite specimens. However, the variability in various fracture characteristics, such as the three stages of the FPZ evolution and its size, is sensitive to all three input parameters.

3.9 Acknowledgement

Funding for this research was provided by the National Science Foundation under award number 1644326. The authors are grateful for this support.

3.10 Coauthor Contributions

Dr. Bhardwaj Pandit and Dr. G. L. Sivakumar Babu aided in performing random variable analysis (Section 3.5) and Global sensitivity analysis (Section 3.6).

CHAPTER 4

FRACTURE PROCESS ZONE EVOLUTION UNDER MODE II LOADING OF BARRE GRANITE USING NOTCHED DEEP BEAM AND SHORT BEAM COMPRESSIONS TESTS

This paper has been submitted for publication in the Engineering fracture mechanics journal (Garg et al., 2023).

Prasoon Garg[3], Ahmadreza Hedayat[3], D.V. Griffiths[3]

4.1 Abstract

Due to rock being commonly subjected to compressive or shear loading, mode II fracture toughness is an important material property in rocks. Fracturing in rocks is governed by the behavior of a nonlinear region surrounding the crack tip called the fracture process zone (FPZ). However, the characteristics of mode II fracture are still determined based on the linear elastic fracture mechanics (LEFM), which assumes that a pure mode II loading always results in a pure mode II fracture. In this study, the FPZ development in Barre granite specimens under mode II loading was investigated using two geometries, namely (a) the notched deep beam (NDB) and (b) the short beam compression (SBC) test. The experimental setup included the simultaneous monitoring of surface deformation using the two-dimensional digital image correlation technique (2D-DIC) to identify fracture mode and characterize the FPZ evolution in Barre granite

[3]Colorado School of Mines, Civil and Environmental Engineering

specimens. Additionally, the influence of lateral confinement in SBC specimens on various characteristics of mode II fracture was studied. The 2D-DIC analysis showed a dominant mixed-mode I/II fracture in the ligament between two notches in the SBC specimens, irrespective of confinement level, while the NDB specimen showed the formation of a mode I fracture from its notch tip.

4.1.1 Introduction

Rock behavior is typically governed by various fracturing processes, such as crack initiation, propagation, and interaction between the new and existing fractures. As a consequence, rock fracture mechanics plays an essential role in the stability of rock structures (slopes, foundations, and tunnels) and other engineering applications such as geologic sequestration of nuclear waste, geothermal energy production, and hydraulic fracturing (Zoback et al., 1977; Hoek et al., 1995). The fracturing in rocks is characterized by the deformation of the inelastic region surrounding the crack tips, also known as the fracture process zone (FPZ) (Backers et al., 2005; Ghamgosar and Erarslan, 2016), especially in lab-scale specimens where its size is often comparable to pre-existing cracks. While the influence of the FPZ in mode I fracture has been extensively investigated, there are limited studies on FPZ development in rocks under pure mode II loading (Ji et al., 2016; Lin et al., 2020; Li et al., 2021).

Over the years, various geometries such as anti-symmetric four-point bending (ASFPB) (Wang et al., 2016), semicircular bend (SCB) with an inclined notch (Aliha et al., 2006), short core in compression (SCC) (Xu et al., 2020) and punch-through shear (PTS) (Backers et al., 2002) have been suggested for proper characterization the mode II fracture toughness of rocks. The application of most of these geometries is based on linear elastic fracture mechanics (LEFM), which assumes a direct equivalence between the mode of loading and the observed

fracture mode. However, this is not always the case, as shown by recent studies (Ji et al., 2016; Zhao et al., 2022; Xing et al., 2020), reporting the formation of mode I fracture, despite the application of mixed-mode I/II or mode II loading at the notch tip in various rocks and rock-like materials. In the study presented here, a distinction is made between the applied mode of loading and the fracture mode. Therefore, most known mode II testing geometries for rocks can be divided into two broad categories (i.e., kink fracture-based and coplanar fracture-based) depending on the obtained fracture pattern.

The geometry of the first category is characterized by creating a 'kink' fracture from the notch tip instead of forming a coplanar shear crack. This includes most disk-type geometries under compression with an inclined notch, such as cracked straight-through Brazilian disc (CSTBD) (Ayatollahi and Sistaninia, 2011), semicircular bend (SCB) specimens under three-point bending (Aliha et al., 2006) (Figure 4-1a-b) and prismatic geometries such as anti-symmetric four-point bending (ASFPB) (Wang et al., 2016) (Figure 4-1c). The initiation and growth of the 'kink' fracture in these geometries have been associated with tensile stress, as evident by their prediction using the maximum tangential stress criterion (MTS) (Rao et al., 2003; Ayatollahi and Sistaninia, 2011; Bahrami et al., 2020). The MTS criterion originally proposed by Erdogan and Sih (1986) is based on the hypothesis that the fracture propagates in a plane perpendicular to the largest tension at the pre-crack tip. Additionally, recent studies (Lin et al., (2019, 2020)) based on different mode II geometries have found the presence of opening displacements along the 'kink' fracture without any signs of mode II component, confirming the formation of mode I crack. However, a detailed analysis of the FPZ characterization for the studied geometries is lacking, and the influence of mode II loading on the FPZ development and other fracture properties, such as critical crack displacements and fracture energy, are unknown.

Optical techniques such as digital image correlation (DIC) and speckle interferometry can be useful tools to investigate the effect of mode II loading on the FPZ development, as they provide direct measurements of the displacement and strain fields inside the FPZ.

The second category encompasses the geometries that show a dominant fracture being formed either in the original notch planes or along the maximum shear stress directions (Xu et al., 2020). Various testing geometries from this category, such as double-edge notched Brazilian disk (DNBD) (Bahrami et al., 2020) (Figure 4-1d), shear box test (Rao et al., 2003) (Figure 4-1e), punch-through shear (Backer et al., 2002) (Figure 4-1f), and short core compression test (Jung et al., 2016) (Figure 4-1g), have been used to characterize mode II toughness of the rocks. The reliability of these geometries lies in the fact that fracture is formed in the intended direction, which also results in values of mode II fracture toughness (K_{IIC}) significantly higher than mode I fracture toughness (K_{IC}) of the same material. For instance, the DNBD test under pure mode II loading on various rocks such as limestone, marble, and granite showed the formation of a dominant coplanar crack connecting two notches that resulted in mode II toughness (K_{IIC}) being 2-4 times the value of mode I toughness (K_{IC}) for the same rock (Bahrami et al., 2020). Due to the ease of preparation and other merits, core-based testing geometries such as punch-through shear and short core compression have been increasingly used for mode II testing of rocks and rock-like materials (Wu et al., 2017; Xu et al., 2020; Yin et al., 2021; Zhang et al., 2022). Despite these applications, deformation behavior and fracture characteristics, such as the shape and size of FPZ in mode II geometries, is not well understood. These investigations are limited in core-based geometry, such as the punch-through shear, where FPZ development and its transition to macro-crack occur inside the specimen and thus cannot be monitored using optical techniques such as DIC. The explicit evidence of the formation of pure mode II fracture

is lacking in these aforementioned geometries, especially at low levels of confining pressure (σ_c < 10 MPa). Additionally, some studies (Merlin et al., 1986; Rao et al., 2003; Lin et al., 2019) have suggested that pure mode II fracture in rocks can be very difficult to create until the tensile stresses at the crack tip are eliminated by applying a high level of confining stresses. Alternatively, a cuboidal shape geometry, such as the short beam in compression (SBC) test (Figure 4-1g), can be more suitable due to its simple loading configuration and planar surface, allowing the estimation of local strain or displacement fields around the fracture. Initially introduced by Watkins and Liu (1985) to measure mode II toughness (K_{IIC}) of concrete specimens, SCB geometry, has also been used for testing Flagstaff sandstone and Coconino sandstone (Ko and Kemeny, 2007; Ko and Jeon, 2017).

The main objective of the study presented here is to characterize the fracture process zone in rocks under pure mode II loading and identify appropriate mode II testing geometry. For this purpose, two mode II configurations, one from each of the two described categories, namely (a) notch deep beam (NDB) and (b) short beam in compression (SBC), were selected to test Barre granite specimens. Both testing configurations have numerous advantages, such as ease of sample preparation, planar surface, and a large ligament length which minimize the boundary effects on the FPZ development. Additionally, multiple configurations for pure mode II loading can be achieved by changing the geometrical factors in both NDB and SBC specimens (Ko, 2008; Luo et al., 2017). The experimental setup in both tests also included the simultaneous monitoring of surface deformation using 2D-DIC imaging, which facilitates the estimation of various fracture characteristics, such as the FPZ evolution and its crack type under mode II loading. The fracture mode was determined based on the displacement approach of 2D- DIC.

Additionally, the influence of confinement on the SBC specimens on the variation in mode II toughness and characteristics of the developed FPZ was explored.

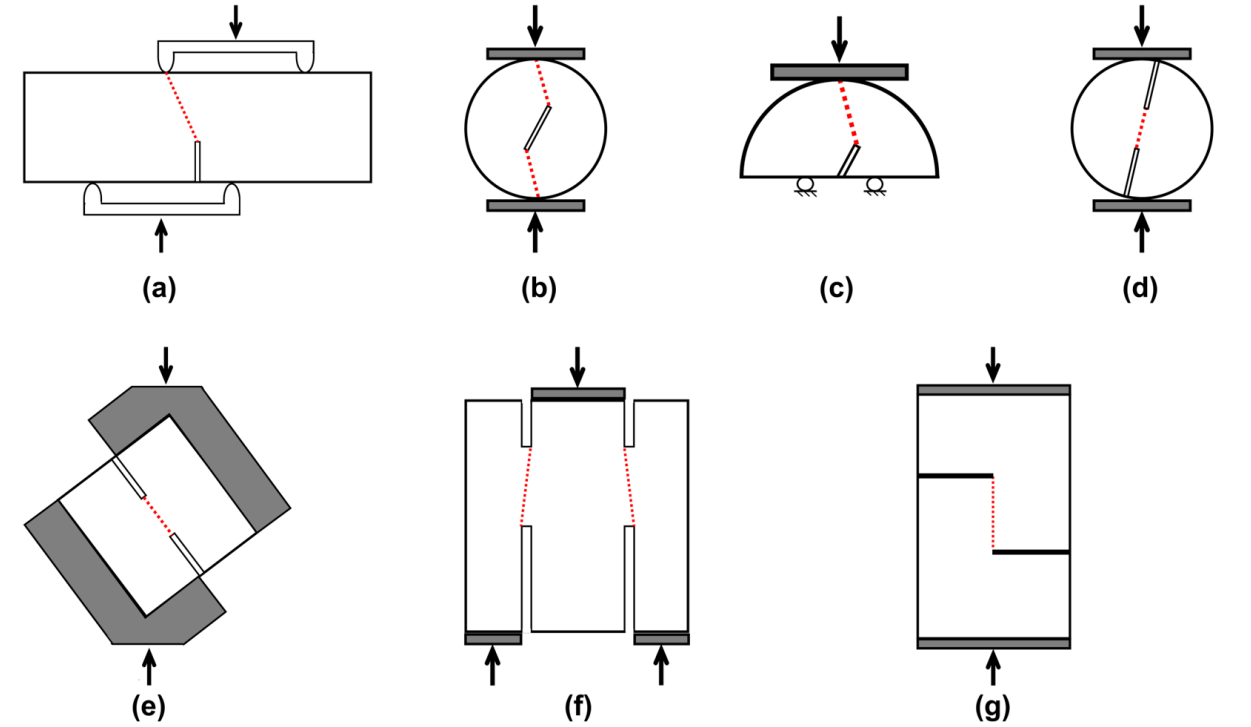

Figure 4-1 Various Mode II geometries. "Kink" fracture from notch tip: (a) Anti-symmetric four-point bending test, (b) Cracked straight-through Brazilian disc, (c) Semi-circular bend with an inclined notch. Fracture aligns with notch or shear direction: (d) Double-edge notched Brazilian disk (DNBD), (e) Shear box test; (f) Punch through shear (PTS), and (g) short core in compression (SCC) and short beam in compression (SBC) (Xu et al., 2020).

4.2 Configurations for Pure Mode II Loading

4.2.1 Notched Deep Beam (NDB) Test

4.2.1.1 Mode II Stress Intensity Factor (SIF)

The NDB specimen is a prismatic specimen with a length-to-width (L/W) ratio of 2, containing an inclined notch of length a, which makes angle α with respect to the vertical direction (Figure 4-2a). The NDB specimen is subjected to symmetrical three-point bending with a span of $2d$ by applying load P at the top roller, as shown in Figure 4-2a. Mode I (K_I) and mode

II (K_{II}) SIFs for NDB specimens under three-point bending can be defined based on the work of Lu et al. (2017):

$$Y_I\left(\frac{a}{W},\frac{d}{W},\alpha\right)=\frac{K_I}{\sqrt{\pi a}}\frac{2WB}{P}$$
$$Y_{II}\left(\frac{a}{W},\frac{d}{W},\alpha\right)=\frac{K_{II}}{\sqrt{\pi a}}\frac{2WB}{P} \quad (4\text{-}1)$$

where B is the specimen's thickness, Y_I and Y_{II} denotes the non-dimensional mode I and mode II geometrical factors. The geometrical factors (Y_I and Y_{II}) depend on various specimen parameters such as the notch inclination angle (α), span-to-width ratio (d/W), and notch length-to-width ratio (a/W). The pure mode I loading in the NDB specimen is achieved for a vertical notch with an inclination angle (α) equal to zero. With the increase in the notch inclination angle (α), the value of mode I SIF decreases, which eventually results in pure mode II loading (K_I = 0) at a specific inclination angle (α) depending on values of the span-to-width ratio (d/W) and notch length-to-width ratio (a/W).

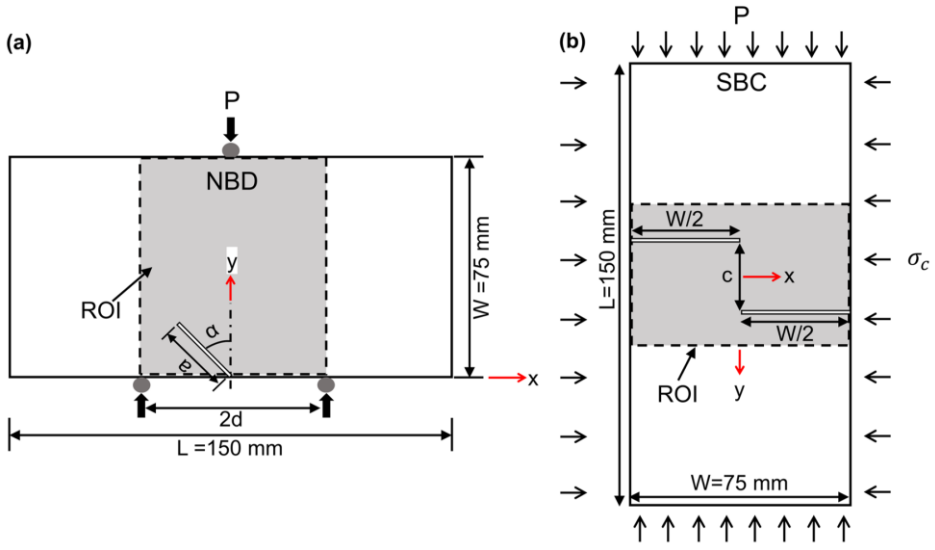

Figure 4-2 Schematics of (a) Notched deep beam (NDB) and (b) short beam in compression (SBC) specimens.

In the current study, the configurations of the NDB specimen corresponding to pure mode II loading at the notch tip were estimated using the 2D finite element model in Abaqus. The model was simulated based on the assumption of LEFM with a seam element used to represent the inclined notch of length 26 mm, which was kept the same in all NDB specimens. Thus, elastic parameters of Barre granite, such as Young's modulus under tension (E_t) of 28 GPa and Poisson's ratio (ν) of 0.16 based on the study by Goldsmith et al. (1976) were used as material properties for the 2D model. The seam element in Abaqus simulates rigid frictionless contact between two crack surfaces, thus ideal for representing a finite aperture notch (Abaqus, 2016). The SIFs in Abaqus are determined using the J-integral method, which characterizes a path-dependent energy release rate for a unit area of fracture growth. This fracture energy can be used to calculate the mode I and mode II SIFs for the NDB specimens. Figure 4-3 presents the finite element mesh of the NDB specimen modeled under plane stress conditions along with the applied boundary conditions. The region around the crack tip was meshed using singular 8-node elements, which mimics the asymptotic displacement field required to calculate path-dependent J-integral values. To smoothen the curves of the J-integral paths, 20 rings of these singular elements (40 elements for each ring) around the crack tip were meshed using the sweep technique (inset of Figure 4-3). The remaining area of the NDB specimen was meshed using 6-noded plane stress quadrilateral elements. The three-point bending of the NDB specimen was performed by deforming it at a constant displacement rate of 0.1 mm/step (1 step =1sec).

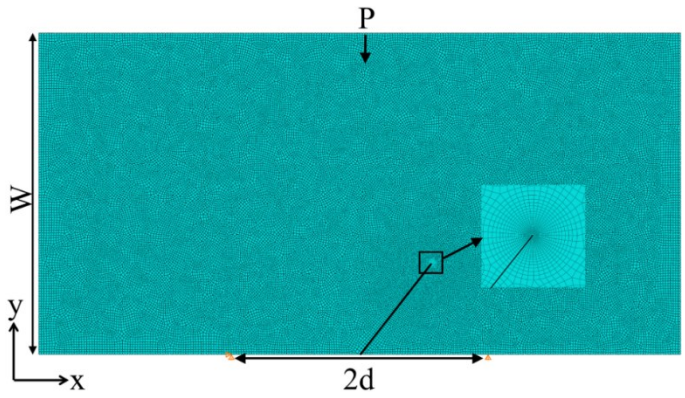

Figure 4-3 Finite element mesh used for estimation of geometrical factors in NDB specimens.

Figure 4-4a-b presents the variations of mode I (Y_I) and mode II (Y_{II}) geometrical factors with notch inclination angle (α) for two cases of NDB specimen with span to width ratio (d/W) of 0.4 and 0.5. In both cases, the mode I geometrical factor (Y_I) is maximum at zero notch inclination angle (α), resulting in pure mode I loading at the notch tip (Figure 4-4). Its value decreased in both cases with an increase in notch inclination angle (α) that resulted in pure mode II loading (i.e.,$Y_I = 0$) at angles of 38.1º and 56.7º for span-to-width ratios (d/W) of 0.4 and 0.5, respectively (Figure 4).

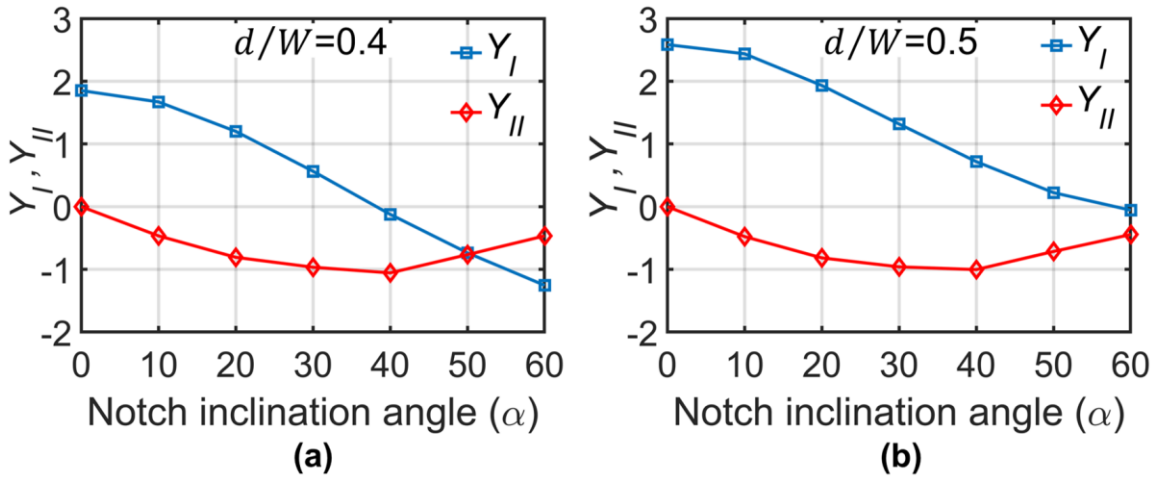

Figure 4-4 Variations of Y_I and Y_{II} for the modeled NDB specimens for (a) d/W =0.4, and (b) d/W =0.5.

4.2.2 Short Beam Compression (SBC) Test

The short beam compression (SBC) test refers to the compression loading of a prismatic specimen with two horizontal notches. These notches extend from the opposite side of the specimen's lateral boundary to its center, forming a rectangular bridge between them (Figure 4-2b). Under compressive loading, the ligament region between two notches experiences high shear stress concentration, resulting in the formation of mode II fracture (Watkins and Liu, 1985). In the current study, two notches with a length of $W/2$ and an aperture of 1.02 mm are separated by distance c (Figure 4-2b). The 'W' denotes the specimen's width, which is half of the specimen's height (L) in the current study.

4.2.2.1 Numerical Model for Stress Analysis

The value of shear stress concentration in the ligament region of the SBC specimen depends on various geometric factors such as width-to-height ratio (W/L) and bridge length-to-height ratio (c/L) (Watkins and Liu, 1985; Ko and Kemeny, 2007). Therefore, it is essential to find the optimum configuration of the SBC test that results in a mode II fracture. For this purpose, a 2D model of the SBC specimen with W/L =2 was simulated in the finite element package Abaqus. The numerical model was used to perform stress analysis for the SBC specimen with four different c/L ratios: 0.1, 0.2,0.3, and 0.4. The values of other geometric parameters of the modeled SBC specimen are shown in Figure 4-2c. The 2D model consists of 53750 quadrilateral linear plane stress elements simulated under linear elasticity conditions with the same material properties as those used for the NDB specimen (section 4.3.1.1). For the stress analysis, a fixed vertical load (P) of 10 kN was applied to all SBC specimens.

Figure 4-5a-d compare the distributions of shear stress (τ_{xy}) and maximum principal stress (σ_{11}) of the SBC specimens with different bridge length-to-height ratios (c/L = 0.1, 0.2, 0.3, and 0.4). It can be inferred from the contours of shear stress (τ_{xy}) that the maximum stress concentration (τ_{xy}) occurs at the tip of two notches in all SBC specimens (dark blue zones). However, the ligament region between the two notches experienced different shear stress distributions in the SBC specimens with different bridge length to height (c/L) ratios. For instance, the shear stress distribution is nearly constant in the ligament length directly connecting two notches in SBC specimens with c/L of 0.1 and 0.2, while it decreased significantly with further increase in c/L (Figure 4-5c-d). This increase in c/L may result in a crack being formed from the notch tip to the nearest end surface of the SBC specimen and not in its ligament region in SBC specimens with c/L greater than 0.3. The contour of maximum principal stress (σ_{11}), shows a similar trend, indicating that only the SBC specimens with c/L of less than 0.3 may experience fracturing in the ligament region, as evident by tensile stress being primarily concentrated in this region (Figure 4-5a-b). The SBC specimens with c/L greater than 0.2 also show high tensile stress concentration at their left and right end surfaces (Figure 4-5c-d). Therefore, the SBC specimen with c/L smaller than 0.3 is required to ensure shear failure along the crack plane in the ligament region. In the current study, the SBC specimen with c/L of 0.2 were tested as they are considered the most favorable configuration, which provides sufficient ligament length to ensure that FPZ is fully developed. The FPZ length in Barre granite specimens of the same size can be as large as 20 mm, as shown by the author's previous study (Garg et al., 2021) on mode I fractures. Thus, the SBC specimen with c/L of 0.2 provides a ligament length of around 30 mm and is expected to allow the FPZ to be fully developed.

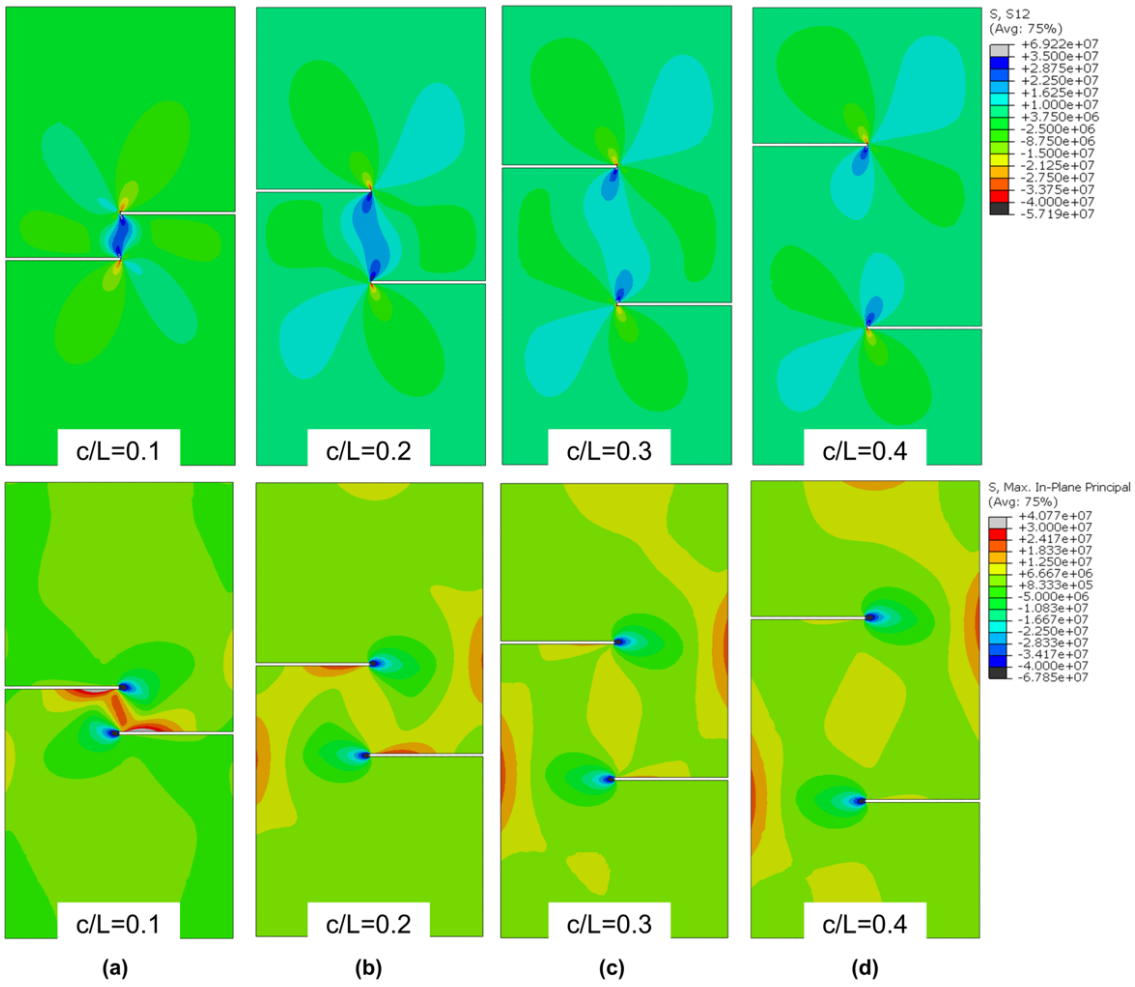

Figure 4-5 Distribution of shear stress (τ_{xy}) and maximum principal stress (σ_{11}) (Unit: Pa) on the 2D model for various c/L ratios: (a) c/L=0.1, (b) c/L=0.2, (c) c/L=0.3, and (d) c/L=0.4.

4.2.2.2 Mode II SIF

Based on earlier stress analysis (section 2.2.1) and other experimental studies (Ko, 2008; Ko and Jeon, 2017), the SBC specimen is typically known to form a vertical shear crack perpendicular to the notch plane. This is different from other mode II testing geometries such as punch through shear test and shear box test, where shear fracture grows nearly parallel to the notch plane (Backers et al., 2002; Rao et al., 2003) and thus doesn't require the consideration of secondary crack formation in the fracture toughness calculation. In contrast, the SBC geometry requires the consideration of secondary cracks perpendicular to the notch plane for the proper estimation of the mode II SIF. Recent studies (Xu et al., 2020; Yao et al., 2021) on short core compression test (the core-based equivalent of the SBC geometry) have estimated the mode II fracture toughness by adding small crack tips along the shear crack plane. The methodology for determining mode II SIF in the SBC geometry in this work is based on the wing crack model (Horii and Nemat-Nasser, 1986), where secondary cracks were assumed to initiate from the tips of the main crack. The SIF in the wing crack model (Horii and Nemat-Nasser, 1986) corresponds to a limiting case where the length of the secondary cracks approaches zero.

In the current study, two secondary shear cracks of the length h_c were added at the tips of two notches in the 2D model of the SBC specimen (see inset of Figure 4-6a). These secondary fractures were modeled using seam cracks in Abaqus. The material behavior was modeled as linearly elastic following the assumption of LEFM with the same material properties used for stress analysis of the SBC specimen (section 3.3.1). Similar to the NDB configuration, the crack tip in the SBC model was meshed using singular elements (see inset of Figure 4-6b), while the remaining region was modeled using the 6-noded plane stress quadrilateral elements. The

modeled SBC specimen has a bridge length-to-height ratio of 0.2 and was loaded in a vertical direction at a displacement rate of 0.1 mm/step (1 step =1sec) at its top surface (Figure 4-6a-b).

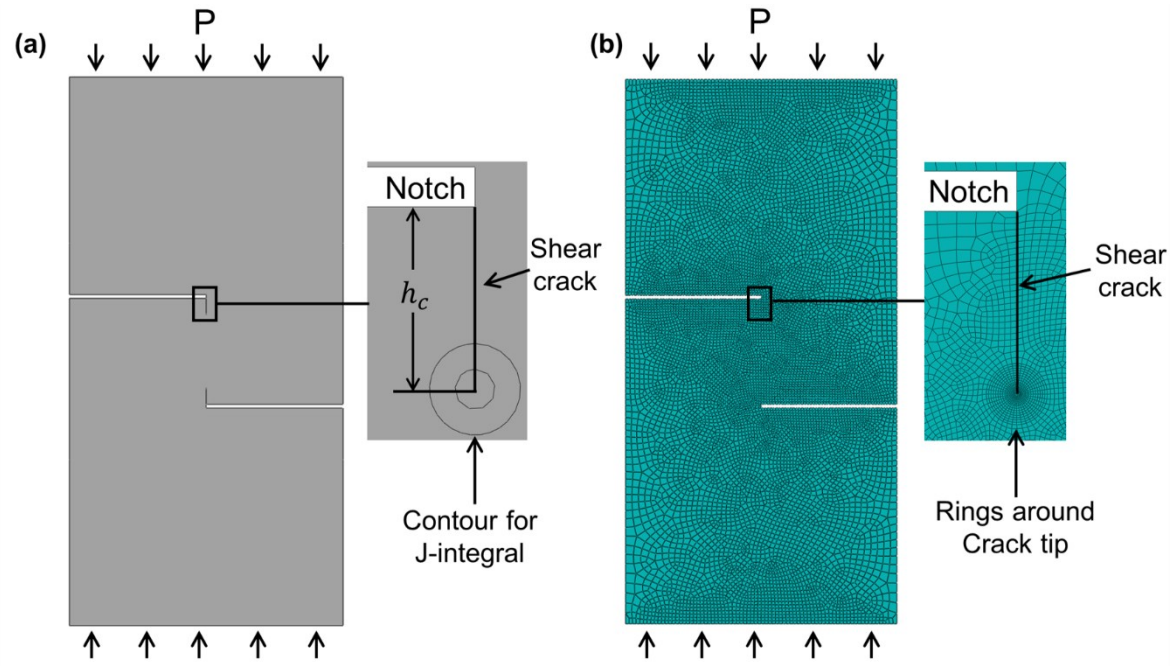

Figure 4-6 Model of SBC specimen for estimation of the mode II geometric factor (Y_{II}) with two secondary cracks (a) Schematic view and (b) finite element mesh.

Figure 4-7 indicates a linear variation of numerical mode II SIF (K_{II}^{num}) with respect to the normalized length of secondary cracks ($2h_c/c$) for the modeled SBC specimen. The experimental value of mode II SIF was estimated based on the displacement extrapolation technique, which determines the value of numerical mode II SIF (K_{II}^{num}) to the limiting case where the secondary cracks' length approaches zero. This intercept value was found to be 3.20 MPa mm$^{0.5}$ (Figure 4-7). This extrapolation approach is needed when the Abaqus model is unable to provide an accurate value of numerical mode II SIF (K_{II}^{num}) for very small shear cracks due to the requirement of dense meshing (element size < 0.001 mm) for these cases. Additionally, the extrapolation approach has been used by other studies to estimate the mode II SIFs in various testing geometries (Xu et al.,

2020; Yao et al., 2021). The mode II SIF (K_{II}) in the SBC specimen can be defined based on the energy approach by Watkins and Liu (1985) as follows:

$$Y_{II}\left(\frac{c}{L}\right) = \frac{K_{II}}{\tau_f\sqrt{\pi a}}\,;\tau_f = \frac{P}{cB} \tag{4-2}$$

where P denotes the vertical load applied on the specimen, B denotes the specimen's thickness, Y_{II} denotes non-dimensional mode II geometrical factor, which primarily depends on bridge length to height ratio (c/L). τ_f represents average shear stress in the ligament region at the peak load of the SBC specimen, and a is the notch length. The mode II geometrical factor (Y_{II}) can be calculated by putting K_{II}^{num} in Eq 4-2 for the limiting case of secondary cracks' length being zero.

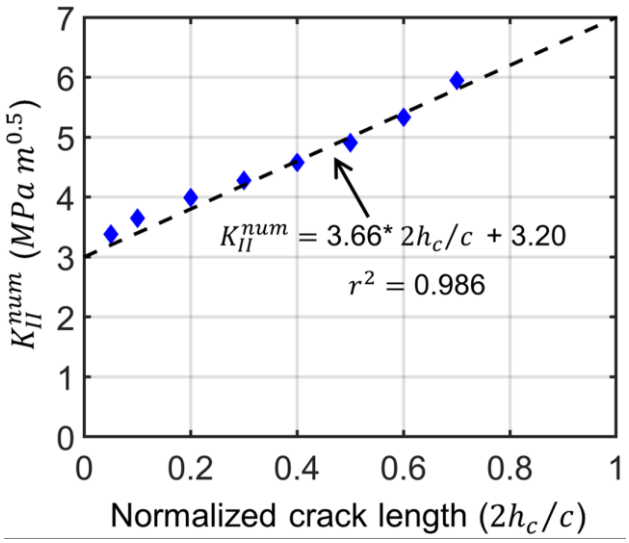

Figure 4-7 Variations of numerical mode II stress intensity factor (K_{II}^{num}) with respect to normalized shear crack length ($2\,h_c/c$) for the modeled SBC specimens with c/L of 0.2.

In the case of SBC specimens under confined conditions, the horizontal stress is applied on its lateral surface (Figure 4-2b), which acts perpendicular to the future crack plane. Therefore, the mode II geometrical factor (Y_{II}) should not change with the application of confining pressure

(σ_c). A similar trend of mode II non-dimensional factor (Y_{II}) has been observed in short core compression geometry by Yao et al. (2021), which is the core-based equivalent of the SBC specimen. However, the confining pressure (σ_c) does increase the shear strength of the ligament region in the SBC specimens, thereby increasing mode II fracture toughness (K_{IIC}) of the rock as shown by Ko and Kemeny (2007) based on testing Flagstaff sandstone under the confining pressures ranging from 0-10 MPa.

4.3 Experimental Design

4.3.1 Specimen Preparation

This study characterizes the fracturing process in Barre granite specimens subjected to pure mode II loading using NDB and SBC testing configurations. Various characteristics of Barre granite and the procedure to prepare prismatic specimens with nominal dimensions of 150 mm x 75mm x 25mm (Figure 4-2a-b) are described in section

Two cases of the NDB specimens with span-to-width ratios (d/W) of 0.4 and 0.5 were tested in this study. For each NDB configuration, the notch inclination angle corresponding to pure mode II loading was calculated (section 4.3.1.1). Additionally, three specimens containing a single notch of 26 mm length were tested for each mode II configuration. The NDB specimens were labeled as "NDB-C-N," where "C" represents the configuration number which can be 1 or 2, representing span-to-width ratios (d/W) of 0.4 and 0.5, respectively. "N" denotes the specimen number for a configuration, "C."

The SBC specimens with a bridge length to height (c/L) ratio of 0.2 were tested at various levels of biaxial confinement (σ_c =0, 1.7, 3.5, and 10.4 MPa). Each SBC specimen has two horizontal notches of 38 mm length. The SBC specimens were labeled as "SBC-σ_c-N" where

"σ_c" represents confinement level, and "N" denotes specimen number for a given confinement level "σ_c". The specifications of all SBC specimens tested in this study are given in Table 4-2.

Generating a random speckle pattern is another part of the specimen preparation process to ensure an accurate estimation of DIC-based surface deformation while minimizing any bias and background noises in the measurement. For this purpose, a combination of white and black paint was sprayed on the specimen's surface based on earlier study on mode I fracture. During the testing of Barre granite specimens, their surface was monitored in real-time using a 2D-DIC system. The details of the 2D-DIC system are the same as described in the section 2.3.3.

4.3.2 Testing Procedure

The Barre granite specimens under pure mode II loading were tested using a servo-controlled loading frame by MTS. In the NDB configuration, three-point bending tests were conducted by loading the specimen at a constant axial displacement of 0.1 μm/sec. A clip-on gauge extensometer measured crack mouth opening displacement (CMOD) in single-notched Barre granite beams (Figure 4-2a). For this purpose, the extensometer was glued to the beam's bottom surface, which then measured CMOD across the gauge length of 12 mm.

In the SBC configuration, Barre granite specimens were loaded using a biaxial device (Figure 4-8). The designed setup for SBC configuration consists of two parts: (a) the horizontal loading frame to apply confinement on the specimen and (b) the MTS machine that loads the specimen in the vertical direction (Figure 4-8). The horizontal loading frame consists of three plates supported by four high-strength steel rods with two outer plates supporting the rock specimen and a hydraulic flat jack (Figure 4-8). The middle plate was used to transfer the confining load in the horizontal direction to the rock specimen that was applied by the flat jack,

which was controlled through a hand-held hydraulic pump (Figure 4-8). The entire assembly was sitting on a base plate placed inside the MTS machine, which applied vertical load on the rock specimen through a steel spacer (dimensions 50 mm x 72 mm x 25 mm) set on its top surface (Figure 4-8). In conjunction with elastic rubber, the Teflon sheets were placed on two lateral surfaces of the specimen to minimize the friction between the steel plates and the rock specimen. The rubber ensured a uniform stress distribution on the lateral surfaces in an irregular-end rock specimen. Before the start of the test, a small seating load was applied in the vertical direction by the MTS machine to securely fix the entire test setup. This was followed by increasing both confining pressures (σ_c) and vertical load in the increment of 0.2 MPa until the desired confinement level was reached. Finally, the vertical load was applied at a constant rate of 0.1 μm/sec till the specimen's failure. The confining pressure (σ_c) acts normal to the future fracture plane, which forms in the rock bridge between two notches (Figure 4-8).

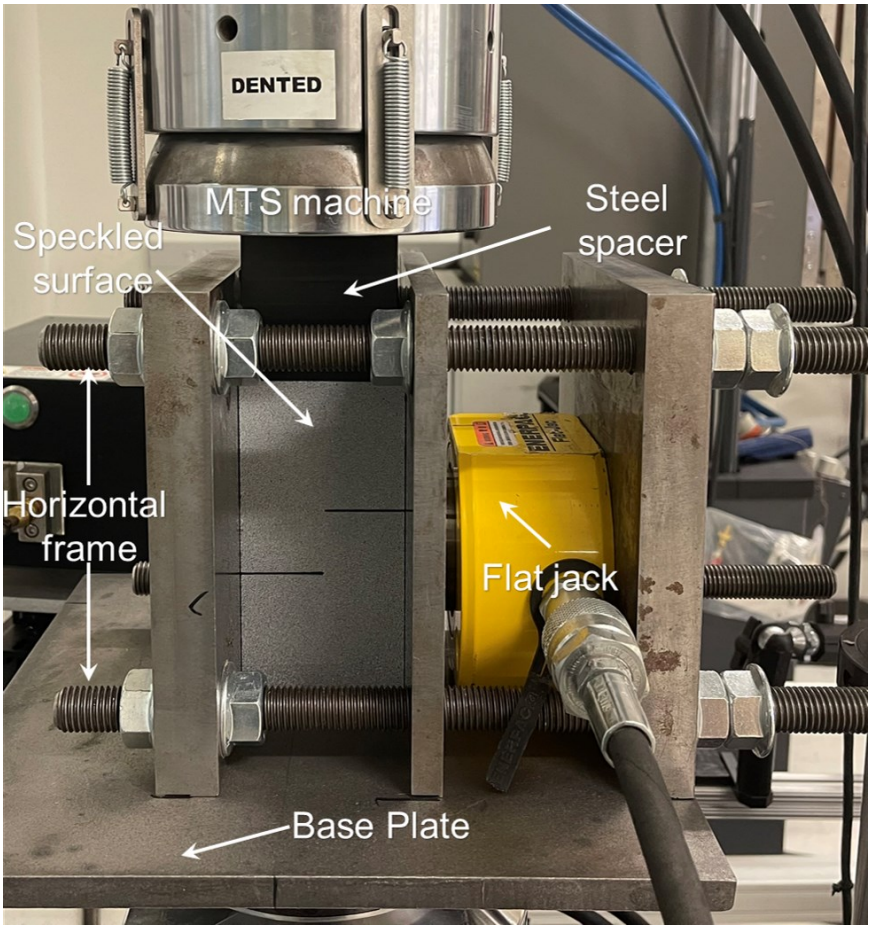

Figure 4-8 The experimental setup for performing the biaxial test on SBC specimens.

4.4 Experimental Results

4.4.1 NDB Specimen

4.4.1.1 Fracture Mode

In this section, the fracture mode in NDB specimens was determined based on the displacement approach of the 2D-DIC. According to the theory of fracture mechanics, crack type can be identified based on the displacement field along the faces of the fracture plane. Thus, mode I (tensile crack) and mode II fractures (shear crack) are characterized by pure opening and pure sliding displacements along their respective faces. The mixed-mode I/II fracture is similarly defined by the presence of both opening and sliding displacement along its faces. Macro-

cracking in most laboratory-scale rock specimens is preceded by the formation of significant-size FPZ (Backer et al., 2005; Tarokh et al., 2017); as a result, fracture mode has been typically determined by analyzing fully developed FPZ (Lin et al., 2014; Ji et al., 2016; Xing et al., 2020). Therefore, this study estimates the fracture mode using the displacement field inside a fully developed FPZ obtained from 2D-DIC. It is to be noted that different studies used different approaches to determine the loading stage corresponding to fully developed FPZ, which in the current research was based on the methodology developed by the authors (see details in Garg et al., 2021).

Figure 4-9a-b present the contours of 2D-DIC-based horizontal (U) and vertical displacement (V) for the specimen NDB-1-1 with a notch inclination angle (α) of 38.1º (Table 4-1) at the peak load stage. The peak load in specimen NDB-1-1 represents the stage just before the formation of the fully developed FPZ and its transition into a macro-crack (Table 4-1). In this study, the displacement fields were estimated with respect to a reference image representing the undeformed state of the specimen. As a result, contours in Figure 4-9a-b present the total displacement of the specimen NDB-1-1 at the peak load stage. A displacement discontinuity represented by merged contours can be seen to have formed above the notch in both horizontal (U) and vertical displacement (V) fields (Figure 4-9a-b). At the peak load stage, this displacement discontinuity signifies the presence of the FPZ that makes an angle β_1 from the notch plane (Figure 4-9a-b), which forms a "kink" fracture in subsequent loading stages.

Table 4-1 Comparison of fracture characteristics between NDB under pure mode II loading and three-point bending (TPB) specimens under pure mode I loading. The results of pure mode I loading were taken from the author's previous study (Garg et al., 2023).

Fracture Parameters	**Mode II loading (NDB)**		**Mode I loading (TPB)**
	NDB-1	**NDB-2**	
Span to Depth ratio (d/w)	0.4	0.5	1.87
Notch inclination angle α (deg.)	38.1º	56.7º	0º
Fracture mode	Mode I	Mode I	Mode I
Peak load (kN)	12.93±1.8	15.69 ±2.4	3.91 ± 0.49
FPZ initiation load (kN) (Pre-peak)	10.5 ±1.6	12.2 ±1.5	3.32 ± 0.48
Macro-crack initiation load (kN) (post-peak)	12.92 ±0.7	15.65 ±1.2	3.58 ± 0.51
Elastic Opening (COD_e) (µm)	11.7±6	3.6±2.0	6.40± 2.10
Critical opening (COD_c) (µm)	42.3±5.0	34±4.0	35.80 ± 3.10
Fully developed FPZ length (mm)	16±2	17±4	16.3± 3.7

The determination of fracture mode requires the estimation of normal and tangential displacement fields along the crack faces, which was done by setting up a local coordinate system $(\dot{x}, \dot{y})$ along the plane of the FPZ. For this purpose, the global coordinate system (x, y) was transformed in such a way that axis $\dot{y}$ is along the FPZ plane, and the origin of the local coordinate system $(\dot{x}, \dot{y})$ coincides with the notch tip (Figure 4-9a). Figure 4-9c-d indicate the formation of the FPZ in the contour of the normal displacement (U_1), while the tangential

displacement fields (V_1) showed a continuous distribution ahead of the notch tip. This suggests that the FPZ is most likely to transition into a mode I fracture despite the presence of pure mode II loading at the notch tip. The crack displacements profiles (both sliding and opening) were estimated using two cross-sections ($\dot{x} = \pm$ 2 mm) parallel to the FPZ to represent two virtual faces of the future crack plane. The considerable distance between two parallel cross-sections ($\dot{x} = \pm$ 2 mm) (can be considered as FPZ's boundary) ensures that the displacement errors near the discontinuity (merged contour in Figure 4-9c) can be ignored. The crack opening and sliding displacement along the FPZ can be estimated as the difference between the normal and tangential displacements between two crack planes. Therefore, the profiles of normal and tangential displacements along various points of two cross-sections ($\dot{x} = \pm$ 2 mm) are plotted in Figure 4-9e-f to obtain information about the crack displacements. The FPZ formed in specimen NDB-1 primarily consists of the mode I component, as evidenced by nonzero crack opening displacement and negligible value of sliding displacement (Figure 4-9e-f). The negligible crack sliding displacement explains the continuous distribution of the tangential displacement (V_1) field above the notch tip (Figure 4-9d). Therefore, it can be concluded that specimen NDB-1-1, despite under pure mode II loading, experienced a pure mode I fracture. This observation is consistent with other studies (Ji et al., 2016; Lin et al., 2019) that found "kink" fracture at the location of maximum tensile stress concentration around the notch tip in disk-shaped rock specimens, despite being subjected to pure mode II loading. The influence of mode II loading can be characterized by the formation of non-symmetric distribution of normal displacement inside the FPZ, as evidenced by its value being larger on the left cross-section section ($\dot{x} = -$ 2 mm) as compared to the right one ($\dot{x} = +$ 2 mm) (Figure 4-9e). For instance, at the notch tip, normal displacement with respect to the central crack plane (shown by the dashed black line

in Figure 4-9e) on the left cross-section (27 μm) is around three times the value on the right cross-section (9 μm). For characterization of the FPZ evolution in the NDB specimens, crack opening ($CTOD$) and crack sliding displacement ($CTSD$) at the notch tip are defined by the relative values of normal and tangential displacement, respectively, between two crack planes ($\dot{x} = \pm 2$ mm) at this location (Figure 4-9e-f).

Similarly, the specimen NDB-2-1 with a notch inclination angle (α) of 56.7º (Table 1) also showed the formation of pure mode I crack from its notch tip. The FPZ with a kinks angle of β_2 from the notch plane is visible in the contour of various displacement fields with respect to both global and local coordinate systems at the peak load stage (Figure 4-10a-d). Additionally, the developed FPZ has a significant tortuosity (Figure 4-10c), which forced the transformation of the local coordinated system based on an approximate crack path along the axis $\dot{y}$. This consequently makes it difficult to ascertain the presence of FPZ in the tangential displacement (V_1) due to distortion in the field around the notch tip (Figure 4-10d). The analysis of normal and tangential displacement profiles along the FPZ boundaries at the peak load stage showed the presence of some crack sliding displacement (~ 4 μm) along with a significant value of opening displacement (~ 31 μm) around the notch tip (Figure 4-10e-f). The non-negligible value of crack sliding displacement can be again attributed to the local coordinated system being transformed based on the approximate crack path (Figure 4-10d). Similar to the first specimen, the NDB-2-1 also had a non-symmetric distribution of normal displacement around the FPZ, with a large opening displacement (with respect to the central crack plane represented by a black dashed line) on the left boundary of the FPZ compared to the value on the right boundary (Figure 4-10e). Therefore, it can be concluded that the NDB specimens under pure mode II loading resulted in a pure mode I fracture based on the DIC analysis.

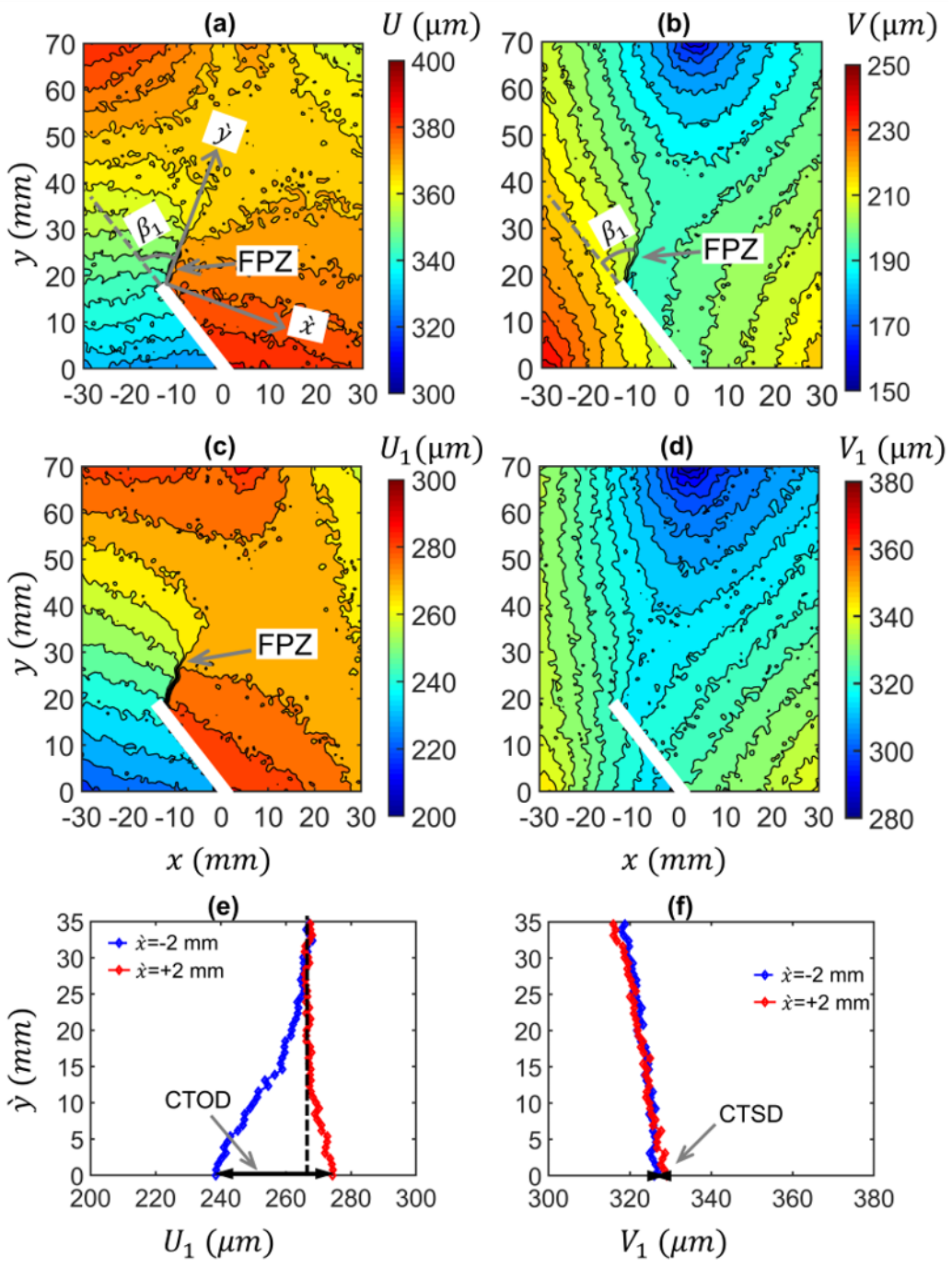

Figure 4-9 Specimen NDB-1-1, at peak load stage: Contours of (a) horizontal displacement field, (b) vertical displacement field, (c) normal displacement field, (d) tangential displacement field; Profiles of (e) normal displacement, (f) tangential displacement along two cross-sections of the FPZ. CTOD is crack tip opening displacement, and CTSD is crack tip sliding displacement.

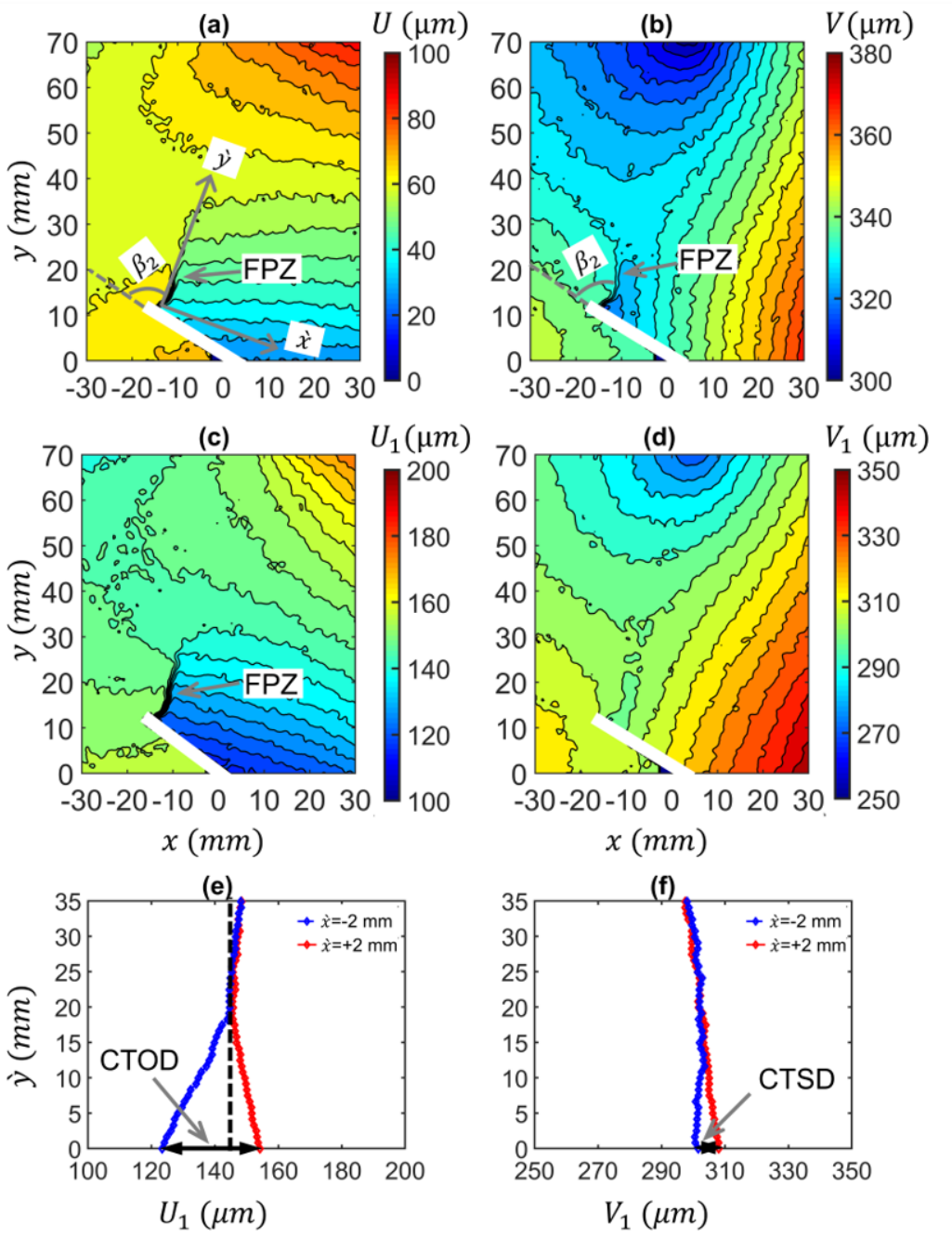

Figure 4-10 Specimen NDB-2-1, at peak load stage: Contours of (a) horizontal displacement field, (b) vertical displacement field, (c) normal displacement field, (d) tangential displacement field; Profiles of (e) normal displacement, (f) tangential displacement along two cross-sections of the FPZ. CTOD is crack tip opening displacement, and CTSD is crack tip sliding displacement.

4.4.1.2 Characterization of the FPZ Development

This study characterized the FPZ evolution in the NDB specimens using a methodology developed in earlier studies by the authors (for details, see Garg et al., (2020, 2021)) for the case of the Barre granite specimens under pure mode I loading. The methodology used the cohesive zone model (CZM) to define three stages of the FPZ evolution: (a) the elastic deformation, (b) the FPZ development, and (c) the macro-crack initiation. The CZM identifies the boundary between the three stages of the FPZ evolution using threshold values of crack displacements, which are considered material properties (Lin et al., 2019b). In the case of mode I fracture, the boundary between the FPZ and the elastic zone is identified using an elastic crack opening (COD_e) displacement while the boundary between the macro-crack and the FPZ is represented by the critical crack opening (COD_c) displacement. Similarly, the CZM uses concepts of elastic crack sliding (CSD_e) and critical crack sliding displacements (CSD_C) to characterize the FPZ evolution in pure mode II fractures. This methodology presents a consistent estimate of both elastic crack opening (COD_e) and critical crack opening (COD_c) displacements by analyzing the evolution of crack opening displacement at the notch tip ($CTOD$), which accounts for the mode I component in the FPZ (Garg et al., 2021). Similarly, the influence of the mode II component in the FPZ evolution is quantified through an equivalent parameter such as crack tip sliding displacement ($CTSD$).

In NDB specimens, the $CTOD$ and $CTSD$ were estimated based on normal and tangential displacements across the two cross-sections ($\dot{x} = \pm 2\ mm$) parallel to the FPZ (represents its virtual boundaries). The evolution of both parameters, the $CTOD$ and $CTSD$ in two NDB specimens (NDB-1-1 and NDB-2-1) is shown in Figure 4-11a-b, which indicate that $CTSD$ is negligible (< 5 μm) compared to the $CTOD$ in both NDB specimens except around the peak load

stage in NDB-2-1. At this loading stage, although the $CTSD$ is 10 μm, its value is still negligible compared to the $CTOD$ (~ 60 μm) in the specimen NDB-2-1 (Figure 4-11a). Additionally, a significant value of the $CTSD$ in the specimen NDB-2-1 compared to NDB-1-1 is due to errors in the crack sliding displacement caused by the tortuous crack path in the former case (Figure 4-10 and 4-10a). Therefore, the three stages of FPZ evolution in NDB specimens can be characterized based on the variation of the $CTOD$ (Figure 4-11a). The novel methodology identifies the elastic stage by the linear variation of the $CTOD$ with normalized load-point displacement (δ_{norm}) as seen in two NDB specimens in the initial loading stages (0-82% peak load in the pre-peak regime) (Figure 4-11 a). In the subsequent loading stage, the FPZ initiated from the notch tip, which in this new methodology is characterized by an accelerated rate of increase in $CTOD$, resulting in its nonlinear variation with respect to normalized load-point displacement (δ_{norm}). The FPZ initiation (shown by point A in Figure 4-11a) occurred at 81% and 78% of the peak load for specimens NDB-1 and NDB-2, respectively, in the pre-peak regime. The onset of non-linearity is defined by the point of the first significant change in the derivative of $CTOD$ with respect to the normalized load-point displacement ($\partial CTOD/\partial\delta_{norm}$) as represented by FPZ-I in Figure 4-11b for two NDB specimens. As loading increased further, the FPZ transitioned into a macro-crack which, based on the novel methodology, is characterized by the point of a rapid jump in $CTOD$ the normalized load-point displacement (δ_{norm}) curve as denoted by point 'B' (Figure 4-11a) for the two NDB specimens. The rapid jump in the $CTOD$ is a consequence of the unstable crack propagation, which indicates the formation of a macro-crack (traction-free crack) at the notch tip. Therefore, the elastic crack opening displacement (COD_e) is defined as the point of non-linearity in $CTOD$ vs. load-point displacement curve, while the critical crack opening displacement (COD_c) is estimated using the point of rapid jump in the $CTOD$. Table 4-1 presents

the results of all NDB specimens tested in this study. Interestingly, the values of both the elastic crack opening (COD_e) and the critical crack opening (COD_c) displacements obtained for the Barre granite specimens under pure mode II loading were similar to values obtained by authors (Garg et al., 2021) for cases of mode I loading on the same rock (Table 4-1). Additionally, the length of fully developed FPZ for all NDB specimens under mode II loading lies in the range obtained in the case of the same specimens under mode I loading (Table 4-1). This indicates that the FPZ evolution for mode I fracture is independent of the loading mode at the notch tip. The length of a fully developed FPZ based on the novel methodology can be estimated using the crack opening displacement profile ($COD_e < COD < COD_c$) along the displacement discontinuity (Figures 4-9c and 4-10c) at the point of rapid jump in each NDB specimen. Therefore, it can be concluded that mode I fracture formed in NDB specimens despite the application of pure mode II loading at their notch tip, with similar FPZ characteristics as in the case of Barre granite samples under pure mode I loading.

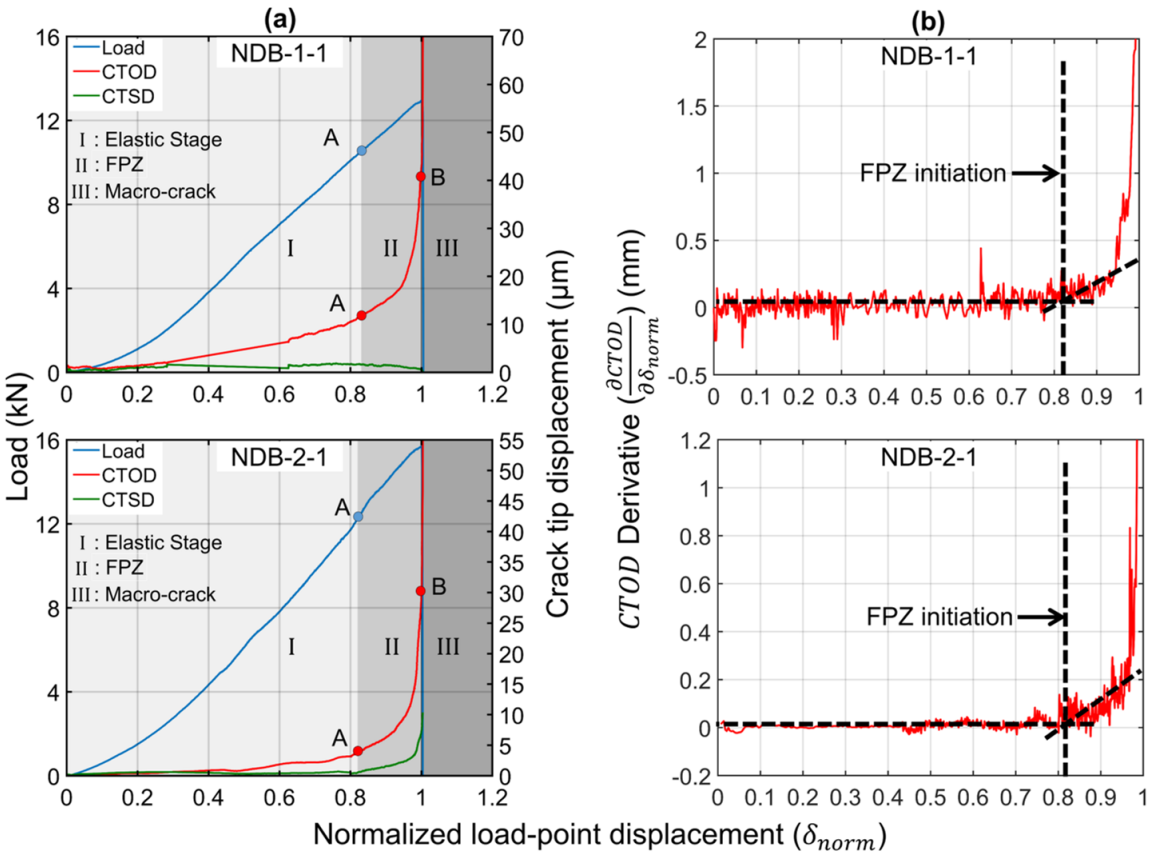

Figure 4-11 (a) Variation of load, $CTOD$, and $CTSD$ with the applied load-point displacement (b) FPZ initiation based on $CTOD$ derivative for two specimens, NDB-1-1 and NDB-2-1.

4.4.2 SBC Specimen

4.4.2.1 Fracture Mode

This section presents the characterization of the fracture mode in SBC specimens using the displacement approach of the 2D-DIC. The SBC specimens in this study showed similar fracture development irrespective of applied confining pressure (σ_c). Thus, the detailed analyses of two SBC specimens (SBC-0-1 and SBC-3.5-1), representing the unconfined and confined loading states on Barre granite, are presented here.

The SBC specimen under the unconfined state (SBC-0-1) exhibited three distinct FPZs (FPZ-1, FPZ-2, and FPZ-3), as visible in the contour of horizontal displacement (U) at the 95%

peak load stage (post-peak regime) (Figure 4-12a). This stage represented the loading point corresponding to unstable crack propagation, which consequently resulted in the complete failure of the specimen SBC-0-1. The FPZ-1 formed a vertical crack covering the entire ligament between two notches and thus failed the specimen. Additionally, the location of FPZ-1 coincided with the area of maximum shear stress concertation (τ_{max}) in the ligament region (Figures 4-5b and 4-12a). The remaining two FPZs (represented by FPZ-2 and FPZ-3 in Figure 4-12a) initiated from the inner surfaces of two notches coinciding with the region of maximum principal stress concentration (σ_{11}) (Figure 4-5b). Additionally, all three FPZs (FPZ-1, FPZ-2, and FPZ-3) were formed within a narrow region in the ligament (Figure 4-12a). This, along with a large elastic deformation in the vertical direction, resulted in the FPZ overlapping in the contour of the vertical displacement (V) field at the 95% peak load stage (post-peak regime) (Figure 4-12b), which only showed the formation of two FPZs (FPZ-1 and FPZ-3). The material between the two notches underwent large elastic deformation in the vertical direction due to the interaction between the two notches. Furthermore, the vertical displacement profiles along three cross-sections (y = -5 mm, 0 mm, and 5 mm in Figure 4-12c) indicated the formation of only one distinct region of positive vertical displacement gradient ($\partial V / \partial x$ >0) (-6 mm < x < 6 mm in Figure 4-12d). This is in contrast with the results of horizontal displacement profiles across three cross-sections (y =-5 mm, 0 mm, and 5 mm) that clearly showed the formation of three distinct regions of positive displacement gradient ($\partial U / \partial x$ >0) (highlighted by shaded regions in Figure 4-12b). The vertical displacement profiles also showed a large extent of positive displacement gradient ($\partial V / \partial x$ > 0) (6 mm < x < 6 mm in Figure 4-12d) as compared to one obtained by the horizontal displacement profiles (0 mm < x < 4 mm in Figure 4-12c). The shaded regions in Figure 4-12c-d represent the approximate width of three FPZs (FPZ-1, FPZ-2, and FPZ-3), as

estimated by the regions of positive horizontal displacement gradient ($\partial U/\partial x > 0$) along three cross-sections (y = -5 mm, 0 mm, and 5 mm). Since the FPZ's width is a material property representing the lateral size of the micro-cracking zone (normal to crack plane), its accurate estimation requires that the influence of nearly distinct FPZs should be minimized. For this purpose, the extent of each FPZ is defined by a small region containing the positive horizontal displacement gradient ($\partial U \,/\, \partial x >0$) (three shaded regions in Figure 4-12c) and not by the vertical displacement profiles.

The FPZ-1 in the SBC-0-1 transitions into a mixed-mode I/II macro-crack between two notches, as indicated by the formation of the positive displacement gradient across its width in both horizontal and vertical displacement profiles (Figure 4-12c-d). Since the multiple FPZs are confined in a narrow region, it is vital to separate the influence of FPZ-1 from other FPZs to estimate crack opening and sliding displacements accurately. For this purpose, two vertical cross-sections along the FPZ boundary (represented by the boundary of shaded region FPZ-1 in Figure 4-12c) were used to calculate the normal and tangential displacement profiles.

Figure 4-12e represents the variation of crack opening displacement (COD) and crack sliding displacement (CSD) along the entire length of FPZ-1. The changes in the values of crack sliding displacement (CSD) along the central portion of ligament length (-2.5 mm < y < 2.5 mm) were small (< 3 μm), while the crack opening displacement (COD) had the maximum value at the ligament center (y=0 mm). The FPZ-1 propagated from the ligament center (y=0 mm) towards two notches, as indicated by decreases in the value of COD along regions towards two notches. Additionally, these two regions near two horizontal notches are influenced by other nearby FPZs (FPZ-2 and FPZ-3 in Figure 4-12a) and thus showed an asymmetry in a variation of COD in two opposite directions. Despite this variation in the COD profile, the central portion (-

2.5 mm < y < 2.5 mm) showed consistent values of COD as evidenced by small variations (< 5 μm) in this region compared to its absolute value at ligament center (~40 μm) (Figure 4-12e). Therefore, the evolution of FPZ-1 was characterized based on crack displacement values in the central portion of the ligament (-2.5mm < y < 2.5 mm).

The SBC specimen under confined conditions (SBC-3.5-1) also showed the formation of the three FPZs (FPZ-1, FPZ-2, and FPZ-3), which were confined to a small region and thus resulted in their overlapping (Figure 4-13a-b). Consequently, only two distinct areas of the positive displacement gradient were observed in horizontal and vertical displacement profiles along three cross-sections (y =-5 mm, 0 mm, and 5 mm) (shaded regions in Figure 4-13c-d). The FPZ-1 in specimen SBC-3.5-1 (Figure 4-13a-b) also resulted in its failure due to the formation of a vertical mixed-mode I/II macro-crack, as evident by a large positive gradient in both horizontal and vertical displacement profiles (shaded regions in Figure 4-13c-d). The width of FPZ-1 in this SBC specimen can be again represented by the small region of positive horizontal displacement gradient ($\partial U / \partial x$ >0) (shown by the shaded region FPZ-1 in Figure 4-13c). Figure 4-13e clearly showed the presence of the central zone in the ligament (-2.5 mm < y < 2.5 mm) with consistent values of both crack displacements, as evidenced by a very small variation in their (< 5 μm) in this region. Therefore, it can be concluded that SBC specimens failed due to the formation of a dominant mixed-mode I/II fracture initiated at the location of the FPZ-1.

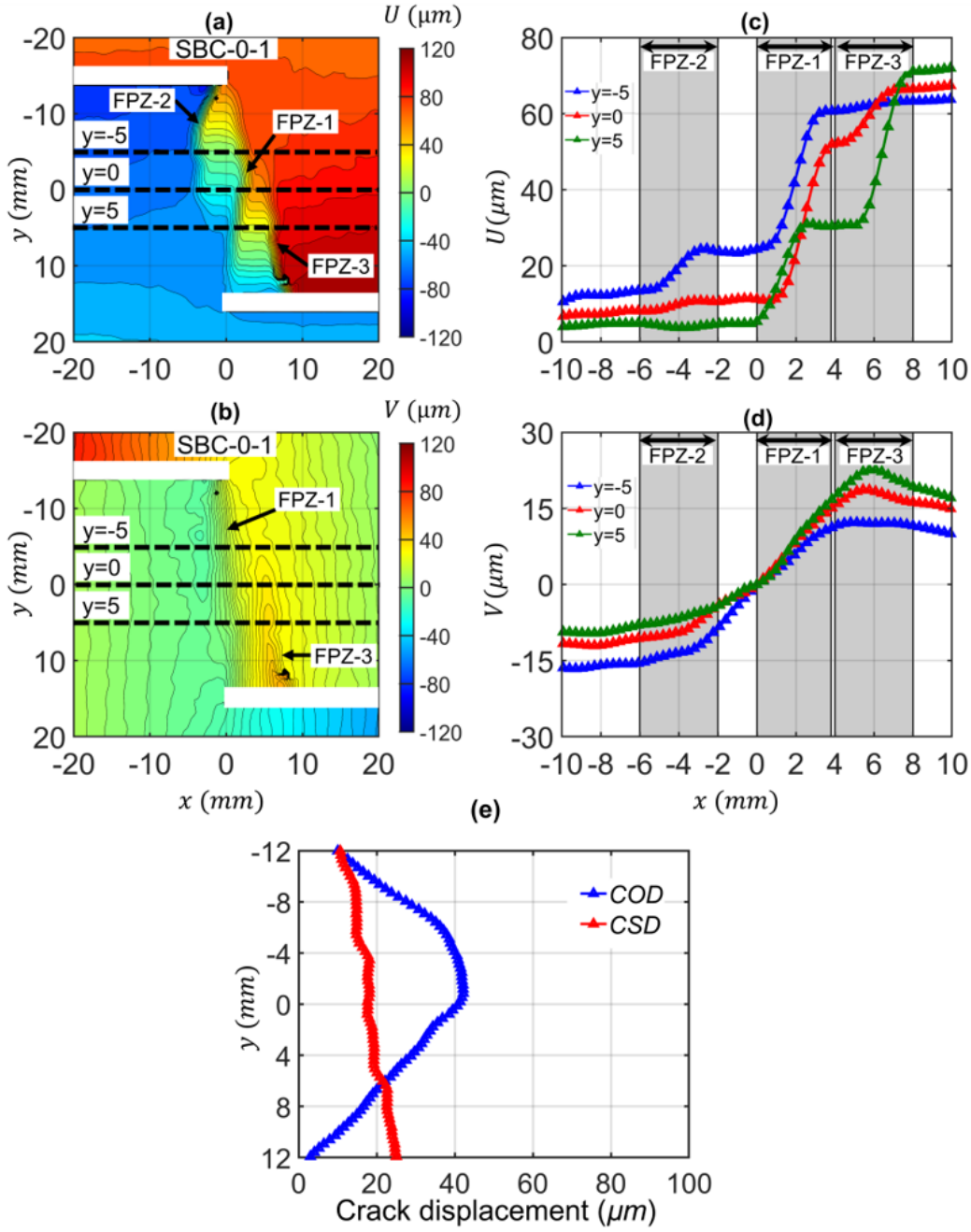

Figure 4-12 Specimen SBC-0-1, at 95% peak load (post-peak regime): Contours of (a) horizontal displacement, (b) vertical displacement; three horizontal cross-sections, i.e., y = -5mm, 0 mm, 5 mm showing, (c) plot of horizontal displacement (U) profiles (d) plot of vertical displacement (V) profiles, (e) variation of crack opening and sliding displacements along the ligament length.

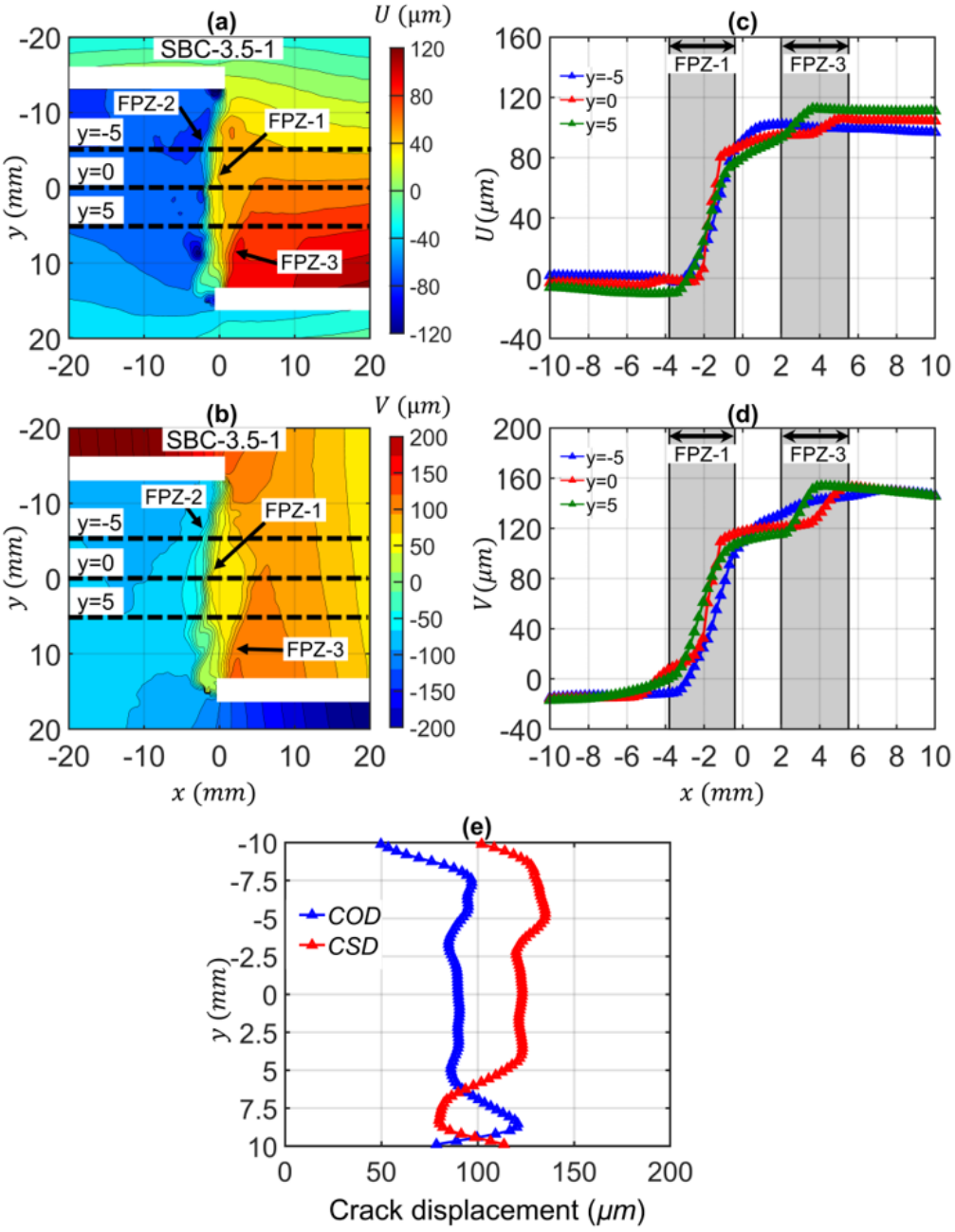

Figure 4-13 Specimen SBC-3.5-1, at peak load stage: Contours of (a) horizontal displacement, (b) vertical displacement, three horizontal cross-sections, i.e., y = -5mm, 0 mm, 5 mm showing (c) plot of horizontal displacement (U) profiles, (d) plot of vertical displacement (V) profiles, (e) variation of crack opening and sliding displacements along the ligament length.

4.4.2.2 Fracture Patterns

This section presents the evolution of fracture patterns in the SBC specimens. As shown by earlier displacement analysis of two specimens (section 4.5.2.1), the SBC configuration typically resulted in similar fracture patterns irrespective of confinement level. Thus, for brevity, the evolution of the fracturing process is only shown for the specimen SBC-3.5-1 based on the strain approach of the 2D-DIC. This approach characterizes fracture using the concept of strain-localized zones. It can also be used to determine the crack type by analyzing the contours of minimum principal strain (ϵ_{22}) and the maximum shear strain (γ_{max}), which provides a qualitative estimate of the damage due to tensile and shear micro-cracks formed inside the localized zones (Jian-po et al., 2015; Shirole et al., 2020a).

Figure 4-14a-d present the evolution of fractures in the specimen SBC-3.5-1 in terms of minimum principal strain (ϵ_{22}) and the maximum shear strain (γ_{max}) contours. During the initial loading stage (about 60% of the peak load in the pre-peak regime), tensile cracks initiated around the inner tip of two horizontal notches (represented by strain localized zones FPZ-2 and FPZ-3). These cracks with subsequent loading also underwent shearing, as indicated by the concentration of the maximum shear strain ($\gamma_{max}\sim$ 1 to 1.5%) inside the FPZ-2 and FPZ-3 at 80% of peak load (pre-peak stage) (Figure 4-14a). The location of these tensile-dominated cracks (FPZ-2 and FPZ-3 in Figure 4-14a) coincided with the region of tensile stress concentration obtained from Abaqus model (Figure 4-5b). In most SBC specimens tested in this study, these tensile-dominated cracks (FPZ-2 and FPZ-3 in Figure 4-14a-c) propagated outward until they reached the ligament center and had the inclination angle in the range of 0º-30º with the vertical plane between two horizontal notches. The formation of the inclined tensile cracks (with respect to the main fracture) has also been observed in other known mode II testing configurations for rocks at low

confining pressure (σ_c < 10 MPa), such as punch through shear test and double edge notched Brazilian disk (DNBD) (Backer et al., 2002; Nejati et al., 2021).

In addition to the tensile-dominated cracks, echelon fracture also formed at the ligament center (represented by strain localized zone FPZ-1 in Figure 4-14a) at 80% of peak load (pre-peak stage). With further loading, more echelon fractures initiated in the ligament, which eventually coalesced to form an almost vertical fracture connecting the inner tip of two notches at the peak stage (FPZ-1 in Figure 4-14c). The presence of patches of high strain concentration zones inside FPZ-1 at the peak load stage (Figure 4-14c) clearly indicated the formation of echelon cracks that merged together and resulted in specimen failure. The vertical fracture is composed of both tensile (negative (−) principal strain representing tension) and shear micro-cracks, as evident by a high strain concentration of both minimum principal (ϵ_{22} < -5%) and the maximum shear strain (γ_{max} > 4%) inside the FPZ-1 (Figure 4-14d). Similarly, all SBC specimens tested in this study showed the formation of a vertical mixed-mode I/II fracture connecting two notches irrespective of applied confining pressure (σ_c). This observation of mixed-mode I/II fracture was also found in other Mode II geometry, such as short core compression tests on limestone specimens (Li et al., 2021).

.

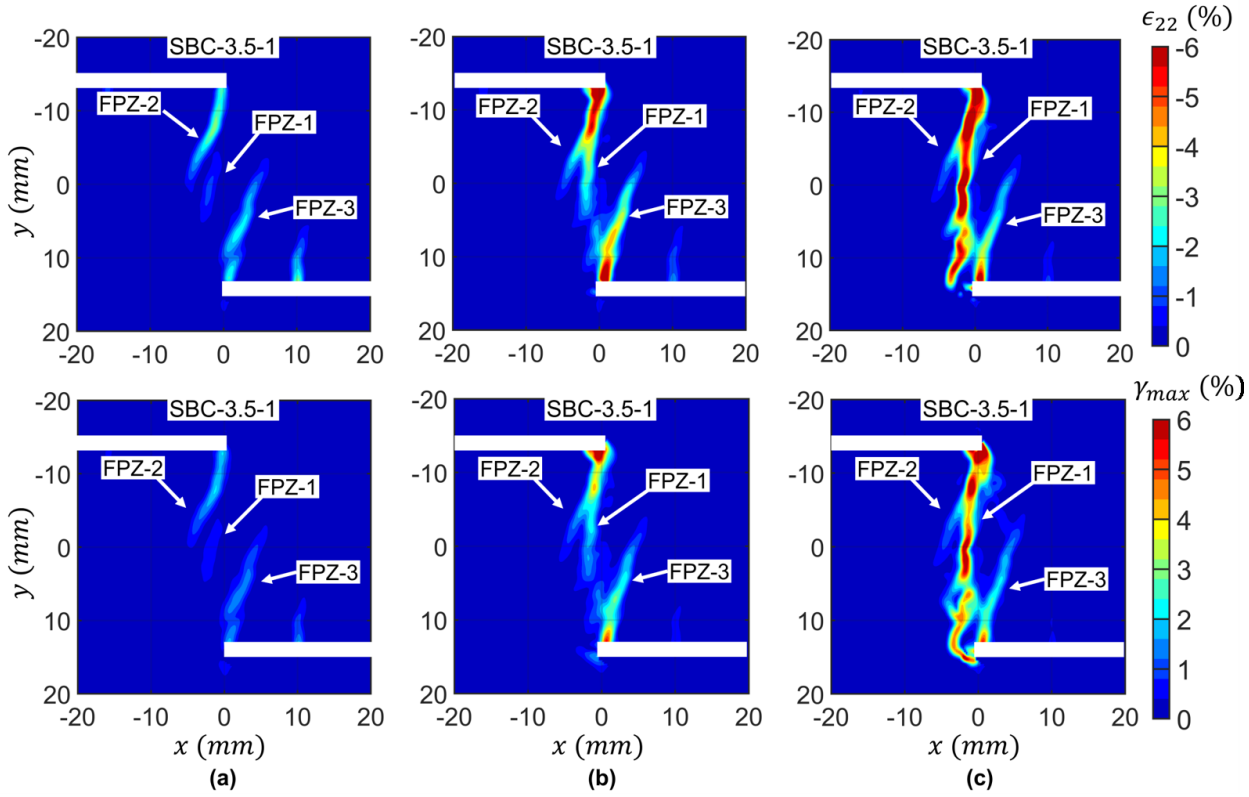

Figure 4-14 Contours of minimum principal strain (ϵ_{22}) and maximum shear strain (γ_{max}) for the specimen SBC-3.5-1 at (a) 80% of the peak load in the pre-peak stage, (b) 95% of the peak load in the pre-peak stage, and (c) the peak load stage. Positive (+) and negative (−) strains represent contraction and extension, respectively.

4.4.2.3 Characterization of the FPZ Development

This section characterizes the FPZ development inside the dominant vertical fracture (represented by FPZ-1) that resulted in the failure of the SBC specimens. As shown in section 4.2.1, variation in the crack displacements along the central portion (-2.5 mm < y < 2.5 mm) are small (section 4.2.1), make the cross-section y=0 mm most suitable for characterizing the FPZ evolution of dominant mixed-mode I/II fracture in the SBC specimens.

Similar to the NDB specimen, the novel methodology by authors (Garg et al. (2020, 2021)) was used to characterize the FPZ development in the SBC specimens. Based on this methodology, the crack opening (COD) and crack sliding (CSD) displacements, calculated at

central cross-section (y=0 mm), were analyzed for two SBC specimens (SBC-0-1 and SBC-3.5-1). Figure 4-15a presents the evolution of crack opening displacements (COD), crack sliding displacement (CSD) and applied force with respect to the normalized load displacement (δ_{norm}) for two SBC specimens (SBC-0-1 and SBC-3.5-1). In the SBC specimens under unconfined conditions (SBC-0-1), both COD and CSD were negligible for most loading stages, with a larger value of CSD near the peak load stage However, in the SBC specimens under confined conditions (SBC-3.5-1), CSD was larger than COD for the entire loading duration in the pre-peak region (Figure 4-15a). The larger value of CSD as compared to COD during early loading can be attributed to the interaction between the two notches due to large vertical deformation under the elastic stage. This is especially true in specimen SBC-3.5-1, which underwent a significant amount of elastic deformation in the vertical direction due to the application of isotropic loading before the start of the test. As a result, CSD in the specimen SBC-3.5-1 was around 5.4 μm at the beginning of the test (Figure 4-15a). Therefore, COD was used to characterize the three stages of FPZ evolution as it was least affected by initial elastic deformation in the vertical direction, which varied depending on applied confining pressure. During the initial loading stages, the ligament center (y=0 mm) underwent elastic deformation, as evident by a linear increase in the COD in specimen SBC-3.5-1, while specimen SBC-0-1 showed a negligible value of COD, indicating the ligament center (y=0 mm) under the elastic stage (Figure 4-15a). The FPZ initiation occurred approximately at peak load and 80% of peak load (pre-peak regime) in specimens SBC-0-1 and SBC-3.5-1, respectively (represented by point A in Figure 4-15a). It is identified using the point of the first significant change in the derivative of COD with respect to normalized load displacement (δ_{norm}) ($\partial COD/\partial\delta_{norm}$) (Figures 15b). In both SBC specimens (SBC-0-1 and SBC-3.5-1), with subsequent loading, both COD and CSD increased at an

accelerated rate and eventually showed a rapid jump in the post-peak regime (Figure 4-15a). The onset of the rapid jump in the COD displacements signified the occurrence of unstable crack propagation (represented by point B in Figure 4-15a), which led to the failure of SBC specimens.

The influence of confining pressure (σ_c) on the SBC specimens can be assessed by analyzing the evolution of COD and CSD inside the FPZ-1 (Figure 4-15a). The transition of FPZ-1 into a macro-crack in the SBC specimen under the unconfined state (SBC-0-1) resulted in an equal proportion of mode I and mode II components, as evident by similar values of critical crack opening (COD_c) and crack sliding displacements (CSD_c) (Figure 4-15a and Table 4-2), while in the SBC specimen under the confined state (SBC-3.5-1), FPZ-1's transition into macro-crack was characterized by a larger proportion of the mode II component with CSD_c being 1.36 times the value of COD_c (Figure 4-15a and Table 4-2). This can be attributed to the significant amount of confining pressure (σ_c =3.5 MPa) in SBC-3.5-1 that increased elastic deformation in the vertical direction along with suppressing the tensile micro-cracking inside FPZ-1. The increased confining pressure decreases the number of tensile micro-cracks inside FPZ-1 and facilitates the generations of more micro-cracks under shear as shown by Wu et al. (2017). However, its effect might be limited since the applied range of confining pressure (σ_c= 0-10.4 MPa) is below the tensile strength of Barre granite (σ_t= 14-18MPa). Additionally, the increasing confining pressure (σ_c) resulted in an increase in damage level inside FPZ-1 before the onset of unstable crack propagation, as evident by the increase in critical values of both crack displacement, i.e., COD_c and CSD_c (Table 4-2). This can be attributed to the delay in unstable crack propagation with an increase in confining pressure (σ_c), which resulted in the ligament's resistance as it can sustain a large magnitude of damage before failure. Both critical

displacements (COD_c and CSD_c) increased with the increase in the confining pressure (σ_c) (Table 4-2).

Table 4-2 Experimental results of the SBC specimens of Barre granite tested in this study

Specimen No	Confining Pressure σ_c (MPa)	Peak load (kN)	K_{II} (MPam $^{0.5}$)	COD_e (µm)	CSD_e (µm)	COD_c (µm)	CSD_c (µm)	$\frac{CSD_c}{COD_c}$
SBC-0-1	0	11.2	2.14	0.89	0.5	7	7	1.00
SBC-0-2	0	12.0	2.30	1.1	0.8	5.2	5	0.96
SBC-1.7-1	1.7	20.7	3.98	3	7	40	48	1.21
SBC-1.7-2	1.7	14.2	2.73	5	8	47	59	1.17
SBC-3.5-1	3.5	36.8	7.05	14	29	100	136	1.36
SBC-3.5-2	3.5	33.9	6.50	11	23	98	129	1.32
SBC-10-1	10	52.2	10.02	12	27	138	162	1.23

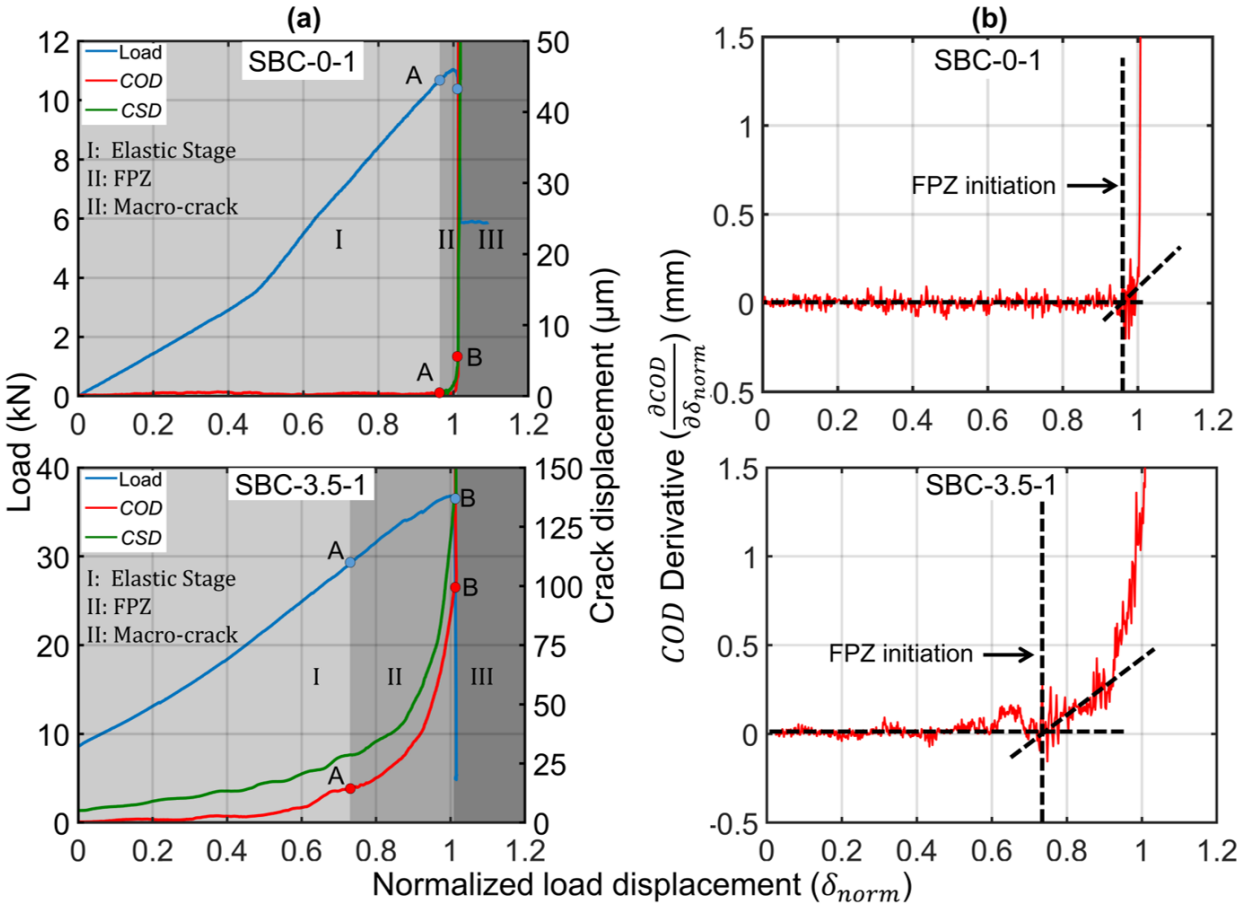

Figure 4-15 (a-b) Variation of load, the COD, and CSD for FPZ-1 with the applied load displacement in two SBC specimens (SBC-0-1 and SBC-3.5-1).

4.4.3 Fracture toughness of Barre granite specimens under mode II loading

The mode II fracture toughness (K_{IIc}) was calculated for both NDB and SBC specimens. For this purpose, values of the axial load, the axial displacement, and the confining pressure (σ_c) were recorded for each test. The mode II fracture toughness (K_{IIc}) was calculated using Eq 4-1 for NDB specimens and Eq 4-2 for SBC specimens. For each testing configuration, the mode II geometrical factor (Y_{II}) was first obtained using Abaqus model (sections 2.2.1 and 2.3.1). Table 4-3 provides a comparison of mode II fracture toughness (K_{IIc}) between SBC and NDB specimens under unconfined conditions (σ_c= 0 MPa). Results of both NDB configurations (d/w =0.4 and 0.5) are presented. Additionally, mode I fracture toughness (K_{Ic}) obtained from three-point bending tests on the same Barre granite specimens (Garg et al., 2021) is also presented in Table 4-3 for proper verification of both mode II testing geometries. The fracture toughness of Barre granite was calculated based on three tests for each testing configuration. It can be seen from Table 3 that mode II fracture toughness (K_{IIc}) of SBC specimens is larger than values obtained from both NDB configurations (d/w =0.4 and 0.5). Furthermore, mode II fracture toughness (K_{IIc}) of both NDB configurations (d/w =0.4 and 0.5) is similar to values of mode I fracture toughness (K_{Ic}) from three-point bending tests on the same rock (Table 4-3). This can be explained by similar fracture characteristics, such as the length of fully developed FPZ and critical crack opening displacement in NDB specimen under mode II loading as obtained from mode I fracture toughness tests on Barre granite (Table 4-1).

In SBC specimens, various levels of confining pressure (σ_c =0, 1.7, 3.5, 10.4 MPa) was applied to assess its influence on the overall fracture resistance of Barre granite rock under mode II loading. Figure 4-16a-b present the variations in the nominal shear strength (τ_f) and mode II fracture toughness (K_{IIc}) under different confining pressures (σ_c). The nominal shear strength

(τ_f) was calculated using Eq 4-2 and represents the average shear stress in the ligament region between two notches at the time of specimen failure. It is clear from Figure 4-16a-b that both nominal shear strength (τ_f) and mode II fracture toughness (K_{IIc}) increased linearly with the applied confining pressure (σ_c) in the range of 0-11 MPa. This linear variation in mode II fracture toughness (K_{IIc}) at low confinement (σ_c < 30 MPa) is consistent with observations of other studies (Backers et al., 2002; Zhang et al., 2022) that performed mode II loading using well-known geometries such as punch-through shear test and short core compression test. For instance, Zhang et al. (2022) found a linear variation in mode II fracture toughness (K_{IIc} = 4-7.5 MPa mm$^{0.5}$) for granite rock with the confining pressures (σ_c) ranging from 0-25 MPa.

Table 4-3 Fracture toughness of Barre granite with different testing geometries

Testing method	**Fracture toughness K_I or K_{II} (MPa m$^{0.5}$)**
Three-point bending (TPB)	1.50± 0.035
Notched deep beam (NDB) (d/w=0.4)	1.3± 0.028
Notched deep beam (NDB)(d/w=0.5)	1.24±0.018
Short beam in compression (SBC)	2.2 ± 0.065

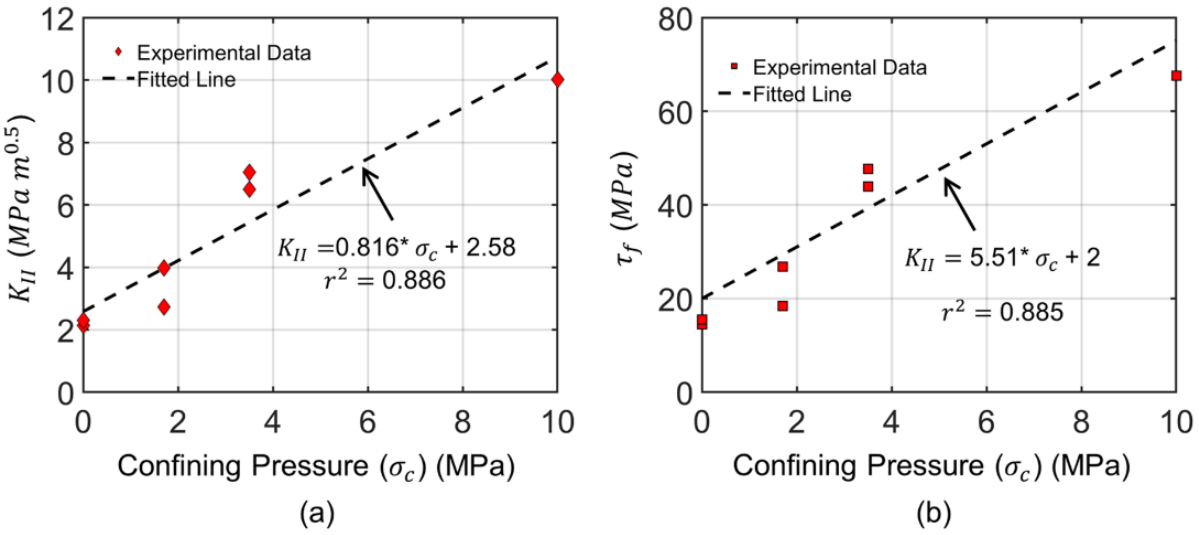

Figure 4-16 Variation of the (a) mode II fracture toughness (K_{IIc}), (b) nominal shear strength (τ_f) with respect to confining pressure (σ_c) for SBC specimens.

4.5 Discussion

4.5.1 Comparison of Failure Pattern in SBC Specimens with Known Mode II Geometries

The fracture patterns observed in SBC specimens were similar to other known mode II geometries such as punch-through shear test, and double-edge notched Brazilian disk. For instance, the formation of the tensile-dominated cracks in SBC specimens is consistent with observations in punch-through shear tests and double-edge notched Brazilian disk tests on various rocks such as Aue granite, Canara marbles, and Grimsel Granite, etc., especially at lower levels of confinement (σ_c < 30 MPa) (Backer, 2005; Nejati et al., 2021). In SBC specimens, tensile-dominated cracks initiated at the inner tip of two notches during initial loading stages (0-70% of peak load in pre-peak regime) for all values of confining pressure (σ_c = 0-10.4 MPa) applied in this study. The formation of these tensile-dominated cracks can be attributed to the presence of a high tensile stress concentration region around the inner surfaces of two notches. Additionally, the tensile-dominated cracks have a negligible effect on mode II fracture toughness

of SBC specimens as no stress drop was found at the time of their initiation in any test signifying minor energy release due to the formation of these cracks.

The dominant vertical fracture that resulted in failure in all SBC specimens primarily comprised of echelon cracks that merged together. Similarly, the main fracture in the punch through shear test mainly contains multiple echelon cracks, typically associated with the mode I component (Backers et al., 2002). The presence of these echelon cracks explained the formation of the mixed mode fracture as determined using the displacement approach of 2D-DIC in all tested SBC specimens.

Similar to punch-through shear geometry, the mode II fracture toughness (K_{IIc}) in the SBC specimens increased linearly at the low level of confining pressure (σ_c =0-10.4 MPa) tested in this study. The DIC analysis showed an increment in both modes I and mode II components inside the FPZ of the dominant fracture (Table 2-1) with an increase in confining stress. This appears to be in contrast with observations of Backer et al. (2005) on punch through shear geometry that showed suppression of tensile micro-cracking with increasing levels of confining stress. This difference in the trend of mode I component can be attributed to the small range of applied confining pressure (σ_c =0-10.4 MPa) in the current study, which was not enough to suppress tensile microcracks due to the high tensile strength of Barre granite (σ_t =14-20 MPa). The applied biaxial confinement only delayed the SBC specimen's lateral expansion, which is mainly responsible for producing the crack opening in the dominant fracture. This in coarse-grained rock such as Barre granite would result in increased tensile micro-cracking at the time of specimen failure. Wu et al. (2017) also observed a similar trend in the DEM-based simulation of punch-through shear tests on Escabrosa Limestone. Wu et al. (2017) showed that a high level of confinement (σ_c > 15 MPa), which was three times its tensile strength, was required for shear

micro-cracks to exceed tensile micro-cracks. They also showed an increase in tensile micro-cracking for confining levels equal to tensile of Escabrosa Limestone (σ_t =6 MPa).

4.6 Conclusion

Despite having various testing geometries to determine mode II fracture toughness in rocks, its proper estimation remains a major challenge due to variability in fracture characteristics between different geometries. In this study, two mode II configurations, namely (a) notched deep beams and (b) short beam in compression, were tested to characterize the development of the FPZ in Barre granite specimens. The DIC imaging was used to estimate various crack characteristics, such as fracture mode, its location, and critical crack displacements. The analysis suggests that the novel DIC-based methodology is reliable for characterizing the FPZ evolution under mode II loading, irrespective of the fracture mode obtained. The main finding of the study are as follows:

- The NDB specimens showed the formation of a "kink" fracture from the notch tip instead of the expected coplanar shear crack under pure mode II loading. The DIC analysis showed that the "kink" fracture primarily contains the mode I component, as evident by the large value of crack opening displacement along the FPZ boundary, while crack sliding displacement was found to be negligible (Figures 4-9e-f).
- The evolution of the FPZ in NDB specimens was characterized using the novel methodology developed for mode I fracture in Barre granite specimens. The FPZ in NDB specimens initiated at the notch tip, with its evolution similar to cases of pure mode I loading on the same rock. As a result, FPZ characteristics, such as its length and critical crack opening displacement (COD_c), lie within the range of values obtained from mode I fracture toughness testing (Table 4-1). This indicated that the mode II loading had negligible influence on the

FPZ development and only resulted in a non-symmetric pattern of normal displacement along the initiated fracture (Figures 4-9e and 4-10e) for NDB specimens.

- In contrast, the SBC specimens formed a dominant vertical fracture which coincided with the location of a high concentration of shear stress (τ_{xy}) region in the ligament between its two horizontal notches (Figures 4-12a and 4-5b). Based on DIC analysis, the vertical fracture was found to be a mixed-mode I/II fracture in all tested SBC specimens. Additionally, the displacement discontinuity of dominant fracture (FPZ-1) in SBC specimens appears to form a merge band between two notches, indicating shear dislocation in the ligament region (Figure 4-12a).
- The FPZ corresponding to the dominant fracture (FPZ-1) initiated around the ligament center, which subsequently covered the entire region between two notches (Figures 4-12a and 4-12e). The evolution of FPZ-1 was characterized by analyzing the variation of both crack opening displacement (COD) and the crack sliding displacement (CSD) at the ligament center (y=0 mm). The FPZ-1 in the SBC specimens initiated under tension and then underwent shearing with an equal amount of mode I and mode II components at the time of its transition into a macro-crack.
- The influence of confining pressure (σ_c) on the SBC specimens was assessed by analyzing the evolution of COD and CSD inside the FPZ-1 that subsequently transitions into the vertical fracture between two notches (Figure 4-15a). The transition of FPZ-1 in the SBC specimen got more delayed with the increase in confining pressure (σ_c) that allowed the ligament region to sustain higher levels of damage, thereby increasing its fracture resistance before its failure. This explains the increase in mode II fracture toughness (K_{IIc}) of the Barre granite specimens with the confining stress (Figure 4-16a). The proportion of mode II component

inside FPZ-1 is higher in the SBC specimen under confined conditions (SBC-3.5-1) as compared to the specimen under the unconfined state (SBC-0-1) (Figure 4-15a).

- The fracture patterns in SBC specimens were consistent with known mode II geometries such as punch through shear and short core compression test, making it a suitable configuration for estimating mode II fracture toughness in rocks.

4.7 Acknowledgement

Funding for this research was provided by the National Science Foundation under Award number 1644326. The authors are grateful for this support.

CHAPTER 5

AN XFEM FORMULATION FOR CRACK-BRANCHING IN QUASI-BRITTLE MATERIALS

This paper has been submitted for publication in the journal Computer and Geotechnics.

Prasoon Garg[4], Ahmadreza Hedayat[4], D.V. Griffiths[4]

5.1 Abstract

Numerical modeling of the cracking process in quasi-brittle material such as rocks is a challenging task due to (a) the formation of an inelastic zone (fracture process zone) at the tips of pre-existing cracks and (b) the occurrence of complex crack interactions that result in the initiation of various crack types from pre-existing fracture. To address this challenge, a novel user element based on the eXtended Finite Element Method (XFEM) was implemented in Abaqus. The developed user element through novel branching methodology facilities fracture intersections and crack branching for quasi-brittle materials. The formation of the FPZ was modeled using cohesive zone models, which defined its constitutive behavior for inelastic deformation. The capability of the XFEM model was tested against various case studies that involved the FPZ formation in both tensile-induced mixed-mode I/II crack and compression-induced mode II crack. The applicability of the crack branching methodology was assessed through fracturing in single-flawed gypsum specimens under compression loading. The analysis

[4] Colorado School of Mines, Civil and Environmental Engineering

showed that the XFEM-based user element could predict both primary and secondary cracks and thus was able to replicate real cracking patterns in studied specimens reasonably.

5.2 Introduction

Fracturing in quasi-brittle materials such as concrete and rocks is often characterized by microcracking region around the pre-existing crack tip, also known as a fracture process zone (FPZ). The formation of the FPZ leads to strain-softening behavior around the crack tip, and its non-negligible size in most quasi-brittle materials often results in violation of linear elastic fracture mechanics (LEFM) (Bazant and Planas, 1998; Yang et al., 2019b). The nonlinear fracture mechanics-based cohesive zone model (CZM) has become a popular tool in characterizing the cracking of various quasi-brittle materials due to its simple and robust representation of the complex micro-cracking process inside the FPZ. The CZM characterizes the finite-width FPZ using a thin interface that undergoes progressive softening based on traction-separation law (Rinehart et al., 2015). As a result, the CZM has been implemented by various studies in simulating rock fracture in a range of geometries, such as the three-point bending test, disk-shaped compact tension test, short-rod fracture test, etc. (Yao et al. 2012; Fakhimi and Tarokh 2013; Khoramishad et al. 2013).

Numerical simulation of the cracking process can provide valuable insights into the FPZ development in quasi-brittle materials due to its capability to model the detailed mechanism of crack processes, especially in the case of complex geometry or loading conditions. Over the years, various numerical methods have been developed to simulate the complex micro-cracking process inside the FPZ, including the phase field method (Zhang et al., 2017; Bryant and Sun,

2018), the gradient-enhanced damage model (Peerling et al., 1996), cracking particles (Rabczuk and Belytschko, 2004) and the extended finite element method (XFEM) (Karihaloo and Xiao, 2003). In recent years, the XFEM has attracted considerable attention due to its effectiveness in modeling discontinuities without the need for the remeshing process along with the facilitation of multiple fracture interactions in the same modeled domain (Daux et al., 2000; Zi and Belytschko, 2003). The XFEM-based models have been extensively used in various crack problems in quasi-brittle materials, such as multiple crack interactions during hydraulic fracturing (Youn, 2016; Cruz et al., 2018; Yang et al., 2019a) and crack propagation from open or closed pre-existing flaws in rocks (Sharafisafa and Nazem, 2014; Zhuang et al., 2014). However, most of these XFEM-based numerical studies in quasi-brittle materials such as concrete and rocks have been mainly limited to cases containing few pre-existing cracks in relatively simple geometries. In this study, the capability of the XFEM model was extended to make it suitable for modeling different crack types along with crack branching in quasi-brittle materials.

The existing XFEM-based numerical studies primarily focused on simulating the FPZ development in quasi-brittle materials subjected to tensile or tensile-shear loading (Moës and Belytschko, 2002; Karihaloo and Xiao, 2003; Meschke and Dumstorff, 2007). The fracturing in quasi-brittle materials under compression or compression-shear loading using the XFEM-based numerical model has rarely been investigated except for a few studies (Liu and Borja, (2008,2009); Sanborn and Prévost, 2011; Liu et al., 2015). The compression-induced shear fractures in most geomaterials have a few distinct characteristics compared to tensile loading-induced fractures. First, friction contact exists between two surfaces of the compression-induced shear fracture, which plays a vital role in the mechanics of crack propagation in addition to

creating residual shear strength of the crack (Borja and Foster, 2007). Second, the softening inside the FPZ of shear fractures strongly depends on existing confining pressure as it affects both the peak and residual strength of the crack (Gill, 2021) and thus requires adequate strength degradation law to account for confinement-dependent material softening.

The few existing XFEM-based numerical studies in geomaterials have mainly focused on investigating frictional contact in existing interfaces such as joints, faults, and closed or infilled flaws (Dolbow et al., 2001; Liu and Borja, 2009) rather than simulating propagating frictional cracks. Additionally, most existing XFEM studies have primarily used the standard plasticity model in conjunction with the Mohr-Coulomb (MC) criterion to simulate the propagation of frictional cracks (Khoei and Nikbakht, 2007; Liu and Borja, 2008; Khoei, 2014), which can reliably capture pressure dependency of peak shear strength. However, these models don't account for material softening that occurs inside the FPZ of the shear cracks. Recent studies (Fei and Choo, 2020; Gill, 2021) have implemented a similar softening model that accounts for the friction-dependent softening behavior of laboratory-scale geomaterials in the phase field model and continuum damage model. These studies have used nonlinear softening law for cohesion degradation in conjunction with frictional sliding in shear cracks to predict failure crack angle in uniaxial and biaxial compression tests of overconsolidated clays. The main advantage of these cohesion degradation models lies in the fact that pressure dependency of both peak and residual shear strength was predicted with reasonable accuracy (Fei and Choo, 2020; Gill, 2021). Thus, this study implemented a new cohesive zone model adapted from the study by Gill (2021) for shear fracture that includes both cohesion degradation and frictional sliding in propagating crack to ensure proper incorporation of confinement-dependent softening inside the FPZ.

Modeling complex cracking patterns in quasi-brittle materials is another major challenge for most XFEM-based numerical models. The cracking in quasi-brittle materials such as rocks and rock-like materials under compressive loading typically results in the formation of various secondary cracks, which are often responsible for their failure (Park and Bobet 2009). These secondary cracks typically comprise different shear crack patterns, such as coplanar, oblique, and out-of-plane (Bobet, 1997; Cheng et al., 2016). In most rocks, these secondary cracks often involve complex combinations of tensile (mode I) and shear (mode II) fractures, such as horsetail cracks and anti-wings, mixed tensile–shear cracks (Wong and Einstein, 2009a; Morgan et al., 2013; Wong and Li, 2011; Lee and Jeon, 2011). The central observation of these experimental studies is the formation of multiple fractures emanating from a preexisting crack, which can be called crack branching based on the theory of fracture mechanics (Fatehi Marji, 2014; Chen and Zhou, 2020). The mechanism of crack branching is a complicated process and typically requires a reliable branching criterion to estimate the point of bifurcation, defined as a point where the single crack tip results in the formation of two cracks (Rabczuk, 2013; Sun et al., 2021). These types of complex crack branching have not been investigated using XFEM-based numerical methods. The initial studies (Belytschko and Black, 1999; Daux et al., 2000) on multiple crack interactions introduced the concept of junction enrichment to model crack intersection inside the elements. This method has been used by various studies (Khoei, 2014; Khoei et al., 2016; Yang et al., 2019a) to model interactions between hydraulic and natural fractures in various rock formations. However, most of these studies are limited to modeling crack coalescence/intersections rather than investigating the crack branching mechanisms, which can be attributed to the lack of a reliable crack branching criterion (Rabczuk, 2013; Sun et al., 2021).

Alternatively, a specialized XFEM method such as the cohesive segment method (Remmers et al., 2003) facilitates nucleation and coalescence of cracks by modeling fracture as a collection of cohesive segments instead of a single entity. The main advantage of this method is that the crack initiation can occur in any arbitrary direction when elements satisfy critical conditions which allow the formation of complex branching patterns (Khoei ,2014). Despite these additional features, the feasibility of the cohesive segment method in predicting crack branching has not been verified in quasi-brittle materials with only a few applications, such as crack interactions in porous rocks (Remij et al., 2015, 2018), debonding of adhesive joints under mixed-mode I/II loading (Remmers et al., 2003; Borst et al., 2006), and soil slope stability analysis (Liu, 2015). Therefore, it is essential to develop proper techniques to simulate crack branching in XFEM that can be used to predict the formation of secondary cracks in quasi-brittle materials.

In this study, a novel XFEM-based user element was implemented in Abaqus/Standard, a finite element software by Simulia (Abaqus, 2014). The built-in XFEM element in Abaqus follows the phantom node technique (Song et al. 2006a) that doesn't require any additional degrees of freedom to enrich cracked elements. Its implementation is easier compared to standard XFEM; as a result, Abaqus has been increasingly used in modeling various fracture problems (Sharafisafa and Nazem, 2014; Xie et al., 2016, 2017; Garg et al., 2020). However, the built-in XFEM element in Abaqus only allows one fracture per element and thus cannot simulate any crack intersections or branching problems. Various studies (Cheng et al., 2014; Cruz et al., 2019) have also implemented their own user element in Abaqus to simulate various fracture problems, including hydraulic fracturing and its interaction with natural joints/faults. However,

most of these studies ignored the influence of the FPZ during the cracking process of quasi-brittle materials.

The current study aimed at creating an XFEM model capable of simulating complex crack interactions and branching in quasi-brittle materials in the context of Abaqus applications. The XFEM-based user element developed in this study is a modification of the one created by (Cruz et al. 2019). The modified user element can simulate the FPZ development in different crack types such as mode I crack, mixed-mode I/II crack, and compression-induced mode II crack. The main novelty of this work includes the capability of modeling crack branching mechanisms and other crack interactions, which facilitated the prediction of multiple crack types originating from pre-existing cracks in quasi-brittle materials. For this purpose, a novel branching methodology was developed that predicted crack branching purely based on the stress state around pre-existing fractures. Various case studies were modeled to assess the accuracy of the CZMs in predicting FPZ formation for different crack types.

The study presented in this paper starts with the description of suitable CZMs used for characterizing the formation of FPZ in various crack types, followed by the user element's theoretical formulation and the novel branching methodology. An overview of implementation aspects of user elements in Abaqus using the numerical suite named XFEMB is presented next. Finally, the simulation of various case studies that highlight various capabilities of the XFEM model is presented.

5.3 Cohesive Crack Formulation

5.3.1 Governing Equation and Weak Formulation

Consider a two-dimensional solid in the domain **Ω** and crossed by discontinuity Γ_d (Figure 1). The essential and natural boundary conditions (BC) applied are as follows:

$$\begin{aligned} u &= \bar{u} \text{ on } \Gamma_u \text{ (Essential BC)} \\ \sigma \cdot n_\Gamma &= \bar{t} \text{ on } \Gamma_t \text{ (Natural BC)} \\ \sigma \cdot n_{\Gamma_d}^+ &= -\sigma \cdot n_{\Gamma_d}^- = t_d \text{ on } \Gamma_d \text{ (Natural BC)} \end{aligned} \tag{5-1}$$

where Γ_u represents Dirichlet boundaries with prescribed displacement $\bar{u}$, σ is Cauchy stress tensor, Γ_t represents Neumann boundaries with outward unit normal vector n_Γ to external boundary of the body where surface tractions $\bar{t}$ is applied (

Figure 5-1). The crack (Γ_d) with positive normal vector given by $n_{\Gamma_d}^+$, leads to a discontinuous displacement field (u) across its internal boundary Γ_d . This consequently results in a displacement jump ($[\![u]\!]$) across the discontinuity Γ_d which is defined as relative displacement between two crack surfaces as given by:

$$[\![u]\!] = u^+ - u^- \tag{5-2}$$

The internal discontinuity Γ_d is typically comprised of two parts, namely, traction free crack (Γ_{tf}) and fracture process zone (Γ_{fpz}) (represented by black and red lines in

Figure 5-1). The cohesive traction (t_d), active over fracture process zone (Γ_{fpz}), act as an opposing force to crack displacements resulting in nonlinear material behavior around the crack

tip. Its variation is defined using a cohesive law that relates the cohesive traction (t_d) to the crack displacement vector ($[\![u]\!]$). Various cohesive laws such as linear law (Bažant and Becq-Giraudon, 2002), bilinear laws (Petersson, 1981), and exponential law (Karihaloo and Xiao, 2003) have been used for quasi-brittle materials such as rocks and concrete. For more details on the comparison of various cohesive laws used, the reader can refer to the study by (Park et al., 2009) and (Dimitri et al., 2015).

In this study, fracture propagation has been assumed to occur in an elastic body, deforming under the assumption of small strain. Additionally, all body forces and inertial effects are ignored. The fracture mechanics problems under a quasi-static state can be described by the following equations:

$$\nabla \cdot \sigma = 0 \quad \text{in } \Omega \tag{5-3}$$

$$\mathrm{d}\sigma = C \cdot d\varepsilon \quad \text{in } \Omega \tag{5-4}$$

$$\varepsilon = \nabla^s u \quad \text{in } \Omega \tag{5-5}$$

$$t_d = D^{tan} \cdot d([\![u]\!]) \quad \text{on } \Gamma_{fpz} \tag{5-6}$$

where C is fourth order elastic stiffness tensor used to define constitutive behavior of the material in Eq 5-4, ε is linear strain tensor, ∇ is the divergence operator, and ∇^s represents the symmetric part of the divergence operator used to define the kinematic relationship between displacement and strain field in Eq 5-5. The constitutive behavior of the fracture is given by a cohesive law, as shown in Eq 5-6, where D^{tan} represents a second-order tangential stiffness matrix of the fracture process zone (Γ_{fpz}).

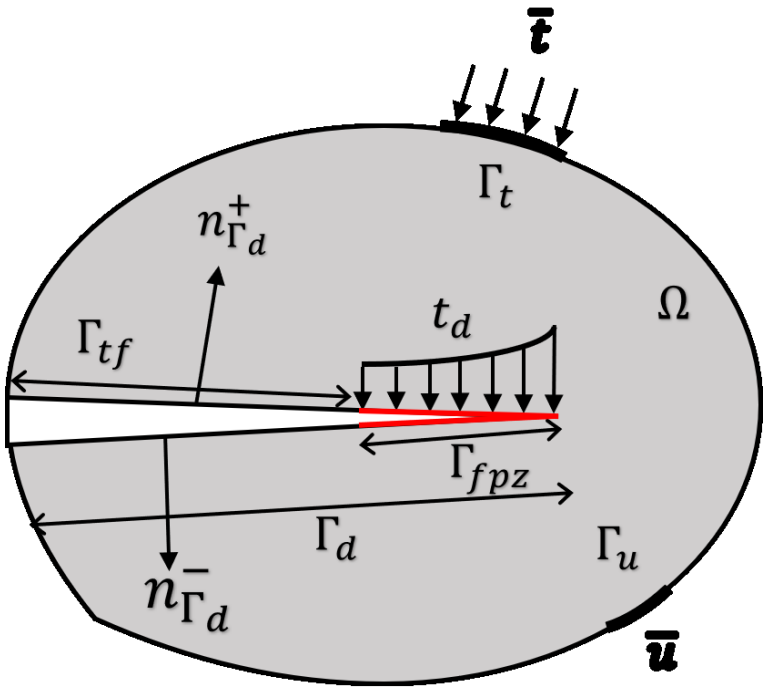

Figure 5-1 Illustration of a cracked domain with discontinuity containing both fracture process zone (represented by red lines) and traction-free part (represented by black lines) (Khoei, 2014).

The weak form of the governing differential equations can be obtained using the principle of virtual work, where the product of the equilibrium equation (Eq 5-3) and admissible test function is integrated over the domain Ω. Additionally, the Divergence theorem is applied for integrating discontinuous functions used for representing multiple cracks in the 2D-body, ensuring accurate fractured domain representation (see Khoei, 2014 for more details). Finally, all boundary conditions, including both natural and essential conditions (Eq 5-1), are imposed to get the following governing equation in the weak form:

$$\int_{\Omega} \nabla^s \delta u : \sigma \, d\Omega + \int_{\Gamma_{fpz}} \delta [\![u]\!] \cdot t_d \, d\Gamma = \int_{\Gamma_t} \delta u \cdot \bar{t} \, d\Gamma \tag{5-7}$$

where δu denotes a virtual displacement field and is used as a test function to apply the principle of virtual work. The colon symbol indicates double contraction. For simplicity, Eq 5-7 represents governing equation for single discontinuity; however, it can be generalized for multiple fractures using the Divergence theorem.

5.3.2 Tensile-shear Mixed mode I/II Crack

In this study, the exponential cohesive zone model (Meschke and Dumstorff, 2007; Zamani et al., 2012) is used to describe fracturing in quasi-brittle materials subjected to mode I or mixed-mode loading I/II. This model is valid for any mixed-mode I/II fracture initiated under tensile loading at the crack tip (Wang and Waisman, 2018). In this model, the fracture energy dissipation inside the FPZ is defined in the form of coupled mode I and mode II mechanisms using the concept of equivalent crack displacement ($[\![u]\!]_{eq}$) and equivalent traction (t_{eq}) as given by:

$$[\![u]\!]_{eq} = \sqrt{([\![u]\!]_n)^2 + (\beta[\![u]\!]_s)^2}\,, \quad t_{eq} = k[\![u]\!]_{eq} \tag{5-8}$$

where β is the weighting parameter that governs the contribution of shear traction and shear stiffness during material softening. The weighting parameter value (β) depends on the micro-scale heterogeneity of the material and needs to be calibrated for a specific material (Dumstorff and Meschke 2007). In the current study, β is selected to be 1, which has been typically assumed for quasi-brittle materials (Meschke and Dumstorff, 2007; Zamani et al., 2012; Wang and Waisman, 2018). $[\![u]\!]_n$ and $[\![u]\!]_s$ denotes the normal and shear components of the crack displacement $[\![u]\!]$, respectively across its two faces. k represents equivalent crack stiffness at any point of material softening (Figure 5-2) as given by:

$$k = \begin{cases} k_P & if\ [\![u]\!]_{eq} \le [\![u]\!]_{eq}^{o} \\ \dfrac{\sigma_t}{[\![u]\!]_{eq}^{max}} exp\left(-\dfrac{\sigma_t}{G_{IC}}\left([\![u]\!]_{eq}^{max} - [\![u]\!]_{eq}^{o}\right)\right) & if\ [\![u]\!]_{eq} > [\![u]\!]_{eq}^{o} \end{cases} \quad (5\text{-}9)$$

where $[\![u]\!]_{eq}^{o} = \sigma_t / k_P$ represents the crack displacement at which the equivalent traction exceeds the tensile strength of the material (σ_t), k_P denotes penalty stiffness, G_{IC} is the critical value of mode I fracture energy. $[\![u]\!]_{eq}^{max}$ denotes the maximum value of equivalent crack displacement achieved during loading history and is used to determine the state of material softening as given by:

$$f_t\left([\![u]\!]_{eq}, [\![u]\!]_{eq}^{max}\right) = [\![u]\!]_{eq} - [\![u]\!]_{eq}^{max} \le 0 \quad (5\text{-}10)$$

where f_t is yield function under tensile loading, which dictates whether the crack is under softening condition ($f_t = 0$) or under elastic unloading/loading condition ($f_t < 0$). The normal (t_n) and shear traction (t_S) at the crack surface are defined in terms of equivalent crack traction (t_{eq}) as:

$$t_{eq} = \sqrt{{t_n}^2 + \left(\frac{t_S}{\beta}\right)^2} \quad (5\text{-}11a)$$

$$t_n = \frac{t_{eq}[\![u]\!]_n}{[\![u]\!]_{eq}} = k[\![u]\!]_n, \quad t_S = \frac{t_{eq}[\![u]\!]_s}{[\![u]\!]_{eq}} = k[\![u]\!]_s \quad (5\text{-}11b)$$

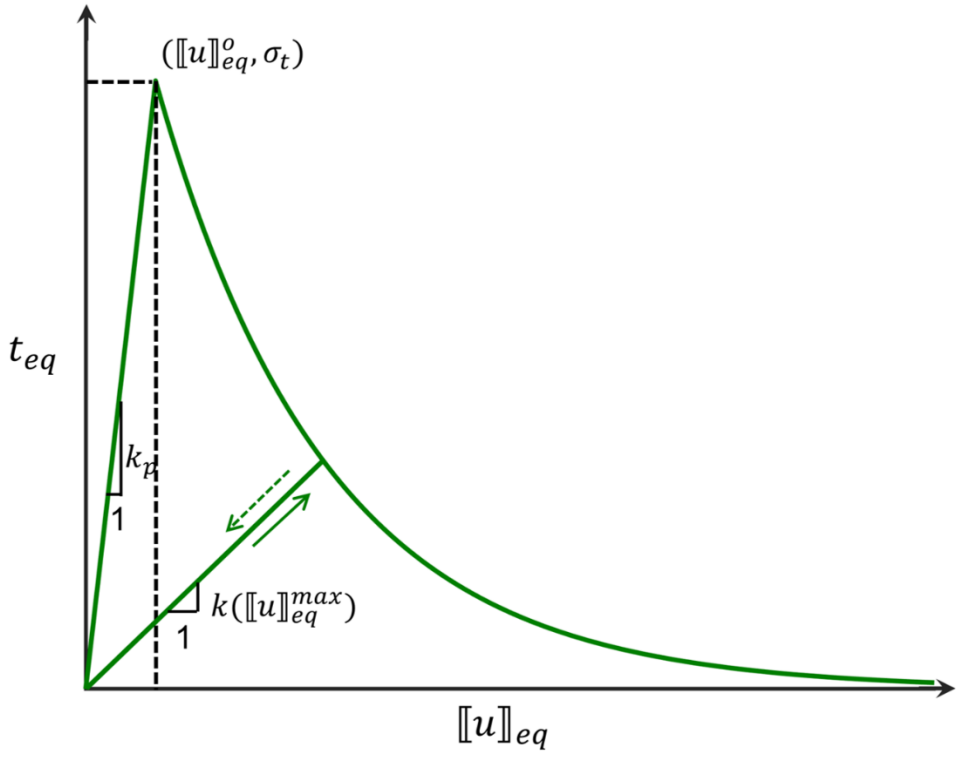

Figure 5-2 Exponential softening law of crack initiation under tensile and tensile-shear loading using the concept of equivalent crack traction (t_{eq}) and displacemnet ($[\![u]\!]_{eq}$). The unloading path is denoted by a dashed arrow, while the elastic reloading path is represented by a solid arrow (after Dumstorff and Meschke, 2007).

The aforementioned relationship between crack tractions and crack displacements in Eq 5-11 can be differentiated with respect to time to get the tangent stiffness matrix of discontinuity (D^{tan}):

$$D^{tan} = \begin{cases} \dfrac{\sigma_t \cdot k}{[\![u]\!]_{eq}} \begin{bmatrix} \dfrac{[\![u]\!]_s^2}{G_{IC}} - \dfrac{[\![u]\!]_n^2}{\sigma_t \cdot [\![u]\!]_{eq}} & [\![u]\!]_n \cdot [\![u]\!]_s \dfrac{G_{IC} + \sigma_t \cdot [\![u]\!]_{eq}}{G_{IC} \cdot \sigma_t \cdot [\![u]\!]_{eq}} \\ [\![u]\!]_n \cdot [\![u]\!]_s \dfrac{G_{IC} + \sigma_t \cdot [\![u]\!]_{eq}}{G_{IC} \cdot \sigma_t \cdot [\![u]\!]_{eq}} & \dfrac{[\![u]\!]_n^2}{G_{IC}} - \dfrac{[\![u]\!]_s^2}{\sigma_t \cdot [\![u]\!]_{eq}} \end{bmatrix} & if\ f_t = 0 \\ k \begin{bmatrix} 1 & 0 \\ 0 & 1 \end{bmatrix} & if\ f_t < 0 \end{cases} \quad (5\text{-}12)$$

In Eq 5-12, D^{tan} is a coupled matrix that provides a consistent relationship between increment crack traction $\{\Delta t_s, \Delta t_n\}^T$ and incremental values of crack displacement $\{\Delta[\![u]\!]_s, \Delta[\![u]\!]_n\}^T$ for softening conditions ($f_t = 0$). While during elastic loading or unloading conditions ($f_t > 0$), an uncoupled tangent matrix (D^{tan}) is obtained (Eq 5-12) due to variation of crack tractions $\{\Delta t_n, \Delta t_s\}^T$ under constant secant stiffness (k). For cracks closure (i.e., $[\![u]\!]_n < 0$), the contact penalty method is used where the impenetrability condition is applied in an approximate sense. In this method, normal traction is assumed to be a linear function of cracks closure ($t_n = k_P \cdot [\![u]\!]_n$) using penalty stiffness (k_P). The value of penalty stiffness should be large enough to limit the non-physical crack penetration, provided that ill-conditioning of the stiffness matrix is avoided.

5.3.3 Shear Crack under Compression

In this study, a cohesive zone model was developed, which characterizes the FPZ development in quasi-brittle materials under compressive loading. The developed cohesive zone model was based on the anisotropic elastic damage model proposed by (Gill, 2021), which accounts for frictional energy dissipation during the propagation of the shear crack. This anisotropic elastic damage model is consistent with the slip surfaces propagation theory developed by (Palmer et al., 1973). The cohesive zone model for mode II crack assumes one yield function for each tensile and compressive loading regime on the crack surface as given by:

$$f_s^{ten} = t_s - t_c \leq 0 \quad \text{if } [\![u]\!]_n \geq 0 \tag{5-13a}$$

$$f_s^{com} = t_s - t_c - \mu t_n \leq 0 \quad \text{if } [\![u]\!]_n < 0 \tag{5-13b}$$

where f_s^{ten} and f_s^{com} are yield functions for mode II crack tensile and compression loading regime, respectively, μ denotes the coefficient of friction of the material, t_c denotes the cohesion value of the crack surface at any point of material softening. For the sake of simplicity, the friction coefficient (μ) is considered constant in this study; however, the cohesive zone model can be easily generalized for variable friction during material softening. The Cohesion (t_c) assumed to vary exponentially with respect to the shear component of crack displacement ($[\![u]\!]_s$) as shown in Figure 5-3, with crack shear stiffness (k_s) defined as:

$$k_s = \begin{cases} k_s^0 & if\ [\![u]\!]_s \le [\![u]\!]_s^o \\ \dfrac{t_c^{max}}{[\![u]\!]_s^{max}} exp\left(-\dfrac{t_c^{max}}{G_{IIC}}([\![u]\!]_s^{max} - [\![u]\!]_s^o)\right) & if\ [\![u]\!]_s > [\![u]\!]_s^o \end{cases} \quad (5\text{-}14)$$

where G_{IIC} is critical value mode II fracture energy, t_c^o denotes initial cohesion of the material, $[\![u]\!]_s^{max}$ denotes the maximum value of the shear component of crack displacement ($[\![u]\!]_s$) achieved during loading history after crack initiation. $[\![u]\!]_s^o = t_c^{max}/k_s^0$ represents the crack displacement at which the maximum shear traction (t_c^{max}) is achieved. The value of maximum shear traction (t_c^{max}) depends on the loading regime at the time of crack initiation. For instance, if the shear crack is initiated under the tensile regime, the normal (t_n) and shear (t_S) components of crack traction are given by:

$$t_n = 0, \quad t_s = t_c = k_s[\![u]\!]_s \ \text{ if } [\![u]\!]_n \ge 0 \quad (5\text{-}15)$$

As shown in Eq 5-15, shear traction (t_S) in tensile regime entirely depend on cohesion (t_c) and thus results in an uncoupled tangent stiffness matrix of discontinuity (D^{tan}) for both softening ($f_s^{ten} = 0$) and elastic loading/unloading conditions ($f_s^{ten} < 0$) as:

$$D^{tan} = \begin{cases} \begin{bmatrix} \dfrac{[\![u]\!]_s \cdot t_c^{max} \cdot k_s}{G_{IIC}} & 0 \\ 0 & 0 \end{bmatrix} & if\ f_s^{ten} = 0 \\ \begin{bmatrix} k_s & 0 \\ 0 & 0 \end{bmatrix} & if\ f_s^{ten} < 0 \end{cases} \tag{16}$$

In the compression regime, the shear crack initiation will have a frictional effect which results in higher shear strength of the crack surface, as shown in Eq 5-13b, where the yield function f_s^{com} has additional force as "μt_n". Therefore, the normal (t_n) and shear (t_s) values of crack traction are defined as:

$$t_n = k_P [\![u]\!]_n, \quad t_s = t_c + \mu t_n \quad \text{if } [\![u]\!]_n < 0 \tag{5-17}$$

Here, normal crack traction (t_n) varies with crack closure ($[\![u]\!]_n < 0$) based on the penalty method described in section 5.3.2. It is clear from Eq 5-17 that shear traction (t_S) depends on both normal and tangential components, crack displacement $\{\Delta[\![u]\!]_s, \Delta[\![u]\!]_n\}$ which results in a non-symmetric coupled tangent stiffness matrix of discontinuity (D^{tan}) under softening conditions ($f_s^{com} = 0$):

$$D^{tan} = \begin{cases} \begin{bmatrix} \dfrac{[\![u]\!]_s \cdot t_c^{max} \cdot k_s}{G_{IIC}} & \mu k_P \\ 0 & k_P \end{bmatrix} & if\ \ f_s^{com} = 0 \\ \begin{bmatrix} k_s & 0 \\ 0 & k_P \end{bmatrix} & if\ f_s^{com} < 0 \end{cases} \tag{5-18}$$

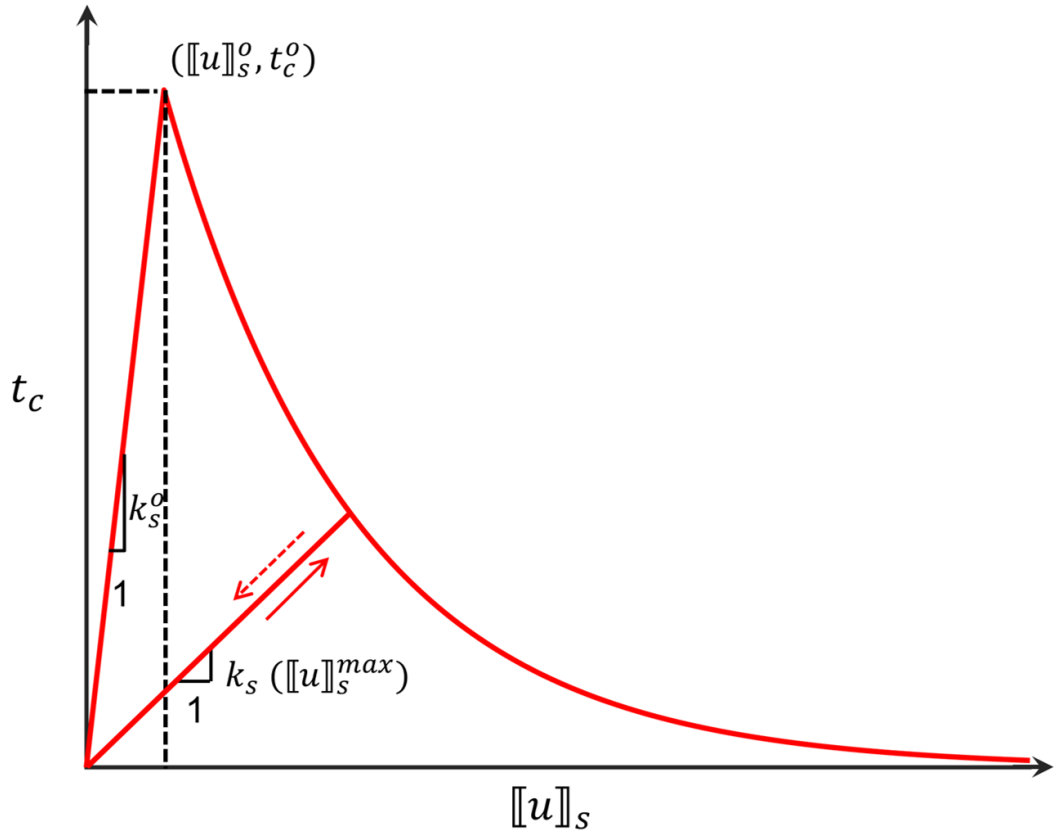

Figure 5-3 Exponential softening law for degradation of crack cohesion (t_c) with respect to the shear component of the crack displacement vector ($[\![u]\!]_s$).

5.3.4 Extended Finite Element Formulation

5.3.4.1 XFEM Discretization

The XFEM uses the concept of partition of unity (PU), introduced by Babuška and Melenk (1996), to account for discontinuity in standard FE approximation. This is done by adopting specialized enrichment functions, which account for discontinuity in the displacement field and additional degrees of freedom. Thus, the displacement field in the XFEM formulation can be approximated as a combination of the continuous part ($u_{std}^h(x)$) and discontinuous part ($u_{enr}^h(x)$) (Belytschko and Black 1999) as given by:

$$u^h(x) = \underbrace{\sum^{I\in\mathcal{N}} N_I^{std}(x)\ \cdot \hat{u}_I}_{u^h_{std}(x)} + \underbrace{\sum^{J\in\mathcal{N}^{dis}} N_J^{std}(x)\cdot\Phi_J(x)\cdot\hat{a}_J}_{u^h_{enr}(x)} \tag{5-19}$$

where $\mathcal{N}$ represents all the nodes in the domain, $\hat{u}_I$ is the nodal vector of standard degrees of freedom, $N_I^{std}(x)$ are the standard FE shape functions, $\mathcal{N}^{dis}$ represents the set of nodes that are enriched with a special function $\Phi_J(x)$ and have associated additional degrees of freedom denoted by $\hat{a}_J$. The selection of proper enrichment function is most vital in XFEM formulation. The current study is limited to interactions between the strong discontinuities such as cracks which typically require two types of enrichment functions, namely, (a) Heaviside function and (b) Branch function. The Heaviside function accounts for displacement jump across crack faces, while the branch function is typically used for simulating near-tip stress singularity (Karihaloo and Xiao, 2003). The classical branch functions are based on linear elasticity, providing an analytical solution for the asymptotic field around the crack tip. Thus, they are unnecessary in cohesive fractures where near-tip stresses are finite (Salimzadeh and Khalili, 2015). Therefore, only a Heaviside enrichment function based on the study by (Zi and Belytschko, 2003) has been employed in this study, and thus special function $\Phi_J(x)$ is given by:

$$\Phi_J(x)\ = H\big(\varphi(x)\big) - H\left(\varphi\big(x_J\big)\right) \tag{5-20}$$

where $H(\varphi)$ is a step Heaviside function, given by:

$$H(\varphi(x))\ = \begin{cases} +1, \varphi(x) \geq 0 \\ -1, \varphi(x) < 0 \end{cases} \tag{5-21}$$

$\varphi(x)$ is a signed distance function with the definition of:

$$\varphi(x) = min\|x - x^*\| \cdot sign\left((x - x^*) \cdot n_{\Gamma_d}\right) \tag{5-22}$$

The signed distance function ($\varphi(x)$) for any point x defines the closet distance from the point x^* that lie on discontinuity. It can be inferred from Eq 5-21 that $\varphi(x)$ is opposite at two sides of the discontinuity, which results in displacement jump across crack faces as given by the definition of the Heaviside function in Eq 5-20. Additionally, the derivative of the signed distance function $\varphi(x)$ is discontinuous along the fracture, making it suitable for modeling strong discontinuities. It is to be noted that the shifted basis Heaviside function in this study (Eq 5-20) as it offers various advantages such as simpler post-processing while minimizing the problem of blending elements (Fries and Belytschko 2010). Additionally, multiple fractures can be included in the domain, which results in displacement discretization in Eq 5-23 for $\mathcal{M}_b$ fractures:

$$u^h(x) = \sum_{I \in \mathcal{N}} N_I^{std}(x) \cdot \hat{u}_I + \sum_{k=1}^{\mathcal{M}_b} \sum_{J \in \mathcal{N}^{dis}} N_J^{std}(x) \cdot \hat{a}_{J,k} \cdot \left(H_k(x) - H_k(x_J) \right) \tag{5-23}$$

5.3.4.2 Branching Enrichment

In the case of crack branching, multiple fractures can exist inside an element in different configurations. These configurations may lead to either one of two kinds of enriched elements as shown in Figure 5-4a-b. The first type of enrichment occurs when the element is crossed by two non-intersecting cracks (Figure 5-4a). In comparison, the second type of enriched element results from the formation of a junction when two cracks intersect inside it (Figure 5-4b). In the former case, the discontinuous part of the displacement field can be written as the superimposition of

two separate enrichment functions for each crack, as described in Eq 5-22. The second type of enrichment (Figure 5-4b) requires a junction enrichment function ($J(x)$) which account for the intersection of two cracks inside the element (Daux et al., 2000). The value of junction function $J(x)$ depends on values of the signed distance function of each fracture given by:

$$J(x) = \begin{cases} H(\varphi_{II}(x)), & If\ H(\varphi_I(x)) = H(\varphi_{II}(x)) \\ 0, & If\ H(\varphi_I(x)) = -H(\varphi_{II}(x)) \end{cases} \quad (5\text{-}24)$$

Here, the two intersecting fractures are classified into the main fracture (solid blue line in Figure 5-4b) with the signed function of $\varphi_I(x)$ and secondary fracture (red dash line in Figure 5-4b). The $\varphi_{II}(x)$ represents signed function of secondary fracture. If a point x lies on the same side of the main fracture as the secondary fracture, its junction enrichment function $J(x)$ depends on Heaviside enrichment of secondary fracture. If point x and secondary fracture lie on the opposite side of the main fracture, the junction enrichment function $J(x)$ for the point x is equal to zero. It is important to note that this junction enrichment function only accounts for T-shaped intersection (main fracture and one secondary fracture) and not X-shaped case when two fracture completely crosses each other. For an X-shaped intersection, two fractures are divided into one main fracture and two secondary fractures, resulting in the assumption of two intersections. In this case, two different junction enrichments $J_I(x)$ and $J_{II}(x)$ are required to describe the intersection between the main fracture and each secondary fracture with a similar definition as used for T-shaped intersections.

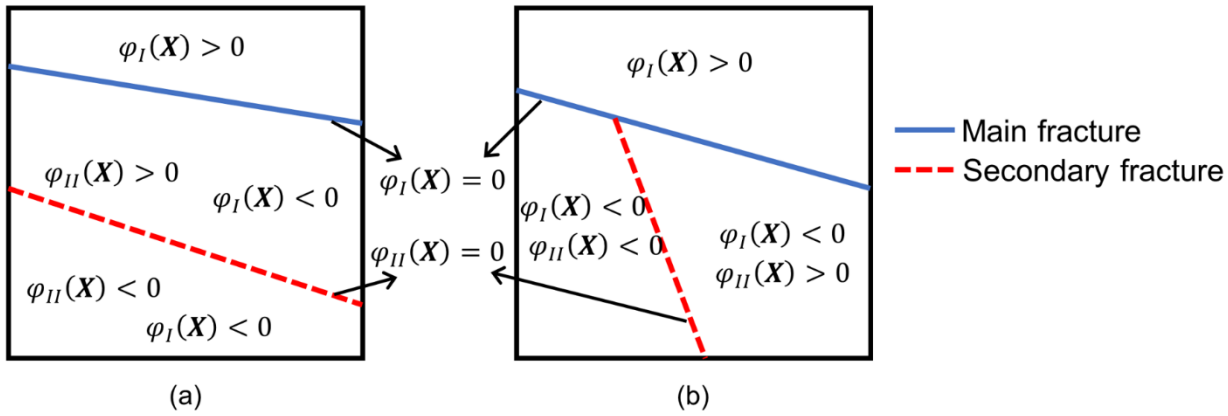

Figure 5-4 Configurations of two fractures inside the element (a) crossed by two separate cracks; (b) two intersecting cracks resulting in the crack junction (after Xu et al. 2014).

The incorporation of crack intersection requires an additional set of degrees of freedom, $\hat{b}_m$ corresponding to specific junction enrichment function $J(x)$. Therefore, the displacement field in XFEM formulation for multiple intersecting fractures can be approximated as:

$$u^h(x) = \sum_{I\in\mathcal{N}} N_I^{std}(x)\cdot \hat{u}_I + \sum_{k=1}^{\mathcal{M}_b}\sum_{J\in\mathcal{N}^{dis}} N_J^{std}(x)\cdot \hat{a}_{J,k}\cdot\left(H_k(x) - H_k(x_J)\right) + \sum_{l=1}^{\mathcal{M}_c}\sum_{m\in\mathcal{N}^{junc}} N_m^{std}(x)\cdot \hat{b}_{m,l}\cdot\left(J_l(x) - J_l(x_m)\right) \tag{5-25}$$

where $\mathcal{M}_c$ denotes the number of crack intersections requiring the extra set of degrees of freedom $\hat{b}_{m,l}$, $\mathcal{N}^{junc}$ denotes the set of nodes supported by all crack junctions present in the domain. The displacement field is implemented using the plane strain linear element (Q4) with four corner nodes. Figure 5-5 presents the various degrees of freedom used for enriching the domain with intersecting cracks.

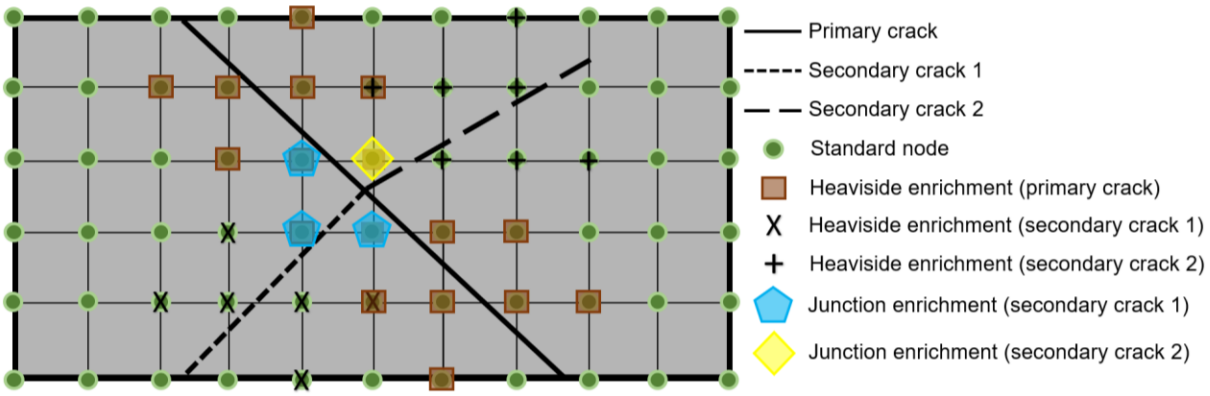

Figure 5-5 Description of various enrichment types used for the domain containing intersecting cracks.

5.3.4.3 Novel Branching Methodology

This section presents a novel branching methodology developed in the current study, inspired by the cohesive segment method (Remmers et al., 2003; de Borst et al., 2006; Remij et al., 2018). The main idea behind the developed branching methodology is to ensure that crack branching emerges at the maximum number of locations and is not limited by any other conditions, such as the intersection of multiple cracks. In the cohesive segment method (de Borst et al. 2006; Remij et al. 2018), crack branching occurs as a special case when two cracks intersect each other, thus needing two or more cracks to mimic the crack branching mechanism. As a result, only a limited number of cases of crack branching can be simulated by the cohesive segment method.

The developed methodology considers four scenarios: a) crack nucleation, b) crack growth, c) crack branching, and d) crack coalescence. Any scenario can be triggered, provided the required conditions are met. For instance, the crack nucleation in the current study will only occur in cases where no pre-existing cracks are present, which is, in contrast, to the approach

used in the cohesive segment method (Remij et al., 2015). Allowing crack nucleation in every case may result in a large concentration of cracks in a small region, increasing the degrees of freedom required per node. However, Abaqus only allow 27 degrees of freedom per node, restricting the number of cracks that can be incorporated into the elements surrounding a given node (Abaqus, 2016). In problems with no pre-existing cracks, the average stress is calculated for every element in the modeled domain, which is then compared with suitable crack initiation criteria to determine the location of crack nucleation. The crack growth/propagation occurs when the average stress in the region around the crack tips (Figure 5-6a) satisfies the suitable crack initiation criterion. First, a square region perpendicular to the crack tip with an area equal to the element size is defined for crack propagation. This is followed by calculating average stress based on the stress field at the integration points inside the region (Figure 5-6a). As the crack initiation criterion is triggered, the crack is extended straight until its tip reaches the element's edge.

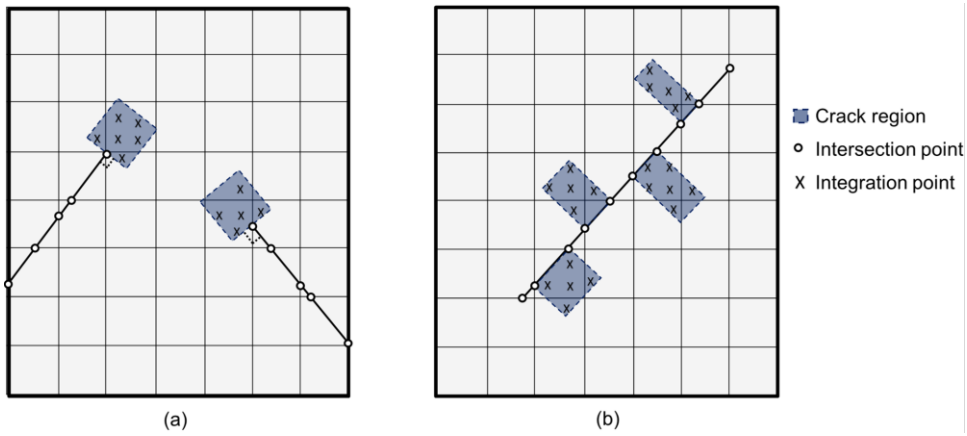

Figure 5-6 Description of crack regions used for (a) crack initiation from the tip; (b) crack branching.

The crack branching in the current study was modeled by allowing the initiation of new cracks from the body of pre-existing cracks. For this purpose, regions are defined along each linear segment, represented by the point of intersection of the pre-existing crack with the mesh, as shown in Figure 5-6b. Additionally, for each linear segment, two regions are defined on either side of the crack to account for the discontinuous stress field across it (Figure 5-6b). These crack branching regions are typically rectangular in shape with an area equal to the element size. Once required crack initiation is triggered in any region, the direction of the new crack branch is estimated using the same criterion. As a result, a new linear branch is formed that extends to the edge of the element (Figure 5-7a). This will result in the formation of one new tip for each crack branch, as shown in Figure 5-7a. It is important to note that the size of the stress check region (Figure 5-6a-b) will only affect the direction of FPZ and, consequently path of new and branched cracks. However, it doesn't influence the size of the FPZ which is a material property as long as the mesh is sufficiently refined (Remmers, 2006). Thus, the size of the check region needs to be optimized to get mesh-independent crack growth, typically achieved by using non-local stress averaging schemes (Wells and Sluys, 2001). These stress-averaging schemes assign weighted functions to stress values of integration points based on ratio of their distance from the crack tip and length scale parameter. The length scale parameter is typically chosen two-three times the element size (Wells and Sluys, 2001; Wang and Waisman, 2018). Thus, stress-averaging schemes works well for predicting crack extensions provided mesh is sufficiently refined, i.e., element size less than one-tenth of fully developed FPZ length (Wells and Sluys, 2001; Remmers, 2006). However, they would not be applicable to the rectangular region used for checking the initiation of crack branching in this study due to the absence of a crack tip. Thus, to

ensure consistency between stress calculation in both crack propagation and branching, the check region with an area equal to the element size is defined based on the study by Cruz et al. (2018).

The crack coalescence is defined as the intersection between two cracks, which in a numerical model can occur in one of two cases, i.e., (a) a tip of one crack encounters the interior surface of another discontinuity, and (b) when two crack tips encounter each other (Remji et al., 2018). In the current study, the scenario of crack coalescence will only be checked when two approaching cracks are separated by the distance of one element or less, as shown in Figure 5-7b-c. Additionally, the shape of crack tip regions may change in the first case of crack coalescence depending on the encountered surface of the crack, as shown in Figure 5-8a. This specific treatment of the crack tip region is necessary due to the discontinuous stress field across the crack, which dictates that the stresses are only calculated in the area on the same side of the crack tip (Figure 5-8a). A similar procedure is used to define crack tip regions in case of further extension after crack coalescence with the interior surface of discontinuity as shown in Figure 5-8b.

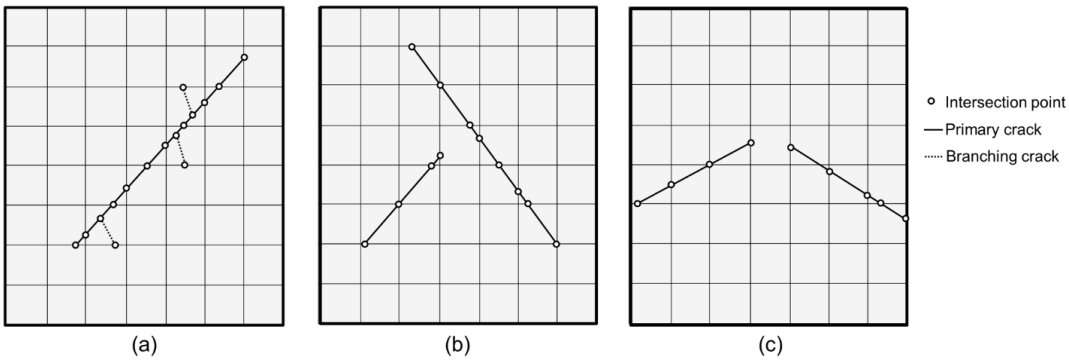

Figure 5-7 Description of crack interactions scenarios (a) crack branching; (b) tip of one crack interacting with the surface of another crack; and (c) tips of two cracks interacting with each other.

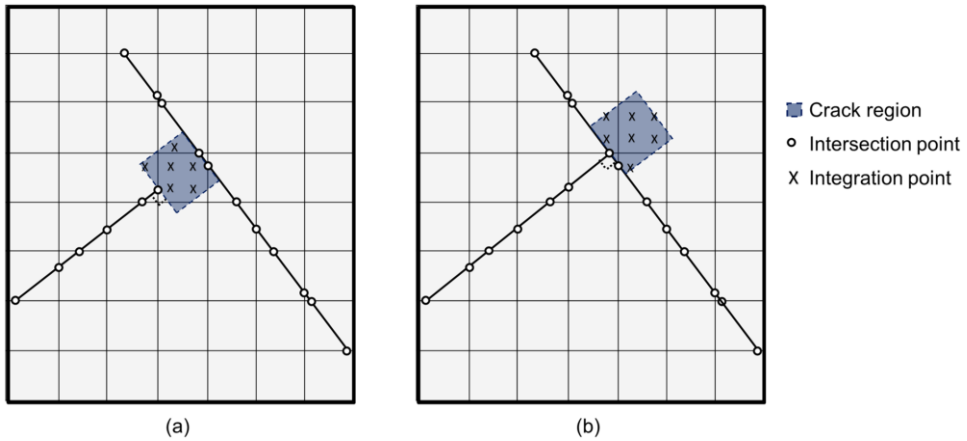

Figure 5-8 Description of crack propagation regions defined in two cases of crack interactions (a) tip about to intersect with another crack; (b) crack interaction with the tip of another crack.

5.3.4.4 Stiffness Matrix Formulation and Numerical Integration

The test function of the displacement field (δu) used in Eq 5-7 is defined in the same space as the displacement field in Eq 5-25. A similar procedure is used for determining the test function of the strain vector. The generalized form of both displacement and strain test functions can be written as:

$$\delta u(x) = N^{std}\delta\hat{\boldsymbol{u}} + N^{enr}\delta\hat{\boldsymbol{c}} \tag{5-26a}$$

$$\delta\varepsilon(x) = B^{std}\delta\hat{\boldsymbol{u}} + B^{enr}\delta\hat{\boldsymbol{c}} \tag{5-26b}$$

where $\hat{\boldsymbol{u}}$ represents the standard degrees of freedom of finite element mesh with standard shape function (N^{std}). The enriched nodal displacement ($\hat{\boldsymbol{c}}$) with enriched shape function (N^{enr}) represents degrees of freedom corresponding to both Heaviside and junction enrichments for all fractures present in the modeled domain. $B^{\alpha} = LN^{\alpha}(x)$ denotes the derivatives of standard and enriched shape functions with matrix L representing the strain differential operator.

The substitution of the discretized form of the test function (δu) into the weak form of virtual work (Eq 5-7) results in a set of nonlinear system of equations that using Newton-Raphson iterative procedure can be discretized into incremental form as given by:

$$\begin{bmatrix} \boldsymbol{K}_{uu} & \boldsymbol{K}_{ua} \\ \boldsymbol{K}_{au} & \boldsymbol{K}_{aa} \end{bmatrix} \begin{Bmatrix} d\hat{\boldsymbol{u}} \\ d\hat{\boldsymbol{c}} \end{Bmatrix} = \begin{Bmatrix} \boldsymbol{f}_u^{ext} \\ \boldsymbol{f}_c^{ext} \end{Bmatrix} - \begin{Bmatrix} \boldsymbol{f}_u^{int} \\ \boldsymbol{f}_c^{int} \end{Bmatrix} \tag{5-27}$$

where $d\hat{u}$ and $d\hat{c}$ denotes the incremental form of standard and enriched nodal displacements, respectively. The components of the stiffness matrix in Eq 5-27 are:

$$\begin{gathered} \boldsymbol{K}_{uu} = \int_{\Omega} (B^{std})^T C B^{std} d\Omega \ , \qquad \boldsymbol{K}_{ua} = \boldsymbol{K}_{au}{}^T = \int_{\Omega} (B^{std})^T C B^{enr} d\Omega \\ \boldsymbol{K}_{aa} = \int_{\Omega} (B^{std})^T C B^{enr} d\Omega + \int_{\Gamma_d} [\![N^{enr}]\!]^T D^{tan} N^{enr} d\Gamma \end{gathered} \tag{5-28}$$

The fourth element of the stiffness matrix ($\boldsymbol{K}_{aa}$) in Eq 5-27 presents the contribution of the cohesive zone model of fracture as the value of tangent stiffness matrix of fracture (D^{tan}) will be estimated based on softening behavior of a given crack type. The internal and external forces in Eq 5-27 can be written as:

$$\begin{gathered} f_u^{int} = \int_{\Omega} (B^{std})^T \sigma d\Omega \ , \quad f_u^{ext} = -\int_{\Gamma_t} (N^{std})^T \bar{t} d\Gamma \\ f_c^{int} = \int_{\Omega} (B^{std})^T \sigma d\Omega \ , \quad f_c^{ext} = \int_{\Gamma_t} (N^{enr})^T \bar{t} d\Gamma + \int_{\Gamma_d} [\![N^{enr}]\!]^T t_d d\Gamma \end{gathered} \tag{5-29}$$

The components of stiffness and force matrices in Eqs 5-28-29 can be numerically integrated using the Gauss-Seidel scheme (Remmers, 2006). In XFEM, numerical integration

using standard Gauss points is no longer sufficient due to the presence of discontinuities in the modeled domain. The enrichment shape functions in XFEM are not smooth and lead to a discontinuous displacement field inside the fractured element. As a result, the accurate estimation of the stress field is no longer possible using the standard Gauss-Seidel scheme; instead, two regions on the opposite of the discontinuity need to be integrated separately and then summed together (Wells and Sluys, 2001). In the current study, the regions on both sides of the discontinuity are divided into several sub-domains based on suggestions by (Fries and Belytschko, 2010) which ensures that the strain field and other matrices are accurately calculated without the use of too many integration points. Figure 5-9 presents various possible cases of element subdivisions implemented in the current study. The subdivision process involves assigning a certain number of sub-domains which depends on the number of sides present in the region. The region with four sides has only one subdomain with Gauss integration points based on the 2d quadrilateral scheme, as shown in Figure 5-9a. The region with three sides has one subdomain with three integration points placed based on triangular elements, as shown in Figure 5-9b. Finally, the region with five or more sides is typically made of three-more triangle subdomains with vertices coinciding with the region's vertices, as shown in Figure 5-9b-c. The integration points in these triangular subdomains are placed again based on the Gauss quadrature scheme for triangular elements.

The cracks in the current study are modeled as fictitious 1D linear segments with the Gauss quadrature scheme of two integration points in each crack segment (Figure 5-10a-c). These integration points are then used to evaluate the stiffness and forces matrices along the fracture surface, and no new degree of freedom is required. It is noted that crack intersections typically

require extra Gauss points to simulate the different behavior on each side of the junction (T-shaped or X-shaped), as shown in Figure 5-10b-c.

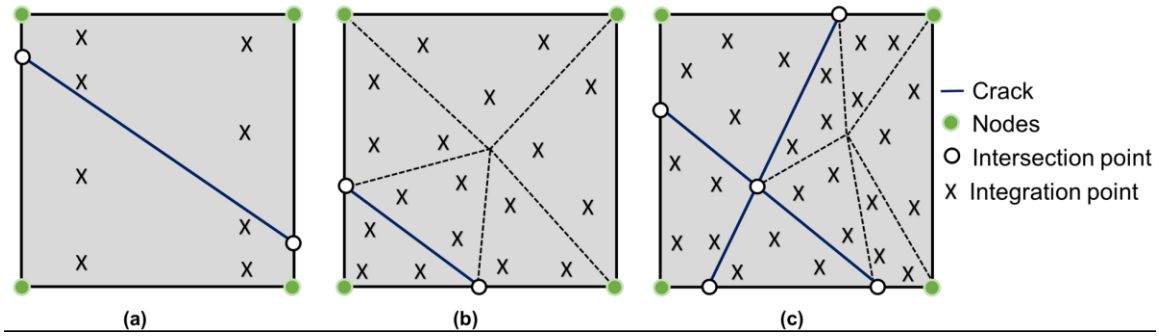

Figure 5-9 Scheme for placement of integration points in various types of sub-domains.

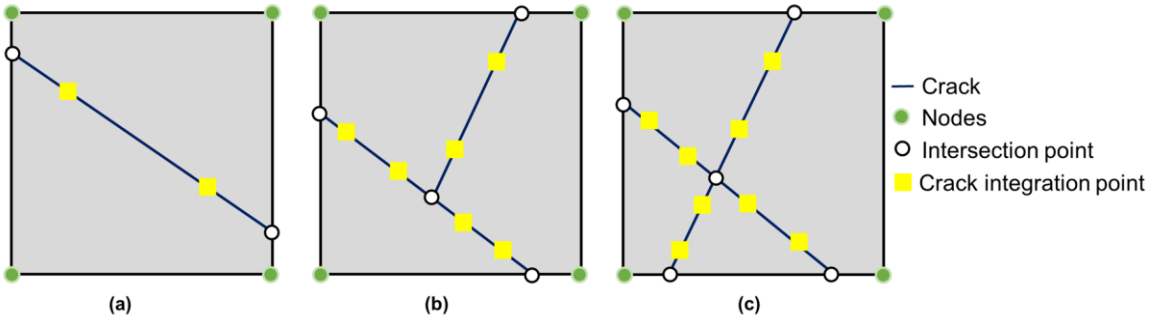

Figure 5-10 Scheme for integration points position in various cracks.

5.4 Implementation

5.4.1 Overview

The XFEM formulation was implemented using a user-defined element in the commercial general-purpose FEA software Abaqus. Along with the user-defined element, various codes in different languages were implemented in a suite titled XFEMB. The XFEMB comprises of three main parts: a) input generator, b) user element and c) output generator. The input generator primarily defined the domain size, initial crack geometry and boundary conditions for each

simulation. For this purpose, various modules in MATLAB were written that processed model information to generate relevant files required by Abaqus at the start of the simulation. Abaqus doesn't support visualization and definitions of user elements, which necessitate post-processing software to obtain stress distribution around the cracks. In the current study, the output of each simulation was visualized using Paraview software (Paraview, 2019). The XFEM-based user element developed in this study is a modification of the one created by Cruz et al. (2019), which was developed for hydraulic fracturing in rocks under the assumption of LEFM. The modifications done in the current study include incorporating various CZMs and adding algorithms for cracking branching that facilitated the initiation and prorogation of different crack types in rocks.

The user-defined element was implemented using various external subroutines of Abaqus, with the subroutine named "UEL" being the most vital one. This subroutine was used to compute stiffness and forces matrices of each element in the problem domain which were then assembled by Abaqus/standard to form a global system of equations. The Abaqus/standard solves these nonlinear systems of equations in multiple increments. The size of an increment was decided automatically by Abaqus/standard solver to ensure convergence at the end of each increment. In each increment, a Newton-Raphson iterative scheme is used to solve the global system of equations which may require more than one iteration to achieve convergence. Since the user element developed in the current study is a modified version of algorithms written by Cruz et al. (2019), only a brief description of its implementation is presented here. The user-defined element consisted of three main procedures: a) Pre-processor, b) UEL subroutine, and c) Post-processor.

The overview of these procedures is summarized in Figure 5-11. The details of each of these procedures are described in the following sections.

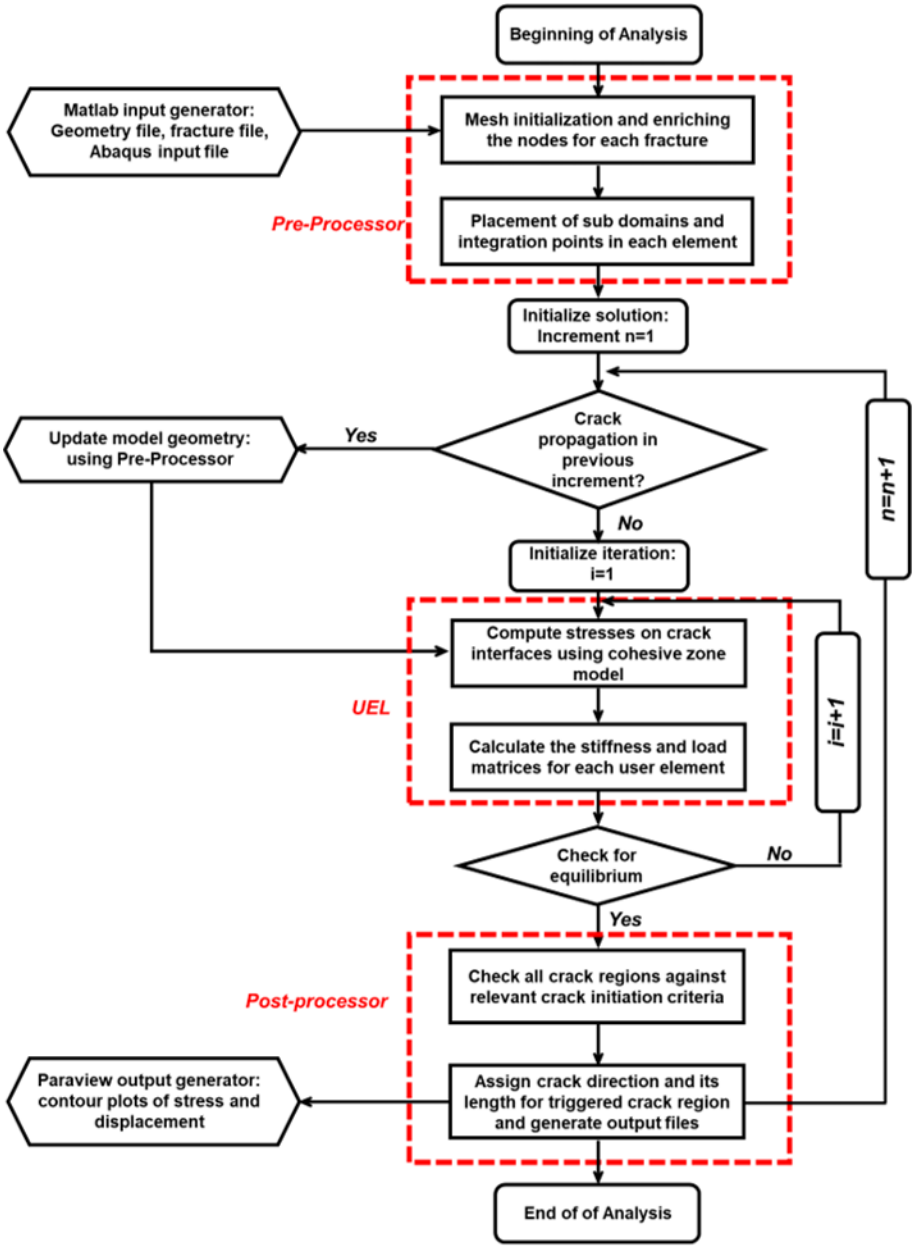

Figure 5-11 A brief overview of the general algorithms implemented in the XFEM model.

5.4.2 Pre-processor

The procedure named "Pre-processor" was implemented at the start of every new increment in the simulation to store enrichment information of each element in the modeled domain (Figure 5-11). This data is then used to compute the element stiffness matrices. The procedure involves storing the value of the enrichment function and the associated degrees of freedom for each node in the modeled domain. Additionally, for elements with multiple fractures, enrichment data for each fracture is stored in their corresponding nodes. Following the calculation of mesh enrichment data, the number of subdomains based on the methodology defined in section 5.3.4.3. was estimated for each element. This was followed by the placement of corresponding integration points in each subdomain. Furthermore, the computation of the location of different fractures allows the placement of integration points in each fracture segment based on the methodology defined in section 5.3.4.3. Therefore, information regarding integration points, such as their location and definitions of local weights, are stored for every element and fracture segment in the modeled domain. It is to be noted that no specific crack tip enrichment was used in the current study. The representation of the crack tip follows the deactivation of nodal enrichments that belong to the element's edge touching the tip. In some cases, this approach of crack tip propagation till the element's edge may impact crack tip velocity, which can be mitigated using fine mesh sizes (Song et al., 2006b). Therefore, mesh sensitivity analysis has been performed in various case studies considered in the current study.

5.4.3 UEL Subroutine

The procedure named "UEL" is a vital step in any FEM simulation as it defines the physical behavior of the governing equations through the element stiffness and forces matrices represented by Eqs 26-27. This procedure is implemented in every iteration of the Abaqus simulation for each element in the modeled domain (Figure 5-11).

The first step of the procedure is to acquire the enrichment information of a given element. Two domains are defined for the cracked element (consisting of one or more fractures): the continuous region and fracture segments. The procedure first loops over all the integration points in the continuous region. For each integration point, it computes the shape functions and their derivatives for both standard and enriched degrees of freedom. This is followed by the computation of stress and material stiffness matrices. After computing the shape function and other matrices in the continuous area, the procedure loops over all the integration points of fracture segments present in the given element. For each fracture integration point, the procedure involves the computation of enriched shape functions, their derivatives, and jump functions (N^{enr}, B^{enr} , and $[\![N^{enr}]\!]$, respectively). It allows the computation of crack traction and tangent stiffness matrices at each integration point.

Finally, all the computed integrals are then used to assemble the stiffness and load matrices of each element in the modeled domain. During the element stiffness matrix calculation, all the rows and columns related to deactivated degrees of freedom are zeroed. All this information is then used by Abaqus/standard to assemble global matrices and solve the nonlinear system of equation.

5.4.4 Post-processor

The procedure named "Post-processor" typically runs at the end of every converged increment to check for initiation of new branching cracks or propagation from the existing crack tip, as shown in Figure 5-11. In this procedure, the location of all possible regions from where crack initiation or propagation can occur is estimated in the first step. This is followed by checking for the condition of cracking in these regions using specific crack initiation criteria. In areas where the stress field triggers the crack initiation criterion, the direction and length of the new crack segments were determined.

The location of cracking regions is determined based on the methodology described in section 5.3.4.3, which covers all possible branching or crack tip propagation situations. In the current study, rectangular regions with the average size of element length were selected (see Figure 5-6a-b), ensuring no preference is given to branching or crack propagation from existing crack tips. The average stress field of each region was compared with the relevant crack initiation criterion. Additionally, in each region, the direction of the new crack segment was determined based on the triggered crack initiation criterion. Finally, the length of crack segments in each region is estimated such that the crack extends to the next element edge. In this research, different crack initiation criteria were adopted in various case studies, and thus relevant criteria will be discussed in the section of each example.

5.4.5 Configuration of User-element and its Limitations

This study implemented the XFEM formulation using 4-noded quadrilateral elements with linear segments under plane strain conditions (Figure 5-9a-c). Each node has 27 degrees of

freedom to store both the standard and enrichened part of the displacement field. For this purpose, the solution procedure named "coupled thermo-mechanical analysis" was used in Abaqus as it provides maximum degrees of freedom per node as opposed to the "static procedure" which only has 6 degrees of freedom per node. In the original user-element by Cruz et al. (2019), various DOFs were assigned to simulate enhanced porous medium and fracture fluid flow. However, in the current study's modified version of the user-defined element, all DOFs were used for enrichening elements with multiple crack interactions. This facilitates more flexibility in the user element by accommodating various fracture intersection and branching scenarios.

Despite the versatility of commercial software, Abaqus has some inherent limitations in implementing the user-defined element, such as no modification of stiffness and load matrices of global assembly is allowed. This prevents adding certain improvements in XFEM, such as preconditioning of stiffness matrix, which minimizes matrix ill-conditioning and allows a faster rate of convergence, especially in cases of multiple crack interactions (Menk and Bordas, 2011; Siavelis et al., 2013).

The lack of a visualization interface for the input and output of user elements is another limitation of Abaqus, which has been mitigated by using additional software in the current study. Additionally, XFEM-based user elements in Abaqus require higher computational time and large memory consumption, which can be attributed to all DOFs being assigned at the beginning of the simulation. As Abaqus doesn't allow adding new DOFs during run time, enrichment corresponding to all possible scenarios, resulting in 27 DOFs per node, must be allocated first.

These DOFs are deactivated by assigning zero to all matrix coefficients related to all future enriched elements.

5.5 Results and Discussion

5.5.1 Crack under Mode I Loading

The first test case used in this study demonstrates the capability of the XFEM-based user element in predicting mode I fracture propagation in a concrete beam under the three-point bending test. The propagation of mode I crack in various quasi-brittle materials such as concrete and rocks has been extensively studied (Song et al., 2005; Hyeok et al., 2006; Zamani et al., 2012; Garg et al., 2020). Under pure I mode loading, the fracture typically propagates vertically at the beam's mid-span from its bottom surface to the top (Figure 5-12b). Figure 5-12a presents the dimensions of the concrete specimen modeled in the current study, along with applied boundary conditions. The concrete specimen was loaded under a displacement-controlled mode, as shown in Figure 5-12a. The material properties used for modeled concrete specimen were based on the study by Xiao et al. (2003), having Young's modulus (E) = 36.5 GPa, Poisson's ratio (ν) = 0.1, tensile strength (σ_t) =3.19 MPa and mode I fracture energy (G_{IC}) = 50 N/m. The initiation of mode I cohesive cracks was predicted based on the Maximum Principal Stress (MPS) criterion, which assumes crack formation in the direction perpendicular to the maximum principal stress. The material softening was modeled using the exponential cohesive zone model for predicting tensile crack propagation (section 5.3.2). The concrete specimen was modeled under plane strain conditions using uniform-size square elements. A mesh convergence analysis was performed by varying elements size from 5 mm to 1 mm.

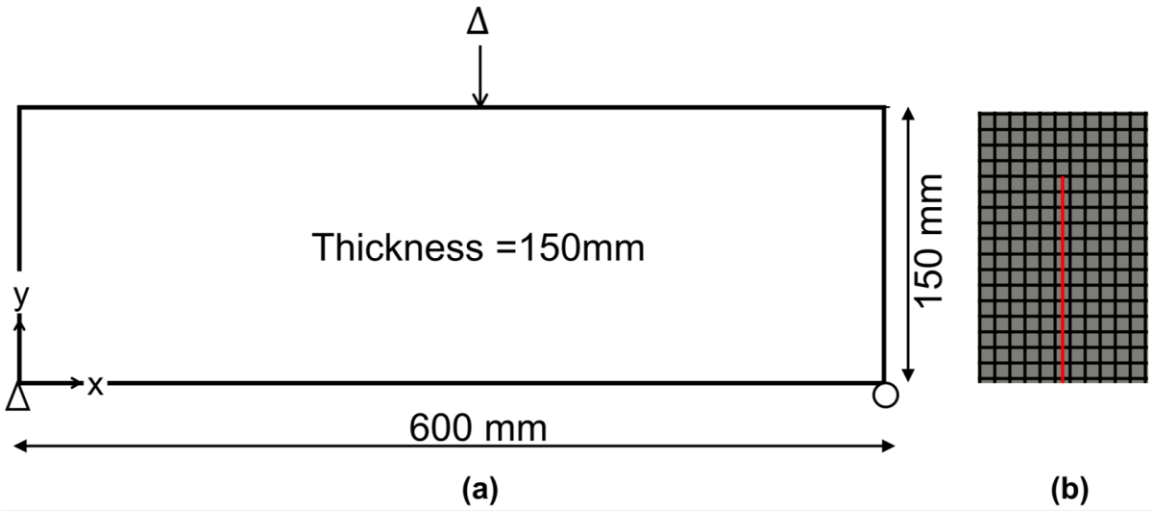

Figure 5-12 Three-point bending beam: (a) geometry and boundary conditions; (b) crack path obtained (represented by a red line).

Figure 5-13a presents the load-deflection curve obtained from the current XFEM-based user model at various mesh sizes. It can be concluded that convergence is obtained in the XFEM-based user model for elements size less than 2 mm, as evident by a similar behavior obtained in both pre-peak and post-peak regimes. Additionally, compared with the results of the numerical study by Zamani et al. (2012), good agreement is obtained in terms of the load-deflection curve except for small differences in post-peak behavior (Figure 5-13a). The difference in post-peak behavior can be attributed to the application of crack tip enrichment and linear softening model in the numerical study by Zamani et al. (2012). The mesh sensitivity analysis was also performed in terms of crack opening displacement profiles obtained at the deflection of 0.075 mm (Figure 5-13b). Similar to the load-deflection curve, elements size less than 2 mm provided convergent opening displacement profiles.

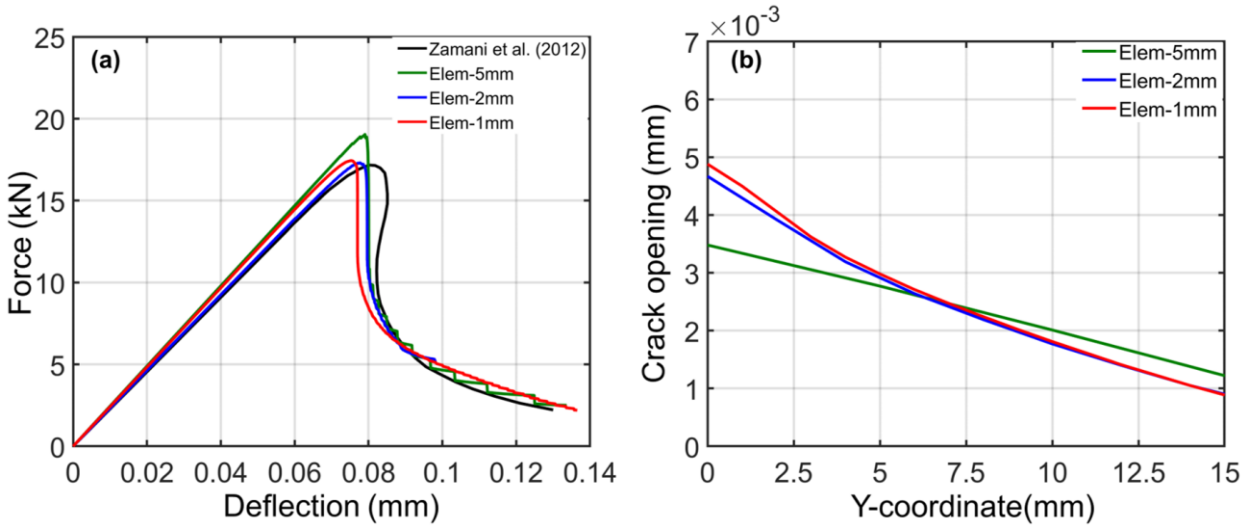

Figure 5-13 Mesh sensitivity analysis in three-point bending of the concrete beam (a) force-deflection curves; (b) crack opening profiles at deflection of 0.075 mm.

5.5.2 Crack under Mixed-mode I/II Loading

The section presents the application of the XFEM-based user element in modeling mixed-mode I/II fracture propagation in a quasi-brittle material. For this purpose, the double-edge notched testing configuration was used to apply tensile and shear loading to the specimen. This geometry was used to characterize mixed-mode I/II crack propagation in mortar specimens by Nooru-Mohamed (1992) at different levels of shear loading. The simulated mortar specimen had the following elastic parameters: Young's modulus (E) = 30 GPa, and Poisson's ratio (ν) = 0.2. The fracture parameters such as tensile strength (σ_t) =2.3 MPa and mode I fracture energy (G_{IC}) = 80 N/m were selected from the work of Wang and Waisman (2018). Figure 14 illustrates the model geometry of double-edge notched specimens with applied boundary conditions. To simulate mixed-mode I/II loading on the double-edge notched specimen, the desired level of shear force (F_s) was first applied along the specimen's upper left and lower right sides (Figure 5-14). This was followed by displacement-controlled tensile loading applied at the upper and

bottom surfaces of the specimen while keeping shear force (F_s) constant (Figure 5-14). The double-edge notched specimens were simulated under plane strain conditions with a uniform square mesh of 1 mm side length. The element size of 1 mm is deemed to provide mesh-independent analysis, as shown by sensitivity analysis performed in the case of the three-point bending test with similar fracture properties (section 5.5.1). The fractures obtained in double-edge notched specimens are typically dominated by a mode I initiation (Meschke and Dumstorff, 2007), and thus crack initiation was predicted using on MPS criterion. Similar to the first case, the material softening behavior was simulated using the exponential cohesive zone model for tensile crack initiation (section 5.3.2).

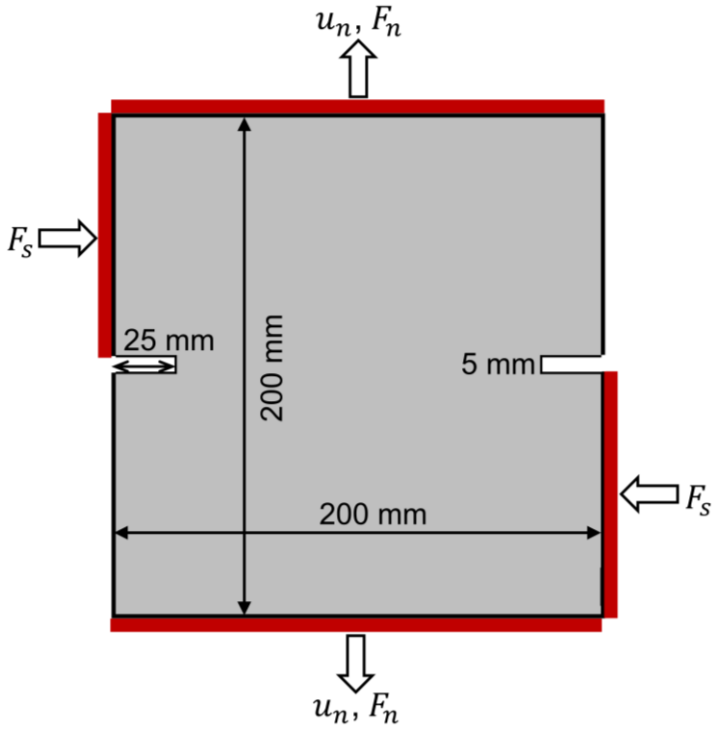

Figure 5-14 Double-edge notched (DEN) geometry with applied boundary conditions.

Figures 5-15a-d compares results obtained from the XFEM-based user model and experimental observations of double-edge notched specimens for two levels of shear force (F_s = 5 kN and 10kN). It is clear from Figure 5-15a-b that both the force (F_n) -displacement (u_n) curve and overall crack path for the case double-edge notched specimen with shear force (F_s) of 5 kN showing a reasonable level of agreement with experimental data despite the uncertainty associated with mortar specimens due to material heterogeneity. A similar agreement was found in the second case of the double-edge notched specimen with shear force (F_s) of 10 kN (Figure 5-15c-d).

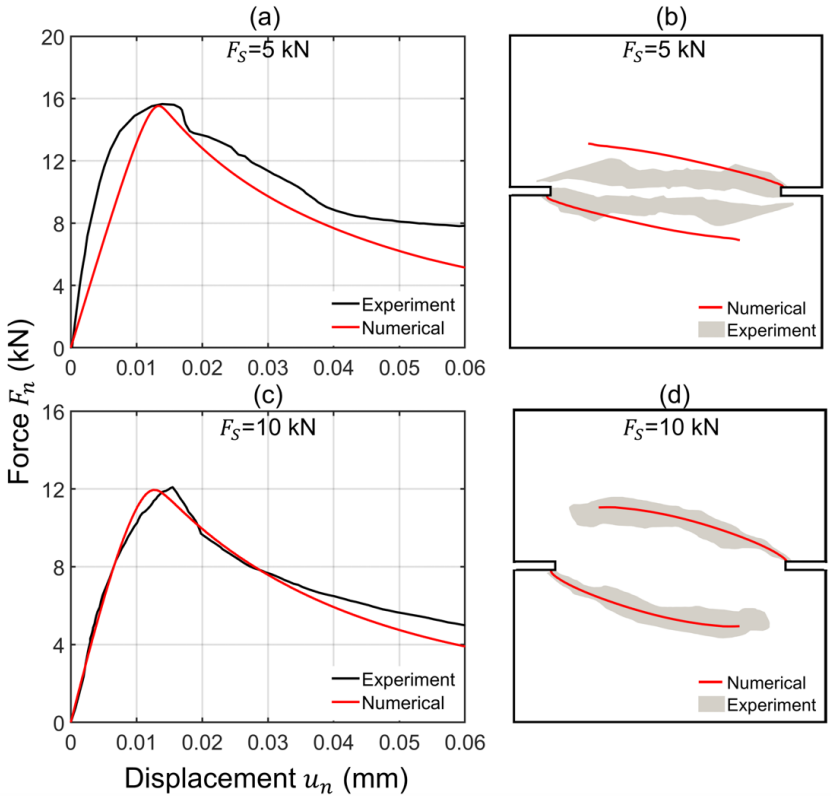

Figure 5-15 Results of double-edge notched beam specimens in terms of force (F_n) versus displacement (u_n) curves along with crack profile at (a) and (b) F_s =5kN; (c) and (d) F_s =10kN. Experimental data from Nooru-Mohamed (1992).

5.5.3 Mode II Crack

The section presents the application of the XFEM-based user element in simulating compression-induced mode II cracks in a quasi-brittle material. For this purpose, a benchmark case of shear cracking in overconsolidated clay subjected to compression loading was selected based on the study by Gill. (2021). The simulated consolidated clay is a relatively weaker material with Young's modulus (E) = 36.5 GPa, Poisson's ratio (ν) = 0.3, cohesion (t_c^{max}) =40 kPa, friction angle (ϕ) =15º, and mode II fracture energy (G_{IIC}) = 30 N/m. In this study, a prismatic specimen of overconsolidated clay was subjected to uniaxial compression loading as shown in Figure 5-16. Additionally, a small square opening of edge length 2 mm was introduced at the specimen's center, ensuring a fixed crack initiation location irrespective of the element size. As explained in section 5.3.4.3, crack initiation is determined based on the average elemental stress. This approach in the current case study might lead to multiple cracking locations, and thus induction of small opening results in a mesh-independent location of crack initiation. Due to a similar reason, the numerical study by Gill. (2021) also created a circular opening in the simulated clay specimen. The difference in the shape of the created opening was attributed to the limitation of the current XFEM-based user model, which only allowed the formation of the structured mesh. Despite this difference, the overall material behavior between the two studies should be similar due to the small opening size compared to the specimen dimension (Figure 5-16). The shear crack initiation was determined using the MC criterion, while the material softening was simulated using an exponential cohesive zone model for shear crack under compression (section 5.3.3). For proper comparison with the numerical study by Gill (2021), the formation of a single shear plane in the clay specimen was allowed. It is important to

note that the developed XFEM-based user model can easily allow the propagation of dual shear failure expected in clay specimens under compression loading. Additionally, two different mesh sizes of 1 mm and 0.5 mm were modeled for each case to ensure mesh-independent shear crack propagation.

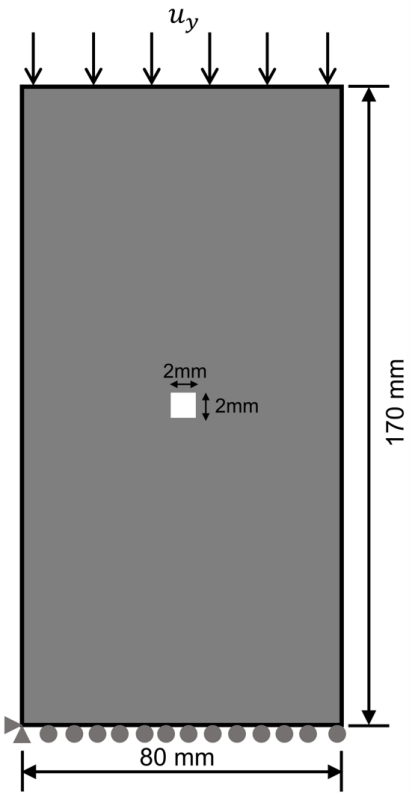

Figure 5-16 Schematic of the compression test on prismatic specimens of overconsolidated clay with a small rectangular opening.

Figure 5-17a indicates a good agreement between the current XFEM model and the numerical study of Gill (2021) for the clay specimen under uniaxial compression loading, as evidenced by similar force-displacement plots with some minor differences in post-peak behavior. This can be attributed to the non-local damage model used in the numerical study by

Gill (2021), which calculated the material softening as a function of strain/displacement averaged across a width of 3-5 elements. In contrast, the material softening in the current XFEM model only relied on crack displacement inside the element that underwent crack initiation. A mesh-independent shear crack propagation is observed as evident by nearly identical overall global behavior of the clay specimen for two element sizes of 1mm and 0.5 mm (Figure 5-17a).

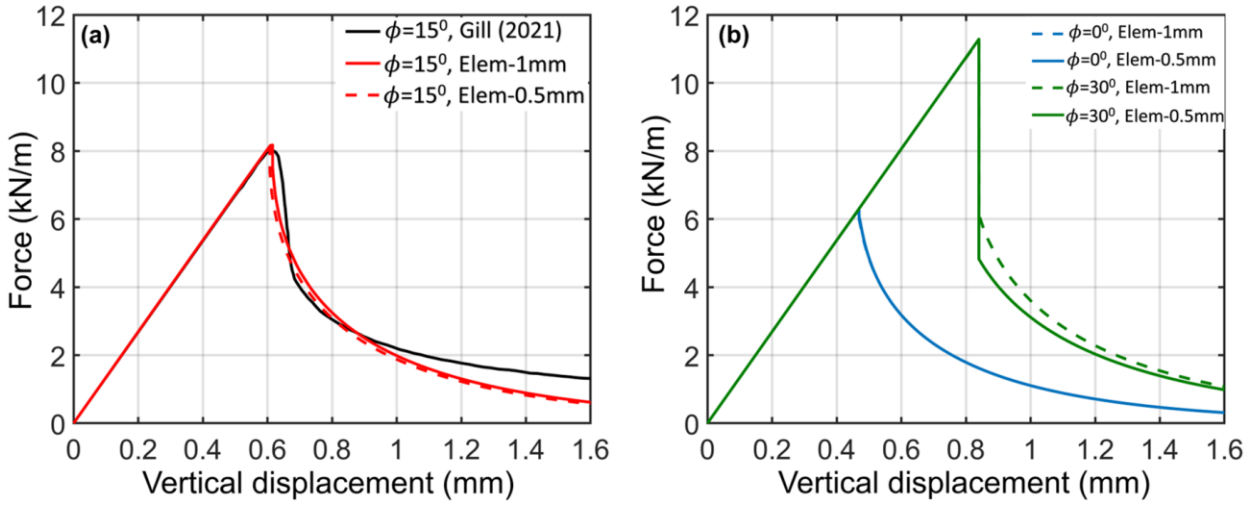

Figure 5-17 Results of the uniaxial compression tests on clays specimens in terms of force-displacement curves at various friction angles (a) ϕ = 0º; (b) ϕ = 15º and 30º.

In the current study, a total of three cases of clay's friction angle (ϕ = 0º, 15º, 30º) were simulated under uniaxial compression loading to assess the ability of the XFEM-based user model to incorporate frictional cracks. The shear plane formed is oriented at the expected failure angle $\theta_f = 45 + \frac{\phi}{2}$ from the horizontal axis in all three cases of clay's friction angle (ϕ = 0º, 15º, 30º) as shown in the angle insets of Figure 5-18a-c. Furthermore, the overall global behavior of the clay specimens in all three cases of clay's friction angle (ϕ = 0º, 15º, 30º) is almost mesh-independent (Figure 5-17a-b).

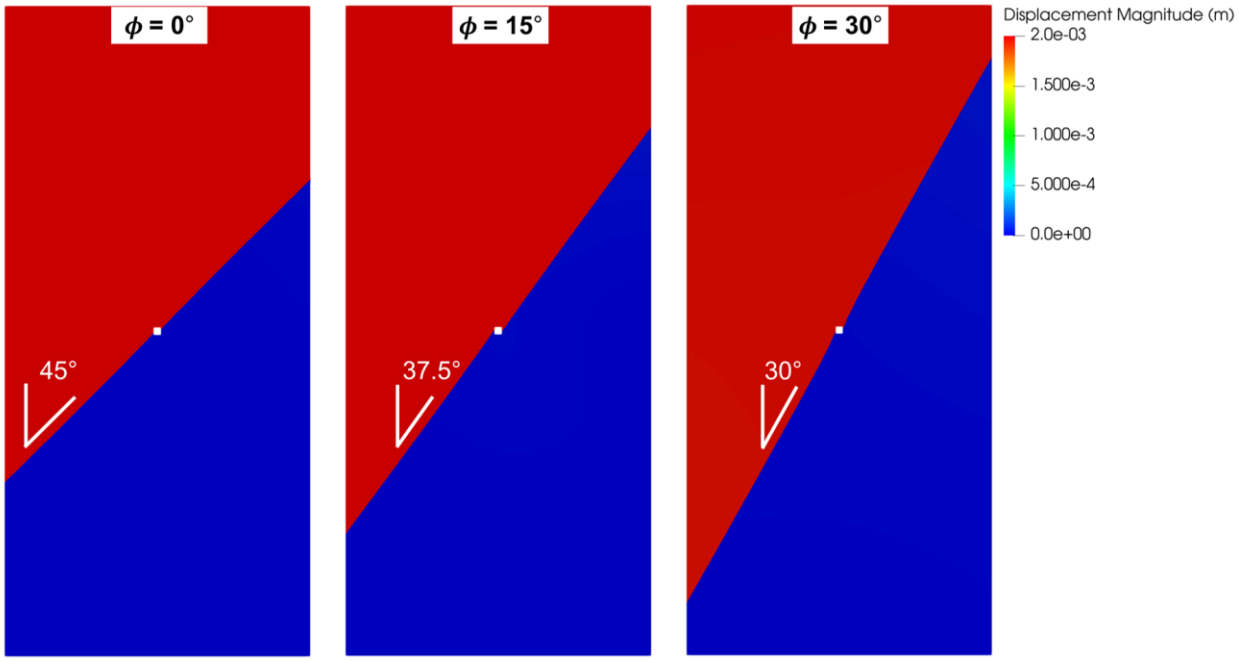

Figure 5-18 Displacement magnitude in uniaxial compression tests of clays specimen for (a) ϕ = 0º; (b) ϕ = 15º; (c) ϕ =30º.

5.5.4 Crack Branching in Uniaxial Compression Loading

The section presents the application of the XFEM-based user element in simulating various crack types formed in quasi-brittle material under compressive loading. The benchmark case of a gypsum specimen containing one inclined pre-existing flaw under uniaxial compression was modeled in this study, as shown in Figure 5-19a. The material and fracture properties of the gypsum specimen used in this study are shown in Figure 5-19a. The elastic and strength parameters were obtained from various experimental studies (Bobet and Einstein 1998; Wei et al. 2020) on gypsum specimens, while fracture energies (G_{IC} and G_{IIC}) were selected based on the study by Fei and Choo (2021). This study primarily focuses on a qualitative comparison of fracture path; thus, no calibration of material parameters was performed. Two orientations of a single flaw from the horizontal axis, i.e., β_w =45º and 60º were simulated (Figure 5-19a). The

open flaw with a length of 12.7 mm was modeled using a line crack with frictionless surfaces (Figure 5-19a). The contact model for the flaw is based on the penalty method, which only requires high normal stiffness (k_p) to avoid closure between two surfaces of the flaw. To simulate actual laboratory testing conditions, displacement-controlled loading at the rate of 1 mm/step (1 step =1sec) was applied at the specimen's top surface while fixing its bottom surface (Figure 5-19a). The model was discretized using a uniform mesh with an edge length of 0.8 mm under plane strain conditions. Various criteria are used in this case study to predict the initiation of different crack types. The tensile crack was predicted based on the MPS criterion in conjunction with an exponential cohesive zone model for tensile crack propagation (section 5.3.2). The shear crack initiation was determined using the Maximum Shear stress (MSS) criterion, which results in crack initiation in the plane of maximum shear stress, thereby ignoring the effect of material friction angle (ϕ). The selection of the MSS criterion for the gypsum specimen is based on the study by Gonçalves Da Silva and Einstein (2013), which showed this criterion to be most suitable for predicting the propagation of coplanar shear cracks. Gonçalves Da Silva and Einstein (2013), based on the simulation of crack propagation in various configurations of single and multiple flaws in gypsum specimens, concluded that friction angle-based criteria, such as the MC criterion, results in odd shear crack propagation inconsistent with experimental data. Thus, the material softening under shear crack development was simulated using a cohesive zone model with zero friction angle (ϕ = 0º) (section 5.3.3).

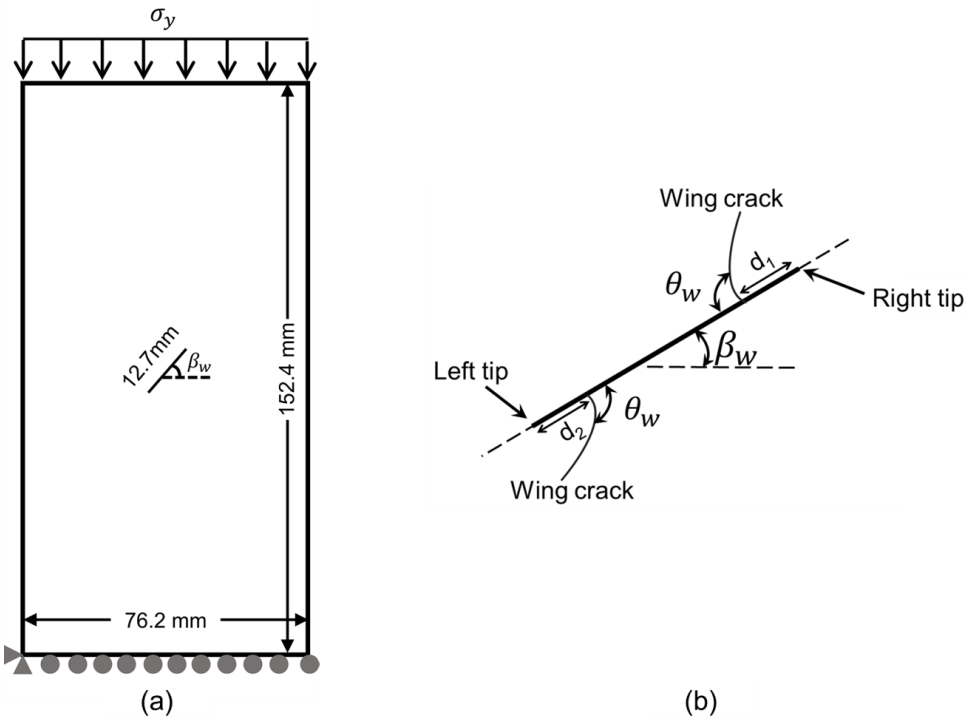

Figure 5-19 (a) Schematic of the uniaxial compression loading on gypsum specimens containing one flaw test with boundary conditions; (b) Representation of the wing crack initiation in gypsum specimen (after Wong, 2008).

Table 5-1 Material parameters of gypsum specimens (Bobet and Einstein 1998; Wei et al. 2020).

Parameter	**Value**
Young's modulus (E) (GPa)	5.6
Poisson's ratio (ν)	0.16
Tensile strength (σ_t) (MPa)	3.2
Cohesion strength (t_C^{max}) (MPa)	10.7
Friction angle (ϕ)	28º
Mode I fracture energy (G_{IC}) (N/m)	16
Mode II fracture energy (G_{IIC}) (N/m)	205

Figures 5-20a-d compare crack patterns obtained using the XFEM model with the one from the experimental results of Wong (2008) in the gypsum specimen with a single flaw oriented at β_w=45º. In the initial loading stages, two tensile wing cracks initiated first, as shown at applied

vertical stress (σ_y) of 4.5 MPa (Figure 5-20a). The application of the crack branching algorithm resulted in tensile wing cracks being initiated at a certain distance from the flaw tips (inset of Figure 5-20a), which is consistent with the observation of experimental studies (Wong, 2008; Zhang and Wong, 2012). The position of tensile cracks at distances d_1 and d_2 from flaw tips, along with the wing crack initiation angle (θ_w) (Figure 5-19b) in the XFEM model were in reasonable agreement with the experimental observation of Wong (2008), as shown in Table 5-2. With further loading, coplanar shear cracks formed at two flaw tips, as shown at the applied vertical stress (σ_y) of 13 MPa (inset of Figure 5-20b). These cracks are typically known as secondary cracks and were consistent with observations of various experimental studies (Bobet and Einstein, 1998a; Wong, 2008) on single flawed gypsum specimens. These coplanar shear cracks eventually transitioned to tensile cracks resulting in the formation of mix-mode secondary fractures at the applied vertical stress (σ_y) of 15 MPa (Figures 5-20c). Additionally, the overall cracking pattern, including the path of various crack types in the XFEM model, was similar to experimental observations (Figures 5-20c-d).

Similarly, in the case of the gypsum specimen with flaw oriented at β_w=60º, characteristics of tensile wing cracks such as its initiation angle (θ_w) and offset distances (d_1 and d_2) from two flaw tips from the XFEM model were within the range of experimental results (Table 5-2). Additionally, the crack initiation stress of wing cracks in case of flaw inclination (β_w) of 60º was around 1.9 times the value obtained in the gypsum specimen with the flaw inclination (β_w) of 45º (Table 2). This increase in crack initiation stress with an increase in flaw inclination (β_w) from 45º and 60º is consistent with the experimental observation of Wong

(2008) on the same gypsum specimens (Table 5-2). With increased loading, secondary shear cracks formed at two flaw tips which subsequently transitioned to tensile fractures (Figures 5-21b-c). The comparison with experimental observation again showed similar crack patterns in the XFEM model (Figures 5-21c-d). Therefore, it can be concluded that the XFEM model can reasonably be used to replicate real cracking in single-flaw gypsum specimens under uniaxial compression loading.

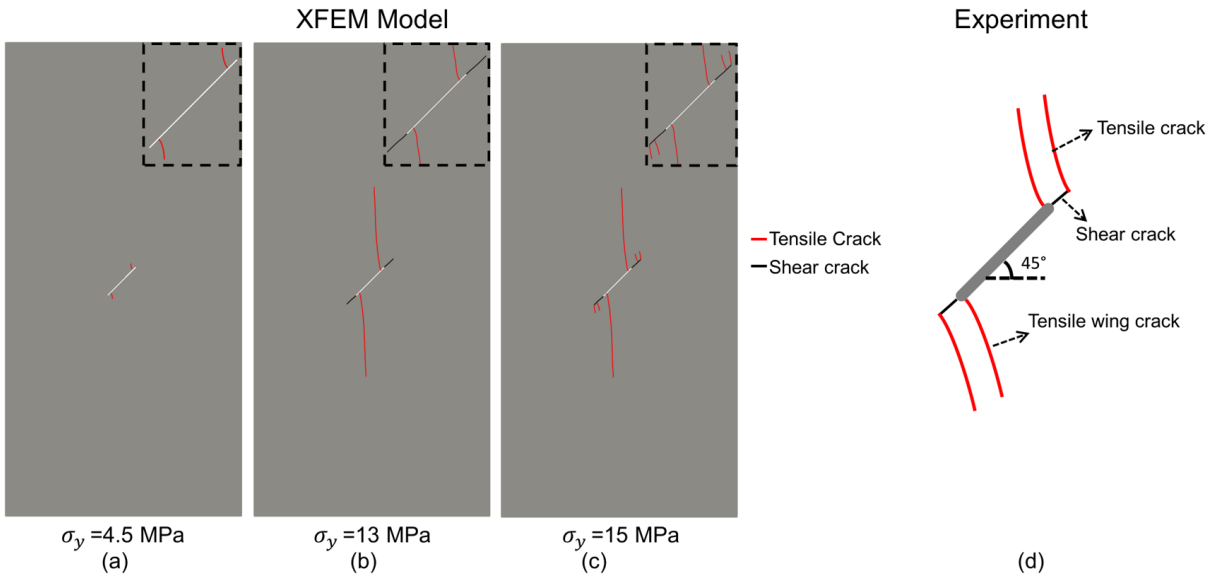

Figure 5-20 Comparison of crack patterns in oriented single flaw (β_w=45º) gypsum specimen between (a-c) XFEM model and (d) experiment. The tensile stress is assumed to be negative in the study. The inset in a-c presents the zoom-in view of crack patterns around the flaw. The crack patterns for experimental data were redrawn from Wong (2008).

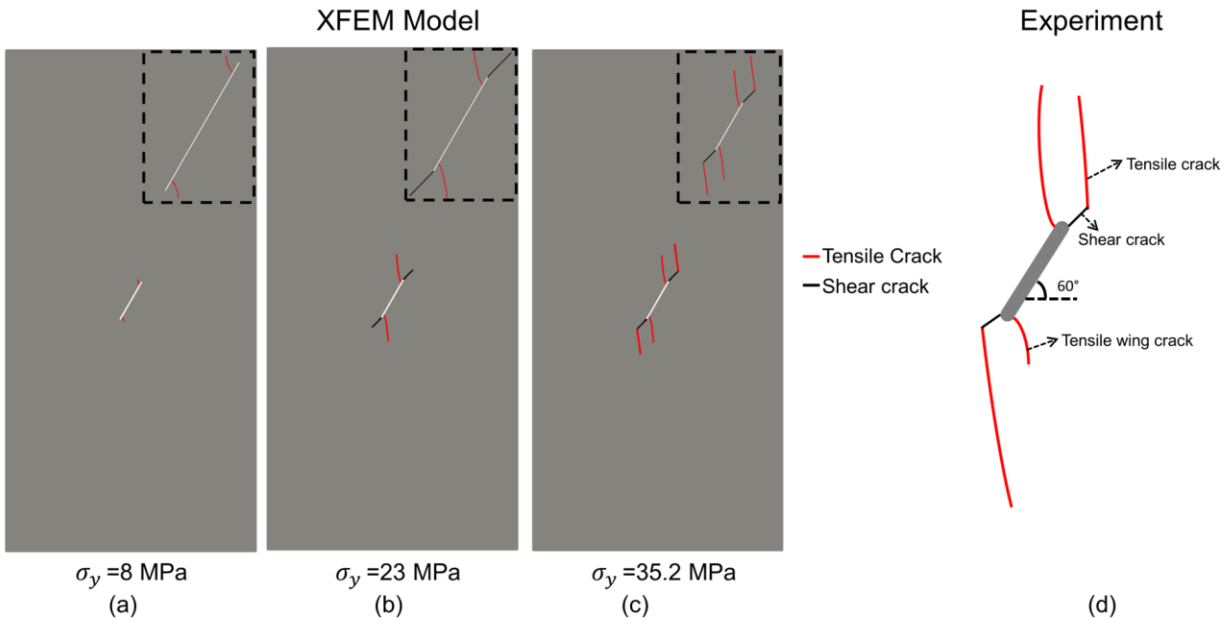

Figure 5-21 Comparison of crack patterns in oriented single flaw (β_w= 60º) gypsum specimen between (a-c) XFEM model and (d) experiment. The inset in a-c presents the zoom-in view of crack patterns around the flaw. The crack patterns for experimental data were redrawn from Wong (2008).

Table 5-2 Comparison of XFEM model with experimental data (from Wong, 2008) of oriented single flaw gypsum specimen.

Flaw inclination Angle (β_w)	**Wing crack initiation angle (θ_w)**		**Wing crack initiation stress (σ_y) (MPa)**		**Distance of wing cracks from flaw tips (d_1, d_2) (mm)**	
	XFEM model	Experiment	XFEM model	Experiment	XFEM model	Experiment
45^0	89^0	85^0	4	25	1.13, 1.15	0.5-2.5
60^0	114^0	110^0	7.6	27	1.11,1.12	0.7-2.2

5.6 Conclusions

This study presented a novel XFEM-based user element in Abaqus with a novel capability of simulating crack branching in quasi-brittle materials. The implemented user element is a modification of code developed initially by Cruz et al. (2019). The original user element by Cruz et al. (2019) only simulated LEFM-based cracking in rocks with limited capabilities of crack interactions. For instance, only crack interactions between hydraulic or natural fractures were modeled, and no crack branching capabilities existed in the original user element by Cruz et al. (2019). The user element modified in this study accounts for FPZ development in different crack types through CZMs that simulates material softening inside the FPZ. Additionally, a novel crack branching methodology was implemented, which facilitated the formation of multiple crack types from pre-existing cracks in the model. The main benefits of the XFEM-based user element were presented along with its inherent limitations. The applicability of the new XFEM model was assessed through various case studies. The findings of the study are summarized as follows:

- Two benchmark cases of mode I and mixed-mode I/II cracking were analyzed to demonstrate the effectiveness of the XFEM-based user element in predicting the FPZ development under tensile loading. The results showed the XFEM model could provide reasonable agreement with other numerical studies /experimental data.
- The capability of the XFEM-based user element in simulating compression-induced mode II cracks was assessed using compression loading of overconsolidated clay specimens. The analysis showed that the XFEM model could predict both the shear crack path and global behaviors of the specimen with reasonable accuracy. Additionally, the simulation of different

cases of specimen's friction angle (ϕ) confirmed the ability of the XFEM model to simulate normal stress-dependent behavior of peak and residual strength of shear cracks.

- The last case study involved uniaxial compression loading of a single flawed gypsum specimen with two flaw inclinations (β_w= 45º, 60º) to assess the applicability of implemented novel crack branching methodology. The analysis showed that the crack branching methodology accurately predicted tensile wing cracks in terms of its location and initiation angle, which may otherwise need enrichment for crack tip singularity in traditional XFEM models. Additionally, the XFEM-based user element was able to predict the formation of both primary and secondary cracks and thus is able to reasonably replicate real cracking patterns.

5.7 Acknowledgement

Funding for this research was provided by the National Science Foundation under Award number 1644326. The authors are grateful for this support.

CHAPTER 6

APPLICATION OF XFEM-BASED USER ELEMENT FOR PREDICTING SECONDARY CRACKS

This chapter is submitted for publication in the International Journal of Rock Mechanics and Mining Science (Garg et al., 2023).

Prasoon Garg[5], Ahmadreza Hedayat[5], D.V. Griffiths[5]

6.1 Abstract

Fracturing in rocks and rock-like materials under compressive loading often involves a wide variety of crack patterns where tensile (mode I) and shear (mode II) fractures are often interwoven. These fractures are usually cohesive (significant size of the micro-cracking zone) and involve frictional sliding during their propagation. Although the eXtended Finite Element Method (XFEM) has been increasingly used for rock fracture modeling, it still lacks the capability to predict mode II and mixed-mode I/II fractures, which often involve complex crack interactions. To address this challenge, this study used a novel XFEM-based user element with the capability to simulate fracture intersections and crack branching for quasi-brittle materials. The study aims to assess the applicability of this XFEM-based user element in predicting overall crack patterns observed in rock-like material under compressive loading, along with quantifying the influence of crack initiation criteria. Additionally, the XFEM-based user element was

[5] Colorado School of Mines, Civil and Environmental Engineering

implemented with cohesive zone models, which defined the constitutive behavior of inelastic material (micro-cracking zone) around the crack tip.

6.2 Introduction

Rock materials' deformation and cracking behavior are of great interest in geomechanics and rock engineering. As rock contains initial defects, such as fissures, and micro-cracks, under external loads, new cracks may initiate and propagate along these defects, and crack coalescence can lead to rock bridge fracture and its subsequent failure. Many experimental studies have investigated the fracture processes of various rocks and rock-like materials such as molded gypsum, granite, sandstone, and marble under compressive loading (Bobet and Einstein, 1998a; Wong, 2008; Yang et al., (2009, 2012); Morgan et al., 2013). The cracks in studies were mostly classified based on the temporal relationships, i.e., primary, and secondary cracks. The first cracks initiated from the flaw tips are called primary cracks, while the rest are classified as secondary cracks, mainly responsible for the overall failure of most rock specimens (Wong and Einstein, 2009). The primary cracks are generally identified as tensile cracks, which tend to propagate in a stable manner (i.e., further propagation of these cracks requires the application of additional load) toward the direction of maximum compression (Park and Bobet, 2009). In comparison, the secondary cracks typically comprise different shear crack patterns, such as coplanar, oblique, and out-of-plane (Bobet, 1997; Cheng et al., 2016). In most rocks, these secondary cracks often involve complex combinations of tensile (mode I) and shear (mode II) fractures, such as horsetail cracks and anti-wings, mixed tensile–shear cracks (Wong and Einstein, 2009; Morgan et al., 2013; Wong and Li, 2011; Lee and Jeon, 2011) as shown Figure 6-1. The central observation of these experimental studies is the formation of multiple fractures

emanating from a pre-existing crack, which can be called crack branching based on the theory of fracture mechanics (Fatehi Marji, 2014; Chen and Zhou, 2020). The proper predictions of these secondary cracks, especially complex crack branching mechanisms, are vital to accurately simulate rock cracking processes, which, unfortunately, a few computational models can accomplish (Li and Wong, 2012; Wong and Li, 2013).

Over the past years, several crack initiation and propagation criteria have been proposed and implemented using various analytical and numerical methods for various rocks and rock-like materials. These criteria were typically divided into three families: (a) stress-based criteria (Khan and Khraisheh, 2000), (b) energy-based criteria (Hussain et al., 1974; Sih, 1974), and (c) strain-based criteria (Gonçalves and Einstein, 2013) as summarized in Table 6-1. Based on their applicability to crack growth in rocks, these criteria can also be grouped into different classes: fracture toughness-based, T-term-based, full-field distribution-based, and Non-linear Elastic Fracture Mechanics (NLFM) based criteria (see the last column of Table 6-1). The fracture toughness-based and T-term -based criteria belong to the category where crack initiation is defined based on a single parameter, such as fracture toughness or critical energy release rate (Wong, 2008). As a result, these fracture criteria can only predict primary cracks in rocks under compressive loading (Ingraffea, 1980; Bobet, 1997). The full-field-based criteria, such as Bobet's stress-based criterion (Bobet, 1997) and the strain-based criterion by Gonçalves and Einstein (2013), have been the most successful in predicting both primary and secondary cracks in rocks under compressive loading. The advantage of these full-field-based criteria lies in the fact that the entire stress field around the crack tip is used to determine the crack initiation, which allows for the prediction of both tensile and shear cracks separately (Wong, 2008; Gonçalves and

Einstein, 2013). However, most of the aforementioned crack initiation criteria are, based on linear elastic fracture mechanics (LEFM) theory that assumes small-scale yielding, i.e., the small size of the inelastic region (also known as FPZ) around the crack tip, and thus elastic deformation of rock is approximated for crack propagation (Gonçalves, 2009). This assumption contrasts with the observation of experimental studies (Labuz et al., 1987; Lin et al., 2019a-b; Zhao et al., 2016; Zhao et al., 2018) that have found the significant size of the FPZ around the crack tip in various laboratory-scale rocks. Alternatively, the nonlinear fracture mechanics-based criterion, such as the cohesive zone model (CZM), has been extensively used in characterizing the complex micro-cracking process inside the FPZ of rocks (Yao et al., 2012; Rinehart et al., 2015; Xie et al., (2016, 2017)). Most of the CZM-based numerical models also require additional LEFM-based criteria to predict the initiation angle and path of the fracture, while CZM simulates the material softening the FPZ of the rocks. Thus, it is essential to use suitable LEFM crack initiation criteria in conjunction with CZM to predict various secondary cracks obtained in rocks accurately. Numerical modeling provides valuable insight into the mechanism of cracking processes, especially in cases of complex geometry or loading conditions, which are difficult to test in the laboratory. Additionally, it has several advantages over theoretical and analytical studies, which are most successful when the failure occurs by the propagation of a single crack. Several numerical models have emerged as valuable tools to simulate the cracking process of rocks, such as the gradient-enhanced damage model (Perling et al., 1996,1998), the Boundary Element (BE) method based FROCK (Bobet and Einstein, 1998b; Goncalves and Einstein, 2013), numerical manifold method (Wu and Wong, 2012; Yang and Tang, 2016), discrete element method (DEM) (Kazerani and Zhao, 2010; Gao et al., 2016; Saadat, 2019), and the

extended finite element method (XFEM) (Well and Sullys, 2001; Karihaloo and Xiao, 2003). In particular, the XFEM has attracted considerable attention due to its effectiveness in modeling discontinuities of multiple fracture interactions in the same domain (Daux et al., 2000; Moës and Belytschko, 2002; Zi and Belytschko, 2003) and material softening inside FPZ using CZM (Liu and Borja, 2009; Xie et al., 2017). The XFEM-based models have been increasingly used in various crack problems in rocks, such as multiple crack interaction during hydraulic fracturing (Youn, 2016; Cruz et al., 2019; Yang et al., 2019) and crack propagation from open or closed pre-existing flaws in rocks (Sharafisafa and Nazem, 2014; Zhuang et al., 2014). Despite the increased application of the XFEM-based numerical model, it suffers some inherent limitations, which decrease its applicability in simulating various fracture patterns obtained in rocks under compressive loading. For instance, traditional XFEM models lack the capability to simulate crack branching, which requires a reliable branching criterion to estimate the bifurcation point, defined as a point where the single crack tip results in the formation of two cracks (Rabczuk, 2013; Sun et al., 2021). Most of the current XFEM studies are limited to modeling crack coalescence/intersection involving two or more cracks interacting with each other. As a result, these studies can only predict primary cracks in rocks that initiate under the tensile mode, as shown by studies of Sharafisafa and Nazem (2014) and Zhuang et al. (2014). Additionally, existing XFEM-based numerical models rarely investigate compression-induced shear fractures (Liu and Borja, 2008; Sanborn and Prévost, 2011), which can be attributed to the lack of reliable softening model which accounts for both cohesion degradation and frictional sliding in propagating fracture

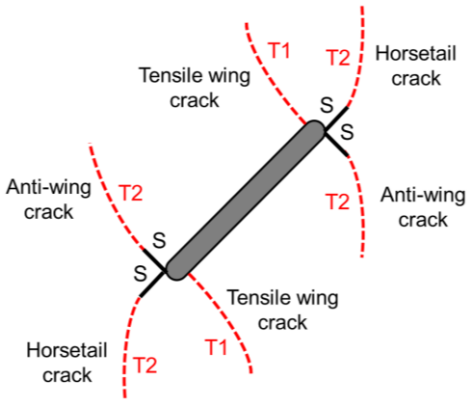

Figure 6-1 Schematic of various crack types (T1 and T2 denote tensile crack segments, S represents shear crack segment) observed in rocks and rock-like specimens containing single flaws subjected to uniaxial compressive loads (modified from Li and Wong, 2014).

To overcome these limitations, the current study used an XFEM-based user element developed by the authors (Section 5.3) and implemented in the commercial software Abaqus. The XFEM-based user elements incorporated a novel branching methodology that allows the simulation of complex crack interactions along with branching in rocks, thereby facilitating the formation of multiple crack types originating from the body of pre-existing flaws. Additionally, the influence of FPZ in the compression-induced shear crack was accounted for using a cohesive zone model capable of simulating frictional energy dissipation during the propagation of the shear crack (section 5.3.3). This study aims to assess the capability of XFEM-based user elements in modeling various types of secondary cracks in single and double-flaw gypsum specimens under compressive loading. Three configurations of single and double-flaw gypsum specimens were simulated and compared with experimental results to assess the applicability of XFEM-based user elements in predicting various crack types. Additionally, two crack initiation criteria, namely (a) Maximum shear stress (MSS) criterion and (b) Traction-based mixed-mode (TMM) criterion, were tried to assess their influence on the overall path of secondary cracks.

Both criteria have been actively used to predict the initiation angle of shear or mixed-mode I/II cracks in rocks and rock-like materials, albeit in different variations (Sweeryn and Mroz, 1995; Bobet and Einstein, 1998; Dobroskok et al., 2005; Wang et al., 2020).

Table 6-1 Summary of crack initiation criteria widely used in rocks (after Wong, 2008; Liu et al., 2018).

Energy-based	**Stress-based**	**Strain-based**	**Group**
Max strain energy release rate (Hussain et al., 1974)	Max tangential stress (MTS) (Erdogan and Sih, 1963)	Max tensile principal strain (Reyes, 1991) criteria	Fracture toughness-based (LEFM)
Min strain energy density (Palaniswamy, 1972)	Improved MTS (IMTS) criterion (Eftekhari et al., 2016)	Maximum Tangential Strain (MTSN) criteria (Chang et al., 1981)	
NT Criterion (Yehia and Shephard, 1987)	Maximum shear stress (MSS) criterion (Otsuka et al., 1975)		
Average strain energy density (ASED) criterion (Lazzarin et al., 2001)	Generalized maximum tangential stress (GMTS) criterion (Smith et al., 2001)	Extended Maximum Tangential Strain (EMTSN) criteria (Mirsayar et al., 2018)	T-term-based (LEFM)
Generalized strain energy density criterion (GSED) (Ayatollahi et al., 2015)			
	Bobet's stress-based criteria (Bobet, 1997)	Stain-based criteria (Gonçalves and Einstein, 2013)	Full-field distribution-based (LEFM)
J contour integral (J) (Rice, 1968)	Traction-based mixed-mode (TMM) criterion	Cohesive zone model (Hillerborg et al., 1976)	Non-elastic fracture mechanics based (NEFM)

6.3 Parameters of Numerical Model

This study modeled gypsum specimens with a pre-existing flaw(s) under uniaxial compression using XFEM-based user elements in Abaqus. The modeled gypsum specimens have the same dimension used in various experimental studies (Bobet and Einstein, 1998; Wong, 2008), shown in Figure 6-2a-b. For the gypsum specimens containing a single flaw, three different orientations with the inclination angle β_w of 30º, 45º, and 60º were modeled (Figure 6-2a). Similarly, three benchmark cases of gypsum specimens with double flaws from the experimental study by Bobet and Einstein (1998) were simulated (Figure 6-2b). All gypsum specimens have flaw inclinations (β_w) of 45º and continuity (C) of 12.7 mm (inset in Figure 6-2b). While three gypsum specimens have different spacing: s=0, =a, =2a, where a denotes the half-flaw length of 6.35 mm (inset in Figure 2b). All modeled gypsum specimens have open flaws of 12.7 mm length, simulated using a line crack with frictionless surfaces (Figure 6-2a-b). The contact model for the flaw is based on the penalty method, which only requires high normal stiffness (k_p) to avoid closure between two surfaces of the flaw. It is important to note here that frictional contacts are being simulated in this study but only for new cracks that initiate from the body of the flaw and not for surfaces of the flaw itself. To simulate actual laboratory testing conditions, displacement-controlled loading at the rate of 1 mm/step (1 step =1sec) was applied at the top surface of each gypsum specimen while fixing its bottom surface (Figure 6-2a-b). The model was discretized using a uniform mesh with an edge length of 0.8 mm under plane strain conditions. The material parameters of the gypsum specimen used in this study are shown in Table 6-1 Summary of crack initiation criteria widely used in rocks (after Wong, 2008; Liu et al., 2018). The elastic and strength parameters were obtained from various experimental studies

(Bobet and Einstein 1998; Wei et al., 2020) on gypsum specimens, while fracture energies (G_{IC} and G_{IIC}) were selected based on the study by Fei and Choo (2021).

Table 6-2 Material parameters of gypsum specimens (Bobet and Einstein, 1998; Wei et al., 2020).

Parameter	Value
Young's modulus (E) (GPa)	5.6
Poisson's ratio (ν)	0.28
Tensile stress (σ_t) (MPa)	3.2
Cohesion strength (t_C^{max}) (MPa)	10.7*
Friction angle (ϕ)	28º
Mode I fracture energy (G_{IC}) (N/m)	16
Mode II fracture energy (G_{IIC}) (N/m)	205

* Indicates that parameters whose values will be adjusted for different crack initiation criteria

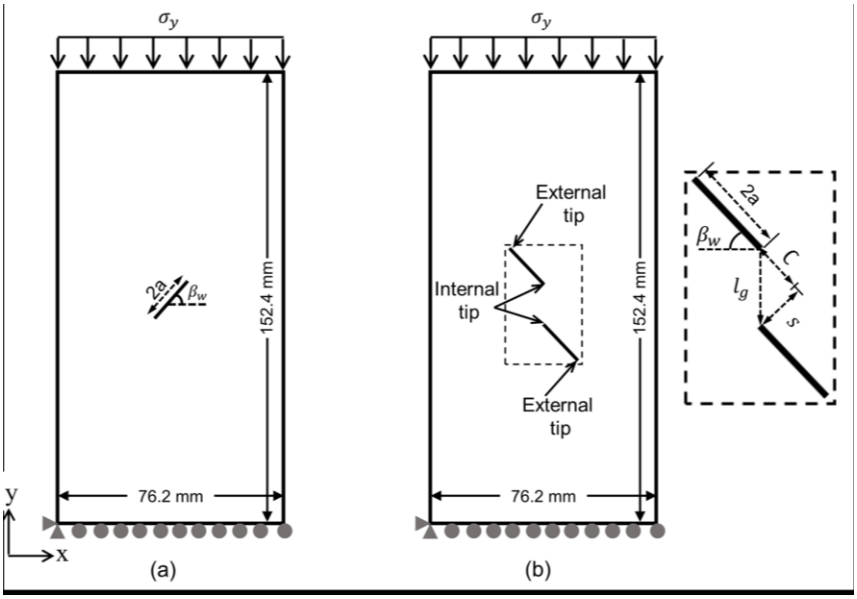

Figure 6-2 Geometry and loading conditions in gypsum specimens with (a) a single flaw and (b) double flaws.

6.4 Crack Initiation Criteria

6.4.1 Criteria for Tensile Cracks

The primary cracks in most rocks and rock-like materials, such as gypsum under uniaxial compression loading, are predominantly tensile cracks (Bobet and Einstein, 1998a; Wong, 2008; Cheng et al., 2016). In this study, the initiation of tensile cracks was predicted using the Maximum Principal Stress (MPS) criterion, which assumes crack formation in the direction perpendicular to the maximum principal stress. The MPS criterion is a modified version of the maximum tangential stress (MTS) criterion (Erdogan and Sih, 1963) which uses the concept of stress singularity at the crack tip to determine the initiation angle of mode I crack. While the MPS criterion without the use of the crack tip singularity is able to predict the path of tensile cracks in rocks under various loading conditions (Sharafisafa and Nazem, 2014; Zhuang et al., 2014; Xie et al., 2017). It is important to note here that the current study assumes tensile stress to be negative and thus, application of the MPS criterion requires comparing values of minimum principal stress (σ_{22}) with respect to the tensile strength of the material. In order to apply suitable criteria, the procedure starts with checking if the minimum principal stress (σ_{22}) exceed the tensile strength (σ_t), which implied tensile crack initiation. Thus, other criteria are only checked when minimum principal stress (σ_{22}) is below the tensile strength.

6.4.1.1 Criteria for Mode II and Mixed-mode I/II Cracks

The secondary cracks in most rocks and rock-like materials are likely to initiate in shear mode and often change their propagation direction due to changes in the fracture mode. As discussed earlier, secondary cracks involve a complex combination of tensile (mode I) and shear (mode II) fractures. Thus, multiple crack initiation criteria might be needed to characterize the

overall crack path of these secondary cracks. In this study, initiation of shear crack and mixed-mode I/II was predicted using two different criteria, namely (a) Maximum shear stress (MSS) criterion and (b) Traction-based mixed-mode (TMM) criterion.

6.4.1.2 Maximum Shear Stress (MSS) Criterion

The maximum shear stress (MSS) criterion originally proposed by Otsuka et al. (1975) has been used for predicting the direction of shear fracture in various materials such as steel, aluminum alloys, granite, marble, molded gypsum (Lo et al., 1996; Chao and Liu, 1997; Isaksson and Stahle, 2002; Rao et al., 2003; Bobet and Einstein, 1998). For rocks, the MSS criterion is applied by comparing local stress at the crack tip against the strength of the material rather than only considering stress intensity factors (SIF) (Wong, 2008). This form of MSS criterion allows us to reliably predict the path of a shear crack and distinguish it separately from other crack types (Bobet and Einstein, 1998b). Most applications of the MSS criterion in rock are based on the assumption of LEFM and use stress singularity at the crack tip to estimate the initiation angle of the shear crack at a certain distance from the crack tip. However, most laboratory-scale specimens of rock and rock-like material typically have a significant size of FPZ which may be comparable to the initial flaw size (Labuz et al., 1987; Lin et al., 2019a; Ghamgosar and Erarslan, 2016). This, in some cases, might lead to FPZ being larger than the singularity-dominated zone (SDZ), which is defined as the region over which stress distribution at the crack tip is estimated using stress singularity (Nejati et al., 2020). To account for the significant size of FPZ, current XFEM-based user elements avoid using crack tip enrichment by allowing the crack to propagate until the next element's edge (details in section 5.3.4.3). Therefore, this study

implemented a modified version of the MSS criterion, which doesn't need to account for stress singularity at the crack tip.

In XFEM-based user elements, the crack stress tensor $\bar{\boldsymbol{\sigma}}$ is calculated by averaging the stress state of all integration points that lie inside the rectangular region around the crack tip (section 5.3.4.3). This crack stress tensor $\bar{\boldsymbol{\sigma}}$ then can be used to calculate the normal (t_n) and shear (t_s) components of the traction along the future fracture plane lie on an imaginary axis η (Figure 6-3). The imaginary axis η is obtained by rotating the local coordinate axis (x_1, y_1) that aligns with the original crack plane by the angle θ as shown in Figure 6-4.

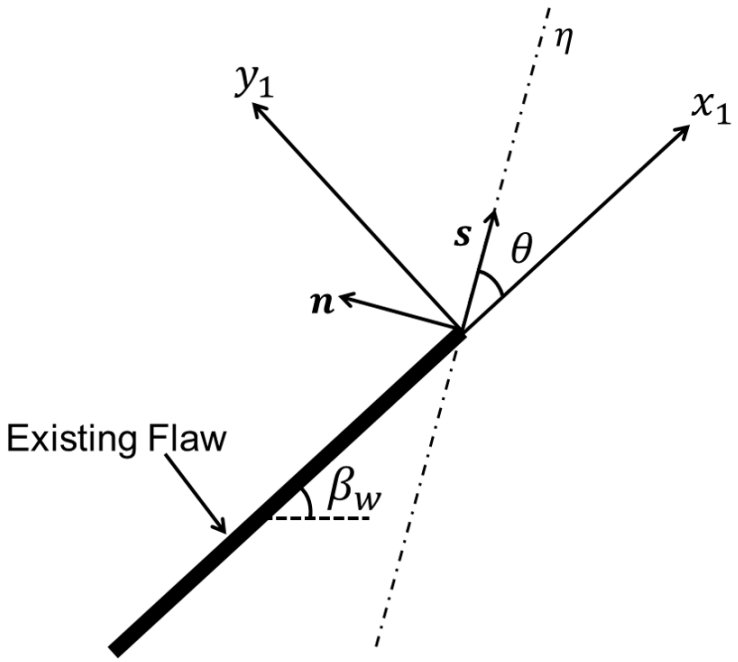

Figure 6-5 Calculation of the crack propagation plane along an imaginary axis η at an angle θ with respect to the x_1-axis.

The crack tractions (t_n, t_s) is given by:

$$t_n = \boldsymbol{n}^T \bar{\boldsymbol{\sigma}}\, \boldsymbol{n}; \qquad t_s = \boldsymbol{s}^T \bar{\boldsymbol{\sigma}}\, \boldsymbol{n} \tag{6-1a}$$

$$\boldsymbol{n} = [-\sin\theta\,, \cos\theta]^T; \quad \boldsymbol{s} = [\cos\theta\,, \sin\theta]^T \tag{6-1b}$$

where $\boldsymbol{n}$ and $\boldsymbol{s}$ are the unit normal and tangent vectors to the η-axis, respectively. The crack initiation criteria used in the current study are stress-based criteria which have been defined using normalized crack driving force (F) based on the work of Dobroskok et al. (2005) written as

$$F = \frac{f(\bar{\boldsymbol{\sigma}})}{\sigma_0} \tag{6-2}$$

where $f(\bar{\boldsymbol{\sigma}})$ and σ_0 denotes crack driving force and material strength, respectively. The normalized crack driving force (F) in Eq 6-2 represents a generalized form that can define any stress-based criterion (Sweeryn and Mroz, 1995; Dobroskok et al., 2005). For the MSS criterion, the normalized crack driving force (F) can be written in the form of shear traction (t_s) and material cohesion (t_C^{max}) to define the critical condition for shear crack initiation as given by:

$$F(\theta) = \frac{t_s(\theta)}{t_C^{max}} \tag{6-3a}$$

$$F(\theta = \theta_0) \geq 1; \quad \left.\frac{dF}{dx}\right]_{\theta=\theta_0} = 0; \; \left.\frac{d^2F}{d^2x}\right]_{\theta=\theta_0} < 0 \tag{6-3b}$$

Where θ_0 denotes the initiation angle with respect to the original fracture plane (Figure 6-5). For a given stress state $(\bar{\boldsymbol{\sigma}})$, the normalized crack driving force (F) is determined for all angles of the imaginary axis η in the range $-\pi/2 < \theta < \pi/2$. Since the current XFEM-user elements don't allow new cracks to turn more than 90^0 with respect to the pre-existing crack plane (Figure

6-3), the new crack should lie in the given range of θ. Figure 6-6 presents an example of the normalized crack driving force ($F(\theta)$) for the case upper flaw tip of the gypsum specimen under compression loading with single-flaw oriented at 45º from the horizontal axis. There are often multiple local maxima along with one global maximum in normalized crack driving force ($F(\theta)$), as shown in Figure 6-6. Thus, the direction of crack propagation ($\theta = \theta_0$) is obtained by estimating normalized crack driving force ($F(\theta)$) for all local maxima using critical conditions defined in Eq 3b and then comparing these values to get the global maximum. Thus, the normalized crack driving force (F) in Eqs 6.3a-b controls the crack initiation stage and the direction in which the crack will propagate.

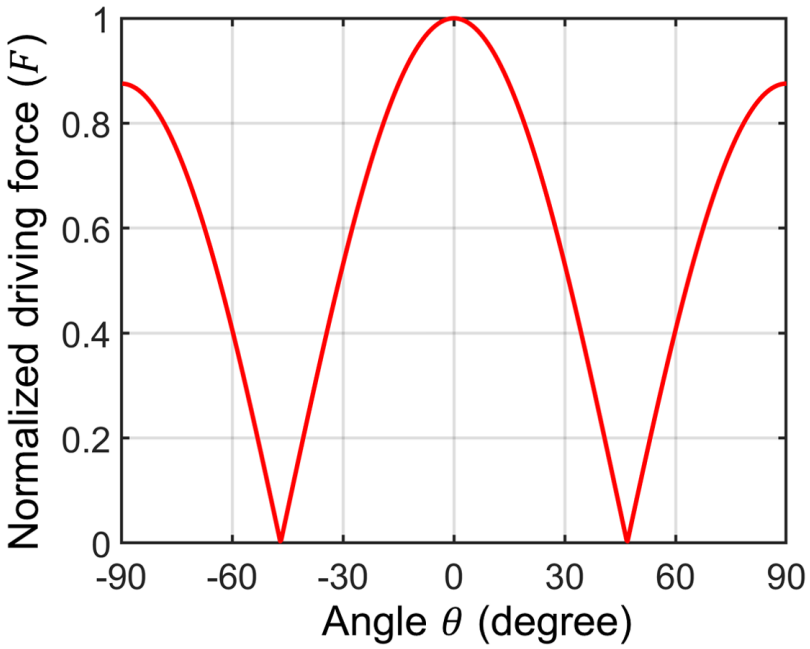

Figure 6-6 Calculation of the normalized crack driving force versus angle θ with respect to the x_1-axis in MSS criterion for the stress state $\bar{\boldsymbol{\sigma}} = [\sigma_{xx}, \sigma_{yy}, \sigma_{xy}]^T = [3, -4, 1]^T$ MPa.

6.4.1.3 Traction-based Mixed-mode I/II Criterion

The Traction-based mixed-mode (TMM) criterion, also known as the quadratic stress criterion, has been extensively used for predicting crack initiation under mixed-mode I/II loading in various materials, such as the delamination of reinforced composites and rock blocks with mortar joints (Camanho et al., 2003; Anyfantis and Tsouvalis, 2012; Venza et al., 2020; Narin and Aimene, 2021) even though in different forms. In recent years, it also has been used for predicting crack initiation in porous rocks under tensile-shear loading (Wang et al., 2020). These studies applied the TMM criterion without using crack tip singularity, which allowed the broad application of this criterion by accounting for the significant size of FPZ in various materials. However, in most of these applications, the TMM criterion is only used for predicting the crack initiation stage under tensile or tensile shear loading, with the fracture path being predetermined. The only exception was a study by Sweeryn and Mroz et al. (1995) that defined a unified criterion for fracturing under different loading conditions and used it to estimate both crack initiation stress and the path of the fracture plane.

This study implemented the TMM criterion based on the formulation given by Sweeryn and Mroz (1995) but with different critical conditions, as the original criterion relied on crack tip singularity to predict the crack initiation stage. In the current study, the normalized crack driving force (F) for the TMM criterion is defined using a generalized case of mixed-mode I/II loading as given by:

$$F = f\left(\frac{t_n}{\sigma_c}, \frac{t_s}{\tau_c}\right) \tag{6-4}$$

where σ_c and τ_c denotes the critical failure stress of material in tension and shear, respectively. The crack tractions (t_n, t_s) along an imaginary axis (Figure 6-3) can be estimated for a given stress state $(\bar{\boldsymbol{\sigma}})$ around the crack tip using Eq 6-1. Thus, the normalized crack driving force (F) for the TMM criterion can be written as:

$$F(\theta) = \left(\frac{t_n(\theta)}{\sigma_t}\right)^2 + \left(\frac{t_s(\theta)}{t_C^{max}}\right)^2 \quad , \; t_n(\theta) \leq 0 \tag{6-5a}$$

$$F(\theta) = \left(\frac{t_s(\theta)}{t_C^{max} + \tan\phi \; t_n(\theta)}\right)^2 \quad , \; t_n(\theta) \; > 0 \tag{6.5b}$$

Eq 6-5a-b defines separate conditions for tensile ($t_n(\theta) \leq 0$) and compression ($t_n(\theta) > 0$) induced fractures. For compression-induced shear fractures effect of both cohesion (t_C^{max}) and friction angle (ϕ) is considered. The assumption that friction is vital for compression-induced shear fractures is consistent with other studies (Rao et al., 2003; Lui et al., 2018). The crack initiation angle (θ_0) with respect to the original fracture plane (Figure 3) can be predicted using the same critical conditions in Eq 6-3b but with different values of the normalized crack driving force (F).

Thus, the TMM criterion can predict mode I, mixed-mode I/II, and compression-induced shear cracks (mode II fractures), depending on the stress state and strength of the material. Figure 6-7 presents an example of the normalized crack driving force $(F(\theta))$ for shear cracks initiation from the upper flaw tip of the gypsum specimen with single-flaw oriented at 45 from the horizontal axis. The procedure for determining the crack initiation angle (θ_0) in the TMM criterion is the same as used for the MSS criterion (section 6.4.1.2). It is important to note that the current study used the TMM criterion only to check the initiation of shear and mixed-mode

I/II cracks. Furthermore, current analysis in all case studies doesn't show the initiation of mixed-mode I/II cracks but rather the transition of shear cracks into the tensile mode during crack propagation.

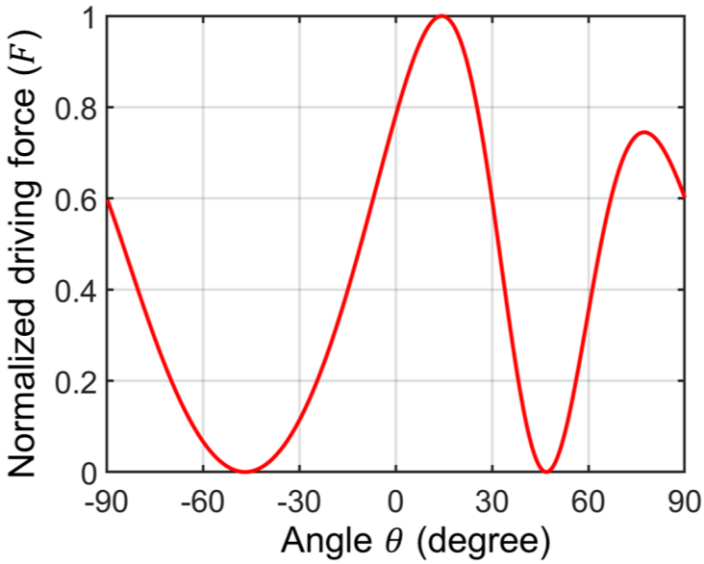

Figure 6-7 Calculation of the normalized crack driving force versus angle θ with respect to the x_1-axis in TMM criterion for the stress state $\bar{\boldsymbol{\sigma}} = \left[\sigma_{xx}, \sigma_{yy}, \sigma_{xy}\right]^T = [3, -4, 1]^T$ MPa.

6.4.1.4 CZM for FPZ Development

For mode I crack, the material softening inside the FPZ was modeled using the exponential cohesive zone model (section 5.3.2). In this model, the fracture energy dissipation inside the FPZ is defined using the concept of equivalent crack displacement ($[\![u]\!]_{eq}$) and equivalent traction (t_{eq}). As a result, the influence of the shear component of crack traction (t_S) during material softening inside FPZ was also accounted for by using the weighting parameter β (section 5.3.2). For mode I crack, equivalent crack traction (t_{eq}) decreased exponentially with its maximum value (t_{eq}^{max}) equal to the tensile strength of the material (σ_t). Similarly, for mixed-mode I/II

crack, the same cohesive zone model can be used with the different value maximum equivalent crack traction (t_{eq}^{max}) as given by:

$$t_{eq}^{max} = \sqrt{(t_n^0)^2 + \left(\frac{t_s^0}{\beta}\right)^2} \tag{6-7}$$

where t_n^0 and t_n^0 denotes initial values of normal and shear components of crack traction, respectively estimated using the TMM criterion at the stage of the fracture initiation. The weighting parameter β was selected to be 1, typically assumed for quasi-brittle materials (Meschke and Dumstorff, 2007; Wang and Waisman, 2018).

For compression induced-shear cracks (mode II fracture), the material softening was simulated using the cohesive zone model developed for frictional cracks (section 5.3.3). This cohesive zone model accounts for both frictional energy dissipation and fracture energy release due to the degradation of the material's cohesion (t_c) during the propagation of the shear crack. The cohesive zone model assumes exponential softening of cohesion (t_c) with respect to crack sliding displacement ($[\![u]\!]_s$). The normal component of the crack traction (t_n) varies based on crack opening displacement ($[\![u]\!]_n$). The frictional resistance is added when the interface undergoes crack closure ($[\![u]\!]_n < 0$) (section 5.3.3).

In this study, the inclusion of frictional dissipation energy in the cohesive zone model would depend on the type of shear crack initiation criteria used for the analysis. For instance, the MSS criterion predicts crack initiation based only on material cohesion (t_c), thereby ignoring the effect of friction angle (ϕ). Thus, for consistency purposes, the material softening under shear crack development for the MSS criterion was simulated using a cohesive zone model with zero

friction angle (ϕ = 0º). In contrast, the TMM criterion considers the frictional resistance of material for shear crack initiation.

6.5 Secondary Cracks in Single-flaw Specimens

6.5.1 Propagation of Shear Cracks only

This section presents a systematic evaluation of the influence of crack initiation criteria on the path of compression-induced shear cracks through XFEM-based user elements. For this purpose, the propagation of secondary cracks was only considered from the gypsum specimen containing a single flaw with an inclination (β_w) of 45º from the horizontal axis. This would facilitate the investigation of the influence of crack initiation criteria on the path of secondary cracks, typically known to initiate under shear mode without any influence of primary cracks. Thus, this model did not consider the formation of tensile and mixed-mode I/II cracks.

Both crack initiation criteria, i.e., MSS and TMM criteria, were considered for predicting initiation and propagation of compression-induced shear cracks from the modeled single flaw gypsum specimens. As mentioned earlier, for compression-induced shear cracks, the two criteria differ in terms of frictional resistance. Because of this difference, overall specimen behavior would also be different between the application of the two criteria. Thus, a proper comparison of the shear crack path between two criteria would require that both criteria result in similar global behavior of specimens defined in terms of the load-displacement curve. For this purpose, input cohesion in cases of MSS criterion was iteratively varied such that both criteria resulted in the same peak load for modeled single-flaw gypsum specimen. Based on this parametric analysis, input cohesion (t_c^{max}) of 18 MPa was found suitable for the MSS criterion, which will be kept

constant for the rest of the study. While input cohesion (t_c^{max}) of 10.7 MPa was used for the TMM criterion in the rest of this study (Table 6-2).

Figure 6-8(a-d) compares the evolution of compression-induced shear cracks in the single-flaw gypsum specimen between two criteria at various loading stages. It is clear from Figure 6-8(a-d) that the shear crack initiated slightly earlier in the TMM criterion compared to the MSS criterion, which can be attributed to the larger value of input cohesion in the latter case. With further loading, coplanar shear cracks propagated in gypsum specimens with the MSS criterion (see inset in Figure 6-8c). While in gypsum specimens with TMM criterion, the shear crack was quasi-coplanar with respect to the flaw plane as it is inclined at 58º from the horizontal axis (see inset in Figure 6-8d). Figure 6-9 presents classification types of crack patterns typically observed in the single-flaw specimens of various rock and rock-like materials (Wong and Einstein, 2009). Based on this classification, the MSS criterion resulted in type 2 shear cracks, while the TMM criterion showed the formation of type 1 shear cracks. It is to be noted that the exact path of type 1 is different from the path obtained from the TMM criterion, which can be attributed to the influence of primary cracks. These primary cracks are known to initiate first in most experiments which have been ignored in numerical models of this section.

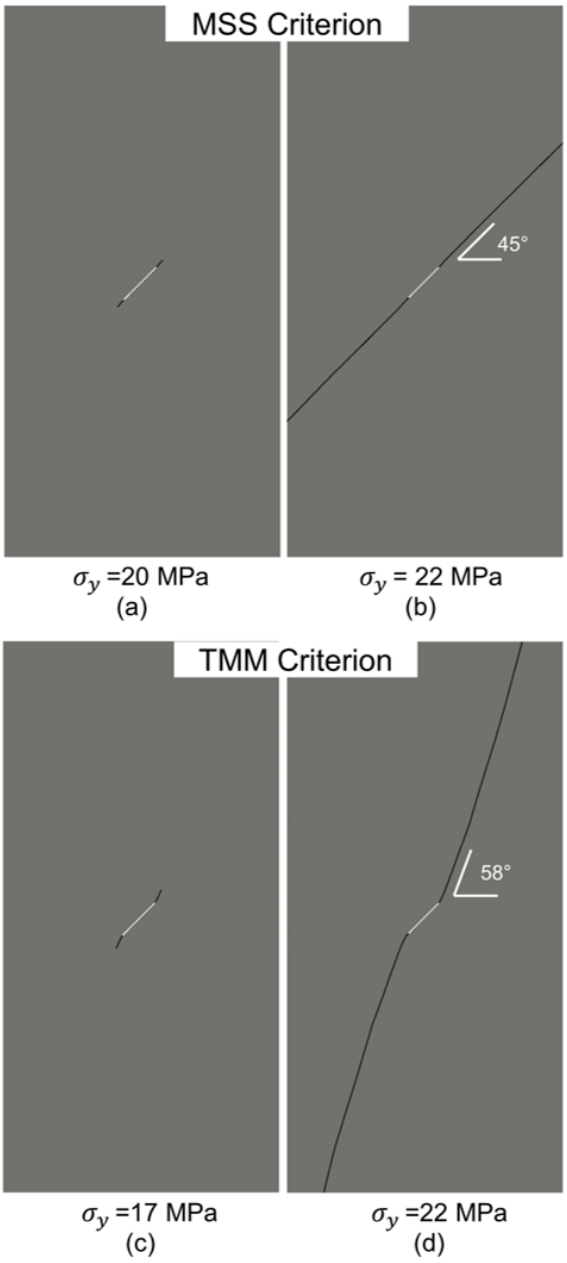

Figure 6-8 Comparison of the shear crack path in XFEM-based numerical model of oriented single flaw (β_w=45º) gypsum specimen between (a-b) MSS criterion and (c-d) TMM criterion.

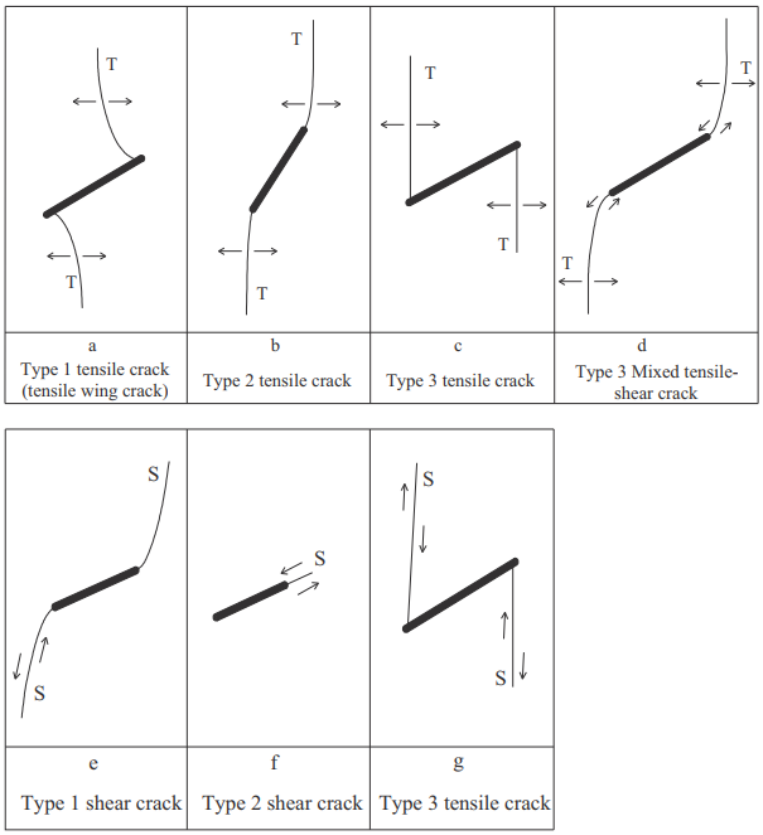

Figure 6-9 Classification of crack types in single-flaw rock specimens (after Wong and Einstein, 2009). T tensile cracking opening, S shearing displacement.

6.5.2 Propagation of Multiple crack types

The present section compares the overall crack pattern obtained in single-flaw gypsum specimens between the XFEM-based numerical model and experimental data, along with assessing the influence of crack initiation criteria on the path of secondary cracks. For this purpose, gypsum specimens with three orientations of single flaw from the horizontal axis, i.e., β_w =30º, 45º and 60º were simulated. The material parameters of the modeled gypsum specimen are shown in Table 6-1. The dimension and other geometric parameters of modeled gypsum specimen are shown in Figure 6-2a. The initiation of tensile crack was predicted using the MPS

criterion. For secondary cracks, both the MSS and the TMM criteria were considered to assess their applicability by comparing the path of secondary cracks with the experimental observations of Wong (2008). Based on triggered crack initiation criteria, the corresponding cohesive zone model was used as described in section 6.4.1.4.

Figure 6-10-6-10 compare crack patterns obtained using two secondary crack initiation criteria with experimental results of the gypsum specimens for three orientations of the single flaw., i.e., β_w =30º, 45º, and 60º, respectively. For each flaw inclination case, crack patterns at various loading stages are presented to assess the influence of two crack initiation criteria on various characteristics of secondary cracks. In all three gypsum specimens (Figures 6-8a, 6-9a, and 6-10a), two tensile wing cracks initiated first from two tips of the single flaw, also called primary cracks. This observation of wing cracks (type 1 tensile cracks in Figure 6-9) being initiated first irrespective of flaw inclination agrees with various experimental (Park and Bobet, 2009; Wong and Einstein, 2009) and numerical studies (Zhang and Wong, 2012; Li and Wong, 2012) done on rocks and rock-like material such as Carrara marble and gypsum. Table 6-2 compares various characteristics of these tensile cracks between the XFEM-based numerical model and the experimental results of Wong (2008). It is clear from Table 6-2 that both the wing crack initiation angle (θ_w) and the position of tensile wing cracks (d_1 and d_2 from the flaw tips) in the XFEM model were in reasonable agreement with the experimental data. The exact definition of these parameters is described in detail in section 5.5.4. Additionally, the crack initiation stress which represents the global stress level at which the new cracks initiated from the flaw tip(s), increased from 3.4 MPa for the flaw inclination angle of 30º to 7.6 MPa for the flaw inclination angle of 60º (Table 6-2). This delay in the initiation of tensile wing cracks is

consistent with the experimental results of Wong (2008) on gypsum specimens despite having significantly large values of crack initiation stress compared to the XFEM-based numerical model (Table 6-2). This large difference in absolute values of crack initiation stress can be attributed to the difference in the methodology used to estimate the primary crack initiation stage between the XFEM-based numerical model and the experimental study. For instance, the crack initiation stress in the experimental research of Wong (2008) was approximated through visual inspection of specimens' surfaces using a high-speed camera which involves a high degree of subjectivity from one rock to another. It would also require a large crack opening displacement (COD > 50 μm) to be properly visible. In contrast, crack initiation stress in the XFEM-based numerical model corresponds to the initiation stage of FPZ, which would have a small crack opening displacement (COD < 2 μm). With subsequent loading, these tensile wing cracks become parallel to the direction of maximum compressive stress (Figures 6-8c, 6-9c, and 6-10c) in all three gypsum specimens. Additionally, the length of these tensile wing cracks decreased with flaw inclination, with the secondary cracks larger than primary cracks in cases of flaw inclination of 60º (Figure 6-12c). This observation agrees with Li and Wong's study (2012), which reported longer cracks for lower flaw inclination angles ($\beta_w \leq 45^{\circ}$) while steeply inclined flaws ($\beta_w \geq 60^{\circ}$) favors the propagation of shear cracks over tensile cracks once both cracks are initiated at the flaw.

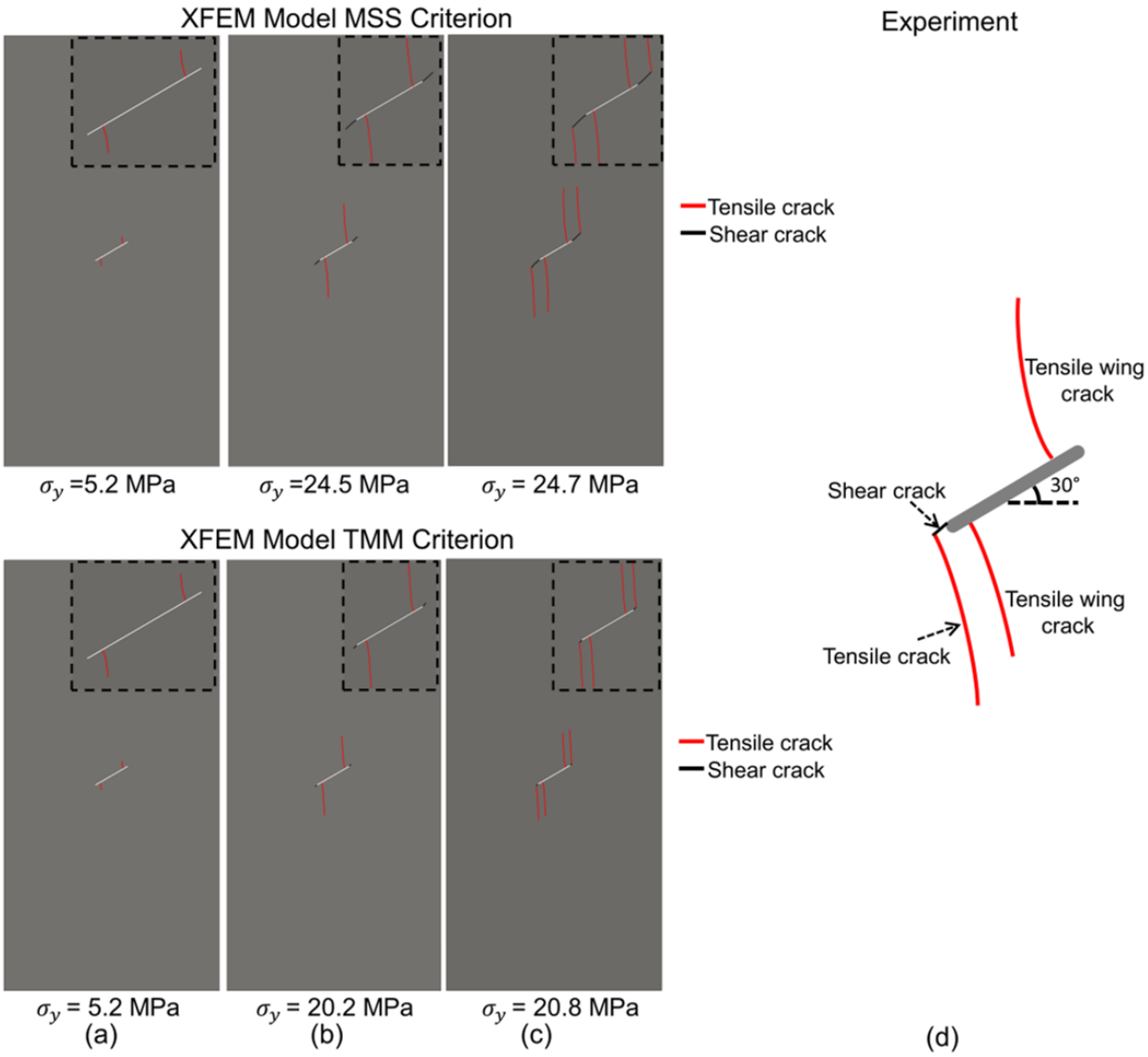

Figure 6-10 Comparison of crack patterns in oriented single flaw (β_w=30º) gypsum specimen between (a-c) XFEM model with MSS and TMM criterion and (d) experiment. The tensile stress is assumed to be negative in the study. The inset in a-c presents the zoom-in view of crack patterns around the flaw. The crack patterns for experimental data were redrawn from Wong (2008).

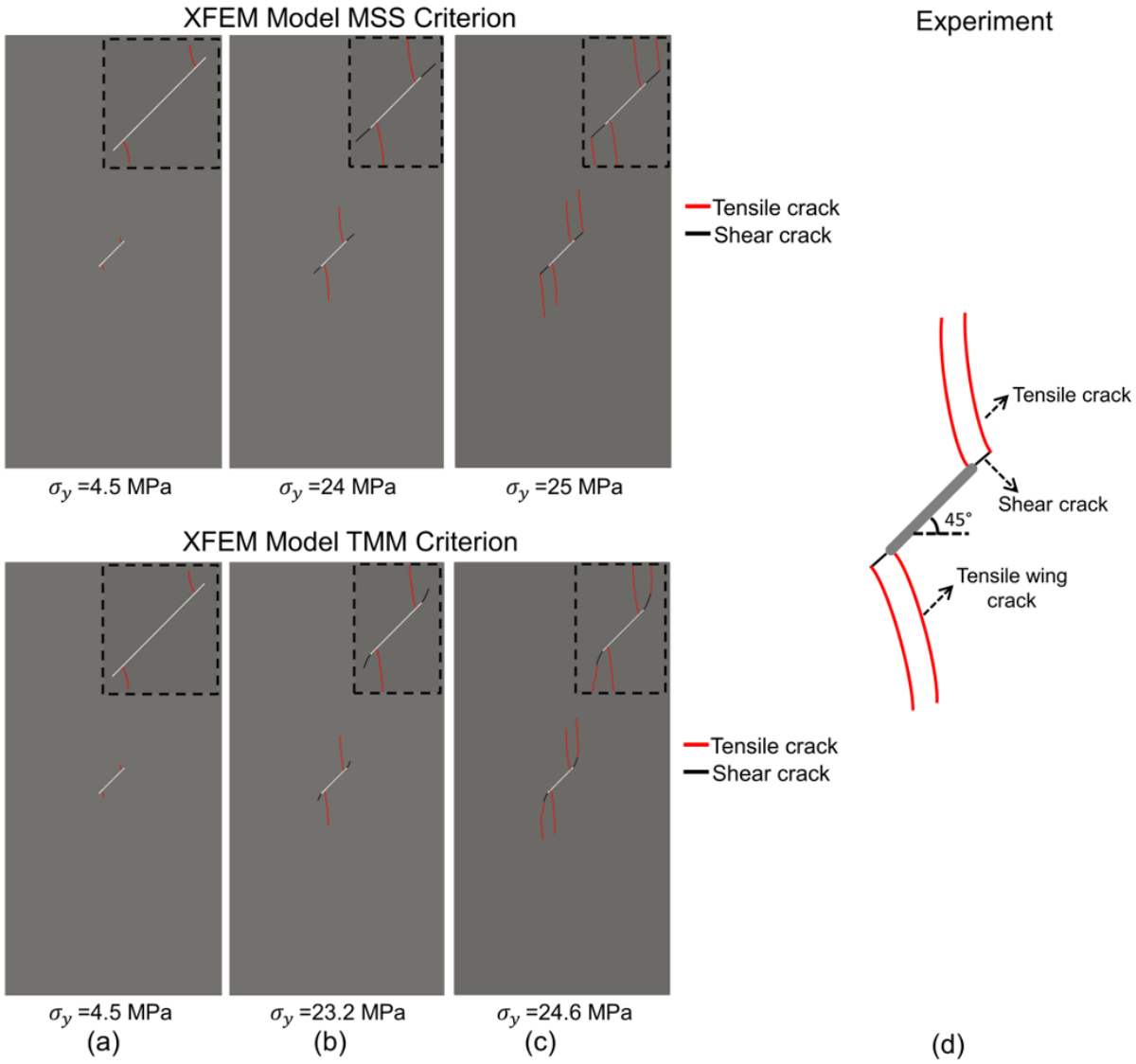

Figure 6-11 Comparison of crack patterns in oriented single flaw (β_w=45º) gypsum specimen between (a-c) XFEM model with MSS and TMM criterion and (d) experiment. The inset in a-c presents the zoom-in view of crack patterns around the flaw. The crack patterns for experimental data were redrawn from Wong (2008).

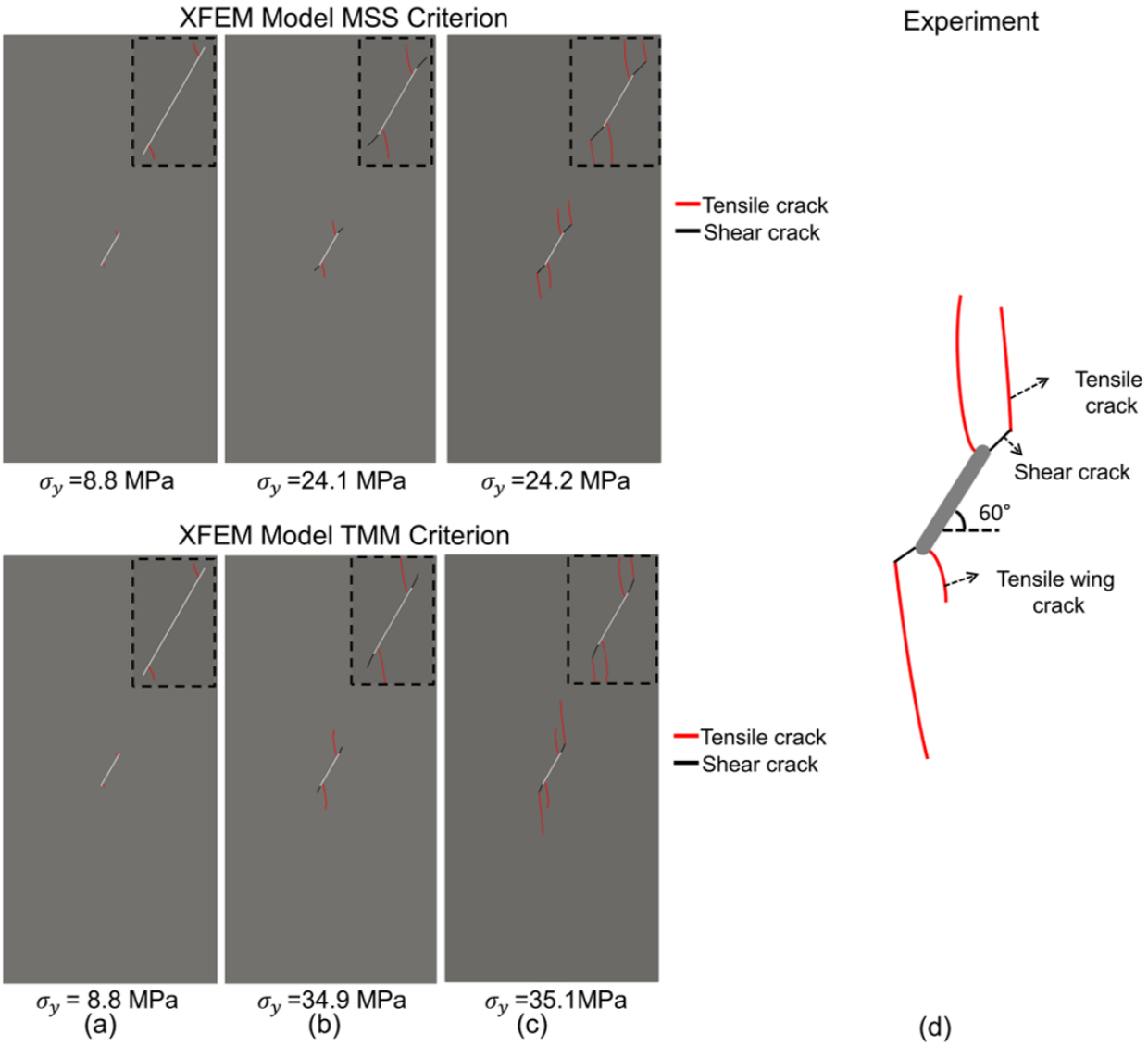

Figure 6-12 Comparison of crack patterns in oriented single flaw (β_w=60º) gypsum specimen between (a-c) XFEM model with MSS and TMM criterion and (d) experiment. The inset in a-c presents the zoom-in view of crack patterns around the flaw. The crack patterns for experimental data were redrawn from Wong (2008).

Table 6-3 Comparison of the XFEM model with experimental results (from Wong, 2008) of primary cracks in single-flaw gypsum specimens.

Flaw inclination angle (β_w)	**Wing crack initiation angle (θ_w)**		**Wing crack initiation stress (σ_y) (MPa)**		**Distance of wing cracks from flaw tips (d_1, d_2) (mm)**	
	XFEM model	Experiment	XFEM model	Experiment	XFEM model	Experiment
30^0	82^0	87^0	3.4	23	1.80, 2.10	0.3-2.3
45^0	89^0	85^0	4	25	1.13, 1.15	0.5-2.5
60^0	114^0	110^0	7.6	27	1.11,1.12	0.7-2.2

The formation of primary cracks in all three gypsum specimens was followed by the initiation of quasi-coplanar shear cracks from two tips of the single flaw irrespective of applied secondary crack initiation criteria (Figures 6-8b, 6-9b, and 6-10b). However, the characteristics of initiated shear crack varied among two crack initiation criteria, as shown in Table 6-4. For instance, the MSS criterion resulted in shear cracks being initiated at the angle of 45^0 from the horizontal axis in all three gypsum specimens (Table 6-4). In contrast, the TMM criterion resulted in shear crack being initiated at variable angles between 50^0-60^0 in three gypsum specimens (Table 6-4). Additionally, the MSS criterion resulted in shear cracks being initiated around similar loading stages in all three gypsum specimens (Table 6-4). While a considerable variation occurs in the initiation stage of shear cracks (Table 6-4) with the TMM criterion, which can be attributed to a different level of confining pressure (σ_3) at the flaw tips among three gypsum specimens. These shear cracks in subsequent loading stages transition into tensile cracks in the formation of mix-mode secondary fractures in all three gypsum specimens flaw,

irrespective of applied secondary crack initiation criteria (Figures 6-8c, 6-9c, and 6-10c). The experimental observations of three gypsum specimens also showed the formation of mixed tensile–shear cracks (Figures 6-8d, 6-9d, and 6-10d). The two crack initiation criteria mainly differ in the length of the shear crack, with the TMM criterion predicting a smaller length of the shear component present in the secondary cracks of all three gypsum specimens (Table 6-4). This observation of shorter shear cracks is consistent with the experimental results of all three gypsum specimens (Figures 6-8d, 6-9d, and 6-10d). Thus, the TMM criterion can be assumed to be more reliable in predicting the formation of mixed tensile–shear cracks observed in most single-flaw specimens. It can be concluded that the XFEM-based numerical model can replicate real cracking in single-flaw gypsum specimens under uniaxial compression loading with a similar cracking pattern, irrespective of applied secondary crack initiation criteria.

Table 6-4 Comparison of various characteristics of secondary cracks in single-flaw gypsum specimens with two different crack initiation criteria.

Flaw inclination angle (β_w)	**Shear crack initiation stress (σ_y) (MPa)**		**Crack initiation angle (θ_s) from the horizontal axis**		**Shear crack length from flaw tip (mm)**	
	MSS criterion	**TMM criterion**	**MSS criterion**	**TMM criterion**	**MSS criterion**	**TMM criterion**
30^0	24.5	19.6	45^0	50^0	4.2	0.9
45^0	23.7	22.8	45^0	58^0	4.5	2.9
60^0	23.8	34.1	45^0	60^0	4.7	3.2

6.6 Secondary Cracks in Double-flaw Specimens

This section compares the overall crack pattern, including the type of crack coalescence obtained in double-flaw gypsum specimens, between the XFEM-based numerical model and experimental data. Additionally, the influence of secondary crack initiation criteria on the path and type of crack coalescence was assessed. For this purpose, three benchmark cases of gypsum specimens with double flaws with different ligament lengths (l_g) were simulated (Figure 6-2b). The material parameters of the modeled gypsum specimen are shown in Table 6-2. The dimension and other geometric parameters of modeled gypsum specimen are shown in Figure 6-2b. The crack initiation criteria used here are the same as those used in cases of single-flaw gypsum specimens.

Figure 6-13(a-d) compares the results of two XFEM-based numerical models with the experimental study of Bobet and Einstein (1998) for the first configuration of double-flaw gypsum specimen with s=0, C=2a, and ligament length (l_g) of 2a, where a denotes half length of the flaws. Two numerical models in Figure 6-13(a-c) correspond to two secondary crack initiation criteria, i.e., MSS and TMM. At the initial loading stages, tensile wing cracks initiated from the outer and inners tips of two flaws as shown at applied vertical stress (σ_y) of 4.1 MPa (Figure 6-13a). Additionally, these wing cracks initiated simultaneously at the outer and inner flaw tips, which is consistent with the observations of the experimental study by Bobet and Einstein (1998). In subsequent loading stages, coplanar and quasi-coplanar shear initiated at the inner tips of the two flaws in cases of MSS and TMM criteria, respectively, as shown in Figure 6-13b. Furthermore, the wing cracks propagated in a stable manner with longer cracks at the outer tips compared to the ones formed at the inner tips of two flaws (Figure 6-13b).

With additional loading, two crack initiation criteria resulted in the different paths of secondary cracks at the inner tips. The MSS criterion resulted in coplanar fracture propagation, mostly under shear mode (Figure 6-13c). In contrast, the TMM criterion leads to the formation of oblique mixed-mode fractures at the inner tips of two flaws (Figure 6-13c). Consequently, gypsum specimens with MSS criterion lead to crack coalescence under the shear mode, which is consistent with experimental observations of Bobet and Einstein (1998) (Figure 6-13(c-d)). In comparison, the TMM criterion showed no crack coalescence, which can be attributed to formations of oblique shear cracks, which transition into vertical tensile fractures (Figure 6-13c). Table 6-5 compares various characteristics of crack coalescence between two XFEM-based numerical models and experimental data. The type of crack coalescence mentioned in Table 6-5 is based on the experimental study of Bobet and Einstein (1998). It is clear from Table 6-5 that gypsum specimens with the MSS criterion can predict both type and mode of crack coalescence obtained in an experimental study with good accuracy.

Figures 6-10 and 6-11 compare the results of XFEM-based numerical models with the experimental data for two configurations of double-flaw gypsum specimens with ligament lengths of 2.2a and 2.9a. Similar to the first double-flaw configurations, the tensile wing cracks initiated first, followed by secondary shear cracks in the remaining two configurations, irrespective of secondary crack initiation criteria. Additionally, both secondary crack criteria resulted in the crack coalescence under mixed-mode I/II fracture in the two remaining configurations. The main difference between the two secondary crack criteria lies in the type of crack coalescence with the MSS criterion providing agreement with experimental results (Table 6-5). In contrast, the TMM criterion showed significant differences in both types of crack

coalescence and overall crack patterns compared to experimental observations (Figures 6-9c-d, 6-10c-d, and Table 6-5).

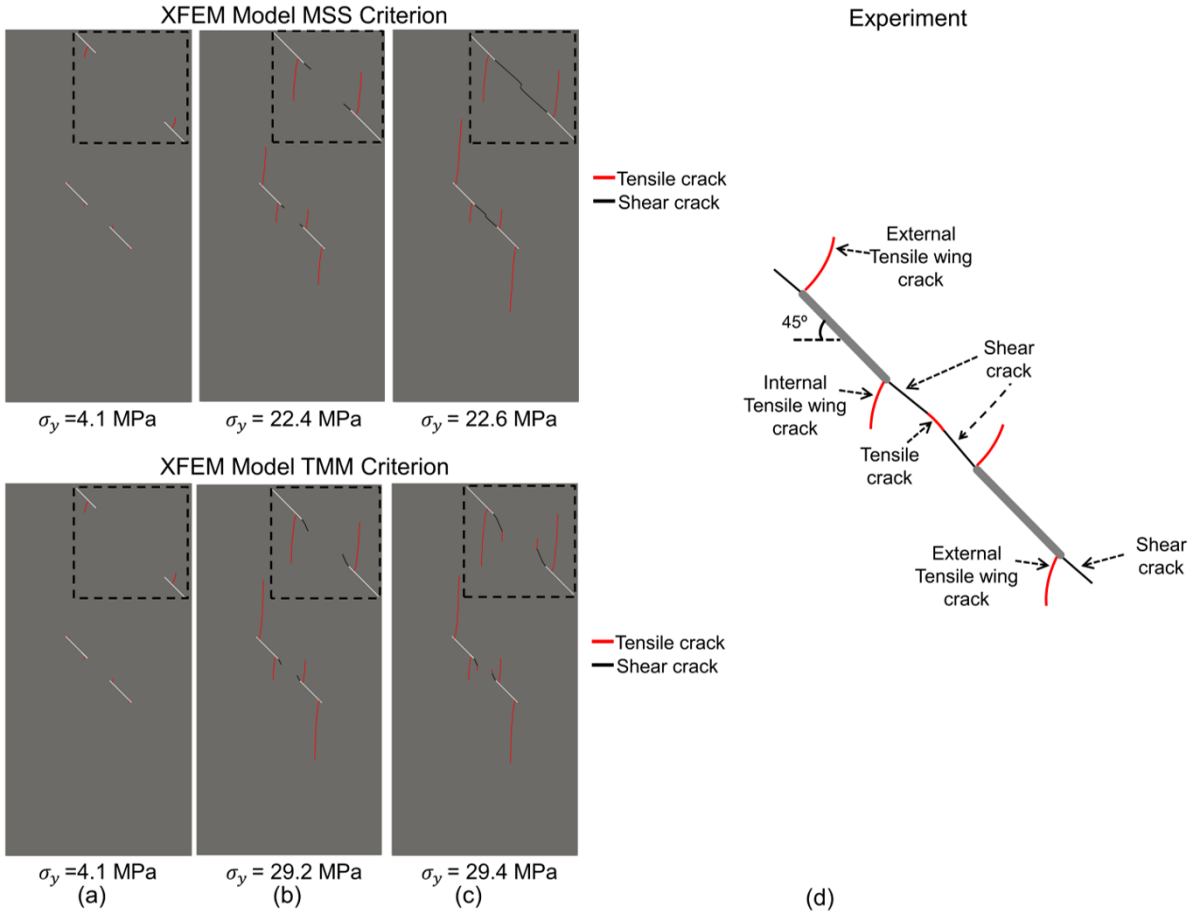

Figure 6-13 Comparison of crack patterns from double flaw gypsum with ligament length (l_g) of 2a, s=0 between (a-c) XFEM model with MSS and TMM criterion and (d) experiment. The inset in a-c presents the zoom-in view of crack patterns in the ligament region between two flaws. The crack patterns for experimental data were redrawn from Bobet and Einstein (1998).

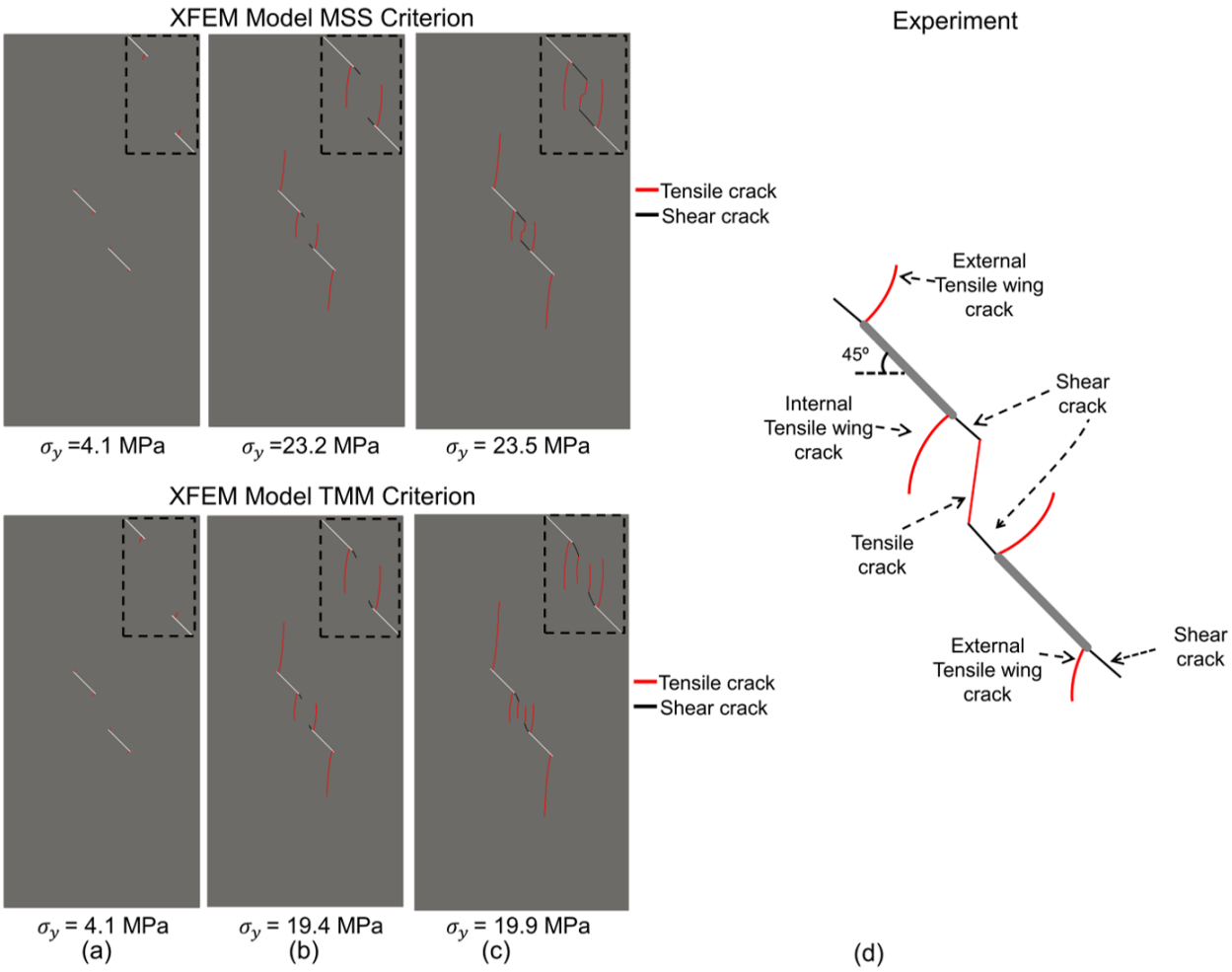

Figure 6-14 Comparison of crack patterns from double flaw gypsum with ligament length (l_g) of 2.2a, s=a between (a-c) XFEM model with MSS and TMM criterion and (d) experiment. The inset in a-c presents the zoom-in view of crack patterns in the ligament region between two flaws. The crack patterns for experimental data were redrawn from Bobet and Einstein (1998).

For quantitative assessment of the XFEM-based numerical model, Table 6-5 compares the coalescence stresses in the two simulations and those measured in the experiments of Bobet and Einstein (1998). In all three configurations of gypsum specimen, the XFEM-based numerical model with the MSS criterion show excellent agreement with the experimental values. Interestingly, the simulation results can capture the increasing trends of the coalescence stresses

with ligament length (l_g) observed from the experiments. It can be concluded that the XFEM-based numerical model with MSS criterion can predict the type of crack coalescence along with the transition of cracking patterns according to changes in the flaw configurations.

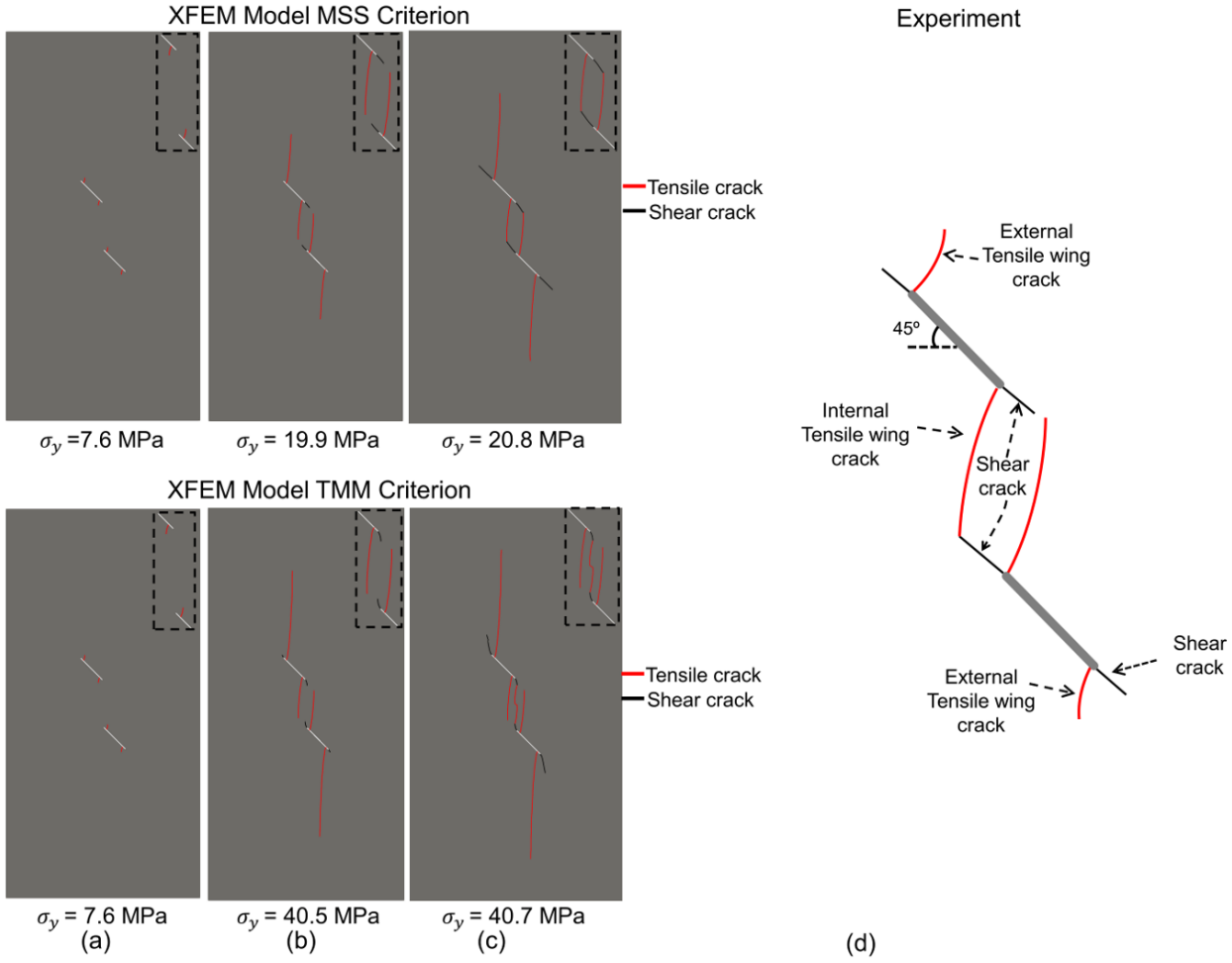

Figure 6-15 Comparison of crack patterns from double flaw gypsum with ligament length (l_g) of 2.9a, s=2a between (a-c) XFEM model with MSS and TMM criterion and (d)experiment. The inset in a-c presents the zoom-in view of crack patterns in the ligament region between two flaws. The crack patterns for experimental data were redrawn from Bobet and Einstein (1998).

Table 6-5 Comparison of various characteristics of crack coalescence in double-flaw gypsum specimens with two different crack initiation criteria and experimental results by Bobet and Einstein (1998).

Flaw configuration (s-β_w- l_g)	**Mode of coalescence**			**Type of coalescence pattern**			**Crack coalescence stress (MPa)**		
	MSS criterion	**TMM criterion**	**Experiments**	**MSS criterion**	**TMM criterion**	**Experiments**	**MSS criterion**	**TMM criterion**	**Experiments**
0 - 45^0 -2a	Shear	-	Shear	Type I	-	Type I	22.6	-	24
a- 45^0 -2.2a	Mixed-mode	-	Mixed-mode	Type II	-	Type II	23.5	-	23
2a-45^0 -2.9a	Mixed-mode	Mixed-mode	Mixed-mode	Type III	Type II	Type III	20.8	40.7	26

6.7 Conclusions

This study applied the novel XFEM-based user element in simulating secondary cracks in pre-cracked gypsum specimens under compressive loading. The novel XFEM-based user element developed by authors (section 5.3.3) has the ability to simulate crack branching in quasi-brittle materials, which was verified in current research. For this purpose, various configurations of gypsum specimens containing single or double flaws were modeled. Additionally, the influence of crack initiation criteria on the path of secondary cracks in gypsum specimens was assessed using two criteria: (a) MSS and (b) TMM criteria. The findings of the study are summarized as follows:

- Two secondary crack initiation criteria mainly differed in the initiation angle of shear cracks with MSS criterion resulting in fracture being initiated at 45^0 from the horizontal axis irrespective of flaw number or its orientation. In contrast, the TMM criteria showed shear cracks initiated at different angles for different flaw configuration
- For the cases of single flaw gypsum specimens, the XFEM-based user element was able to accurately predict various characteristics of tensile wing cracks, such as its initiation angle and offset distance (Table 6-2) which can be attributed to the novel crack branching methodology. Additionally, both crack initiation criteria showed similar patterns of secondary cracks, which agreed with experimental observations. The two secondary crack initiation criteria mainly differed in the path and length of shear cracks, with the TMM criterion predicting shorter shear cracks (Table 6-3).
- Three configurations of double flaw gypsum specimens were simulated to assess the applicability of XFEM-based user element in modeling the crack coalescence mechanism. The analysis showed that the XFEM-based user element with MSS criterion could predict crack coalescence in both qualitative (coalescence type and its mode) and quantitative (crack coalescence stress) sense and thus can reasonably replicate real cracking patterns.

6.8 Acknowledgment

Funding for this research was provided by the National Science Foundation under Award number 1644326. The authors are grateful for this support.

CHAPTER 7

THESIS CONTRIBUTIONS AND RECOMMENDATIONS FOR FUTURE WORK

The focus of this thesis was to provide an improved understanding of fracture processes in quasi-brittle material under various loading conditions through laboratory-scale experiments and numerical modeling. The research involved an application of NDT techniques such as 2D-Digital image correlation (2D-DIC) and Acoustic emission (AE) to investigate the influence of fracture process zone in pre-cracked rock specimens. In addition, a novel extended Finite element XFEM-based user element has been developed to simulate the crack branching in quasi-brittle materials.

The main goal here is to provide a detailed characterization of the fracture process zone (FPZ) in quasi-brittle material under various loading conditions, from pure mode I loading to compression-induced mixed-mode I/II and shear loading. The existing studies primarily focused on characterizing FPZ development under mode I loading only. This is further complicated by the fact various mode II geometries don't even result in a mode II fracture. Consequently, there is a lack of suitable criterion that can describe the material softening behavior inside FPZ of mixed-mode I/II and mode II cracks. This limitation also exists in numerical models in simulating cracks, with most studies focusing on mode I fractures. Hence, this thesis implemented an extensive laboratory-scale experimental program that characterizes FPZ evolution in Barre granite specimens under mode I and mode II loading. The laboratory testing used in conjunction with NDT techniques such as DIC provided a quantitative estimate of the FPZ evolution and other crack properties, such as critical crack displacements, which can be used to develop

suitable constitutive models for FPZ. The applicability of these FPZ-based constitutive models required an advanced numerical modeling program, especially for compression-induced shear cracks that need the incorporation of frictional sliding during their propagation. For this purpose, a novel XFEM-based user element was developed, capable of simulating the FPZ development in various crack types. The approach to meet this thesis' objectives, the tasks carried out, and the corresponding significant outcomes are summarized in Table 7.1.

Table 7-1 Summary of the approach, tasks, and outcomes to meet the thesis objectives.

Thesis Objectives	**Approach**	**Tasks**	**Outcome**
Objective 1	Characterization of FPZ development for mode I fracture and identification of suitable model for material softening inside the FPZ of Barre granite.		
	Experimental Testing with DIC and AE	Developed DIC-based methodology for FPZ development	LCZM for mode I fracture
Objective 2	Evaluation of LCZM's performance in predicting the FPZ evolution in Barre granite specimens using an integrated approach.		
	Numerical modeling and uncertainty propagation under mode I loading	Quantifying uncertainty in fracture parameters under mode I loading, its influence on material response, and global sensitivity analysis.	Variability quantification in fracture behavior under mode I loading and importance ranking of material parameters
Objective 3	Determination of a suitable geometry for mode II fracture testing and evaluating the influence of pure mode II loading on the FPZ evolution in Barre granite specimens.		
	Experimental testing with DIC	Explored two mode II testing geometries along with the characterization of FPZ	SBC geometry suitable for mode II testing

Table 7-1 Continued

Objective 4	Development of a novel XFEM-based user element capable of simulating FPZ development and crack branching in quasi-brittle materials.		
	Numerical Modelling with XFEM-based user element	Developed a new XFEM-based user element with CZM to account for FPZ influence for multiple crack types	User element capable of simulating shear crack propagation and crack branching
Objective 5	Application of XFEM-based user element in modeling the secondary cracks in rock-like material under compressive loading.		
	Numerical Modelling with XFEM-based user element	Application of the XFEM model with two secondary crack initiation criteria	XFEM model capable of predicting secondary cracks and crack coalescence mechanisms

7.1 Major Conclusions

Based on the findings and results obtained from the laboratory experiments and numerical modeling, the major conclusions of this thesis are presented in the following subsections.

7.1.1 Characterization of FPZ Development in Mode I Fracture of Barre Granite Specimens

- This study presented a novel DIC-based methodology to characterize the FPZ evolution in a consistent manner for Barre granite specimens under mode I loading. The FPZ characteristics, such as its length and shape estimated from DIC analysis, were corroborated with AE measurements. The AE technique provides a quantitative estimate of micro-cracking activity inside the FPZ in the form of event locations and local energy dissipation.

- Both DIC-based (such as crack tip opening displacement ($CTOD$)) and AE-based measurements (AE event rate and associated energy release) can be independently used to characterize three stages of the FPZ evolution. The elastic stage was described by the linear variation of $CTOD$, which also resulted in negligible AE activity. The FPZ initiation from the notch tip was characterized by an accelerated rate of increase in $CTOD$, which was found to be a consequence of consistent AE activity with the initiation of high-energy events. The macro-crack initiation, which results in unstable crack propagation, was marked by the rapid jump in all three parameters $CTOD$, cumulative AE events, and cumulative AE event energy. Additionally, the macro-crack initiation occurred in the post-peak regime in all Barre granite specimens.
- The FPZ length at a given load stage was identified using the DIC-based COD profile along the fracture plane, which was corroborated using AE-based measurement. The FPZ identification using AE analysis included localized AE energy release inside the FPZ. For instance, the FPZ length and width were determined as the region containing a cluster of high-energy AE events. Both AE and DIC-based analysis showed a similar variation of FPZ length with applied load except for the small difference (~ 1 mm) after the macro-crack initiation from the notch tip. However, the FPZ width from the AE analysis was found to be two times larger than the value obtained from the DIC analysis.
- The linear cohesive zone model (LCZM) was found most suitable for characterizing material behavior inside the FPZ for Barre granite specimens under mode I loading, based on the linear relationship between FPZ length and inelastic $CTOD$ (both identified using DIC) in all tested Barre granite specimens.

- The failure mode inside the FPZ of Barre granite specimens under mode I loading was determined using a combination of AE and DIC analysis. The AE-based analysis includes the use of the moment tensor inversion technique. In DIC analysis, the strain field inside the FPZ was characterized by analyzing the minimum principal strains and maximum shear strain (γmax). Both analyses showed the presence of both tensile and shear micro-cracks with a significantly higher concentration of tensile events than shear. The presence of shear events can be attributed to the tortuous crack path, which in the relatively coarse grain structure of Barre granite, resulted in several shear microcracks being formed across multiple grain boundaries.

7.1.2 Integrated Approach for Evaluating the Linear Cohesive Zone Model's performance in the Fracturing of Barre granite Specimens.

- This study used an integrated approach to evaluate the linear cohesive zone model's (LCZM) capability in predicting the fracture processes in notched Barre granite specimens under mode I loading. The approach included four steps: (a) experimental testing, (b) numerical simulation, (c) uncertainty quantification of material response, and (d) global sensitivity analysis.
- The LCZM implementation using the deterministic numerical model (XFEM-based simulation) was found inadequate in representing the variability in fracture behavior defined in terms of the peak load and the FPZ size observed in laboratory-scale Barre granite specimens. This variability can be attributed to variability in its input parameters, such as tensile strength, critical inelastic crack opening, and elastic modulus.

- Despite variability in input parameters of the LCZM, a significant size of the FPZ around the notch tip was observed, indicating the large scale yielding in the laboratory scale Barre granite specimens under mode I loading. As a result, macro-crack initiation is most likely to occur in the post-peak regime.
- The results from Global sensitivity analysis indicated that tensile strength is the predominantly sensitive parameter towards variability in the global response of the Barre granite specimens. However, the variability in various fracture characteristics, such as the three stages of the FPZ evolution and its size, is sensitive to all three input parameters.

7.1.3 Fracture Process Zone Evolution under Mode II Loading

- In tested NDB specimens, a kinked fracture was observed from the notch tip instead of the expected coplanar shear crack under pure mode II loading. The fracture mode was estimated using the displacement approach of DIC, which showed that the FPZ primarily consists of the mode I component. This was evident by the presence of a large value of opening displacement while sliding displacements were found to be negligible, indicating crack initiation under pure mode I.
- The evolution of the FPZ in NDB specimens was characterized using the novel methodology developed for mode I fracture in Barre granite specimens. The FPZ in NDB specimens initiated at the notch tip, with its evolution similar to cases of pure mode I loading on the same rock. As a result, FPZ characteristics, such as its length and critical crack opening displacement, were found to be within the range of values obtained from mode I fracture toughness testing. This indicated that the mode II loading had negligible

influence on the FPZ development and only resulted in a non-symmetric pattern of normal displacement along the initiated fracture.

- In contrast, the SBC specimens resulted in a dominant vertical fracture that coincided with the location of a high concentration of shear stress region in the ligament between its two horizontal notches. The DIC analysis showed that the vertical fracture in SBC specimens consists of a merge band between two notches, indicating shear dislocation in the ligament region. The fracture mode of this vertical fracture was found to be mixed-mode I/II with a similar contribution of mode I and mode II components.
- The evolution of FPZ in SBC specimens was characterized by analyzing the variation of both crack opening displacement and the crack sliding displacement at the ligament center. The analysis showed that the FPZ initiated around the ligament center under the tensile mode, which then underwent shearing as it covered the entire region between its two notches.
- The influence of confining pressure in the SBC specimens was assessed by analyzing the evolution of crack opening and sliding displacements inside the FPZ of dominant vertical fracture. With an increase in confining pressure, the transition of FPZ into a macro-crack got delayed, allowing the ligament region to sustain higher levels of damage, thereby increasing its fracture resistance before its failure. This was corroborated by the increase in mode II fracture toughness of the Barre granite specimens with the confining stress.
- The fracture patterns observed in SBC specimens were similar to other known mode II geometry, such as punch through the shear test, making it a suitable configuration for estimating mode II fracture toughness in rocks.

7.1.4 XFEM-based User-elements for Crack Branching in Quasi-brittle Materials

- In this study, a novel XFEM-based user element was developed with the capability of simulating complex crack interaction, including crack branching in quasi-brittle materials. The XFEM-based user element also accounts for FPZ development in different crack types through Cohesive zone models that simulate material softening inside the FPZ
- The XFEM-based user element was validated using two benchmark case studies of mode I and mixed-mode I/II loading. The results showed that the XFEM-based user element could simulate FPZ development under tensile and tensile-shear loading, as the results obtained agreed with other numerical studies /experimental data
- In the case of compression-induced shears loading, XFEM-based user elements were able to predict both the shear crack path and global behaviors of the overconsolidated clay specimen with reasonable accuracy. Additionally, the simulation of different cases of the overconsolidated clay specimen's friction angle confirmed the XFEM model's ability to simulate normal stress-dependent behavior of peak and residual strength of shear cracks.
- The capability of novel crack branching methodology of XFEM-based user elements was assessed using single flawed gypsum specimens under uniaxial compression loading. The analysis showed that the crack branching methodology accurately predicted tensile wing cracks in terms of their location and initiation angle, which may otherwise need enrichment for crack tip singularity in traditional XFEM models. Additionally, the XFEM-based user element was able to predict the formation of both primary and secondary cracks and thus can replicate real cracking patterns with reasonable accuracy.

7.1.5 Application of XFEM-based User-elements in Predicting Secondary Cracks under Compression Loading

- This study assessed the applicability of the XFEM-based user element in simulating secondary cracks in pre-cracked gypsum specimens under compressive loading, along with investigating the influence of crack initiation criteria on the path of secondary cracks. Two secondary crack initiation criteria, namely: (a) Maximum shear stress (MSS) and (b) Traction-based mixed-mode (TMM) criteria, were used in this study. The two criteria mainly differed in the initiation angle of shear cracks. The MSS criterion resulted in fracture being initiated at 450 from the horizontal axis irrespective of flaw number or its orientation. In contrast, the TMM criteria showed shear cracks initiated at different angles for different flaw configurations of gypsum specimens.
- In single-flaw gypsum specimens, the XFEM-based user element could accurately predict various characteristics of tensile wing cracks, such as its initiation angle and offset distance. Additionally, both crack initiation criteria showed similar patterns of secondary cracks, which agreed with experimental observations. The two secondary crack initiation criteria mainly differed in the path and length of shear cracks, with the TMM criterion predicting shorter shear cracks.
- In double flaw gypsum specimens, XFEM-based user elements with MSS criterion predicted crack coalescence in both qualitative (coalescence type and its mode) and quantitative (crack coalescence stress) sense, thereby replicating overall cracking patterns.

7.2 Major Contribution

The specific scientific contributions of this thesis to advance the state of knowledge associated with the fracture processes zone development in quasi-brittle materials can be summarized in detail as follows:

- A novel DIC-based methodology was developed that can characterize the FPZ evolution in Barre granite specimens in a consistent manner. This methodology showed significantly lower variability in FPZ characteristics, such as its length and width, and parameters of the cohesive zone model, such as critical opening displacement, compared to existing studies on mode I loading in rocks.
- For the first time, a unique integrated approach was used to quantify uncertainty in material and fracture properties, along with assessing their effect on the variability in the overall fracture behavior of Barre granite specimens.
- For the first time, a systematic evolution was done toward the relative importance of fracture properties of Barre granite specimens in governing its global response and FPZ development under mode I loading.
- It was established that the novel DIC-based methodology is also a reliable approach for characterizing the FPZ evolution under mode II loading, irrespective of the fracture mode obtained.
- It was established that the SBC geometry could be a good alternative for estimating mode II fracture toughness compared to other known testing configurations, such as punch-through shear tests based on similar fracture patterns obtained in two geometries. The

SBC geometry can be monitored using optical techniques such as DIC, which provide explicit evidence of the fracture mode and other deformation characteristics that cannot be applied to the punch-through shear testing.

- It was established from the DIC-based analysis that known mode II geometries, such as punch-through shear and SBC tests, might not necessarily result in pure shear cracks, especially when applied confining stress is lower than the material's tensile strength.
- A novel XFEM-based user element was developed in this research capable of simulating multiple crack interactions, including crack branching mechanism in quasi-brittle materials traditionally limited to dynamic fracture problems. As a result, the XFEM-based user element can simulate the formation of multiple crack types from the body of pre-existing cracks. This was a major shortcoming of other XFEM models that limited their application to rock fracturing problems.
- A new cohesive zone model for compression-induced shear cracks was implemented that accounts for both cohesion degradation and frictional sliding in the propagating fracture. This model accounts for both frictional energy dissipation and fracture energy release during the FPZ development, making it consistent with the fracture mechanics theory of frictional cracks.

7.3 Recommendations for Future Research

The thesis aimed to provide an improved understanding of the fracture process zone and its influence on fracturing in quasi-brittle material using laboratory testing and computational modeling. There are various ways to expand the research pursued in this thesis, which could include the following.

- The development of experimentally verified softening models for mode II and mixed-mode I/II fractures in rocks. As current research mainly focuses on identifying suitable geometry for mode II testing. The next critical step is determining a reliable constitutive model that accounts for the material softening inside the FPZ of mode II and mixed-mode I/II cracks. This would expand the capability of a numerical model in predicting the initiation and propagation of various crack types in quasi-brittle materials such as rocks and other rock-like materials. To circumvent this limitation, existing numerical studies assume similar constitutive behaviors of material for mode I and mode II cracks, along with calibrating fracture properties to match the experimental results. This can work for homogeneous and isotropic materials such as gypsum, as shown in current research; however, it may not be applicable to other heterogeneous rocks.
- The XFEM-based user element developed in this thesis represents an important starting point for a compelling computational framework for its applications in the rock structures, such as slope stability and tunnel design across multiple rock formations. For instance, this XFEM-based user element, due to its capability to simulate multiple crack types and their interactions, can become an effective tool in investigating failure mechanisms of jointed rock slopes.
- Simulating heterogeneous rock material using random field theory which allows the incorporation of spatial variation of fracture properties through finite element mesh, can be another addition to the XFEM model. The current research used the random variable approach to investigate the influence of variability in the material parameters of Barre granite. However, this approach may not be applicable to highly heterogeneous and

anisotropic rocks such as shale, where localized material behavior would significantly affect the fracture path and its overall failure. Alternatively, the XFEM model using random field theory can account for random fracture propagation patterns in such rocks due to its capability of simulating crack branching in quasi-brittle material.

REFERENCES

Aggelis DG, Verbruggen S, Tsangouri E, et al (2013) Characterization of mechanical performance of concrete beams with external reinforcement by acoustic emission and digital image correlation. Construction and Building Materials 47:1037–1045.

Alam, S. Y., Loukili, A., Grondin, F., & Rozière, E. (2015). Use of the digital image correlation and acoustic emission technique to study the effect of structural size on cracking of reinforced concrete. Engineering Fracture Mechanics, 143, 17–31.

Aliabadian, Z., Zhao, G. F., & Russell, A. R. (2019). Crack development in transversely isotropic sandstone discs subjected to Brazilian tests observed using digital image correlation. International Journal of Rock Mechanics and Mining Sciences, 119, 211–221.

Aliha, M R M, Ashtari, R., & Ayatollahi, M. R. (2006). Mode I and Mode II Fracture Toughness Testing for a Coarse Grain Marble. Applied Mechanics and Materials, 5–6, 181–188.

Aliha, M R M, Ayatollahi, M. R., & Kharazi, B. (2009a). Mode II Brittle Fracture Assessment Using ASFPB Specimen. International Journal of Fracture, 159(2), 241.

Aliha, M R M, Ayatollahi, M. R., Smith, D. J., & Pavier, M. J. (2010). Geometry and size effects on fracture trajectory in a limestone rock under mixed mode loading. Engineering Fracture Mechanics,77(11),2200–2212.

Aliha, M. R.M., Mahdavi, E., & Ayatollahi, M. R. (2018a). Statistical Analysis of Rock Fracture Toughness Data Obtained from Different Chevron Notched and Straight Cracked Mode I Specimens. Rock Mechanics and Rock Engineering, 51(7), 2095–2114.

Aliha, M. R.M., Mousavi, S. S., & Ghoreishi, S. M. N. (2019). Fracture load prediction under mixed mode I + II using a stress based method for brittle materials tested with the asymmetric four-point bend specimen. Theoretical and Applied Fracture Mechanics, 103.

Aliha, Mohammad Reza Mohammad, Mahdavi, E., & Ayatollahi, M. R. (2017). The Influence of Specimen Type on Tensile Fracture Toughness of Rock Materials. Pure and Applied Geophysics, 174(3), 1237–1253.

Al-Shayea, N. A. (2005). Crack propagation trajectories for rocks under mixed mode I–II fracture. EngineeringGeology,81(1),84–97.

Ayatollahi, M. R., & Aliha, M. R. M. (2007). Wide range data for crack tip parameters in two disc-type specimens under mixed mode loading. Computational Materials Science, 38(4), 660–670.

Ayatollahi, M. R., & Sistaninia, M. (2011). Mode II fracture study of rocks using Brazilian disk specimens. International Journal of Rock Mechanics and Mining Sciences, 48(5), 819–826.

Ayatollahi, M. R., Rashidi Moghaddam, M., & Berto, F. (2015). A generalized strain energy density criterion for mixed mode fracture analysis in brittle and quasi-brittle materials. Theoretical and Applied Fracture Mechanics, 79, 70–76.

Backers, T., Stanchits, S., & Dresen, G. (2005). Tensile fracture propagation and acoustic emission activity in sandstone: The effect of loading rate. International Journal of Rock Mechanics and Mining Sciences, 42(7), 1094–1101.

Ban, H., Im, S., & Kim, Y.-R. (2015). Mixed-mode fracture characterization of fine aggregate mixtures using semicircular bend fracture test and extended finite element modeling. Construction and Building Materials, 101, 721–729. https://doi.org/https://doi.org/10.1016/j.conbuildmat.2015.10.083.

Bažant Z, Yu Q (2011) Size-Effect Testing of Cohesive Fracture Parameters and Nonuniqueness of Work-of-Fracture Method. Journal of Engineering Mechanics 137:580–588.

Bažant ZP (2002) Concrete fracture models: testing and practice. Engineering Fracture Mechanics 69:165–205. https://doi.org/https://doi.org/10.1016/S0013-7944(01)00084-4

Bažant ZP, Becq-Giraudon E (2002) Statistical prediction of fracture parameters of concrete and implications for choice of testing standard. Cem Concr Res 32:529–556.

Belytschko T, Black T (1999) Elastic crack growth in finite elements with minimal remeshing. Int J Numer Methods Eng 45:601–620.

Bhowmik S, Ray S (2019) An experimental approach for characterization of fracture process zone in concrete. Engineering Fracture Mechanics 211:401–419.

Bobet, A., & Einstein, H. H. (1998). Numerical modeling of fracture coalescence in a model rock material. International Journal of Fracture, 92(3), 221.

Borja RI, Foster CD (2007) Continuum mathematical modeling of slip weakening in geological systems. J Geophys Res Solid Earth 112:.

Borst R de, Remmers JJC, Needleman A (2006) Mesh-independent discrete numerical representations of cohesive-zone models. Eng Fract Mech 73:160–177.

Bryant EC, Sun W (2018) A mixed-mode phase field fracture model in anisotropic rocks with consistent kinematics. Comput Methods Appl Mech Eng 342:561–584.

Chabot, A., Hammoum, F., & Hun, M. (2017). A 4pt bending bond test approach to evaluate water effect in a composite beam. European Journal of Environmental and Civil Engineering, 21(sup1), 54–69.

Chang, S.-H., Lee, C.-I., & Jeon, S. (2002). Measurement of rock fracture toughness under modes I and II and mixed-mode conditions by using disc-type specimens. Engineering Geology, 66(1), 79–97.

Chen, M., Yang, S., Gamage, R. P., Yang, W., Yin, P., Zhang, Y., & Zhang, Q. (2019). Fracture processes of rock-like specimens containing nonpersistent fissures under uniaxial compression. Energies, 12(1).

Cheng H, Zhou X (2020) An energy-based criterion of crack branching and its application on the multidimensional space method. Int J Solids Struct 182–183:179–192.

Cheng, W., Jin, Y., Chen, M. (2014) A criterion for identifying hydraulic fractures crossing natural fractures in 3D space. Petroleum Exploration and Development 41:371–376.

Cheng, Y., & Wong, L. N. Y. (2018). Microscopic Characterization of Tensile and Shear Fracturing in Progressive Failure in Marble. Journal of Geophysical Research: Solid Earth, 123(1), 204–225.

Chu, T.C., Ranson, W.F., Sutton, MA (1985) Applications of digital-image-correlation techniques to experimental mechanics. Experimental Mechanics 25:232–244.

Cruz, F., Roehl, D., Vargas, E.do A. (2018) An XFEM element to model intersections between hydraulic and natural fractures in porous rocks. International Journal of Rock Mechanics and Mining Sciences 112:385–397.

Cruz, F., Roehl, D., Vargas, E.do A. (2019) An XFEM implementation in Abaqus to model intersections between fractures in porous rocks. Comput Geotech 112:135–146.

Dai F, Xia K (2010) Loading Rate Dependence of Tensile Strength Anisotropy of Barre Granite. Pure and Applied Geophysics 167:1419–1432.

Dautriat J, Bornert M, Gland N, et al (2011) Localized deformation induced by heterogeneities in porous carbonate analysed by multi-scale digital image correlation. Tectonophysics 503:100–116.

Daux C, Moës N, Dolbow J, et al (2000) Arbitrary branched and intersecting cracks with the extended finite element method. Int J Numer Methods Eng 48:1741–1760.

De Borst R (2003) Numerical aspects of cohesive-zone models. Engineering Fracture Mechanics 70:1743–1757.

Dimitri R, Trullo M, de Lorenzis L, Zavarise G (2015) Coupled cohesive zone models for mixed-mode fracture: A comparative study. Eng Fract Mech 148:145–179.

Dobroskok, A., Ghassemi, A., & Linkov, A. (2005). Extended structural criterion for numerical simulation of crack propagation and coalescence under compressive loads. International Journal of Fracture, 133(3), 223–246.

Dolbow J, Moës N, Belytschko T (2001) An extended finite element method for modeling crack growth with frictional contact. Comput Methods Appl Mech Eng 190:6825–6846.

Dong, W., Wu, Z., Zhou, X., Dong, L., & Kastiukas, G. (2017). FPZ evolution of mixed mode fracture in concrete: Experimental and numerical. Engineering Failure Analysis, 75, 54–70.

Dual J, Schwarz T (2012) Acoustofluidics 3: Continuum mechanics for ultrasonic particle manipulation. Lab on a Chip 12:244–252.

Dugdale, D. S. (1960). Yielding of steel sheets containing slits. Journal of the Mechanics and Physics of Solids, 8(2), 100–104.

Dumstorff P, Meschke G (2007) Crack propagation criteria in the framework of X-FEM-based structural analyses. Int J Numer Anal Methods Geomech 31:239–259.

Dutler, N., Nejati, M., Valley, B., Amann, F., & Molinari, G. (2018). On the link between fracture toughness, tensile strength, and fracture process zone in anisotropic rocks. Engineering Fracture Mechanics, 201, 56–79.

Eberhardt, E., Stead, D., Stimpson, B., & Read, R. (1998). Identifying crack initiation and propagation thresholds in brittle rock. Canadian geotechnical journal, 35 (2), 222–233

Elices M, Guinea G v, Gómez J, Planas J (2002) The cohesive zone model: advantages, limitations and challenges. Engineering Fracture Mechanics 69:137–163.

Erdogan, F., & Sih, G. C. (1963). On the Crack Extension in Plates Under Plane Loading and Transverse Shear. Journal of Basic Engineering, 85(4), 519–525.

Fakhimi A, Tarokh A (2013) Process zone and size effect in fracture testing of rock. International Journal of Rock Mechanics and Mining Sciences 60:95–102.

Fan, C., & Jing, X. Q. (2013). Numerical Study of Crack Propagation Path in Three-Point Bending Beam Using Extended Finite Element Method. Applied Mechanics and Materials, 353–356, 3615–3618.

Fatehi Marji M (2014) Numerical analysis of quasi-static crack branching in brittle solids by a modified displacement discontinuity method. Int J Solids Struct 51:1716–1736.

Fei F, Choo J (2020) A phase-field model of frictional shear fracture in geologic materials. Comput Methods Appl Mech Eng 369:113265.

Fei F, Choo J (2021) Double-phase-field formulation for mixed-mode fracture in rocks. Comput Methods Appl Mech Eng 376:113655.

Fries T-P, Belytschko T (2010) The extended/generalized finite element method: An overview of the method and its applications. Int J Numer Methods Eng 84:253–304.

Garg P, Hedayat A, Griffiths D v. (2020) Numerical simulation of fracture initiation in barre granite using an experimentally validated XFEM model. In: 54th U.S. Rock Mechanics/Geomechanics Symposium.

Garg, P., Pandit, B., Hedayat, A, Griffiths, D.V., and Lakshminarasimha Sivakumar Babu, G. (2022). An Integrated Approach for Evaluation of Linear Cohesive Zone Model's Performance in Fracturing of Rocks. Rock Mechanics and Rock Engineering

Garg, P., Hedayat, A., and Griffiths, D.V. (2023) A novel methodology for characterizing fracture process zone evolution in Barre granite specimens under three-point bending. Theoretical and Appled fracture mechanics.

Garg, P., Hedayat, A., and Griffiths, D.V. (2023). An XFEM formulation for crack branching in quasi-brittle materials. Computers and Geotechnics (Under Review).

Garg, P., Hedayat, A., and Griffiths, D.V. (2023). Fracture process evolution under mode II loading of Barre granite using notched beam and short beam compression tests. Engineering Fracture Mechanics (Under Review).

Garg, P., Hedayat, A., and Griffiths, D.V. (2023). Application of XFEM-based element for predicting secondary cracks. the International Journal of Rock Mechanics and Mining Science (Under Review).

Ghamgosar M, Erarslan N (2016) Experimental and Numerical Studies on Development of Fracture Process Zone (FPZ) in Rocks under Cyclic and Static Loadings. Rock Mechanics and Rock Engineering 49:893–908.

Ghazvinian, A., Nejati, H. R., Sarfarazi, V., & Hadei, M. R. (2013). Mixed mode crack propagation in low brittle rock-like materials. Arabian Journal of Geosciences, 6(11), 4435–4444.

Gill SPA (2021) A damage model for the frictional shear failure of brittle materials in compression. Comput Methods Appl Mech Eng 385:114048.

Giner E, Sukumar N, Tarancón JE, Fuenmayor FJ (2009) An Abaqus implementation of the extended finite element method. Engineering Fracture Mechanics 76:347–368.

Goldsmith W, Sackman JL, Ewerts C (1976) Static and dynamic fracture strength of Barre granite. International Journal of Rock Mechanics and Mining Sciences & Geomechanics Abstracts 13:303–309.

Gonçalves Da Silva B, Einstein HH (2013) Modeling of crack initiation, propagation and coalescence in rocks. International Journal of Fracture 182:167–186.

Gongalves Da Silva, B. M., & Einstein, H. H. (2009). Modeling of Crack Initiation, Propagation and Coalescence in Rocks.

Ha, K., Baek, H., & Park, K. (2015). Convergence of fracture process zone size in cohesive zone modeling. Applied Mathematical Modelling, 39(19), 5828–5836.

Harr ME (1989) Probabilistic estimates for multivariate analyses. Applied Mathematical Modelling 13:313–318.

Hedayat A, Pyrak-Nolte LJ, Bobet A (2014) Multi-Modal Monitoring of Slip Along Frictional Discontinuities. Rock Mechanics and Rock Engineering 47:1575–1587.

Hedayat, A., & Walton, G. (2017). Laboratory determination of rock fracture shear stiffness using seismic wave propagation and digital image correlation. Geotechnical Testing Journal, 40(1), 92–106.

Hillerborg, A., Modéer, M., & Petersson, P.-E. (1976). Analysis of crack formation and crack growth in concrete by means of fracture mechanics and finite elements. Cement and Concrete Research, 6(6), 773–781.

Hoagland, R. G., Hahn, G. T., & Rosenfield, A. R. (1973). Influence of microstructure on fracture propagation in rock. Rock Mechanics, 5(2), 77–106.

Hoek E, Kaiser PK, Bawden WF (1995) Support of Underground Excavations in Hard Rock, 1st Edition. CRC Press, London

Hong HP (1998) An efficient point estimate method for probabilistic analysis. Reliability Engineering & System Safety 59:261–267.

Hussain, M. A., Pu, S. L., & Underwood, J. (1974). Strain Energy Release Rate for a Crack Under Combined Mode I and Mode II. In G. R. Irwin (Ed.), Fracture Analysis: Proceedings of the 1973 National Symposium on Fracture Mechanics, Part II (pp. 2–28). ASTM International.

Hyeok SS, H PG, G BW (2006) Simulation of Crack Propagation in Asphalt Concrete Using an Intrinsic Cohesive Zone Model. J Eng Mech 132:1215–1223.

Im S, Ban H, Kim Y-R (2014) Characterization of mode-I and mode-II fracture properties of fine aggregate matrix using a semicircular specimen geometry. Construction and Building Materials 52:413–421.

Ingraffea, A. R., & Heuze, F. E. (1980). Finite element models for rock fracture mechanics. International Journal for Numerical and Analytical Methods in Geomechanics, 4(1), 25–43.

Iqbal MJ, Mohanty B (2007) Experimental Calibration of ISRM Suggested Fracture Toughness Measurement Techniques in Selected Brittle Rocks. Rock Mechanics and Rock Engineering 40:453

Janssen, C., Wagner, F. C., Zang, A., & Dresen, G. (2001). Fracture process zone in granite: A microstructural analysis. International Journal of Earth Sciences, 90(1), 46–59.

Ji WW, Pan PZ, Lin Q, et al (2016) Do disk-type specimens generate a mode II fracture without confinement? International Journal of Rock Mechanics and Mining Sciences 87:48–54.

Jiang Q, Zhong S, Cui J, et al (2016) Statistical Characterization of the Mechanical Parameters of Intact Rock Under Triaxial Compression: An Experimental Proof of the Jinping Marble. Rock Mechanics and Rock Engineering 49:4631–4646.

Jianye C, Kok-Kwang P (2019) Constructing Site-Specific Multivariate Probability Distribution Model Using Bayesian Machine Learning. Journal of Engineering Mechanics 145:04018126.

Kao C-S, Carvalho FCS, Labuz JF (2011) Micromechanisms of fracture from acoustic emission. International Journal of Rock Mechanics and Mining Sciences 48:666–673.

Karihaloo, B. L., & Xiao, Q. Z. (2003). Modelling of stationary and growing cracks in FE framework without remeshing: a state-of-the-art review. Computers & Structures, 81(3), 119–129.

Kataoka, M., Obara, Y., & Kuruppu, M. (2015). Estimation of Fracture Toughness of Anisotropic Rocks by Semi-Circular Bend (SCB) Tests Under Water Vapor Pressure. Rock Mechanics and Rock Engineering, 48(4), 1353–1367.

Kaung Jain Chang. (1981). On the maximum strain criterion—a new approach to the angled crack problem. Engineering Fracture Mechanics, 14(1), 107–124.

Kazerani, T., & Zhao, J. (2010). Micromechanical parameters in bonded particle method for modelling of brittle material failure. International Journal for Numerical and Analytical Methods in Geomechanics, 34(18), 1877–1895.

Khoei AR (2014) Extended Finite Element method: Theory and Applications, 1st Edition. John Wiley & Sons, Ltd., West Sussex United Kingdom.

Khoei AR, Mohammadnejad T (2011) Numerical modeling of multiphase fluid flow in deforming porous media: A comparison between two- and three-phase models for seismic analysis of earth and rockfill dams. Computers and Geotechnics 38:142–166.

Khoei AR, Nikbakht M (2007) An enriched finite element algorithm for numerical computation of contact friction problems. Int J Mech Sci 49:183–199.

Khoei AR, Vahab M, Hirmand M (2016) Modeling the interaction between fluid-driven fracture and natural fault using an enriched-FEM technique. Int J Fract 197:1–24.

Khoei, A. R., & Mohammadnejad, T. (2011). Numerical modeling of multiphase fluid flow in deforming porous media: A comparison between two- and three-phase models for seismic analysis of earth and rockfill dams. Computers and Geotechnics, 38(2), 142–166.

Khoramishad H, Akbardoost J, Ayatollahi MR (2013) Size effects on parameters of cohesive zone model in mode I fracture of limestone. International Journal of Damage Mechanics 23:588–605.

Knuth, M. W., Tobin, H. J., & Marone, C. (2013). Evolution of ultrasonic velocity and dynamic elastic moduli with shear strain in granular layers. Granular Matter, 15(5), 499–515.

Krishnamurthy T (2003) Response Surface Approximation with Augmented and Compactly Supported Radial Basis Functions. In: 44th AIAA/ASME/ASCE/AHS/ASC Structures, Structural Dynamics, and Materials Conference. American Institute of Aeronautics and Astronautics

Kuruppu, M D, Obara, Y., Ayatollahi, M. R., Chong, K. P., & Funatsu, T. (2014a). ISRM-Suggested Method for Determining the Mode I Static Fracture Toughness Using Semi-Circular Bend Specimen. Rock Mechanics and Rock Engineering, 47(1), 267–274.

Kurz, J. H., Grosse, C. U., & Reinhardt, H.-W. (2005). Strategies for reliable automatic onset time picking of acoustic emissions and of ultrasound signals in concrete. Ultra-sonics, 43 (7), 538–546.

Labuz JF, Biolzi L (1991) Class I vs Class II stability: a demonstration of size effect. International Journal of Rock Mechanics and Mining Sciences & Geomechanics Abstracts 28:199–205

Labuz JF, Shah SP, Dowding CH (1987) The fracture process zone in granite: evidence and effect. International Journal of Rock Mechanics and Mining Sciences & Geomechanics Abstracts 24:235–246.

Le J-L, Manning J, Labuz JF (2014) Scaling of fatigue crack growth in rock. International Journal of Rock Mechanics and Mining Sciences 72:71–79.

Lee, H., & Jeon, S. (2011). An experimental and numerical study of fracture coalescence in pre-cracked specimens under uniaxial compression. International Journal of Solids and Structures, 48(6), 979–999.

Li, Bing Q., & Einstein, H. H. (2019). Direct and Microseismic Observations of Hydraulic Fracturing in Barre Granite and Opalinus Clayshale. Journal of Geophysical Research: Solid Earth, 124(11), 11900–11916.

Li, Bing Qiuyi, & Einstein, H. H. (2017). Comparison of Visual and Acoustic Emission Observations in a Four Point Bending Experiment on Barre Granite. Rock Mechanics and Rock Engineering, 50(9), 2277–2296.

Li, H., & Wong, L. N. Y. (2012). Influence of flaw inclination angle and loading condition on crack initiation and propagation. International Journal of Solids and Structures, 49(18), 2482–2499.

Lin Q, Fakhimi A, Haggerty M, Labuz JF (2009) Initiation of tensile and mixed-mode fracture in 990 sandstone. International Journal of Rock Mechanics and Mining Sciences 46:489–497. 991 https://doi.org/https://doi.org/10.1016/j.ijrmms.2008.10.008.

Lin Q, Labuz JF (2013) Fracture of sandstone characterized by digital image correlation. International Journal of Rock Mechanics and Mining Sciences 60:235–245.

Lin Q, Wan B, Wang Y, et al (2019b) Unifying acoustic emission and digital imaging observations of quasi-brittle fracture. Theoretical and Applied Fracture Mechanics 103.

Lin Q, Wang S, Pan PZ, et al (2020) Imaging opening-mode fracture in sandstone under three-point bending: A direct identification of the fracture process zone and traction-free crack based on cohesive zone model. International Journal of Rock Mechanics and Mining Sciences 136:104516. https://doi.org/https://doi.org/10.1016/j.ijrmms.2020.104516

Lin Q, Yuan H, Biolzi L, Labuz JF (2014) Opening and mixed mode fracture processes in a quasi-brittle material via digital imaging. Engineering Fracture Mechanics 131:176–193. https://doi.org/10.1016/j.engfracmech.2014.07.028

Lin, Q., Ji, W. W., Pan, P. Z., Wang, S., & Lu, Y. (2019a). Comments on the mode II fracture from disk-type specimens for rock-type materials. Engineering Fracture Mechanics, 211, 303–320. https://doi.org/10.1016/j.engfracmech.2019.02.024

Lin, Q., Mao, D., Wang, S., & Li, S. (2018). The influences of mode II loading on fracture process in rock using acoustic emission energy. Engineering Fracture Mechanics, 194, 136–144. https://doi.org/10.1016/j.engfracmech.2018.03.001

Lin, Q., Wan, B., Wang, S., Li, S., & Fakhimi, A. (2019b). Visual detection of a cohesionless crack in rock under three-point bending. Engineering Fracture Mechanics, 211, 17–31. https://doi.org/10.1016/j.engfracmech.2019.02.009

Lin, Q., Wan, B., Wang, Y., Lu, Y., & Labuz, J. F. (2019c). Unifying acoustic emission and digital imaging observations of quasi-brittle fracture. Theoretical and Applied Fracture Mechanics, 103. https://doi.org/10.1016/j.tafmec.2019.102301

Lin, Q., Wang, S., Pan, P. Z., Ji, W. W., & Lu, Y. (2020). Fracture initiation under pure shear revisited: Remarks on the mode II fracture in quasi-brittle materials. Theoretical and Applied Fracture Mechanics, 109. https://doi.org/10.1016/j.tafmec.2020.102700

Lin, Q., Yuan, H., Biolzi, L., & Labuz, J. F. (2014). Opening and mixed mode fracture processes in a quasi-brittle material via digital imaging. Engineering Fracture Mechanics, 131, 176–193. https://doi.org/10.1016/j.engfracmech.2014.07.028.

Liu F, Borja RI (2008) A contact algorithm for frictional crack propagation with the extended finite element method. Int J Numer Methods Eng 76:1489–1512. https://doi.org/https://doi.org/10.1002/nme.2376

Liu F, Borja RI (2009) An extended finite element framework for slow-rate frictional faulting with bulk plasticity and variable friction. Int J Numer Anal Methods Geomech 33:1535–1560. https://doi.org/https://doi.org/10.1002/nag.777

Liu P (2015) Extended finite element method for strong discontinuity analysis of strain localization of non-associative plasticity materials. Int J Solids Struct 72:174–189. https://doi.org/https://doi.org/10.1016/j.ijsolstr.2015.07.021.

Liu, H. Z., Lin, J. S., He, J. da, & Xie, H. Q. (2018). Dominant mode of planar fractures and the role of material properties. Engineering Fracture Mechanics, 195, 57–79. https://doi.org/10.1016/j.engfracmech.2018.03.024

Lu, Y., Li, W., Wang, L., Meng, X., Wang, B., Zhang, K., & Zhang, X. (2019). In-situ microscale visualization experiments on microcracking and microdeformation behaviour around a pre-crack tip in a three-point bending sandstone. International Journal of Rock Mechanics and Mining Sciences, 114, 175–185. https://doi.org/10.1016/j.ijrmms.2019.01.002

Lua, J., Zhang, T., Fang, E., & Song, J. H. (2016). Explicit phantom paired shell element approach for crack branching and impact damage prediction of aluminum structures. International Journal of Impact Engineering, 87, 28–43. https://doi.org/10.1016/j.ijimpeng.2015.07.007

Luo, L., Li, X., Qiu, J., & Zhu, Q. (2017). Study on Fracture Initiation and Propagation in a Brazilian Disc with a Preexisting Crack by Digital Image Correlation Method. Advances in Materials Science and Engineering, 2017.

Luzio, G. D. and Cusatis, G (2018) Cohesive crack analysis of size effect for samples with blunt notches and generalized size effect curve for quasi-brittle materials, Engineering Fracture Mechanics,204, 15-28.

Maeda, N. (1985). A method for reading and checking phase times in autoprocessing system of seismic wave data. Zisin, 38 , 365–379.

Maji, A. K., & Wang, J. L. (1992). Rock Mechanics and Rock Engineering Experimental Study of Fracture Processes in Rock.

Melenk, J. M., & Babuskab3, I. (1996). The partition of unity finite element method: Basic theory and applications. In Comput. Methods Appl. Mech. Engrg (Vol. 139).

Melin, S. (1986). Fracture from a straight crack subjected to mixed mode loading. International Journal of Fracture, 32(4), 257–263.

Menk A, Bordas SPA (2011) A robust preconditioning technique for the extended finite element method. Int J Numer Methods Eng 85:1609–1632.

Meschke G, Dumstorff P (2007) Energy-based modeling of cohesive and cohesionless cracks via X-FEM. Comput Methods Appl Mech Eng 196:2338–2357.

Miao, S., Pan, P. Z., Wu, Z., Li, S., & Zhao, S. (2018). Fracture analysis of sandstone with a single filled flaw under uniaxial compression. Engineering Fracture Mechanics, 204, 319–343. https://doi.org/10.1016/j.engfracmech.2018.10.009

Miller JT (2008) Crack coalescence in granite. MSc Thesis, Massachusetts Institute of Technology.

Mindess, S. (1984). The effect of specimen size on the fracture energy of concrete. Cement and Concrete Research, 14(3), 431–436.

Mirsayar, M. M., Razmi, A., Aliha, M. R. M., & Berto, F. (2018). EMTSN criterion for evaluating mixed mode I/II crack propagation in rock materials. Engineering Fracture Mechanics, 190, 186–197.

Moazzami, M., Ayatollahi, M. R., & Akhavan-Safar, A. (2020). Assessment of the fracture process zone in rocks using digital image correlation technique: The role of mode-mixity, size, geometry and material. International Journal of Damage Mechanics, 29(4), 646–666.

Modiriasari, A., Pyrak-Nolte, L. J., & Bobet, A. (2018). Emergent Wave Conversion as a Precursor to Shear Crack Initiation. Geophysical Research Letters, 45(18), 9516–9522.

Moës, N., & Belytschko, T. (2002). Extended finite element method for cohesive crack growth. Engineering Fracture Mechanics, 69(7), 813–833.

Mohtarami, E., Baghbanan, A., & Hashemolhosseini, H. (2017). Prediction of fracture trajectory in anisotropic rocks using modified maximum tangential stress criterion. Computers and Geotechnics, 92, 108–120.

Montgomery DC (2019) Design and Analysis of Experiments 8th Edition, 10th edition.

Moradian Z, Einstein HH, Ballivy G (2016) Detection of Cracking Levels in Brittle Rocks by Parametric Analysis of the Acoustic Emission Signals. Rock Mechanics and Rock Engineering 49:785–800.

Morgan SP, Johnson CA, Einstein HH (2013) Cracking processes in Barre granite: Fracture process zones and crack coalescence. International Journal of Fracture 180:177–204.

Moriasi D, Arnold J, Liew M, et al (2007) Model Evaluation Guidelines for Systematic Quantification of Accuracy in Watershed Simulations. Transactions of the ASABE 50:885–900.

Muralidhara S, Prasad BKR, Eskandari H, Karihaloo BL (2010) Fracture process zone size and true fracture energy of concrete using acoustic emission. Construction and Building Materials 24:479–486.

Nasseri MHB, Grasselli G, Mohanty B (2010) Fracture Toughness and Fracture Roughness in Anisotropic Granitic Rocks. Rock Mechanics and Rock Engineering 43:403–415.

Nooru-Mohamed MB (1992) Mixed-mode fracture of concrete: An experimental approach. Delft University of Technology

Oakley JE, O'Hagan A (2004) Probabilistic sensitivity analysis of complex models: a Bayesian approach. Journal of the Royal Statistical Society: Series B (Statistical Methodology) 66(3):751-769.

Obara Y, Nakamura K, Yoshioka S, et al (2020) Crack Front Geometry and Stress Intensity Factor of Semi-circular Bend Specimens with Straight Through and Chevron Notches. Rock Mechanics and Rock Engineering 53:723–738.

Oh J-C, Kim H-G (2013) Inverse estimation of cohesive zone laws from experimentally measured displacements for the quasi-static mode I fracture of PMMA. Engineering Fracture Mechanics 99:118–131.

Ohno, K. (2015). Identification of the fracture process zone in concrete materials by acoustic emission. In Acoustic Emission (AE) and Related Non-destructive Evaluation (NDE) Techniques in the Fracture Mechanics of Concrete: Fundamentals and Applications (pp. 41–55). Elsevier Inc.

Otsuka, A., Mori, K., & Miyata, T. (1975). The condition of fatigue crack growth in mixed mode condition. Engineering Fracture Mechanics, 7(3), 429–439.

Palmer AC, Rice JR, Hill R (1973) The growth of slip surfaces in the progressive failure of over-consolidated clay. Proceedings of the Royal Society of London A Mathematical and Physical Sciences 332:527–548.

Pan B, Asundi A, Xie H, Gao J (2009) Digital image correlation using iterative least squares and pointwise least squares for displacement field and strain field measurements. Optics and Lasers in Engineering 47:865–874.

Pandit B, Tiwari G, Latha GM, Babu GLS (2019) Probabilistic Characterization of Rock Mass from Limited Laboratory Tests and Field Data: Associated Reliability Analysis and Its Interpretation. Rock Mechanics and Rock Engineering 52:2985–3001.

Pandit, B., & Babu, G. L. (2020) Global Sensitivity Analysis of Rockmass and Support Design Parameters in Tunnel-Support System. In 54th US Rock Mechanics/Geomechanics Symposium. American Rock Mechanics Association.

Parisio F, Tarokh A, Makhnenko R, et al (2019) Experimental characterization and numerical modelling of fracture processes in granite. International Journal of Solids and Structures 163:102–116.

Park CH, Bobet A (2009) Crack coalescence in specimens with open and closed flaws: A comparison. International Journal of Rock Mechanics and Mining Sciences 46:819–829.

Park K, Paulino GH, Roesler JR (2009) A unified potential-based cohesive model of mixed-mode fracture. J Mech Phys Solids 57:891–908.

Park, C. H., & Bobet, A. (2009). Crack coalescence in specimens with open and closed flaws: A comparison. International Journal of Rock Mechanics and Mining Sciences, 46(5), 819–829.

Peerlings, R.H.J., De Borst R., Brekelmans W.A.M., De J.H.P., (1996). Gradient Enchanced Damage for quasi-brittle materials. . Int J Numer Methods Eng 39:3391–3403.

Petersson P-E (1981) Crack growth and development of fracture zones in plain concrete and similar materials. Sweden

Planas, J., Elices, M., Guinea, G. v, Gómez, F. J., Cendón, D. A., & Arbilla, I. (2003). Generalizations and specializations of cohesive crack models. Engineering Fracture Mechanics, 70(14), 1759–1776.

Rabczuk T (2013) Computational Methods for Fracture in Brittle and Quasi-Brittle Solids: State-of-the-Art Review and Future Perspectives. ISRN Applied Mathematics 2013:1–38.

Rabczuk T, Belytschko T (2004) Cracking particles: a simplified meshfree method for arbitrary evolving cracks. Int J Numer Methods Eng 61:2316–2343.

Rao, Q., Sun, Z., Stephansson, O., Li, C., & Stillborg, B. (2003). Shear fracture (Mode II) of brittle rock. International Journal of Rock Mechanics and Mining Sciences, 40(3), 355–375.

Remij EW, Remmers JJC, Huyghe JM, Smeulders DMJ (2018) On the numerical simulation of crack interaction in hydraulic fracturing. Comput Geosci 22:423–437.

Remij EW, Remmers JJC, Pizzocolo F, et al (2015) A Partition of Unity-Based Model for Crack Nucleation and Propagation in Porous Media, Including Orthotropic Materials. Transp Porous Media 106:505–522.

Remmers JJC, de Borst R, Needleman A (2003) A cohesive segments method for the simulation of crack growth. Comput Mech 31:69–77.

Ren, L., Zhu, Z., Yang, Q., & Ai, T. (2013). Investigation on the Applicability of Several Fracture Criteria to the Mixed Mode Brittle Fractures. Advances in Mechanical Engineering, 5, 545108.

Rice, J. R. (1968). A Path Independent Integral and the Approximate Analysis of Strain Concentration by Notches and Cracks. Journal of Applied Mechanics, 35(2), 379–386.

Richefeu V, Chrysochoos A, Huon V, et al (2012) Toward local identification of cohesive zone models using digital image correlation. European Journal of Mechanics - A/Solids 34:38–51.

Rinehart, A. J., Bishop, J. E., & Dewers, T. (2015). Fracture propagation in Indiana Limestone interpreted via linear softening cohesive fracture model. Journal of Geophysical Research: Solid Earth, 120(4), 2292–2308.

Roesler J, Paulino GH, Park K, Gaedicke C (2007) Concrete fracture prediction using bilinear softening. Cement and Concrete Composites 29:300–312.

Rubin AM (1993) Tensile fracture of rock at high confining pressure: Implications for dike propagation. Journal of Geophysical Research: Solid Earth 98:15919–15935.

Saadat M, Taheri A (2019) Modelling Micro-cracking Behaviour of Pre-cracked Granite Using Grain-Based Distinct Element Model. Rock Mechanics and Rock Engineering 52:4669–4692.

Sagong, M., & Bobet, A. (2002). Coalescence of multiple flaws in a rock-model material in uniaxial compression. International Journal of Rock Mechanics and Mining Sciences, 39(2), 229–241.

Salimzadeh S, Khalili N (2015) A three-phase XFEM model for hydraulic fracturing with cohesive crack propagation. Comput Geotech 69:82–92.

Saltelli A, Ratto M, Andres T, et al (2008) Global sensitivity analysis: The Primer, 1st Edition. John Wiley & Sons Ltd, West Sussex.

Sarkar, S., Kumar, R., & Murthy, V. M. S. R. (2019). Experimental and Numerical Simulation of Crack Propagation in Sandstone by Semi Circular Bend Test. Geotechnical and Geological Engineering, 37(4), 3157–3169.

Saucedo L, Yu RC, Ruiz G (2012) Fully-developed FPZ length in quasi-brittle materials. International Journal of Fracture 178:97–112.

Schreier H, Orteu J-J, Sutton MA (2009) Image Correlation for Shape, Motion and Deformation Measurements. Springer US, Boston, MA

Sharafisafa M, Nazem M (2014) Application of the distinct element method and the extended finite element method in modelling cracks and coalescence in brittle materials. Computational Materials Science 91:102–121.

Sharafisafa, Mansour, Shen, L., & Xu, Q. (2018). Characterisation of mechanical behaviour of 3D printed rock-like material with digital image correlation. International Journal of Rock Mechanics and Mining Sciences, 112, 122–138.

Sharpe WN (2008) Springer Handbook of Experimental Solid Mechanics, William N. Springer US, Boston, MA

Shet C, Chandra N (2004) Effect of the Shape of T–δ Cohesive Zone Curves on the Fracture Response. Mechanics of Advanced Materials and Structures 11:249–275.

Shirole D, Hedayat A, Walton G (2020a) Illumination of Damage in Intact Rocks by Ultrasonic Transmission-Reflection and Digital Image Correlation. Journal of Geophysical Research: Solid

Shirole D, Walton G, Hedayat A (2020b) Experimental investigation of multi-scale strain-field heterogeneity in rocks. International Journal of Rock Mechanics and Mining Sciences 127.

Shirole, D., Hedayat, A., & Walton, G. (2019). Experimental Relationship Between Compressional Wave Attenuation and Surface Strains in Brittle Rock. Journal of Geophysical Research: Solid Earth, 124(6), 5770–5793.

Siavelis M, Guiton MLE, Massin P, Moës N (2013) Large sliding contact along branched discontinuities with X-FEM. Comput Mech 52:201–219. https://doi.org/10.1007/s00466-012-0807-6

Sih, G. C. (1974). Strain-energy-density factor applied to mixed mode crack problems. International Journal of Fracture, 10(3), 305–321. https://doi.org/10.1007/BF00035493

Skarżyński, Ł., Kozicki, J., & Tejchman, J. (2013). Application of DIC Technique to Concrete—Study on Objectivity of Measured Surface Displacements. Experimental Mechanics, 53(9), 1545–1559.

Skarżyński, Ł., Syroka, E., & Tejchman, J. (2011). Measurements and Calculations of the Width of the Fracture Process Zones on the Surface of Notched Concrete Beams. Strain, 47(s1), e319–e332.

Smith, D. J., Ayatollahi, M. R., & Pavier, M. J. (2001). The role of T-stress in brittle fracture for linear elastic materials under mixed-mode loading. Fatigue & Fracture of Engineering Materials & Structures, 24(2), 137–150.

Soares JB, de Freitas FAC, Allen DH (2003) Considering Material Heterogeneity in Crack Modeling of Asphaltic Mixtures. Transportation Research Record 1832:113–120.

Sobol I.M. (1993) Sensitivity estimates for nonlinear mathematical models. Math. Mod. Comput. Exp. 1:407-414.

Song HS, H PG, G BW (2006) Simulation of Crack Propagation in Asphalt Concrete Using an Intrinsic Cohesive Zone Model. Journal of Engineering Mechanics 132:1215–1223.

Song J-H, Areias PMA, Belytschko T (2006a) A method for dynamic crack and shear band propagation with phantom nodes. Int J Numer Methods Eng 67:868–893.

Sun Y, Edwards MG, Chen B, Li C (2021) A state-of-the-art review of crack branching. Eng Fract Mech 257:108036.

Sutton MA, Yan JH, Deng X, et al (2007) Three-dimensional digital image correlation to quantify deformation and crack-opening displacement in ductile aluminum under mixed-mode I/III loading. Optical Engineering 46:1–17. https://doi.org/10.1117/1.2741279

Tang, S. B., Bao, C. Y., & Liu, H. Y. (2017). Brittle fracture of rock under combined tensile and compressive loading conditions. Canadian Geotechnical Journal, 54(1), 88–101.

Tutluoglu, L., & Keles, C. (2011). Mode I fracture toughness determination with straight notched disk bending method. International Journal of Rock Mechanics and Mining Sciences, 48(8), 1248–1261. https://doi.org/https://doi.org/10.1016/j.ijrmms.2011.09.019

Vallejo, L. E. (1988). The brittle and ductile behavior of clay samples containing a crack under mixed mode loading.

Vásárhelyi, B., & Bobet, A. (2000). Modeling of Crack Initiation, Propagation and Coalescence in Uniaxial Compression. Rock Mechanics and Rock Engineering, 33(2), 119–139.

Wang C, Zhu ZM, Liu HJ (2016) On the I–II mixed mode fracture of granite using four-point bend specimen. Fatigue and Fracture of Engineering Materials and Structures 39:1193–1203.

Wang H, Zhang C, Yang L, You Z (2013) Study on the rubber-modified asphalt mixtures' cracking propagation using the extended finite element method. Construction and Building Materials 47:223–230.

Wang JT (2012) Investigating Some Technical Issues on Cohesive Zone Modeling of Fracture. Journal of Engineering Materials and Technology 135.

Wang Q, Fang H, Shen L (2016) Reliability analysis of tunnels using a metamodeling technique based on augmented radial basis functions. Tunnelling and Underground Space Technology 56:45–53.

Wang X, Asem P, Hu C, Labuz JF (2021) Microcracking in tensile fracture of a brittle rock. Engineering Fracture Mechanics 251:107789.

Wang Y, Hu X (2017) Determination of Tensile Strength and Fracture Toughness of Granite Using Notched Three-Point-Bend Samples. Rock Mechanics and Rock Engineering 50:17–28.

Wang Y, Waisman H (2018) An arc-length method for controlled cohesive crack propagation using high-order XFEM and Irwin's crack closure integral. Eng Fract Mech 199:235–256.

Wang, C., Zhu, Z. M., & Liu, H. J. (2016). On the I–II mixed mode fracture of granite using four-point bend specimen. Fatigue and Fracture of Engineering Materials and Structures, 39(10), 1193–1203.

Wang, H., Zhang, C., Yang, L., & You, Z. (2013). Study on the rubber-modified asphalt mixtures' cracking propagation using the extended finite element method. Construction and Building Materials, 47, 223–230.

Wei MD, Dai F, Xu NW, et al (2016) Experimental and numerical study on the fracture process zone and fracture toughness determination for ISRM-suggested semi-circular bend rock specimen. Engineering Fracture Mechanics 154:43–56.

Wei S, Wang C, Yang Y, Wang M (2020) Physical and Mechanical Properties of Gypsum-Like Rock Materials. Advances in Civil Engineering 2020:3703706.

Wei, M.-D., Dai, F., Xu, N.-W., Liu, Y., & Zhao, T. (2017). Fracture prediction of rocks under mode I and mode II loading using the generalized maximum tangential strain criterion. Engineering Fracture Mechanics, 186, 21–38.

Wells GN, Sluys LJ (2001) A new method for modelling cohesive cracks using finite elements. Int J Numer Methods Eng 50:2667–2682. https://doi.org/https://doi.org/10.1002/nme.143

Whittaker, B. N., Singh, R. N., & Sun, G. (1992). Rock Fracture Mechanics: Principles, Design and Applications. Elsevier Science Publishers.

Wittmann FH, Hu X (1991) Fracture process zone in cementitious materials. International Journal of Fracture 51:3–18.

Wong LNY, Guo TY (2019) Microcracking behavior of two semi-circular bend specimens in Mode I fracture toughness test of granite. Engineering Fracture Mechanics 221:106565.

Wong NY (2008) Crack Coalescence in Molded Gypsum and Carrara Marble

Wong, Louis Ngai Yuen, & Li, H. Q. (2013). Numerical study on coalescence of two pre-existing coplanar flaws in rock. International Journal of Solids and Structures, 50(22–23), 3685–3706.

Wu Z (1995) Compactly supported positive definite radial functions. Advances in Computational Mathematics 4:283.

Wu ZM, Rong H, Zheng JJ, et al (2011) An experimental investigation on the FPZ properties in concrete using digital image correlation technique. Engineering Fracture Mechanics 78:2978–2990.

Wu, L. Z., Li, B., Huang, R. Q., & Wang, Q. Z. (2016). Study on Mode I–II hybrid fracture criteria for the stability analysis of sliding overhanging rock. Engineering Geology, 209, 187–195.

Wu, Z. M., Rong, H., Zheng, J. J., Xu, F., & Dong, W. (2011). An experimental investigation on the FPZ properties in concrete using digital image correlation technique. Engineering Fracture Mechanics, 78(17), 2978–2990.

Xie Y, Cao P, Liu J, Dong L (2016) Influence of crack surface friction on crack initiation and propagation: A numerical investigation based on extended finite element method. Comput Geotech 74:1–14.

Xie, Y., Cao, P., Jin, J., & Wang, M. (2017). Mixed mode fracture analysis of semi-circular bend (SCB) specimen: A numerical study based on extended finite element method. Computers and Geotechnics, 82, 157–172.

Xing, Y., Zhang, G., Wan, B., & Zhao, H. (2019). Subcritical Fracturing of Sandstone Characterized by the Acoustic Emission Energy. Rock Mechanics and Rock Engineering, 52(7), 2459–2469.

Xu D, Liu Z, Liu X, et al (2014) Modeling of dynamic crack branching by enhanced extended finite element method. Comput Mech 54:489–502. https://doi.org/10.1007/s00466-014-1001-9

Xu Y, Li X, Wang X, Liang L (2014) Inverse parameter identification of cohesive zone model for simulating mixed-mode crack propagation. International Journal of Solids and Structures 51:2400–2410.

Yang D, Zhou Y, Xia X, et al (2019a) Extended finite element modeling nonlinear hydro-mechanical process in saturated porous media containing crossing fractures. Comput Geotech 111:209–221.

Yang J, Lian H, Liang W, et al (2019) Model I cohesive zone models of different rank coals. International Journal of Rock Mechanics and Mining Sciences 115:145–156.

Yang, J., Lian, H., Liang, W., Nguyen, V. P., & Bordas, S. P. A. (2019). Model I cohesive zone models of different rank coals. International Journal of Rock Mechanics and Mining Sciences, 115, 145–156.

Yang, S.-Q. (2011). Crack coalescence behavior of brittle sandstone samples containing two coplanar fissures in the process of deformation failure. Engineering Fracture Mechanics, 78(17), 3059–3081.

Yao, Y. (2012). Linear Elastic and Cohesive Fracture Analysis to Model Hydraulic Fracture in Brittle and Ductile Rocks. Rock Mechanics and Rock Engineering, 45(3), 375–387.

Yin, Q., Jing, H., & Su, H. (2018). Investigation on mechanical behavior and crack coalescence of sandstone specimens containing fissure-hole combined flaws under uniaxial compression. Geosciences Journal, 22(5), 825–842.

Youn DJ (2016) Hydro-mechanical coupled simulation of hydraulic fracturing using the extended finite element method (XFEM)

Yu, M., Wei, C., Niu, L., Li, S., & Yu, Y. (2018). Calculation for tensile strength and fracture toughness of granite with three kinds of grain sizes using three-point-bending test. PLoS ONE, 13(3).

Yue, Z., Song, Y., Li, P., Tian, S., Ming, X., & Chen, Z. (2019). Applications of Digital Image Correlation (DIC) and the Strain Gage Method for Measuring Dynamic Mode I Fracture Parameters of the White Marble Specimen. Rock Mechanics and Rock Engineering, 52(11), 4203–4216.

Zamani A, Gracie R, Reza Eslami M (2012) Cohesive and non-cohesive fracture by higher-order enrichment of XFEM. Int J Numer Methods Eng 90:452–483.

Zdenek P. Bazant, Jaime Planas (1998) Fracture and Size Effect in Concrete and Other Quasibrittle Materials, 1st Edition. CRC Press, Routledge

Zhang C, Hu X, Wu Z, Li Q (2018) Influence of grain size on granite strength and toughness with reliability specified by normal distribution. Theoretical and Applied Fracture Mechanics 96:534–544.

Zhang X, Sloan SW, Vignes C, Sheng D (2017) A modification of the phase-field model for mixed mode crack propagation in rock-like materials. Comput Methods Appl Mech Eng 322:123–136.

Zhang XP, Wong LNY (2012) Cracking processes in rock-like material containing a single flaw under uniaxial compression: A numerical study based on parallel bonded-particle model approach. Rock Mech Rock Eng 45:711–737.

Zhang, G., Xing, Y., & Wang, L. (2018). Comprehensive sandstone fracturing characterization: Integration of fiber Bragg grating, digital imaging correlation and acoustic emission measurements. Engineering Geology, 246, 45–56.

Zhao, C., Ma, C., Zhao, C., Du, S., & Bao, C. (2018). Crack propagation simulation of rock-like specimen using strain criterion. European Journal of Environmental and Civil Engineering, 22(sup1), s228–s245.

Zhou X-P, Chen J-W, Berto F (2020) XFEM based node scheme for the frictional contact crack problem. Computers & Structures 231:106221.

Zhou, X. P., Lian, Y. J., Wong, L. N. Y., & Berto, F. (2018). Understanding the fracture behavior of brittle and ductile multi-flawed rocks by uniaxial loading by digital image correlation. Engineering Fracture Mechanics, 199, 438–460.

Zhuang, X., Chun, J., & Zhu, H. (2014). A comparative study on unfilled and filled crack propagation for rock-like brittle material. Theoretical and Applied Fracture Mechanics, 72, 110–120.

Zi G, Belytschko T (2003) New crack-tip elements for XFEM and applications to cohesive cracks. International Journal for Numerical Methods in Engineering 57:2221–2240.

Zietlow, W. K., & Labuz, J. F. (1998). Measurement of the intrinsic process zone in rock using acoustic emission. International Journal of Rock Mechanics and Mining Sciences, 35(3), 291–299.

APPENDIX A

PERMISSION FROM PUBLISHERS AND CO-AUTHORS

Prasoon Garg

From: Permissions Helpdesk <permissionshelpdesk@elsevier.com>
Sent: Tuesday, January 10, 2023 4:05 PM
To: Prasoon Garg
Subject: [External] Re: Request permissions to repreint the paper authored by me (Prasoon Ga) [230111-004995]

Dear Customer

Thank you for contacting Elsevier's Permissions Helpdesk.

This is an automated acknowledgement to confirm we have received your query. Ticket number 230111-004995 has been opened on your behalf and we aim to respond within two business days.

Regards,

Permissions Helpdesk

From: Prasoon Garg
Date: 10/01/2023 11.04 PM

Dear Elsevier,

I would like to request permission to use the one paper that I published with Elsevier in my PhD thesis.

Paper (Published):
Title: Prasoon Garg, Sana Zafar, Ahmadreza Hedayat, Omid Z Moradian, D.V. Griffiths. (2023). A novel methodology for characterizing fracture process zone evolution in Barre granite specimens under mode I loading,
Journal Theoretical and Applied Fracture Mechanics,123, 0167-8442,
https://doi.org/10.1016/j.tafmec.2022.103727.

I would like to reprint this paper in my PhD thesis, but I am required by the school to firstly obtain the permission from the publishers.
I kindly request you to grants me permission to use the papers in my thesis.
Thanks for the help and your time.

Prasoon Garg

From: Permissions Helpdesk <permissionshelpdesk@elsevier.com>
Sent: Wednesday, January 11, 2023 8:21 AM
To: Prasoon Garg
Subject: [External] Re: Request permissions to repreint the paper authored by me (Prasoon Ga) [230111-004995]

Dear Prasoon Garg,

Thank you so much for contacting us.

Please note that, as one of the authors of this article, you retain the right to reuse it in your thesis/dissertation. You do not require formal permission to do so. You are permitted to post this Elsevier article online if it is embedded within your thesis subject to proper acknowledgment;

Our preferred acknowledgement wording will be:

Example: "This article/chapter was published in Publication title, Vol number, Author(s), Title of article, Page Nos, Copyright Elsevier (or appropriate Society name) (Year)."

All the best for your thesis submission!

Kind regards,

Kaveri Thakuria

Senior Copyrights Coordinator

ELSEVIER | HCM - Health Content Management

Visit Elsevier Permissions

Prasoon Garg

From: no-reply@email.copyright.com
Sent: Tuesday, January 10, 2023 4:18 PM
To: Prasoon Garg
Subject: [External] Thank you for your order with RightsLink / Springer Nature

SPRINGER NATURE

Thank you for your order!

Dear Mr. Prasoon Garg,

Thank you for placing your order through Copyright Clearance Center's RightsLink® service.

Order Summary

Licensee:	Colorado School of Mines
Order Date:	Jan 10, 2023
Order Number:	5465571305692
Publication:	Rock Mechanics and Rock Engineering
Title:	An Integrated Approach for Evaluation of Linear Cohesive Zone Model's Performance in Fracturing of Rocks
Type of Use:	Thesis/Dissertation
Order Total:	0.00 USD

View or print complete details of your order and the publisher's terms and conditions.

Sincerely,

Copyright Clearance Center

Tel: +1-855-239-3415 / +1-978-646-2777
customercare@copyright.com
https://myaccount.copyright.com

CCC RightsLink

1

SPRINGER NATURE LICENSE
TERMS AND CONDITIONS

Jan 10, 2023

This Agreement between Colorado School of Mines -- Prasoon Garg ("You") and Springer Nature ("Springer Nature") consists of your license details and the terms and conditions provided by Springer Nature and Copyright Clearance Center.

License Number	5465571305692
License date	Jan 10, 2023
Licensed Content Publisher	Springer Nature
Licensed Content Publication	Rock Mechanics and Rock Engineering
Licensed Content Title	An Integrated Approach for Evaluation of Linear Cohesive Zone Model's Performance in Fracturing of Rocks
Licensed Content Author	Prasoon Garg et al
Licensed Content Date	Jul 2, 2021
Type of Use	Thesis/Dissertation
Requestor type	academic/university or research institute
Format	print and electronic
Portion	full article/chapter
Will you be translating?	no

Circulation/distribution	500 - 999
Author of this Springer Nature content	yes
Title	Graduate research assistant
Institution name	Colorado school of mines
Expected presentation date	Jan 2023
Requestor Location	Colorado School of Mines 1518 Washington Ave GOLDEN, CO 80401 United States Attn: Colorado School of Mines
Total	0.00 USD

Terms and Conditions

Springer Nature Customer Service Centre GmbH Terms and Conditions

The following terms and conditions ("Terms and Conditions") together with the terms specified in your [RightsLink] constitute the License ("License") between you as Licensee and Springer Nature Customer Service Centre GmbH as Licensor. By clicking 'accept' and completing the transaction for your use of the material ("Licensed Material"), you confirm your acceptance of and obligation to be bound by these Terms and Conditions.

1. Grant and Scope of License

1. 1. The Licensor grants you a personal, non-exclusive, non-transferable, non-sublicensable, revocable, world-wide License to reproduce, distribute, communicate to the public, make available, broadcast, electronically transmit or create derivative works using the Licensed Material for the purpose(s) specified in your RightsLink Licence Details only. Licenses are granted for the specific use requested in the order and for no other use, subject to these Terms and Conditions. You acknowledge and agree that the rights granted to you under this License do not include the right to modify, edit, translate, include in collective works, or create derivative works of the Licensed Material in whole or in part unless expressly stated in your RightsLink Licence Details. You may use the Licensed Material only as permitted under this Agreement and will not reproduce, distribute, display, perform, or otherwise use or

exploit any Licensed Material in any way, in whole or in part, except as expressly permitted by this License.

1. 2. You may only use the Licensed Content in the manner and to the extent permitted by these Terms and Conditions, by your RightsLink Licence Details and by any applicable laws.

1. 3. A separate license may be required for any additional use of the Licensed Material, e.g. where a license has been purchased for print use only, separate permission must be obtained for electronic re-use. Similarly, a License is only valid in the language selected and does not apply for editions in other languages unless additional translation rights have been granted separately in the License.

1. 4. Any content within the Licensed Material that is owned by third parties is expressly excluded from the License.

1. 5. Rights for additional reuses such as custom editions, computer/mobile applications, film or TV reuses and/or any other derivative rights requests require additional permission and may be subject to an additional fee. Please apply to journalpermissions@springernature.com or bookpermissions@springernature.com for these rights.

2. Reservation of Rights

Licensor reserves all rights not expressly granted to you under this License. You acknowledge and agree that nothing in this License limits or restricts Licensor's rights in or use of the Licensed Material in any way. Neither this License, nor any act, omission, or statement by Licensor or you, conveys any ownership right to you in any Licensed Material, or to any element or portion thereof. As between Licensor and you, Licensor owns and retains all right, title, and interest in and to the Licensed Material subject to the license granted in Section 1.1. Your permission to use the Licensed Material is expressly conditioned on you not impairing Licensor's or the applicable copyright owner's rights in the Licensed Material in any way.

3. Restrictions on use

3. 1. Minor editing privileges are allowed for adaptations for stylistic purposes or formatting purposes provided such alterations do not alter the original meaning or intention of the Licensed Material and the new figure(s) are still accurate and representative of the Licensed Material. Any other changes including but not limited to, cropping, adapting, and/or omitting material that affect the meaning, intention or moral rights of the author(s) are strictly prohibited.

3. 2. You must not use any Licensed Material as part of any design or trademark.

3. 3. Licensed Material may be used in Open Access Publications (OAP), but any such reuse must include a clear acknowledgment of this permission visible at the same time as the figures/tables/illustration or abstract and which must indicate that the Licensed Material is not part of the governing OA license but has been reproduced with permission. This may be indicated according to any standard referencing system but must include at a minimum 'Book/Journal title, Author, Journal Name (if applicable), Volume (if applicable), Publisher, Year, reproduced with permission from SNCSC'.

4. STM Permission Guidelines

4. 1. An alternative scope of license may apply to signatories of the STM Permissions Guidelines ("STM PG") as amended from time to time and made available at https://www.stm-assoc.org/intellectual-property/permissions/permissions-guidelines/.

4. 2. For content reuse requests that qualify for permission under the STM PG, and which may be updated from time to time, the STM PG supersede the terms and conditions contained in this License.

4. 3. If a License has been granted under the STM PG, but the STM PG no longer apply at the time of publication, further permission must be sought from the Rightsholder. Contact journalpermissions@springernature.com or bookpermissions@springernature.com for these rights.

5. Duration of License

5. 1. Unless otherwise indicated on your License, a License is valid from the date of purchase ("License Date") until the end of the relevant period in the below table:

Reuse in a medical communications project	Reuse up to distribution or time period indicated in License
Reuse in a dissertation/thesis	Lifetime of thesis
Reuse in a journal/magazine	Lifetime of journal/magazine
Reuse in a book/textbook	Lifetime of edition
Reuse on a website	1 year unless otherwise specified in the License
Reuse in a presentation/slide kit/poster	Lifetime of presentation/slide kit/poster. Note: publication whether electronic or in print of presentation/slide kit/poster may require further permission.
Reuse in conference proceedings	Lifetime of conference proceedings
Reuse in an annual report	Lifetime of annual report
Reuse in training/CME materials	Reuse up to distribution or time period indicated in License
Reuse in newsmedia	Lifetime of newsmedia
Reuse in coursepack/classroom materials	Reuse up to distribution and/or time period indicated in license

6. Acknowledgement

6. 1. The Licensor's permission must be acknowledged next to the Licensed Material in print. In electronic form, this acknowledgement must be visible at the same time as the figures/tables/illustrations or abstract and must be hyperlinked to the journal/book's homepage.

6. 2. Acknowledgement may be provided according to any standard referencing system and at a minimum should include "Author, Article/Book Title, Journal name/Book imprint, volume, page number, year, Springer Nature".

7. Reuse in a dissertation or thesis

7. 1. Where 'reuse in a dissertation/thesis' has been selected, the following terms apply: Print rights of the Version of Record are provided for; electronic rights for use only on institutional repository as defined by the Sherpa guideline (www.sherpa.ac.uk/romeo/) and only up to what is required by the awarding institution.

7. 2. For theses published under an ISBN or ISSN, separate permission is required. Please contact journalpermissions@springernature.com or bookpermissions@springernature.com for these rights.

7. 3. Authors must properly cite the published manuscript in their thesis according to current citation standards and include the following acknowledgement: '*Reproduced with permission from Springer Nature*'.

8. License Fee

You must pay the fee set forth in the License Agreement (the "License Fees"). All amounts payable by you under this License are exclusive of any sales, use, withholding, value added or similar taxes, government fees or levies or other assessments. Collection and/or remittance of such taxes to the relevant tax authority shall be the responsibility of the party who has the legal obligation to do so.

9. Warranty

9. 1. The Licensor warrants that it has, to the best of its knowledge, the rights to license reuse of the Licensed Material. **You are solely responsible for ensuring that the material you wish to license is original to the Licensor and does not carry the copyright of another entity or third party (as credited in the published version).** If the credit line on any part of the Licensed Material indicates that it was reprinted or adapted with permission from another source, then you should seek additional permission from that source to reuse the material.

9. 2. EXCEPT FOR THE EXPRESS WARRANTY STATED HEREIN AND TO THE EXTENT PERMITTED BY APPLICABLE LAW, LICENSOR PROVIDES THE LICENSED MATERIAL "AS IS" AND MAKES NO OTHER REPRESENTATION OR WARRANTY. LICENSOR EXPRESSLY DISCLAIMS ANY LIABILITY FOR ANY CLAIM ARISING FROM OR OUT OF THE CONTENT, INCLUDING BUT NOT LIMITED TO ANY ERRORS, INACCURACIES, OMISSIONS, OR DEFECTS CONTAINED THEREIN, AND ANY IMPLIED OR EXPRESS WARRANTY AS TO MERCHANTABILITY OR FITNESS FOR A PARTICULAR PURPOSE. IN NO EVENT SHALL LICENSOR BE LIABLE TO YOU OR ANY OTHER PARTY OR ANY OTHER PERSON OR FOR ANY SPECIAL, CONSEQUENTIAL, INCIDENTAL, INDIRECT, PUNITIVE, OR EXEMPLARY DAMAGES, HOWEVER CAUSED, ARISING OUT OF OR IN CONNECTION WITH THE DOWNLOADING, VIEWING OR USE OF THE LICENSED MATERIAL REGARDLESS OF THE FORM OF ACTION, WHETHER FOR BREACH OF CONTRACT, BREACH OF WARRANTY, TORT, NEGLIGENCE, INFRINGEMENT OR OTHERWISE (INCLUDING, WITHOUT LIMITATION, DAMAGES BASED ON LOSS OF PROFITS, DATA, FILES, USE, BUSINESS OPPORTUNITY OR CLAIMS OF THIRD PARTIES), AND WHETHER OR NOT THE PARTY HAS BEEN ADVISED OF THE POSSIBILITY OF SUCH

DAMAGES. THIS LIMITATION APPLIES NOTWITHSTANDING ANY FAILURE OF ESSENTIAL PURPOSE OF ANY LIMITED REMEDY PROVIDED HEREIN.

10. Termination and Cancellation

10. 1. The License and all rights granted hereunder will continue until the end of the applicable period shown in Clause 5.1 above. Thereafter, this license will be terminated and all rights granted hereunder will cease.

10. 2. Licensor reserves the right to terminate the License in the event that payment is not received in full or if you breach the terms of this License.

11. General

11. 1. The License and the rights and obligations of the parties hereto shall be construed, interpreted and determined in accordance with the laws of the Federal Republic of Germany without reference to the stipulations of the CISG (United Nations Convention on Contracts for the International Sale of Goods) or to Germany´s choice-of-law principle.

11. 2. The parties acknowledge and agree that any controversies and disputes arising out of this License shall be decided exclusively by the courts of or having jurisdiction for Heidelberg, Germany, as far as legally permissible.

11. 3. This License is solely for Licensor's and Licensee's benefit. It is not for the benefit of any other person or entity.

Questions? For questions on Copyright Clearance Center accounts or website issues please contact springernaturesupport@copyright.com or +1-855-239-3415 (toll free in the US) or +1-978-646-2777. For questions on Springer Nature licensing please visit https://www.springernature.com/gp/partners/rights-permissions-third-party-distribution

Other Conditions:

Version 1.4 - Dec 2022

Questions? customercare@copyright.com or +1-855-239-3415 (toll free in the US) or +1-978-646-2777.

Prasoon Garg

From: Omid Moradian
Sent: Thursday, January 12, 2023 4:01 PM
To: Prasoon Garg
Subject: Re: Co-author Permission Garg

Hello Prasoon,
Sure, I hereby give you my consent to use the full content of the paper in your Phd thesis.
Best
Omid

From: Prasoon Garg <pgarg@mines.edu>
Sent: Thursday, January 12, 2023 3:52:35 PM
To: Omid Moradian <moradian@mines.edu>
Subject: Co-author Permission Garg

Hello Dr. Omid,

Please disregard the earlier email. I hope you are doing well. I'm close to submitting my Ph.D. thesis work here at the Colorado School of mines.

I am writing this email to kindly ask your consent to use the full content of the paper entitled below:

A novel methodology for characterizing fracture process zone evolution in Barre granite specimens under mode I loading.

to be included in my Ph.D. thesis as required by the school. The co-author permission can be given by responding to this email.

I am thankful for your time.

Prasoon Garg
Ph.D. Candidate
Coolbaugh Hall- 108
Department of Civil and Environmental Engineering
Colorado School of Mines
Golden, Colorado, USA.

Prasoon Garg
Ph.D. Candidate
Coolbaugh Hall- 108
Department of Civil and Environmental Engineering
Colorado School of Mines
Golden, Colorado, USA.

Prasoon Garg

From: Sana Zafar
Sent: Thursday, January 12, 2023 3:57 PM
To: Prasoon Garg
Subject: RE: Co-author Permission Garg

Yes.

Sana

From: Prasoon Garg <pgarg@mines.edu>
Sent: Thursday, January 12, 2023 3:55 PM
To: Sana Zafar <sanazafar@mines.edu>
Subject: Co-author Permission Garg

Hello Sana,

I hope you are doing well. I'm close to submitting my Ph.D. thesis work here at the Colorado School of mines.

I am writing this email to kindly ask your consent to use the full content of the paper entitled below.

A novel methodology for characterizing fracture process zone evolution in Barre granite specimens under mode I loading.

to be included in my Ph.D. thesis as required by the school. The co-author permission can be given by responding to this email.

I am thankful for your time.

Prasoon Garg
Ph.D. Candidate
Coolbaugh Hall- 108
Department of Civil and Environmental Engineering
Colorado School of Mines
Golden, Colorado, USA.

1

Prasoon Garg

From: Bhardwaj Pandit < bhardwajpandit93@gmail.com>
Sent: Thursday, January 12, 2023 6:56 PM
To: Prasoon Garg
Subject: [External] Re: Co-author Permission Garg

Dear Prasoon,

I give my approval to have the aforementioned work (paper) to be included in your thesis.

On Fri, Jan 13, 2023 at 4:27 AM Prasoon Garg <pgarg@mines.edu> wrote:

> Hello Dr. Pandit,
>
> I hope you are doing well. I'm close to submitting my Ph.D. thesis work here at the Colorado School of mines.
>
> I am writing this email to kindly ask your consent to use the full content of the paper entitled below:
>
> *An Integrated Approach for Evaluation of Linear Cohesive Zone Model's Performance in Fracturing of Rocks*
>
> to be included in my Ph.D. thesis as required by the school. The co-author permission can be given by responding to this email.
>
> I am thankful for your time.
>
> **Prasoon Garg**
>
> **Ph.D. Candidate**
>
> Coolbaugh Hall- 108
>
> Department of Civil and Environmental Engineering
> Colorado School of Mines
> Golden, Colorado, USA.

1

Prasoon Garg

From: Prof. Sivakumar babu G L <glsivakumar@gmail.com>
Sent: Thursday, January 12, 2023 6:39 PM
To: Prasoon Garg
Cc: Sivakumar Babu; Bhardwaj Pandit
Subject: [External] Re: Co-author Permission Garg

Dear Prasoon

It is fine with me.

Best wishes

On Fri, Jan 13, 2023, 04:32 Prasoon Garg <pgarg@mines.edu> wrote:

> Hello Prof. Babu,
>
> I hope you are doing well. I'm close to submitting my Ph.D. thesis work here at the Colorado School of mines.
>
> I am writing this email to kindly ask your consent to use the full content of the paper entitled below:
>
> *An Integrated Approach for Evaluation of Linear Cohesive Zone Model's Performance in Fracturing of Rocks*
>
> to be included in my Ph.D. thesis as required by the school. The co-author permission can be given by responding to this email. I hope you will not mind and can grant such permission to me.
>
> I am thankful for your time.
>
> **Prasoon Garg**
>
> **Ph.D. Candidate**
>
> Coolbaugh Hall- 108
>
> Department of Civil and Environmental Engineering
> Colorado School of Mines
> Golden, Colorado, USA.